SISSA
Scuola
Internazionale
Superiore di
Studi Avanzati

Physics Area - PhD course in
Astrophysics and Cosmology

Exploring Dark Matter's Nature from Local Galactic Dynamics to High-z JWST Observations

Candidate:
Giovanni Gandolfi

Supervisors:
Prof. Andrea Lapi
Prof. Stefano Liberati

Academic Year 2022-23

Questo è l'Isonzo
E qui meglio
Mi sono riconosciuto
Una docile fibra
Dell'universo

Giuseppe Ungaretti

Declaration of Authorship

I, Giovanni Gandolfi, declare that this thesis titled, *Exploring Dark Matter's Nature from Local Galactic Dynamics to High-z JWST Observations* and the work presented in it are my own. I confirm that:

- This work was done wholly or mainly while in candidature for a research degree at SISSA.
- Where any part of this thesis has previously been submitted for a degree or any other qualification at SISSA or any other institution, this has been clearly stated.
- Where I have consulted the published work of others, this is always clearly attributed.
- Where I have quoted from the work of others, the source is always given. With the exception of such quotations, this thesis is entirely my own work.
- I have acknowledged all main sources of help.
- Where the thesis is based on work done by myself jointly with others, I have made clear exactly what was done by others and what I have contributed myself.

Abstract

Exploring Dark Matter's Nature from Local Galactic Dynamics to High-z JWST Observations

by Giovanni Gandolfi

The Cold Dark Matter paradigm emerged as the prevailing solution to the cosmic missing mass conundrum. While highly successful on cosmological scales, this model is partially inconsistent with galaxy-scale observations. This thesis addresses such a challenge by pursuing a dual approach.
The first part presents a model featuring a dynamical non-minimal dark matter-gravity coupling originally developed in Bettoni et al. (2014). Such an effect is theoretically motivated and could solve some of the long-standing galaxy-scale issues of the Cold Dark Matter paradigm exploiting a single free parameter: the non-minimal coupling lengthscale. To begin with, I will study the self-gravitating equilibria of the dark matter halo predicted by this framework. Remarkably, the non-minimal coupling can produce cored dark matter halo profiles, similar in shape to the phenomenological Burkert model. Moreover, the predicted profiles are consistent with the core-surface density relation observed for dwarf galaxies. A Bayesian analysis will then test the non-minimally coupled dark matter model against stacked rotation curves of a broad sample of spiral galaxies. In terms of reduced chi-squared, the fits yielded by this model are always superior to the standard, Cold Dark Matter Navarro–Frenk–White profile and always competitive with the phenomenological Burkert profile. On the other hand, I will show how this model can explain the observed interplay between dark matter and baryons in late-type galaxies, embodied by tight dynamical scaling relations such as the Radial Acceleration Relation.
The analysis predicts a power-law relationship between the non-minimal coupling lengthscale and the virial mass of dark matter haloes. After using the non-minimally coupled dark matter model to fit galaxy clusters' pressure profiles from the X-COP collaboration, I will show that such scaling holds consistently from the dwarf-galaxy regime up to galaxy clusters' virial masses. Overall, this single-parameter simple model shows a rich phenomenology in a comprehensive set of scales capable of addressing long-standing issues of the Cold Dark Matter paradigm.
In the second part of the thesis, I will discuss how high-redshift observations from new, high-resolution instruments such as the James Webb Space Telescope can sig-

nificantly enhance our knowledge about dark matter. Specifically, I will present a new technique to constrain dark matter astroparticle properties that relies on JWST's cutting-edge high-redshift observations of the cosmic star formation rate density. The forecasts obtained with this technique demonstrate how upcoming ultra-faint galaxy surveys in the (pre) reionization era will be determinant to probe the microscopic nature of the elusive dark matter particles, potentially ruling out alternative dark matter models to the pure Cold Dark Matte framework.
In summary, the apparatus created within this thesis introduces novel techniques that have the potential to play a crucial role in the evaluation of both established and future models concerning dark matter or modified gravity theories. On the one hand, the analysis framework developed for assessing the characteristics of the non-minimally coupled dark matter model can be adapted for scrutinizing other alternative dark matter scenarios or modified gravity theories, including the ongoing investigation of the Fractional Gravity framework. On the other hand, the extensive observations conducted by JWST will extend further into the high-redshift Universe, rendering the methodologies outlined in this thesis exceptionally valuable in generating new and competitive constraints on the nature of dark matter.

This Ph.D. thesis is based on the following publications and submitted papers:

1. Self-gravitating Equilibria of Non-minimally Coupled Dark Matter Halos, by **Gandolfi G.**; Lapi, A.; and Liberati, S., *The Astrophysical Journal, Volume 910, Number 1*.

2. Empirical Evidence of Nonminimally Coupled Dark Matter in the Dynamics of Local Spiral Galaxies?, by **Gandolfi G.**; Lapi, A.; and Liberati, S., *The Astrophysical Journal, Volume 929, Number 1*.

3. Astroparticle Constraints from the Cosmic Star Formation Rate Density at High Redshift: Current Status and Forecasts for JWST, **Gandolfi G.**; Lapi, A.; Ronconi, T.; and Danese, L., *Universe 2022, 8(11), 589*.

4. Looking for Traces of Non-minimally Coupled Dark Matter in the X-COP Galaxy Clusters Sample, by **Gandolfi G.**; Haridasu, B. S.; Liberati, S.; and Lapi, A., *The Astrophysical Journal, Volume 952, Number 2*.

5. Dark Matter in Fractional Gravity I: Astrophysical Tests on Galactic Scales, by Benetti, F.; Lapi, A.; **Gandolfi G.**; Salucci, P.; and Danese, L., *The Astrophysical Journal, Volume 949, Number 2*.

6. Delving deep: A population of extremely dusty dwarfs observed by JWST, by Bisigello, L.; **Gandolfi G.**; Grazian, A.; Rodighiero, G.; Costantin, L.; Cooray, A. R.; Feltre, A.; Gruppioni, C.; Hathi, N. P.; Holwerda, B. W., Koekemoer, A. M.; Lucas, R. A.; Newman, J. A., Pérez-González, P. G.; L. Y. A., Yung; de la Vega, A.; Arrabal Haro, P.; Bagley, M. B.; Dickinson, M.; Finkelstein, S. L.; Kartaltepe, J. S.; Papovich, C.; Pirzkal, N.; and Wilkins, S., *Astronomy & Astrophysics, Volume 676*.

7. Dark Matter in Fractional Gravity II: Tests in Galaxy Clusters, by Benetti, F.; Lapi, A.; Haridasu, B. S.; Danese, L.; **Gandolfi G.**; Salucci, P.; and Danese, L., *Universe 2023, 9(7), 329*.

8. Dark Matter in Fractional Gravity III: Dwarf Galaxies Kinematics, by Benetti, F.; Lapi, A.; **Gandolfi G.**; Butt, M. A.; Boumechta, Y.; Haridasu, B. S.; and Baccigalupi, C., *Universe 2023, 9(11), 478*.

Other publications, submitted and forthcoming papers:

1. The Way of Water: ALMA resolves H_2O emission lines in a strongly lensed dusty star-forming galaxy at z ~ 3.1, by Perrotta F., Giulietti, M.; Massardi, M.; **Gandolfi, G.**; Ronconi, T.; Zanchettin, M. V.; D'Amato, Q.; Behiri, M.; Torsello, M.; Gabrielli, F.; Boco, L.; Galluzzi, V.; and Lapi, A., *The Astrophysical Journal, Volume 952, Number 1*.

2. Constraining the Initial Mass function in the Epoch of Reionization from Astrophysical and Cosmological data, by Lapi, A.; **Gandolfi, G.**; Boco, L.; Massardi, M.; Haridasu, B. S.; Baccigalupi, C.; Bressan, A.; and Danese, L., *in preparation*.

3. Observing Galaxies at the Cosmic Noon through Gravitational Lensing: Perspectives from New Generation Telescopes, by Giulietti, M.; **Gandolfi, G.**; Massardi, M.; Behiri, M.; and Lapi, A., *in preparation*.

Acknowledgments

This thesis straddles both theory and observations. It reflects my ongoing effort to build a hybrid expertise between these two poles. In an academic world that is increasingly hyperspecialized, I hope to be, in my own small way, a person who connects. I was lucky enough to get my PhD in a place where this path was understood: SISSA. Although I do not know if I will succeed in my aim in the future, I know for sure that this doctorate has been an intense and fruitful experience, both from an academic and personal point of view. Due thanks, therefore, are in order.

I want to thank my supervisors: Stefano, for the insightful discussions and sagacious humour and Andrea, who guided me into the great zoo of possibilities offered by that dark forest that is sometimes academia, opening a portal towards new, exciting opportunities. I thank all my collaborators, especially Francesco Benetti and the GOTHA team's people. Thanks to Giulia Rodighiero, Paolo Cassata, Laura Bisigello, Andrea Grazian and the others from the Padua group for allowing me to begin an exciting journey to the most extreme edges of the cosmos. Thanks to Tiberiu Harko and Paolo Cassata who read this thesis and allowed me to improve my work even further.

On a more personal note, I thank my mother Agnese, Cesi, Davide, and Paolo for always being by my side and all the friends with whom I shared goals and doubts (especially We'll be back, Kolla & Joennas). I thank the Giovani Sissaioli for being incredible travel companions in this journey: Giulia for the confidences, insights and deep discussions, Mattia for bringing healthy lightness where it was needed, Kevin for being an excelent musical partner and Marika, who, from an office mate turned to be a life companion.

Sometimes, when we face the mysteries of the cosmos, dejection may take hold for a little while. During this time, science outreach was essential to revive my inner spark and remind me in darker moments of that enlightening enthusiasm that guides me in doing this work. I therefore thank Francesa Rizzato, Aldo Rampioni, Paola Rodari and the other friends of SISSA Medialab; Donato Ramani, Chiara Saviane and Francesca de Ruvo and the SISSA Press Office staff; Aura Bernardi and the team of Immaginario Scientifico; the FameLab Italia staff and all the people I met during this exciting experience.

I crossed ESA's European Space Operations Center threshold in Darmstadt twice

during this PhD. The first time was as a science communicator (on the occasion of the launch of JUICE), the second as a musician (for Euclid's launch). I therefore thank Bettina Braunstein, Adam Majorosi, Bernadette Calderone, The ESA JUICE SocialSpace group organizers and members, and that incredible, big family that is the European Space Agency. Thank you for making me feel like one of you, touching the excitement and anxiety you feel during a launch, and giving me the chance to connect my two greatest passions: space and music. It's Dance at the Event Horizon, baby!

Contents

List of Figures

List of Tables

List of Abbreviations

ψDM Fuzzy-**D**ark **M**atter

AQUAL **A** **QUA**dratic **L**agrangian

BAO **B**aryonic **A**coustic **O**scillation

BBN **B**ig **B**ang **N**ucleosynthesis

BEC **B**ose–**E**instein **C**ondensate

BIC **B**ayes **I**nformation **C**riterion

BIMOND **B**imetric **MOND**

BTFR **B**aryonic **T**ully–**F**isher **R**elation

CDM **C**old **D**ark **M**atter

CEERS **C**osmic **E**volution **E**arly **R**elease **S**cience **S**urvey

CLASH **C**luster **L**ensing and **S**upernova survey with **H**ubble

CMB **C**osmic **M**icrowave **Background**

cSFR density **C**osmic **S**tar-**F**ormation **R**ate density

DE **D**ark **E**nergy

DIC **D**eviance **I**nformation **C**riterion

DM **D**ark **M**atter

ED **E**lectron **D**ensity

EFE **E**xternal **F**ield **E**ffect

EGS **E**xtended **G**roth **S**trip

EoS **E**quation **o**f **S**tate

GEA **G**eneralized **E**instein **A**ether theories

GR **G**eneral **R**elativity

GRB **G**amma-**R**ay **B**urst

GW **G**ravitational **W**ave

HDM **H**ot **D**ark **M**atter

HMF **H**alo **M**ass **F**unction

HST **H**ubble **S**pace **T**elescope

ICM **I**ntra**c**luster **M**edium

IMF **I**nitial **M**ass **F**unction

JWST **J**ames **W**ebb **S**pace **T**elescope

LF **L**uminosity **F**unction

LSB **L**ow **S**urface **B**rightness

MACHO **M**assive **H**alo **C**ompact **O**bject

MCMC **M**onte **C**arlo **M**arkov **C**hain

MIRI **M**id-**I**nfra**R**ed **I**nstrument

MOND **M**odified **N**ewtonian **D**ynamics

NFW **N**avarro–**F**renk–**W**hite

NIRCam **N**ear **I**nfrared **C**amera

NIRSpec **N**ear **I**nfrared **Spec**trograph

NMC **N**on-**M**inimal **C**oupling

QCD **Q**uantum **C**hromodynamics

QUMOND **QU**asilinear **MOND**

RAQUAL **R**elativistic **A** **QUA**dratic **L**agrangian

RAR **R**adial **A**cceleration **R**elation

RC **R**otation **C**urve

RMOND **R**elativistic **MOND**

SED **S**pectral **E**nergy **D**istribution

SEP **S**trong **E**quivalence **P**rinciple

SET **S**tress **E**nergy **T**ensor

SIDM **S**elf-**I**nteracting **D**ark **M**atter

SZ **S**unyaev–**Z**el'dovich

TeVeS **T**ensor **V**ector **S**calar theories

TRIMOND **TRI**potential **MOND**

UV **U**ltra**V**iolet

WDM **W**arm **D**ark **M**atter

WIMP **W**eakly **I**nteracting **M**assive **P**article

X-COP **X**MM-**N**ewton - **C**luster **O**utskirts **P**roject

Chapter 1

Introduction

Cosmological observations tantalised us with a profound revelation: more than 80% of the Universe's mass is dark matter (DM; Aghanim et al. 2020). From the end of the radiation era (around 70,000 years after the Big Bang) up to redshifts of $z \geq 0.5$, DM has been dominant in shaping the cosmos around us. This cosmic enigma embodies the key to comprehending the Universe's past, its present, and the mysteries of its future.

While the current ΛCDM paradigm can withstand most cosmological tests, galaxy-scale observations hint at potential gaps in our understanding of DM — or perhaps even the nature of gravity itself. Thus, the relentless quest to understand this fundamental cosmic cornerstone continues.

On the one hand, uncovering the secrets of DM requires robust and creative theoretical frameworks to articulate its physical nature. On the other hand, a thorough comparison with empirical data and a deep understanding of potential degeneracies between new physics and experimental errors are necessary to identify which models can be viable. Thus, this thesis follows a dual path between theory and observations.

Chapter 1 provides a brief introduction to the concept of DM and its interpretation in the concordance cosmological model (i.e., the Cold Dark Matter paradigm, or CDM).

Chapter 2 presents the challenges of the CDM paradigm on galactic scales, along with a review of the scientific community's main proposals to address these discrepancies.

Chapter 3 introduces a model where DM is non-minimally coupled to gravity, an effect designed to resolve the galactic-scale problems associated with CDM. The chapter discusses the characteristics of the DM halos predicted by this model and its phenomenology on galactic and galaxy cluster scales, highlighting ongoing and future developments.

Chapter 4 forecasts how cutting-edge observations from the James Webb Space Telescope (JWST) can impose astroparticle constraints on DM, potentially distin-

guishing between alternative DM models and CDM.

Chapter 5 draws the due conclusions and explores the new avenues that would naturally expand the work hereby presented.

Throughout this thesis I will adopt the standard, flat cosmology of Aghanim et al. (2020) with rounded parameter values: matter density $\Omega_M \sim 0.31$, baryon density $\Omega_b \sim 0.05$, Hubble constant $H_0 = 100h kms^{-1}\text{Mpc}^{-1}$ with $h \sim 0.68$. A Chabrier (2003) initial mass function (IMF) is assumed.

1.1 A brief history of Dark Matter

Galileo used his telescope to reveal an unseen part of the Universe, showing that the cosmos is more than what meets the eye. In the following centuries, the technological and epistemological ground that led to the discovery of DM became more and more fertile. French mathematician Friederich Bessel (1844) discussed how stars' proper motions could unveil the presence of faint companions via gravity. This is one of the first attempts to predict the existence of undiscovered astronomical objects based only on their gravitational influence. Then, the invention of astrophotography in the late 19th century led to a baffling discovery: stars are unevenly distributed across the sky. The scientific community was surprised: were these dark patches in dense star fields related to an actual lack of stars, or were they produced by the presence of opaque matter along the line of sight? The problem led to the development of several ingenious techniques. Lord Kelvin and Henri Poincaré proposed to describe stars in the Milky Way as a gas of particles acting under the influence of gravity and to use their velocity dispersion to constrain the amount of unseen matter (which Poincaré dubbed *matière obscure*, i.e. *dark matter*; Kelvin 1904; Poincare 1906). Their work was followed by the ones of scientists such as Ernst Öpik, Jacobus Kapteyn and his pupil Jan Oort.

Hubble and Humason (1931) noticed that the Coma galaxy cluster exhibited a larger velocity dispersion than other clusters. Two years later, Swiss-American astronomer Fritz Zwicky had a brilliant insight. He exported from the world of thermodynamics a theorem that he used to estimate the mass of the Coma cluster: the virial theorem. His analysis indicated that the measured velocity dispersion differed from that expected by more than an order of magnitude, suggesting the presence of an unseen component of matter in the cluster far more abundant than visible matter (Zwicky 1933). Today, we know that $\sim 80\%$ of clusters' mass is DM, while most of the baryonic mass is attributable to the intracluster gas. Only a few per cent of the total mass budget is contained in the optically visible galaxies (e.g., Voit 2005; Gonzalez et al. 2013).

Interestingly, in the subsequent paper Zwicky (1937), the astronomer discusses the possibility of studying rotation curves (RCs) of galaxies to infer their mass distribution. Early analysis of M31's RC indicated a rising trend at large radii (Babcock 1939; Schwarzschild 1954; van de Hulst et al. 1957; Schmidt 1957; Kahn & Woltjer 1959). The significant contrast between RCs predicted through pho-

tometry and those measured through 21-cm observations started to suggest the presence of substantial, unseen mass in the outer regions of galaxies. Nonetheless, it was in the 1970s that the concept of requiring extra mass in the outer sections of certain galaxies started to gain widespread acceptance within the scientific community. The high-quality radio measurements by Brandt (1965); Roberts (1966); Shobbrook & Robinson (1967) and most notably by Rubin & Ford (1970) allowed to map the RCs of galaxies beyond the optical disc, showing that the observed RCs peaked at larger radii than predicted (see e.g. the modelling by Freeman 1970). In later years, new observations showed how the problem of missing mass at large radii extended to most spiral galaxies (Rogstad & Shostak 1972; Roberts & Rots 1973; Bosma 1978; Rubin et al. 1978).

In the late 1980s, the idea that the absent mass might be composed of one or more undiscovered subatomic particle species had garnered substantial backing, propelling it to the forefront as the prevailing concept for DM. Concurrently, during that same period, some pioneering research (Peebles 1982; Blumenthal et al. 1984; Davis et al. 1985) was laying the foundation for the predominant framework characterising DM phenomena which endures to this day: the CDM model.

1.2 The ΛCDM Universe

The CDM model describes DM's phenomenology in the context of the concordance cosmological model, i.e. ΛCDM, which details the formation of the Universe over the time since the Big Bang in remarkable precision. The ΛCDM framework divides the mass-energy budget of the Universe into a dark energy (DE) component (parametrised by a cosmological constant Λ), CDM and baryonic (i.e., standard, visible) matter. The relative contributions of DE and DM are estimated as $\Omega_\Lambda \sim 68.7\%$ and $\Omega_{\rm CDM} \sim 26.4\%$, while baryonic matter makes up only about 4.9 % (Aghanim et al. 2020). This framework assumes inflationary initial conditions and General Relativity (GR) as the correct theory of gravity.

According to the ΛCDM paradigm, the Universe's evolution began about 13.8 billion years ago with the Big Bang. At that time, the Universe was a hot and dense plasma in almost perfect thermal equilibrium. At just about $t \sim 10^{-35}$ s after the beginning of everything, space expanded exponentially by many orders of magnitude in a process called *inflation*, required to explain the observed isotropy of the Cosmic Microwave Background (CMB). The scalar field driving the expansion fluctuated, and these quantum fluctuations started to seed the formation of cosmic structures. Right after inflation, something crucial happened: the Universe reheated to a very dense and hot plasma, and then it adiabatically cooled once again, continuing its expansion. It is in this reheating phase that the first Standard Model particles were produced (e.g., Allahverdi et al. 2010). As the plasma cooled down, the temperature fell below the reaction energies of the different interactions, and the Universe's constituents underwent phase transitions. At some point between the Quantum Chromodynamics (QCD) phase transition (i.e., when quarks formed protons and neutrons) and the first recombination of nuclei and

electrons to bound atom states, another essential transition took place: the decoupling of DM particles from thermal equilibrium (also known as *freeze-out*). Then, about three minutes from the beginning, nuclear reactions thermally formed the first light elements in the Universe, such as helium, deuterium or lithium. This process is known as Big Bang nucleosynthesis (BBN) (Weinberg 1979). Knowing the corresponding reaction rates, one can calculate the primordial abundances of these light elements, which can be compared with present Universe abundances (accounting for stellar evolution reprocessing). Besides lithium, a good agreement between these quantities is generally found.

As the early Universe unfolded, primordial fluctuations generated sound waves that, like ripples, travelled through the photon-baryon plasma. As recombination happened, these plasma density waves could not propagate anymore, being frozen into place. These baryonic acoustic oscillations (BAOs) were imprinted in the CMB signal originating at this epoch ($z \sim 1100$). No longer diluted by radiation pressure, baryons started falling into the gravitational wells provided by DM. Indeed, the tiny fluctuations in the plasma seen in the CMB suggest that the evolution of cosmic structures was propelled by matter that had separated from the influence of photons prior to the recombination era.

In the first few hundred million years of the Universe, the first stars and galaxies had formed[1] (see, e.g., Bromm et al. 2009). Their radiation provided the energy for the reionisation of the Universe, turning most of the neutral atoms back into a plasma of ions and electrons (e.g., Robertson et al. 2010). Slowly, even larger structures like galaxy clusters and superclusters begin to form. It is thought that most clusters with masses above $10^{15} M_{\odot}$ formed at redshifts $z < 1$ (Voit 2005). At this very epoch, DE, interpreted as a time-independent cosmological constant, started to dominate the energy density of the Universe and to reaccelerate its expansion.

Currently, the ΛCDM model boasts numerous observational achievements on cosmic scales. This framework precisely anticipates the presence and characteristics of the CMB, including its temperature anisotropies and polarisation (Hinshaw et al. 2007; Shafieloo & Hazra 2017; Aghanim et al. 2020). ΛCDM is also consistent with the broad, large-scale structure of the Universe reconstructed through the observation of baryons, e.g. in sky surveys like 2dFGRS (Folkes et al. 1999), SDSS (Abazajian et al. 2003) to Lyman-α forest observations (Weinberg et al. 2003), which map the distribution of neutral hydrogen. DM structures can be indirectly observed through galaxy clustering and gravitational lensing (e.g., Massey et al. 2010). Moreover, CDM predicts the observed abundances of hydrogen, deuterium and helium (Jedamzik & Pospelov 2009).

[1]Further details on how cosmic structures form within the CDM framework will be given in Sec. (1.3.2).

1.3 The Cold Dark Matter model

1.3.1 CDM particle properties

In the CDM paradigm, DM comprises particles that interact minimally, primarily through long-range gravitational forces or, in some cases, weak nuclear interactions. These particles are termed *cold* since they featured non-relativistic velocities at decoupling. These low velocities impart a vanishing equation of state in a cosmological context, effectively rendering CDM as pressureless dust within this environment. As stated, CDM particles are thought to freeze-out of thermal equilibrium in the early Universe, becoming cold relics. As such, they must have a substantial mass, typically ranging from the MeV to the GeV scale and beyond.

Probably the most well-known CDM particle candidate is the hypothetical non-baryonic weakly interacting massive particle (WIMP; e.g., Jungman et al. 1995), which fits the model of early Universe relic DM particles. The Standard Model of particle physics does not predict WIMP-like particles. However, various extensions, such as Supersymmetry, predict hypothetical elementary particles that are good WIMP candidates (this coincidence is sometimes dubbed the *WIMP miracle*; Jungman et al. 1995).

The present-day relic abundance of DM derived from the most inclusive data combination in Aghanim et al. (2020) reads as $\Omega_{\rm CDM}h^2 = 0.120 \pm 0.001$. One can constrain WIMPs' cross-section by comparing this value with theoretical predictions of WIMPs' relic density (e.g., Feng 2010). At the high temperatures of the early Universe, DM particles and their antiparticles form from and annihilate into lighter Standard Model particles[2]. As the Universe expands and cools, the average thermal energy of these lighter particles decreases, becoming insufficient to form DM particle-antiparticle pairs. Parallely, the annihilation of DM particle-antiparticle pairs still proceeds. Net, the number density of DM particles starts decreasing exponentially after crossing the temperature $T \sim m_{\rm DM}/20$ (Kamionkowski 1998), with $m_{\rm DM}$ being the DM particle mass. The DM particle number density drops, becoming so low that particle-antiparticle reactions cease entirely. As the Universe expands, the total DM particle number remains roughly constant (Griest 1993). Now, the self-annihilation cross-section only weakly depends on the DM particle mass and hence can be approximated as

$$\sigma_v \ [\mathrm{cm^3\ s^{-1}}] \approx \frac{3 \times 10^{-27}\ \mathrm{cm^3\ s^{-1}}}{\Omega_{\rm CDM}h^2}.$$

The measured density $\Omega_{\rm CDM}h^2 \sim 0.1$ is then achieved by a self-annihilation cross-section of $\sigma_v \sim 10^{-26}\mathrm{cm^3\ s^{-1}}$ (Bertone & Hooper 2018), a value roughly corresponding to the cross-section for the weak interaction. Particles with a larger interaction cross-section would continue to annihilate for a longer time and thus would have a smaller number density when the annihilation interaction ceases.

In recent years, the astrophysical community has shown interest in QCD axions as possible WIMP candidates. These particles were originally theorised to resolve

[2]DM is initially in thermal equilibrum with the early Universe particle bath, meaning that particle processes creating and destroying DM happen at equal rates.

the strong CP problem in QCD. Other potential WIMPs include massive neutrinos (whether sterile or not) and supersymmetric particles like neutralinos, gravitinos, sneutrinos, axinos (Jungman et al. 1995), and Kaluza-Klein particles (Cheng et al. 2002).

An alternative idea envisages CDM as an ensemble of compact celestial objects. These objects would elude traditional observations because of their faint luminosity, lower than typical stars. In principle, these objects could consist of planets, brown dwarfs, red dwarfs, white dwarfs, neutron stars, and black holes. Collectively, these are known as Massive Halo Compact Objects, or *MACHOs*. However, extensive searches for MACHOs through gravitational microlensing surveys (Paczynski 1986; Nemiroff 1987; Lasserre et al. 2000; Tisserand et al. 2007) and measurements of cosmic baryon density, derived from observations of primordial light element abundances and the CMB (e.g., Fukugita et al. 1998), have convincingly demonstrated that these entities cannot constitute the primary component of DM within galaxies.

1.3.2 Structure formation in the CDM framework

CDM particles exhibit negligible free streaming velocities. This means they do not diffuse away from density perturbations before gravitational collapse. As a result, CDM structures grow over time, coalescing in a hierarchical, stochastic bottom-up process: non-linear, virialised DM structures (i.e., haloes) form earlier as mass decreases. These structures originate from the collapse of primordial mass density perturbations dominated by CDM. Then, baryons cool and collapse within the potential wells sourced by such perturbations, and galaxies form. The higher gas densities at high redshifts render this cooling process more efficient at earlier epochs. Parallely, the inverse Compton cooling rate increases markedly with redshift, and this catalyses the rapid condensation of small, dense gas clouds. These condensing clouds subsequently lose both energy and orbital angular momentum through dynamical friction interactions with the surrounding DM halo.

As stated, cosmic structures start from non-relativistic and collisionless CDM density perturbations. As long as these perturbations are small, their growth can be described via Newtonian gravity. Their evolution equation reads as

$$\delta(r,t) \equiv \frac{\rho(r,t) - \bar{\rho}(t)}{\bar{\rho}(t)},$$

with $\rho(r,t) = \bar{\rho}(t)[1 + \delta(r,t)]$ being the matter density at a position r and time t, and $\bar{\rho}(t)$ being the average density of the Universe at a time t.

In the linear regime ($\delta \ll 1$), the perturbations' evolution is well described by hydrodynamical equations for a pressureless fluid, i.e., the mass conservation, Euler and Poisson equations. These equations are linear, and thus one can factorise the density perturbation $\delta(x,t)$ as $\delta(x,t) = D(t)\delta(x,t_0)$, with $D(t)$ being the growth factor of cosmological perturbations (normalised so that $D(t_0) = 1$ at the present cosmic time t_0).

As a density perturbation becomes non-linear ($\delta \geq 1$), its evolution can be described only through simulations or analytical approximations. A meaningful

approximation is given by the spherical collapse model, which sees perturbations as uniform spherical regions with an initial density contrast $0 < \delta \ll 1$ at $z \sim z_{\rm rec}$. As time passes, the spherical region expands more slowly than the background, and the density contrast can grow in the linear regime up to $\delta \sim 1$. When $\delta \sim 1.686$, the expansion of the sphere stops, and the enclosed mass starts to collapse, forming, in the context of this idealised model, a singularity.

Reality, though, is far more complex. The collapse of matter overdensities is not expected to obey spherical symmetry, nor is its density distribution expected to be uniform. During an actual collapse, DM particles experience phase mixing and violent relaxation. Instead of collapsing into a singularity, they form an equilibrium system that satisfies the virial theorem. Denoting K as the system's kinetic energy and W as its gravitational energy, the virial theorem states that at equilibrium $K = -W/2$. Assuming an Einstein–de Sitter cosmology, virialised halos are characterised by a typical overdensity $\rho/\bar{\rho} = 18\pi^2 \sim 178$. Note that the average matter density of the Universe can be written as $\bar{\rho} = \Omega_{\rm m}\rho_{\rm crit}$, where $\Omega_{\rm m}(z)$ is the matter density parameter and $\rho_{\rm crit}\,(z)$ the critical density, related to the present-day critical density $\rho_{\rm crit\,,0}$ by $\rho_{\rm crit}\,(z)/\rho_{\rm crit\,,0} = H^2(z)/H_0^2$.

Virialised DM halos do not have a uniform density distribution, and neither do they own a well-defined edge. Yet, it is helpful to define the mass and radius of a DM halo. The size of a halo is usually associated with its virial radius $r_{\rm v}$, commonly defined as the radius of a sphere at redshift z containing an overdensity with average density $\Delta_{\rm c}\rho_{\rm crit}$, where $\Delta_{\rm c}$ is the critical overdensity for virialisation. For an Einstein–de Sitter Universe, $\Delta_{\rm c} = 18\pi^2$, yet, in general, this quantity depends on redshift. In ΛCDM cosmology, $\Delta_{\rm c} \sim 101$ at $z = 0$ and $\Delta_{\rm c} \sim 178$ at high redshifts. However, a wildly adopted and simple choice is the redshift-independent value $\Delta_{\rm c} \sim 200$.

The total mass of a DM halo is traditionally associated with its virial mass:

$$M_{\rm v} \equiv \frac{4\pi}{3}\Delta_{\rm c}\rho_{\rm crit}\, r_{\rm v}^3, \tag{1.1}$$

and thus, the virial radius reads as

$$r_{\rm v} = \left[\frac{2GM_{\rm v}}{\Delta_{\rm c}(z)H^2(z)}\right]^{1/3}.$$

At z=0 and for $\Delta_{\rm c} = 200$, one obtains

$$r_{200} \simeq 206.3\left(\frac{M_{200}}{10^{12}M_\odot}\right)^{1/3}\left(\frac{h}{0.7}\right)^{-2/3}\ {\rm kpc}. \tag{1.2}$$

1.3.3 Statistical properties of CDM haloes

Sec. (1.3.2) described the evolution of a DM overdensity up until virialisation. Yet, rather than focusing on single overdensities, one can consider the statistical properties of the cosmological perturbations and their evolution, studying cosmological DM halos as an evolving population. The perturbation $\delta(r)$ is then considered a realisation of an underlying probability distribution, i.e., a random

field. A valuable tool to describe the statistical properties of this distribution is the correlation function:

$$\xi(x) \equiv \left\langle \delta\left(\vec{x}'\right) \delta\left(\vec{x}' + \vec{x}\right) \right\rangle,$$

where $\vec{x}$ and $x = |\vec{x}|$ represent comoving coordinates and $\langle \cdots \rangle$ denotes the average over x'. Note that the correlation function depends only on the modulus of $\vec{x}$ due to the expected isotropy of the fluctuation density field.

The characteristic spatial scales of the density fluctuation field can be easily estimated in Fourier space. If the Universe is homogeneous and isotropic on large scales, one can take a Universe's cubic volume V sufficiently large that fluctuations in the field can be considered periodic since they happen on smaller scales than the box size. Under this approximation, the field $\delta(\vec{x})$ can be re-written as a Fourier series:

$$\delta(\vec{x}) = \sum_{\vec{k}} \delta_{\vec{k}} e^{i\vec{k}\cdot\vec{x}},$$

where the Fourier coefficients $\delta_{\vec{k}}$ are given by

$$\delta_{\vec{k}} = \frac{1}{V} \int_V \delta(\vec{x}) e^{-\mathrm{i}\vec{k}\cdot\vec{x}} \, \mathrm{d}^3\vec{x}.$$

Here, $\vec{k}$ is a vector with components $k_i = 2\pi N_i / l$, with N_i being integers ($i = 1, 2, 3$) and $l = V^{1/3}$.

The power spectrum of the fluctuations is defined as

$$P(k) \equiv V \left\langle \left|\delta_{\vec{k}}\right|^2 \right\rangle,$$

with $k = |k|$ being the wavenumber and $\langle \cdots \rangle$, now denoting an average over different realisations of the perturbation's field. Indeed, $P(k)$ measures the amount of fluctuations on scales $\lambda = 2\pi/k$. Note also that, by definition, the correlation function and the power spectrum are the Fourier transforms of one another.

The global amount of fluctuations due to modes with all possible wavenumbers is given by the variance of the perturbation field σ:

$$\sigma^2 = \frac{1}{2\pi^2} \int_0^\infty P(k) k^2 \, \mathrm{d}k.$$

One can express the field's variance contributed by fluctuations on scales above a given threshold (e.g., by smoothing the field on scales smaller than a particular value $2\pi/K$):

$$\sigma_K^2(\mathcal{M}) = \frac{1}{2\pi^2} \int_0^\infty W_K(k) P(k) k^2 \, \mathrm{d}k.$$

Here, $W_K(k)$ is a k-space filter function (i.e., $W_K \approx 1$ for $k \lesssim K$ and $W_K \approx 0$ for $k \gtrsim K$), and the mass M associated with the wavenumber K scales as $\mathcal{M} \propto K^{-3}$. If

the power spectrum trends as the power-law $P(k) \propto k^{n_s}$ (with n_s being its spectral index), then $\sigma_K^2 \propto \mathcal{M}^{-(3+n_s)/3}$, which is the case of the primordial power spectrum.

The power spectrum at a time t after recombination can be parameterised as

$$\frac{P(k,t)}{P_0\,(k_0)} = D^2(t)T^2(k)\left(\frac{k}{k_0}\right)^{n_s},$$

where $T(k)$ is the transfer function, parametrising the different evolution of perturbations with different characteristic scales, k_0 is a reference wavenumber and $P_0(k) \equiv P(k, t_0)$. Since by definition $D\,(t_0) = 1$, the present-day ($t = t_0$) linearly extrapolated power spectrum $P_0(k)$ is given $P_0(k)/P_0\,(k_0) = T^2(k)\,(k/k_0)^{n_s}$.

The effect of the transfer function in CDM cosmology is to partially suppress fluctuations on smaller scales (i.e., larger k). In this framework, the transfer function's shape is determined by the presence of a finite horizon — at any finite time t, the size of the observable and causally connected Universe is of the order of ct. Perturbations on scales larger than the horizon size are purely affected by gravity, and hence they are free to grow. Instead, the growth of perturbations on smaller scales is damped by radiation pressure, especially until matter is still coupled with radiation. Specifically, since the radiation-driven expansion timescale is shorter than the collapse timescale, perturbations entering the horizon during the radiation-dominated era ($z_{eq} \sim 3400$) grow slower than those entering during the matter era.

The CDM transfer function $T \to 1$ for $k \ll k_{eq}$, while $T \to 0$ for $k \gg k_{eq}$, with k_{eq} being the wavenumber associated to the size of the horizon $2\pi/k_{eq} \sim 125$ Mpc at the epoch of matter–radiation equivalence. When DM is not cold, the transfer function may also account for the effect of free streaming. Indeed, particles with non-negligible kinetic energy are not confined by the potential wells of small-scale fluctuations, which are further damped. As discussed in Sec.(2.2.2) and displayed in Fig. (4.2), the power spectrum of a model such as Warm Dark Matter differs from the CDM one for the presence of a cut-off at high k.

A pivotal quantity to the statistic description of DM halo populations is the halo mass function (HMF), which returns the number density of haloes with masses between M and $M + dM$. The HMF can be estimated analytically using the Press–Schechter formalism (Press & Schechter 1974):

$$\frac{\mathrm{d}n}{\mathrm{d}\mathcal{M}}(\mathcal{M}) = \sqrt{\frac{2}{\pi}}\frac{\bar{\rho}}{\mathcal{M}^2}\frac{\delta_c}{\sigma_K}\exp\left(-\frac{\delta_c^2}{2\sigma_K^2}\right)\left|\frac{\mathrm{d}\ln\sigma_K}{\mathrm{d}\ln\mathcal{M}}\right|. \tag{1.3}$$

The HMF's shape is determined by $\sigma_K(M)$, and thus the HMF depends on the power spectrum $P(k)$. Also, for a fixed $P(k)$, the HMF depends on redshift through the critical overdensity for collapse $\delta_c(z)$, which scales increasingly with z. The redshift dependence of the Press-Schechter HMF is illustrated in Fig.(1.1).

The Press–Schechter framework served as a basis to develop more sophisticated formalisms (e.g., Sheth & Tormen 1999; Warren et al. 2006; Tinker et al. 2008; Angulo et al. 2012; Bocquet et al. 2016; Despali et al. 2016; Diemer 2020). The majority of these models can account for DM subclumps embedded in larger

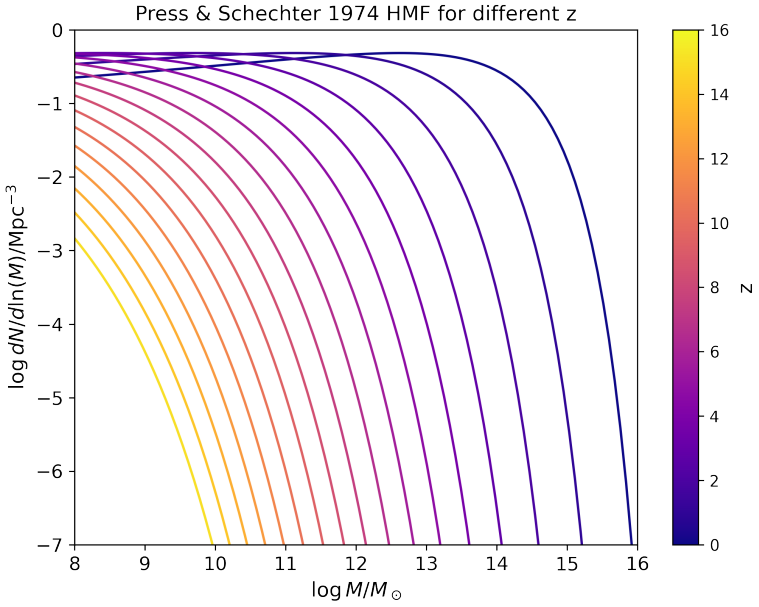

Figure 1.1: Redshift dependence of the Press-Schechter HMF given by Eq.(1.3) for a Aghanim et al. (2020) cosmology generated utilising the `COLOSSUS` python package (Diemer 2018).

ones. Moreover, they can connect the properties of progenitor and descendant halos, allowing them to construct halo merger trees.

1.3.4 The Navarro–Frenk–White profile

Once CDM haloes are virialised, a precise analytical expression can characterise their internal density distribution. Gravity-only N-body simulations of collisionless CDM particles predict self-similar DM haloes that, over a broad range of masses and redshift, show an internal DM density distribution following the universal Navarro–Frenk–White (NFW) profile (see Navarro et al. 1996; Łokas & Mamon 2001):

$$\rho_{\rm DM}(r) = \frac{\delta_{\rm c}\rho_{\rm c} r_s^3}{r\,(r+r_s)^2}. \tag{1.4}$$

Here, δ_c is the dimensionless characteristic overdensity of the halo, $\rho_{\rm c} = 3H_0^2/8\pi G$ is the local critical density, and r_s is a scale radius of the profile. The virial mass M_v of Eq. (1.1) and the concentration $c \equiv r_{\rm v}/r_s$, defined in terms of the virial radius expressed by Eq. (1.2), can be used to fully characterise the profile since $\delta_c\rho_c = M_{\rm v}c^3 g(c)/4\pi r_{\rm v}^3$ with $g(c) \equiv [\ln(1+c) - c/(1+c)]^{-1}$.

The overall trending of the NFW profile is shown in Fig.(1.2) for different values of the scale radius r_s. The asymptotic behaviour of the NFW profile at $r \gg r_s$ returns $\rho(r) \propto r^{-3}$. Instead, for small radii $r \ll r_s$, Eq. (1.4) diverges as $\rho(r) \propto r^{-1}$, indicating a steep slope near the centre of the DM halo.

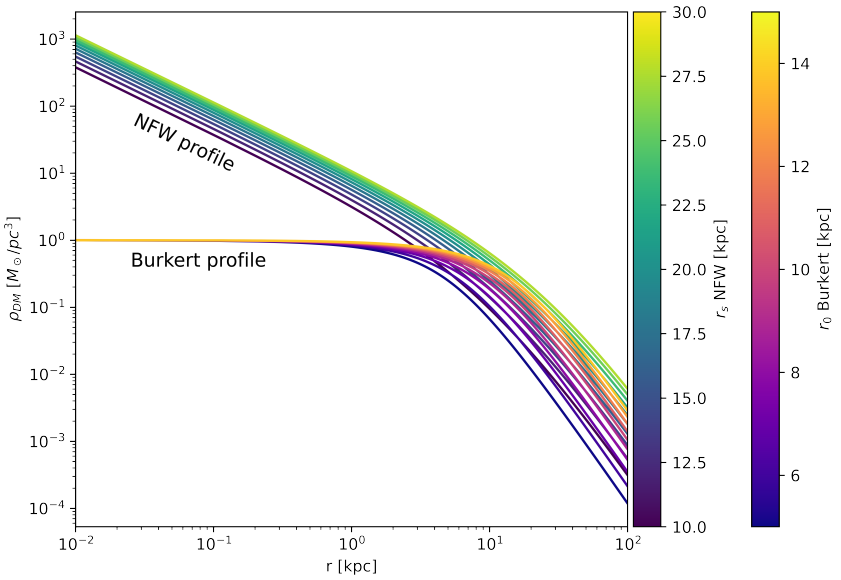

Figure 1.2: A qualitative comparison between the NFW profile given by Eq. (1.4) (fixing $\rho_{0,\mathrm{NFW}} = \delta_c \rho_c = 0.38\ \mathrm{M}_\odot/\mathrm{pc}^3$) and the Burkert profile given by Eq. (1.5) (fixing $\rho_{0,\mathrm{Burkert}} = 1\ M_\odot/\mathrm{pc}^3$) varying the NFW scale radius 10 kpc $\lesssim r_s \lesssim$ 30 kpc and the Burkert core radius 5 kpc $\lesssim r_0 \lesssim$ 15 kpc.

1.4 Galaxy-scale issues of the Cold Dark Matter model

The CDM paradigm has proven highly successful in replicating the observed phenomenology of DM on cosmological scales. Yet, this framework encounters challenges when attempting to account for certain observed behaviours of DM on galactic scales. In this section, I review the major controversies associated with the CDM paradigm on these small scales, whereas possible solutions are detailed in Chapter 2.

1.4.1 The Core-Cusp problem

Addressed earlier in Sec. (1.3.4), CDM gravity-only N-body simulations produce a steep, power-law-like density profile for halos at inner radii, well characterised by the NFW profile in Eq. (1.4). However, observations present a contrasting picture, revealing a flat, or *cored* DM density in the inner regions of galaxies, particularly in the case of DM-dominated dwarf galaxies. DM density profiles for these galaxies are well approximated by the phenomenological Burkert profile (Burkert 1995):

$$\rho_{\mathrm{DM}}(r) = \frac{\rho_0 r_0^3}{(r + r_0)\left(r^2 + r_0^2\right)}. \tag{1.5}$$

Here, ρ_0 and r_0 denote the density and radius associated with the DM halo core (i.e., the region where the profile's slope is flat). The observed inconsistency

between these empirical cored profiles and the steeper predictions of the CDM model has been coined the *core-cusp problem* (e.g., Boylan-Kolchin & Ma 2004; Navarro 2006; de Blok 2010; Navarro et al. 2017). Fig.(1.2) contains a visual depiction of such discrepancy.

1.4.2 Missing satellites problem

CDM simulations predict galaxies like the Milky Way should count hundreds of sub-halos. Observations instead revealed only tenths ($\sim$ 60) of these satellites (Klypin et al. 1999; Moore et al. 1999; Drlica-Wagner et al. 2015; Bechtol et al. 2015; Koposov et al. 2015). This observed discrepancy is termed *missing satellites problem*. The leading explanation for this conundrum envisages small DM halos as inefficient in forming stars (e.g., Wheeler et al. 2014; Shen et al. 2014). Hence, these haloes could easily fall below the sensitivity thresholds of current instrumentation. Indeed, simulations estimate that the Milky Way should host hundreds of faint, luminous satellites (Tollerud et al. 2008; Hargis et al. 2014; Newton et al. 2018; Jethwa et al. 2018). Hence, it is essential to consider completeness corrections when comparing simulation results to Milky Way subhaloes surveys. Doing so suggests that the number of Milky Way satellites agrees with the number of luminous satellites predicted by CDM down to halo masses of $\sim 10^8 M_\odot$ (Kim et al. 2018). However, the missing satellite problem could still apply to ultra-faint dwarf galaxies (with typical halo masses ranging even below $10^5 M_\odot$, Acuna et al. 2023).

1.4.3 The too-big-to-fail problem

Milky Way satellites' predictions of the CDM model needed to be reconciled with observations. Hence, a hypothesis emerged: many satellites might exist, but their stars had been stripped away through tidal interactions, rendering them invisible. This proposed solution, however, gave rise to a new challenge termed *too-big-to-fail problem* (e.g., Boylan-Kolchin et al. 2011; Boylan-Kolchin et al. 2012; Garrison-Kimmel et al. 2014; Smercina et al. 2018). Indeed, satellite galaxies predicted by simulations should be so massive that they should unmistakably harbour visible stars. The observed luminosity function (or one accounting for baryonic physics) predicts numerous intermediate-mass systems within the Local Group and similar nearby systems. Yet, these satellites seem nowhere to be found (e.g., Tremaine & Richstone 1977). Observationally, this translates into a large gap between the brightness of the first and second-brightest galaxies in groups and clusters. Stellar feedback processes may reduce the density within the centres of satellite galaxies, resulting in shallower density profiles partially devoided of stars (e.g., Lovell et al. 2017). However, this solution remains a topic of debate (e.g., Papastergis & Shankar 2016). Tidal effects, such as shocks and stripping, may modify the mass distribution of dark and baryonic matter in satellites (Tomozeiu et al. 2016), as well as gravitational interactions and merging processes within groups and clusters (Ostriker & Hausman 1977; Choi et al. 2017). Notably, recent literature suggests that the observed gap between the first and second-brightest

satellites is well-replicated in state-of-the-art simulations of galaxy formation, such as EAGLE (Schaye et al. 2015) and Illustris (Genel et al. 2014). After all, it is possible that modern CDM simulations do not suffer from the too-big-to-fail problem at all (e.g., Ostriker et al. 2019).

1.4.4 Angular momentum problem

In the prevailing hierarchical clustering framework, galactic discs take shape within the gravitational wells of DM halos as baryonic matter cools and condenses through dissipative processes. Discs formed in this manner are expected to possess the observed angular momentum and spatial extent for a given mass and profile shape (e.g., Fall & Efstathiou 1980). However, this hinges on the crucial condition that the infalling gas conserves most of its original angular momentum. CDM numerical simulations have consistently indicated a persistent challenge in this sense (see, e.g., Navarro & Benz 1991; Haslbauer et al. 2022). When these simulations exclusively consider cooling processes, the infalling gas undergoes substantial angular momentum loss. Consequently, the resulting discs appear significantly smaller than what observational data demand. This discrepancy is aptly called the *angular momentum problem*. To solve it, a mechanism is required to impede, or at the very least delay, the collapse of small protogalactic gas clouds. Such a mechanism would allow the gas to retain a larger fraction of its angular momentum as it settles into the forming disc. In contrast, calculations of galaxy formation through semi-analytical techniques, which assume an initial angular momentum distribution in baryons identical to that of DM and the conservation of this distribution during baryonic collapse, demonstrate better agreement with observed disc sizes (Fall & Efstathiou 1980; Mo et al. 1998; Cole et al. 2000).

1.4.5 The Radial Acceleration Relation and the DM-baryons interplay

Observations revealed robust empirical scaling relationships between baryons and DM in spiral galaxies, which are *a priori* unexpected within the CDM framework (see, e.g., Lapi et al. 2018). The most renowned is the baryonic Tully–Fisher relation (BTFR). The BTFR links a spiral galaxy's asymptotic circular velocity $V_{\rm flat}$ to its baryonic mass $M_{\rm b}$ as $V_{\rm flat}^4 \sim M_{\rm b}$ (McGaugh et al. 2000; Papastergis et al. 2016; Zackrisson et al. 2015; Lelli et al. 2016; Lelli et al. 2019). NFW profiles of CDM haloes predict a curvature in the BTFR that contradicts observed data (Desmond 2017). Yet, abundance matching techniques between the HMF and the luminosity distribution of galaxies predict a relationship between the stellar and halo mass whose normalisation is close to the BTFR one, particularly for baryonic masses around $10^{10} M_\odot$ (Di Cintio & Lelli 2016; Desmond 2017). However, at higher masses, abundance matching overestimates the halo mass of disc galaxies, failing to reproduce the BTFR's shape. Furthermore, the exceptionally low intrinsic scatter of the BTFR contradicts abundance matching predictions (Posti et al. 2019).

Additionally, CDM struggles to explain the diversity of RC shapes in galaxies with matching asymptotic circular velocities (and total baryonic mass on the

BTFR). These RCs encompass a range of central DM density profiles, from cuspy NFW-like central distributions projected in DM-only simulations to expansive, constant-density DM cores (Ogle et al. 2019). Moreover, observations revealed a direct correlation between the average DM density within 2 kpc and the baryon-induced rotational velocity at that radius (Ghari et al. 2019a). This subtends a link between RC shapes and baryon surface density (Donato & Salucci 2004; Swaters et al. 2009).

The unexpected diversity of RCs at a given velocity scale, their uniformity at a specific baryonic surface density scale, and their adherence to the BTFR are summarised by the so-called Radial Acceleration Relation (RAR). The RAR is a tight empirical relationship between two *a priori* independent quantities: the (total) gravitational radial acceleration $g_{\rm tot} = {\rm GM_{tot}}(< r)/r^2$ inferred from galaxy RCs with different masses and velocities and the acceleration associated with the luminous matter distribution $g_{\rm bar} = {\rm GM_{bar}}(< {\rm r})/{\rm r}^2$, which is mainly probed by photometric observations. The RAR was initially proposed in McGaugh et al. (2016) by exploiting the individual high-quality RCs of the SPARC sample (see Lelli et al. 2016). In Lelli et al. (2017), an overall representation of the RAR was introduced in terms of the following function:

$$g_{\rm tot} = \frac{g_{\rm bar}}{1 - e^{-\sqrt{g_{\rm bar}/g_\dagger}}} + \hat{g} e^{-\sqrt{g_{\rm bar} g_\dagger / \hat{g}^2}}, \tag{1.6}$$

with $g_\dagger = (1.20 \pm 0.24) \times 10^{-10}$ m s^{-2} and $\hat{g} = (9.2 \pm 0.2) \times 10^{-12}$ m s^{-2} being fitting parameters, whose values were derived from the analysis of the SPARC sample. The recent literature argued that the parameter $g_\dagger$ could represent an acceleration scale governing the average internal dynamics of galaxies. Since the existence of such a scale in the standard cosmological model is far from trivial, this phenomenon has been interpreted as a possible sign of modified gravity (e.g., Hossenfelder & Mistele 2018; Green & Moffat 2019; O'Brien et al. 2019; Islam & Dutta 2020; Petersen & Lelli 2020). More specifically, the empirical constant $g_\dagger$ would be interpreted as the fundamental acceleration scale a_0 in the MOND framework (see Sec. (2.2.6)). Indeed, the value of $g_\dagger$ derived both in McGaugh et al. (2016) and Lelli et al. (2017) is compatible with the expected value of the MONDian characteristic acceleration scale $a_0 \sim 1.2{\times}10^{-10}$ m s^{-2}. Notice, however, that such an interpretation is still highly debated, with some works supporting it (see, e.g., Li et al. 2018; Ghari et al. 2019b) and some others ruling it out (e.g., Marra et al. 2020; Rodrigues & Marra 2020). Yet, the ongoing debate around the hypothesised fundamental nature of the RAR is beyond the scope of this thesis.

The RAR has been studied in various galaxy samples (Lelli et al. 2017; Rong et al. 2018; Chae et al. 2019; Oman et al. 2020; Brouwer et al. 2021), including dwarf disc and low surface brightness galaxies (Di Paolo et al. 2019), as well as in galaxy clusters (Tian et al. 2020; Chan & Del Popolo 2020; Pradyumna et al. 2021; Pradyumna & Desai 2021; Eckert et al. 2022; Tam et al. 2023). Albeit hydrodynamical simulations in the ΛCDM framework have succeeded in reproducing the overall observed shape of the galactic RAR (Eckert et al. 2022; Ludlow et al. 2017; Garaldi et al. 2018; Dutton et al. 2019; Paranjape & Sheth 2021), its precise normalisation and minimal scatter continue to present an intriguing challenge for

this paradigm.

This Chapter explored the core attributes of the CDM paradigm and highlighted its contrasts with the observed phenomena of DM at the galactic level. The following Chapter will provide an overview of the primary mechanisms put forward by the astrophysical community to address these problematics.

Chapter 2

Solving CDM's galaxy scales controversies

Why is CDM at variance with galaxy-scale observations? Some astrophysicists think the missing piece of this dark puzzle should be sought in galaxy-scale baryonic physics. Baryonic processes can indeed reshape part of CDM haloes' potential well. Another possiblity is that DM is not cold at all. This scenario then calls for new DM particle candidates substantially different from CDM ones. These new particle properties should agree with the observed DM galaxy-scale phenomenology of DM, yet at the same time, they should recover a similarly successful cosmology with respect to CDM. Other physicists, instead, believe that the CDM paradigm is correct and that gravity should be modified. A more radical class of modified gravity theories eliminates the need for DM in the cosmos. In the subsequent section, I will offer a brief review of these concepts, evaluating their merits in solving CDM's galaxy scale issues and lingering questions.

2.1 Baryonic processes

As baryons get accreted by DM halos, various processes may come into play, potentially altering the halo's structure. Indeed, some authors argue how baryonic processes could alleviate the core-cusp problem (e.g., Zentner et al. 2022), the missing satellites problem (Wheeler et al. 2014; Shen et al. 2014) or even reproduce the non-trivial tight dynamical scaling laws between DM and baryons such as the RAR (Di Cintio et al. 2014; Di Cintio & Lelli 2016; Santos-Santos et al. 2016; Keller & Wadsley 2017; Ludlow et al. 2017; Desmond 2017; Navarro et al. 2017; Wheeler et al. 2019). This section briefly recaps some of the leading processes discussed in the literature.

2.1.1 Feedback processes

Baryonic feedbacks encompass several processes supplying energy to the interstellar medium, potentially altering DM haloes' potential distribution. These processes source from radiation pressure, stellar winds, supernovae and the activity of supermassive black holes in galaxies (Natarajan 1999; Efstathiou 2000;

Gnedin & Zhao 2002; Peirani et al. 2006; Mashchenko et al. 2008; Kereš et al. 2009; Dutton & van den Bosch 2009; Sawala et al. 2010; Governato et al. 2010, 2012; Scannapieco et al. 2012; Agertz et al. 2013; Freundlich et al. 2016; Read et al. 2016; Katz et al. 2018; Bose et al. 2019). Feedback mechanisms produce rapid fluctuations in the halo's potential, transferring their energy to DM particle orbits (Teyssier et al. 2013; Pontzen & Governato 2014). The net effect is that DM particles may be prevented from penetrating into the halo's inner regions, creating a cored distribution. Although baryonic feedback may mitigate the core-cusp issue, its effectiveness in redistributing DM within halos without some degree of fine-tuning is debated (Mac Low & Ferrara 1999; Mo & Mao 2004; Kuzio de Naray & Spekkens 2011; Oñorbe et al. 2015; Bland-Hawthorn et al. 2015; McGaugh 2021). This is especially true in low-mass, DM-dominated dwarf galaxies, typically characterised by cored DM halo profiles (e.g., Ferrero et al. 2012). Indeed, analytical models suggest that in galaxies with stellar masses $M_* \lesssim 10^7 M_\odot$ there is not enough energy in supernovae alone to create DM cores extending above $\sim$ 1 kpc (Peñarrubia et al. 2012). Furthermore, episodic feedback simulations showed how the energy required for solving the too-big-to-fail problem exceeds that available from supernovae in galaxies with $M_* \lesssim 10^7 M_\odot$ (Garrison-Kimmel et al. 2013). Finally, baryonic feedbacks may increase the angular momentum of DM haloes (e.g., Couchman & Thacker 2003; Zhang & Dai 2021).

2.1.2 Adiabatic contraction

As baryons condense in the centre of DM haloes, they may pull DM particles inward, thereby increasing their density in central regions (Blumenthal et al. 1986; Gnedin et al. 2004; Gustafsson et al. 2006). As a response, the DM halo contracts adiabatically, diminishing its radius[1]. In the simplest modelisations of this process, the halo can be seen consisting of spherical shells which contract but do not cross each other (Blumenthal et al. 1986). The resulting deepening of the gravitational potential may trigger a star formation burst in the halo's central region. At this point, feedback (e.g., from supernovae or supermassive black holes) might then eject a significant portion of the baryonic material, lowering the DM halo's concentration and creating a flatter inner radii shape for the halo density profile (Navarro et al. 1996; Read & Gilmore 2005; Pontzen & Governato 2012; Benítez-Llambay et al. 2017; Bose et al. 2019; Li et al. 2023).

2.1.3 Dynamical friction and dynamical flattening

Clumpy material falling into the centre of the DM halo during galaxy formation may experience significant dynamical friction. Contrarily to radiative dissipation, the resulting energy and momentum loss are conserved and transferred to the DM background. This process may expand the DM halo and heat its central region, inducing a uniform DM density at inner radii (El-Zant et al. 2001; El-Zant et al.

[1]In reality, the gas can be re-heated by shocks during halo mergers and accretion along the surrounding filaments. Also, dissipationless evolution may erase the effect of gas cooling on the DM distribution, e.g., Gao et al. (2004)

2004; Tonini et al. 2006; Romano-Diaz et al. 2008; Goerdt et al. 2010; El-Zant et al. 2016). Other dynamical processes may also erase the central DM cusp predicted by CDM. In principle, the growth of supermassive black holes, especially when surrounded by a dense star cluster (as in the Milky Way centre), could lead to a shallower central DM distribution (Merritt et al. 2002; Gnedin & Primack 2004). Moreover, if a supermassive black hole forms through a merger, DM particles might be ejected from the central halo region via three-body interactions (Gnedin & Primack 2004).

2.2 Alternative DM scenarios

A class of solutions to the galaxy scale problems of the CDM paradigm hypothesises new properties for DM that depart from the original Cold picture. The astrophysics community has considered numerous alternative models to CDM, and in this section, I will summarise the main paradigms discussed in the modern literature.

2.2.1 Hot Dark Matter

Hot dark matter (HDM) envisages DM as a low-mass thermal relic particle. Possible candidates are neutrinos with typical velocities $\sim$ 100 km s^{-1}, axions with $\sim$ 1 eV mass (Hannestad et al. 2005, 2007; Hannestad et al. 2008; Hannestad et al. 2010; Archidiacono et al. 2013) or possibly light dark photons (i.e., force carriers associated with a new, hidden or dark U(1) gauge symmetry; e.g., Eddine Ennadifi 2022). The typical high velocities of these particles ($\gtrsim$ 100 km s^{-1}) are larger than the characteristic speed associated with the potential wells of galaxies ($\sim$ 100 km s^{-1}). Hence, HDM particles are prevented from being gravitationally bound on galaxy scales, in a phenomenon called *free streaming*. The magnitude of these free streaming effects implies that galactic DM cannot be made entirely of HDM. Moreover, the high uniformity of CMB speaks against these particles' high velocity since they cannot form clumps as small as galaxies beginning from such a smooth initial state. Indeed, the bulk of the recent literature only considers mixed Hot and Cold DM scenarios (e.g., Das et al. 2022; Hervas Peters et al. 2023).

2.2.2 Warm Dark Matter

The Warm Dark Matter (WDM) paradigm is a midpoint between the Hot and Cold DM models. Even if observations rule out HDM, non-negligible velocity dispersions corresponding to keV-scale particles represent a viable region of parameter space that could solve CDM challenges. Various theoretical models of WDM particles have been proposed, considering different production mechanisms, decoupling temperatures, interactions and decay mechanisms. Spin-1/2 particles, such as sterile neutrinos, can be viable WDM candidates. These are particles produced at the early Universe's high temperatures that may have never been in thermal equilibrium (Lovell et al. 2014; Kennedy et al. 2014; Lovell et al.

2017; Boyarsky et al. 2019; Sen 2021; Dekker et al. 2022; Yunis et al. 2023; Horner et al. 2023). Masses of sterile neutrinos depend on the particular model of particle production, but $\sim$ 1 keV masses show good agreement with simulations and observations (de Vega & Sanchez 2010; de Vega et al. 2012; de Vega & Sanchez 2012; de Vega & Sanchez 2012; Destri et al. 2013a,b; Destri et al. 2013; de Vega et al. 2014; Sanchez et al. 2016; Villanueva-Domingo et al. 2018). Other WDM particle candidates are axinos, hypothetical fermionic superpartners of axions (Kim 2002; Seto & Yamaguchi 2009; Bae et al. 2018; Vogel & Abazajian 2023). Another possibility is offered by spin-3/2 particles such as gravitinos, theoretical particles appearing in Standard Model extensions, constrained by cosmological observations to have masses $\lesssim$ 1 keV (Pagels & Primack 1982; Blumenthal et al. 1982; Bond et al. 1982; Abazajian et al. 2001; Baltz & Murayama 2003; Asaka et al. 2006; O'Shea & Norman 2006; Gorbunov et al. 2008; Vogel & Abazajian 2023; Dayal & Giri 2023), or non-supersimmetric particles. Simulations and observations suggest that keV-scale WDM particles could be immune to some of CDM's small-scale issues, such as the core-cusp problem, the too-big-too-fail problem and satellite counts and distribution (e.g., Lovell et al. 2012; Anderhalden et al. 2013). In this mass range, WDM particles are interested by non-negligible free streaming effects. Hence, these particles suppress structures on Mpc scales and below. Indeed, this suppression is what distinguishes WDM from CDM in simulations (see, e.g., Fig. (4.2)). However, galaxy counts, strong lensing phenomena, observations of stellar streams, Lyman-α forest observations and combinations of these set lower limits on the WDM particle mass at significantly greater scales than the optimal scale of 1-2 keV (Polisensky & Ricotti 2011; Iršič et al. 2017b; Cherry & Horiuchi 2017; Nadler et al. 2019; Gilman et al. 2020; Nadler et al. 2021; Gilman et al. 2021). For instance, the combined constraints from strong lensing and galaxy counts hint at a lower limit of approximately 9.8 keV (at the 95% confidence level; Zelko et al. 2022). This lower limit rises to 11 keV when combining limits from stellar streams, galaxy counts, and lensing (Banik et al. 2021).

2.2.3 Fuzzy Dark Matter

Fuzzy Dark Matter (ψDM) postulates that DM is composed of non-interacting ultra-light scalar particles with a mass around $m \sim 10^{-22}$ eV (e.g., Hu et al. 2000; Schive et al. 2014a; Hui et al. 2021). Interestingly, particles with $m \ll 1$ eV attain extremely high occupation numbers in galactic halos. Hence, ψDM behaves as a classical field $\phi = A\cos(mt - \alpha)$ (with A and α being amplitude and phase terms), which can be described with a collective wavefunction[2] $\Psi(\vec{r}, t) = Ae^{i\alpha}$ out of the amplitude and phase of the field itself. Indeed, ψDM displays a unique astrophysical behaviour due to its macroscopic kpc-scale de Broglie wavelength $\lambda_{\rm dB} \equiv \frac{2\pi}{mv}$ (with m and v being the typical particle masses and velocities), and hence quantum effects are significant at a galaxy-scale level. ψDM particles cannot be confined to scales smaller than their de Broglie length. Thus, per the Uncertainty Principle, this translates into a wide dispersion in the particle momenta's space.

[2]This wavefunction obeys Eq.(2.2.4), yet, differently from the BEC DM model described in Sec. (2.2.4), no self-interaction term is present.

Hence, ψDM particles exert a quantum pressure opposing gravity, giving rise to a rather interesting phenomenology. On galactic scales, this quantum pressure can counterbalance the gravitational effects of DM. Indeed, ψDM simulations anticipate the presence of spherical solitonic standing wave cores with few kiloparsecs diameters. Consequently, the ψDM paradigm generates cored DM halo profiles through the effects of quantum pressure (Schive et al. 2014a,b; Schive et al. 2016). These cores exhibit small-scale fluctuations characterised by fringes attributed to wave interference, often called *granules* (Schive et al. 2014a; Mocz et al. 2017; Veltmaat et al. 2018; Hui et al. 2017). Such characteristic sets ψDM cores apart from the smoother structure of, e.g., WDM ones. Moreover, quantum pressure renders ψDM haloes more concentrated than in other DM paradigms (Mocz et al. 2019). Smaller galaxies are expected to possess broader cores with lower densities because the soliton size increases at lower momentum levels (Pozo et al. 2023). However, Burkert (2020) shows that ψDM cores cannot reproduce the observed core surface density scaling for dwarf galaxies with halo masses $M \leq 10^{11} M_{\odot}$ (Salucci & Burkert 2000; Burkert 2015; see Sec. (3.2.5)).

ψDM predicts almost identical large-scale structures to CDM in terms of the network of filaments and clusters (Schive et al. 2014a; Mocz et al. 2017). However, quantum pressure suppresses structures below $\sim 10^{9} M_{\odot}$ for particle masses $\sim 10^{-22}$ eV (Schive et al. 2016), and galaxy formation is delayed with respect to CDM. In the CDM framework, gravitational attraction from the early formation of the first halos disrupts filaments earlier than in ψDM. The extended filaments' lifetimes in this framework promote the formation of a more significant number of stars within them. This results in a notable disparity in the location and extent of stellar profiles in CDM and ψDM galaxies (Mocz et al. 2019, 2020). Furthermore, this phenomenon causes baryonic objects to appear more diffuse or smoothed compared to CDM, suggesting their potential as effective tracers of DM in the ψDM model.

Various observational studies constrained the ψDM particle's mass: Jeans modelling of dwarf spheroidal galaxies (dSphs, $m \geq 10^{-22}$ eV; Schive et al. 2014a,b; Mocz et al. 2017; Veltmaat et al. 2018; Chen et al. 2017; Niemeyer 2020; Safarzadeh & Spergel 2020; Hayashi et al. 2021); the analysis of stellar dispersion in ultra-faint dwarf galaxies ($m > 3 \times 10^{-19}$ eV; Dalal & Kravtsov 2022); Lyman-α forest observations of cosmic structures ($m > 3.8 \times 10^{-21}$ eV from Iršič et al. 2017a and $m > 2 \times 10^{-20}$ eV from Rogers & Peiris 2021); Milky Way subhalo population observations ($m > 2.9 \times 10^{-21}$ eV; Nadler et al. 2021); Milky Way stellar streams observations ($m > 2.2 \times 10^{-21}$ eV; Banik et al. 2021) and flux ratio anomalies in gravitationally lensed quasars ($m > 10^{-21}$ eV; Laroche et al. 2022).

2.2.4 Bose–Einstein Condensate Dark Matter

The Pauli exclusion principle postulates that fermions are prohibited from occupying identical quantum states. Bosons, however, do not adhere to this restriction. Consequently, when the bosons' density is sufficiently high, and their temperature is significantly low, they merge into a unified quantum state called Bose–Einstein condensate (BEC). BECs are describable through a wave function at a nearly

macroscopic scale. In this regime, bosons become correlated as their wavelengths overlap, specifically when their thermal wavelength surpasses the mean inter-particle distance. This requires the particle temperature to fall below the critical threshold $T_c = 2\pi\hbar^2 n^{2/3}/mk_B$, which is determined by the mass of the condensate particles m and their number density n, with $\hbar$ being the reduced Planck constant and k_B being the Boltzmann's constant (Dalfovo et al. 1999; Cornell & Wieman 2002; Pethick & Smith 2002; Griffin et al. 2009).

The macroscopic wave function of the condensate and its dynamics can be described through the Gross–Pitaevskii equation, which provides a mean-field description of the condensate's behaviour, treating the many-particle quantum system as a single, coherent entity. The time-dependent Gross–Pitaevskii equation reads as:

$$i\hbar\frac{\partial\Psi(\vec{r},t)}{\partial t} = \left(-\frac{\hbar^2}{2m}\nabla^2 + V(\vec{r}) + g|\Psi(\vec{r},t)|^2\right)\Psi(\vec{r},t).$$

Here, $\Psi(\vec{r},t)$ represents the total BEC wavefunction, which in the Hartree–Fock approximation can be expressed as the product of the single bosonic particle wavefunctions. The term $-\hbar^2/(2m)\nabla^2$ describes a repulsive effect stemming from the quantum pressure developed by the Uncertainty Principle (analogously to ψDM, see Sec. (2.2.3)), whereas V is the potential acting on the condensate. Finally, g represents the strength of the inter-particle interactions and reads as $g = 4\pi\hbar^2 a_s/m$, with a_s being the scattering length.

BECs are characterised by an intrinsic lengthscale called the *healing length* of the condensate. This lengthscale parametrises how quickly the wavefunction of the BEC can adjust to changes in the potential, characterising the typical scale of time/space variations of the condensate amplitude. The healing length ξ can be found by equating the quantum pressure and the interaction energy of the condensate:

$$\xi = \frac{1}{\sqrt{8\pi n a_s}}. \tag{2.1}$$

The concept of healing length will be reprised in Sec. (3.1.3) when discussing the characteristics of the non-minimally coupled DM model presented in Chapter 3.

The process of Bose–Einstein condensation was initially observed experimentally in 1995 with dilute alkali gases, such as rubidium and sodium vapours, which were confined in a magnetic trap and cooled to extremely low temperatures (Anderson et al. 1995; Bradley et al. 1995; Davis et al. 1995). Subsequently, quantum degenerate gases have been created by combining laser and evaporative cooling techniques, opening up exciting avenues of research at the intersection of atomic, statistical, and condensed matter physics. The concept that DM could exist in the form of a BEC was first contemplated in the works of Sin (1994) and Ji & Sin (1994). These studies used the non-relativistic Gross–Pitaevskii equation to describe the condensate, deriving numerical solutions. An alternative approach was proposed by Boehmer & Harko (2007), who introduced the Madelung representation of the wave function, an equivalent alternative formulation of the Schrödinger equation

using hydrodynamical variables (Madelung 1926). Within this framework, DM is believed to consist of non-relativistic bosons condensing into gravitationally confined Newtonian condensates (Harko & Madarassy 2012; Harko & Lobo 2015). In this scenario, the BEC DM's density and pressure are described by a barotropic equation of state with index $n = 1$.

The repulsive interaction developed by bosons occupying the same ground energy state hinders the formation of central density cusps in DM haloes. Indeed, BEC DM has proven to suitably fit RCs of dwarf galaxies, low surface brightness galaxies, and regular spiral galaxies (Harko 2011; Dwornik et al. 2013; Zhang et al. 2018; Crăciun & Harko 2020; Harko & Madarassy 2022). The size and mass of BEC DM haloes and the condensate's collapse time significantly depends on two key parameters: the DM particle's mass and the scattering length (Harko 2014). An analysis carried out on galaxy cluster scales has suggested that BEC DM's particle mass is approximately on the order of μeV, with a scattering length of 10^{-7} fm (Harko et al. 2015). Studies of Milky Way satellites in BEC DM instead hint at particle masses of 10^{-22} eV (Lee & Lim 2010), whereas fits to RCs of spiral galaxies suggest the $10^{-6} - 10^{-4}$ eV range, with a lower bound for the scattering length of 10^{-14} fm (Pires & de Souza 2012).

BEC DM has undergone testing on various fronts, such as the study of the collapse of BEC DM haloes (Harko 2019; Harko et al. 2022), gravitational lensing (Harko & Lobo 2015), the formation of BEC DM structures on stellar scales (Li et al. 2012), and the cosmological ramifications of this condensation process (Harko 2011; Harko & Mocanu 2012). While quantum mechanical effects dominate at small scales and shape the DM halo mass distribution, BEC DM resembles an assembly of cold particles at larger scales. Indeed, BEC DM particles are light enough to produce small mass condensates that naturally coalesce over cosmic time, forming structures akin to the bottom-up hierarchical clustering of CDM (Harko 2011).

2.2.5 Self-Interacting Dark Matter

The CDM model suggests that DM is non-relativistic and interacts primarily through gravity. However, one intriguing avenue is the potential introduction of new forces beyond gravity between DM particles. Indeed, this reciprocal scattering of DM particles could enhance galactic and sub-galactic DM phenomenology. Such interaction may also produce deviations from CDM in the DM power spectrum, influencing individual halos and their statistical properties (see, e.g., Fig. (4.2)). This is the core idea behind the Self-Interacting Dark Matter (SIDM) paradigm.

As the halo grows, the self-interaction transfers energy from the outer and hotter parts of the halo to the inner and colder ones. This exchange renders the halo inner region isothermal, creating flat cores, while the outer region is well-described by the NFW profile (Ray et al. 2022). SIDM predicts halo shapes remarkably different from the CDM paradigm. Self-interactions isotropise DM particle's orbits, leading to closely spherical inner halo regions (Peter et al. 2013). Instead, CDM's halo velocity dispersion anisotropy can be substantial, with the

halos' shapes being distinctly triaxial in the centre. It is also argued that the SIDM paradigm can alleviate the missing satellites problem since interactions between DM particles can kick particles out of subhalos (e.g., Spergel & Steinhardt 2000). This effect, coupled with the increased tidal disruption of cored subhalos compared to cuspy subhalos, leads to fewer Milky Way satellites than in CDM cosmology. However, constant cross-section SIDM models predict mass losses due to scattering events inefficiently altering the subhalo mass function (Vogelsberger et al. 2012; Dooley et al. 2016). Furthermore, the observed great variety in the shapes of RCs (e.g., de Blok et al. 2001; Simon et al. 2005; Kuzio de Naray et al. 2010; Adams et al. 2014) could be explained in the SIDM framework since it is unclear if the physics of star formation can create the observed diversity of density profiles (Oman et al. 2015; Creasey et al. 2017; Kamada et al. 2017; Valli & Yu 2018; Robertson et al. 2018; Ren et al. 2019; Zavala et al. 2019).

SIDM models positing DM self-scattering as the only relevant dark sector interaction can recover the successes of ΛCDM at cosmological scales. Mass and momentum conservation ensures a large-scale linear density perturbation evolution unaffected by DM self-interactions (Cyr-Racine et al. 2016), featuring a linear power spectrum identical to the CDM one. However, new DM interaction beyond self-scattering could alter the evolution of DM density fluctuations, e.g., when a relativistic or massless particle mediates self-interactions (see the review Adhikari et al. 2022). In a scenario where DM interacts with a relativistic species during the early Universe, a phenomenon similar to BAOs emerges, known as *dark acoustic oscillations*. However, the amplitude of such oscillations in the matter power spectrum can be notably larger due to the greater abundance of DM than baryons. Consequently, the damping effect resulting from the relativistic species diffusing out of DM overdensities can profoundly affect the formation of cosmic structures, effectively erasing density perturbations on scales below the mean free path of the relativistic species. The specific scale at which this erasure occurs and the shape of the damping envelope in the matter power spectrum depends on the type and strength of the interaction between DM and the relativistic species (e.g., Feng et al. 2009; Cyr-Racine & Sigurdson 2013). When the momentum transfer rate involved in elastic scattering process goes below the Hubble rate, kinetic decoupling occurs, and the kinetic decoupling temperature dictates the deviation of the SIDM matter power spectrum from the standard CDM case (Huo et al. 2018).

2.2.6 MOND and modified gravity theories

Modifying gravity is a possible avenue that can be adopted to solve the galaxy-scales issues of the CDM paradigm. There are a plethora of scenarios contemplating DM in modified gravity frameworks (e.g., Benetti et al. 2023a,b) or that aim to eliminate the need for DM in the cosmos, such as $f(R)$ or $f(R,T)$ theories (e.g. Sotiriou & Faraoni 2010; Shabani & Moraes 2023), or MOdified Gravity (MOG, Moffat 2005; Nieuwenhuizen et al. 2018). However, in this thesis I will mainly focus on Modified Newtonian Dynamics (MOND; Milgrom 1983), one of the most popular modified gravity theories born to solve the missing mass

problem without recurring to DM.

There is a fundamental idea that motivated the introduction of MOND: while Newton's laws were accurately tested in high-acceleration settings (i.e., within the Solar System and on Earth), these laws needed to be experimentally validated in extremely low acceleration regimes, e.g. in the outskirts of galaxies. Consequently, Milgrom (1983) proposed that the gravitational acceleration acting on an object should read as

$$\mu\left(g/a_0\right)\vec{g} = \vec{g}_N$$

where $a_0 \sim 1.2 \times 10^{-10} m/s$ is an empirical scale acceleration that separates MONDian (low accelerations, $g < a_0$) and Newtonian (high accelerations $g > a_0$) regimes, and it is a universal constant. The function $\mu(x)$, with $x = g/a_0$, is known as *interpolation function*. MOND does not yield a definite theoretical prediction on the analytical shape of μ, yet it should generally behave as

$$\mu(x) = \begin{cases} 1 & \text{if } |x| \geqslant 1 \\ x & \text{if } |x| \ll 1 \end{cases}. \tag{2.2}$$

This behaviour of μ lets Eq.(2.2.6) recover Newtonian gravity for $a > a_0$. In general, two families of interpolation functions are widely used in the MONDian literature:

$$\mu(x) = \left[\frac{1 + (1 + 4x^{-p})^{1/2}}{2}\right]^{1/p},$$
$$\mu(x) = \left[1 - \exp\left(-x^{\delta/2}\right)\right]^{-1/\delta},$$

with the parameters p and δ being positive real numbers. For the p-family, $p = 1$ and $p = 2$ return the so-called *simple* and *standard* interpolating functions, respectively. For the δ-family, $\delta = 1$ returns the interpolation function corresponding to Eq.(1.6), i.e., the one best describing the RAR in galaxies (Famaey & McGaugh 2012; Dutton et al. 2019). These functions alongside Eq.(2.2.6) were used to fit a wide range of spirals' RCs (Li et al. 2021; López-Corredoira & Betancort-Rijo 2021; Mohanty & Harish 2023; Lelli et al. 2023).

Note that MOND phenomenology can be interpreted either as a modification of gravity or a modification of inertia itself, depending if, in the non-relativistic action of the theory, one alters the kinetic or the potential term (Milgrom 2002; Milgrom & Sanders 2005). It is yet to be clear whether if data favour modified gravity or modified inertia MOND (Lelli et al. 2016; Petersen & Frandsen 2017; Li et al. 2018; Frandsen & Petersen 2018; Petersen 2019), yet the two frameworks could be discriminated by measuring suitably extended and finely-sampled RCs of extremely low-surface-brightness galaxies (Petersen & Lelli 2020). In this thesis, I will refer to MOND in the modified gravity interpretation.

Non-relativistic extensions of the standard MOND framework are AQUAL (a quadratic Lagrangian; Tiret & Combes 2007; Bekenstein 2009; Skordis & Zlosnik

2012; López-Corredoira & Betancort-Rijo 2021; Milgrom 2023), QUMOND (quasi-linear MOND; McGaugh et al. 2012; Galianni et al. 2012; Trenkel & Wealthy 2014; López-Corredoira & Betancort-Rijo 2021; Milgrom 2023) and TRIMOND (tripotential theories; Milgrom 2023), comprising both AQUAL and QUMOND. Instead, there are several relativistic extensions of MOND. A common feature is their capability to reduce to standard MOND in the non-relativistic limit. However, their predictions in the relativistic regime can vary significantly from paradigm to paradigm. Among the first relativistic extensions proposed for MOND, one can find RAQUAL (Relativistic AQUAdratic Lagrangian; Bekenstein & Milgrom 1984), TeVeS (Tensor Vector Scalar theories; Bourliot et al. 2007), GEA theories (Generalised Einstein Aether; Zlosnik et al. 2008; Thomas et al. 2023), Bimetric MOND (BIMOND; Clifton & Zlosnik 2010; Milgrom 2022) or Relativistic MOND (RMOND; Skordis & Złośnik 2021; Kashfi & Roshan 2022). Recently, these relativistic extensions of MOND were constrained by the observation of gravitational wave signals (Sanders 2018).

GR is the only 4D tensorial theory of gravity obeying the Strong Equivalence Principle (SEP)[3], and hence, 4D tensorial theories departing from GR can break the SEP in different ways. Specifically, MOND's breaking of SEP manifests by the introduction of an *External Field Effect* (EFE) in the model's action (Milgrom 1983). The internal dynamics of MONDian subsystems embedded in larger systems may be influenced by their potential (even if the gravitational field is constant). In MOND, the EFE should be relevant for binary stars, star clusters, and satellite galaxies embedded in the field of a larger galaxy. Also, galaxies falling in the potential of clusters or the general surrounding large-scale structure should feel the EFE. This effect is a generic prediction of all MOND formulations (Milgrom 2014) and there are some claims of its observations in dwarf, ultra-diffuse and normal spiral galaxies (McGaugh & Milgrom 2013; Lelli et al. 2016; Chae et al. 2020, 2021; Chae 2022). Moreover, the EFE has been recently studied in the context of simulations and numerical studies (e.g., Zonoozi et al. 2021; Oria et al. 2021).

Over the years, MOND has been thoroughly tested against RCs of spirals. Since it is a phenomenological model designed for this task, it generally yielded remarkable results while keeping the parameter a_0 at a fixed value (Sanders 2019; Lelli et al. 2023). Furthermore, MOND could be exempt from the angular momentum problem (Haslbauer et al. 2022). Also, this framework may naturally explain the existence of the RAR[4] (Kroupa et al. 2018; Desmond 2023) and other empirical relationships linking DM to baryons in spiral galaxies. Indeed, the MONDian framework predicts naturally a relation linking the asymptotic velocity v_f of a galaxy with its baryonic mass M_b, namely $v_f^4 = a_0 G M_b$, which is in perfect accordance with the observed BTFR. However, the recent literature debates MOND's capability in explaining the baryons-DM interplay in galaxies (e.g., Desmond et al. 2023; Rodrigues & Marra 2020) and in galaxy clusters (Pradyumna & Desai

[3]Besides GR, there is another theory obeying the SEP in 4D — Nördstrom Gravity. Yet, differently from GR, this theory describes gravity by a scalar field in flat spacetime, and it has been ruled out by simple arguments (such as the lack of light deflection or failure in accounting for Mercury's periastron precession, see, e.g., Deruelle 2011).

[4]In this case, the acceleration scale $g_\dagger$ appearing in Eq. (1.6) is interpreted as a fundamental acceleration scale in galaxies, which is remarkably close to the value of a_0.

2021). Moreover, MOND struggles to reproduce the mass distribution of clusters (McGaugh 2015), the observed collisionless behaviour of a substantial mass component in colliding clusters (e.g. the *Bullet Cluster*[5]; Clowe et al. 2006), and to develop a cosmological extension in agreement with CMB anisotropies and matter power spectra observations (Dodelson 2011). Recently, it was claimed that RMOND is consistent with these observables. Yet, although there is no DM particle postulated in this framework, the corrections that are induced to the standard Friedmann equations via the existence of the extra vector and scalar fields appearing in RMOND may just mimic the DM behaviour.

Overall, the challenges faced by the CDM framework on galaxy scales remain without a conclusive and all-encompassing resolution, leaving the discussion ongoing. In the following Chapter, I will present an alternative approach to constructing a DM phenomenology tailored to galaxy-scale dynamics while preserving the achievements of the CDM paradigm at cosmological levels. This approach introduces a model in which DM exhibits non-minimal coupling to gravity.

[5]Some efforts to reconcile MOND with merging clusters and clusters' dynamical mass estimates have been carried out in the literature, albeit they require a certain fine tuning (e.g., Li et al. 2013; López-Corredoira et al. 2022).

Chapter 3

Non-Minimally Coupled Dark Matter

3.1 Theoretical Background

This section explores the possibility that DM is dynamically non-minimally coupled with gravity. The particular coupling adopted here was originally presented in Bettoni et al. (2011); Bettoni et al. (2012, 2014); Bettoni & Liberati (2015), and this Chapter aims to characterise and test its interesting phenomenology from the scales of dwarf galaxies up to cluster ones. The following sections are based on the discoveries presented in Gandolfi et al. (2021); Gandolfi et al. (2022a); Gandolfi et al. (2023).

3.1.1 Motivation

How can one build a model capable of keeping DM's non-collisionality in a cosmological setting while enhancing its phenomenology at the scales of galaxies? One of the possible answers is to consider a non-minimal coupling (NMC) between DM and gravity. Introducing such NMC has a double-fold advantage. On the theoretical side, it is allowed by the Einstein Equivalence Principle (Buchbinder et al. 1992, Di Casola et al. 2015), and it might be required for the renormalizability of quantum field theories in curved spacetimes (e.g., Sonego & Faraoni 1993; Bruneton et al. 2009). Observationally, the NMC may help explain the puzzling empirical relationships between DM and baryons recalled in Chapter 1, which are not trivially explainable based on galaxy formation processes (see Sec. (1.4.5)). Indeed, these relationships may hint at the presence of a DM-baryon interaction. If such interaction is non-negligible, it cannot be accounted for by weak DM-baryons interaction predicted by beyond-Standard Model physics. Consequently, I will not deal with any specific DM particle model, instead adopting a standard fluid approximation and describing DM as a simple scalar field[1].

[1]Such a fluid approximation might not describe the entire matter fields' microphysics. However, neglecting these effects is a reasonable approximation when describing astrophysical (i.e., macroscopic) systems such as galaxies or clusters of galaxies.

How can one explain the observed interplay between DM and baryons within galaxies? Possibly, DM could behave geometrically at specific scales, providing an effective metric for baryons in galactic environments. Thus, baryons would play their dynamics on some modified gravitational background. In this scenario, the gravitational metric (i.e., the metric associated with the Einstein frame, describing gravitational field's dynamics, whose lead contribution is DM's) and the physical metric (the metric experienced by baryons) will not coincide anymore, unlike in the standard GR picture. The DM field's properties may also determine the physical metric experienced by baryons, and thus, the two metrics should be linked by a reasonable kind of transformation depending on the DM scalar field. As shown in Bekenstein (1993), disformal transformations are the most general class of transformations between physical and gravitational metrics, preserving causality and the Weak Equivalence Principle. Disformal transformations are commonly utilised to model relativistic extensions of MOND (e.g., TeVeS and RAQUAL; see Sec. (2.2.6)). However, the model hereby presented assumes that DM is indeed present in the Universe (unlike what happens in TeVes and RAQUAL theories).

Identifying the gravitational metric with $g_{\mu\nu}$ and the physical metric with $\tilde{g}_{\mu\nu}$, a general expression of a disformal transformation linking the two is given by:

$$\tilde{g}_{\mu\nu} = e^{2\varphi}\left[\mathcal{A}(\varphi, X)g_{\mu\nu} + \mathcal{B}(\varphi, X)\nabla_\mu\varphi\nabla_\nu\varphi\right]. \tag{3.1}$$

Here $\mathcal{A}$ and $\mathcal{B}$ are functions to be specified (if $\mathcal{B} = 0$ a conformal transformation is recovered), φ is an extra scalar field (identified as DM) and $X = -\frac{1}{2}g_{\mu\nu}\nabla^\mu\varphi\nabla^\nu\varphi$ is the standard field's kinetic term. Bruneton & Esposito-Farese (2007) and Bruneton et al. (2009) proved that it is possible to force the DM field φ to recover a MOND-like phenomenology at galaxy scales with the following choice of the coefficients $\mathcal{A}$ and $\mathcal{B}$:

$$\begin{aligned}\mathcal{A} &= \left(e^{\alpha\varphi} - \frac{\varphi}{\alpha}Xe^{m\omega}u(X)\right)^2 - 1,\\ \mathcal{B} &= -4\frac{\varphi}{\alpha}\frac{Xe^{m\omega}}{(\partial\varphi)^2}.\end{aligned} \tag{3.2}$$

Here α is a pure number characterizing the coupling of φ to matter and X, ω and u being functions defined as

$$\begin{aligned}\omega &= \left(\frac{\sqrt{(\partial\varphi)^2}}{\varphi} - m\right)^{-1},\\ X &= \frac{\sqrt{\alpha a_0}}{c}\sqrt{\frac{\omega}{-\varphi e^{m\omega}}},\\ u(x) &= (1+x)^{-1} + \ln(1+x).\end{aligned} \tag{3.3}$$

However, as conjectured in Bettoni et al. (2011); Bettoni et al. (2012, 2014) and Bettoni & Liberati (2015), way simpler choices for the coefficients of the disformal transformation expressed in Eq. (3.1) can yield to an interesting phenomenology for DM at galactic scales.

3.1.2 Action and field equations

To determine which kind of interaction can translate into an effective coupling via the disformal metric in Eq. (3.1), one can start from a general action of the form

$$S = S_{\rm EH}[g_{\mu\nu}] + S_{\rm bar}[g_{\mu\nu}, \psi] + S_{\rm DM}[g_{\mu\nu}, \varphi] + S_{\rm int}[g_{\mu\nu}, \psi, \varphi]\,. \tag{3.4}$$

Here $S_{\rm EH} = \kappa \int {\rm d}^4x\, \sqrt{-g}\, R$ (with $\kappa = 1/(16\pi G)$) represents the standard general relativity Einstein-Hilbert action expressed in terms of the Ricci scalar R in natural units $c = \hbar = 1$; $S_{\rm bar}$ and $S_{\rm DM}$ respectively represents the baryonic and DM actions, and $S_{\rm int}$ is the interaction term. The scalar fields ψ and φ are thought of as collective variables, respectively encoding baryons and DM.

The interaction term $S_{\rm Int}$ should produce an effective metric along which standard matter propagates:

$$S_{\rm bar}[g_{\mu\nu}, \psi] + S_{\rm int}[g_{\mu\nu}, \psi, \varphi] \approx S_{\rm bar}[\tilde{g}_{\mu\nu}, \psi, \varphi] = S_{\rm bar}[g_{\mu\nu} + h_{\mu\nu}, \psi, \varphi], \tag{3.5}$$

with $h_{\mu\nu}$ being a generic symmetric tensor parametrising the transformation between the physical and gravitational metric. If one wants such transformation to be a disformal one as in Eq. (3.1), then $h_{\mu\nu} \propto \nabla_\mu\varphi\nabla_\nu\varphi$. Expanding Eq. (3.5) up to $O(h^2)$ order, one obtains:

$$S_{\rm bar}[\tilde{g}_{\mu\nu}, \psi] = S_{\rm bar}[g_{\mu\nu} + h_{\mu\nu}, \psi, \varphi] \approx S_{\rm bar}[\tilde{g}_{\mu\nu}]\big|_{h_{\mu\nu}=0} + h_{\mu\nu}\left.\frac{\delta S_{\rm bar}}{\delta \tilde{g}_{\mu\nu}}\right|_{h_{\mu\nu}=0} + O(h^2) =$$

$$= S_{\rm bar}[g_{\mu\nu}] + h_{\mu\nu}\frac{\delta S_{\rm bar}}{\delta g_{\mu\nu}} + O(h^2) = S_{\rm bar}[g_{\mu\nu}] - \frac{1}{2}\int {\rm d}^4x\, \sqrt{-g}\, T^{\mu\nu}_{\rm bar}\, \nabla_\mu\varphi\nabla_\nu\varphi + O(h^2).$$

Hence, the desired interaction term in Eq. (3.4, 3.5) is, up to $O(h^2)$:

$$S_{\rm int}[g_{\mu\nu}, \psi, \varphi] \propto \int {\rm d}^4x\, \sqrt{-g}\, T^{\mu\nu}_{\rm bar}\, \nabla_\mu\varphi\nabla_\nu\varphi, \tag{3.6}$$

where $T^{\mu\nu}_{\rm bar}$ is the baryonic matter stress-energy tensor (SET). The interaction term in Eq. (3.6) implicitly implies choosing $\mathcal{A} = \mathcal{B} = 1$ for the disformal transformation expressed in Eq. (3.1).

If one expresses the full action in terms of the physical metric $\tilde{g}_{\mu\nu} \equiv g_{\mu\nu} + h_{\mu\nu}$ (which is equivalent to choose a frame in which baryons follow the geodesics of this metric, i.e., the Jordan frame), then the DM field gets non-minimally coupled to gravity:

$$S = S_{\rm EH}[\tilde{g}_{\mu\nu}] + S_{\rm bar}[\tilde{g}_{\mu\nu}, \psi] + S_{\rm DM}[\tilde{g}_{\mu\nu}, \varphi] + \epsilon L^2 \int {\rm d}^4x\, \sqrt{-\tilde{g}}\, \tilde{G}^{\mu\nu}\, \nabla_\mu\varphi\nabla_\nu\varphi. \tag{3.7}$$

The last term in the above action is an NMC between gravity and the DM scalar field. Here, L is a coupling lengthscale introduced for dimensional consistency, and it constitutes the true free parameter of this model. $\epsilon = \pm 1$ is instead a unitary, dimensionless constant representing the coupling's polarity (undetermined

a priori), serving as a bookkeeping parameter to keep track of the effects of the NMC easily. Finally, $\tilde{G}^{\mu\nu}$ is the Einstein tensor expressed in terms of the physical metric $\tilde{g}_{\mu\nu}$, and the DM field has been implicitly redefined through a conformal factor. This is the same kind of NMC considered, e.g., in Bettoni et al. (2014) and Ivanov & Liberati (2020), whereas the shape of $h_{\mu\nu}$ is radically different from the one considered in the MOND-inspired scenario of Bruneton et al. (2009).

As argued in Bettoni et al. (2014) and Bettoni & Liberati (2015), the only other NMC term with the same physical dimensions that still leads to second-order field equations would be proportional to the Ricci scalar as $\mathcal{X}R$. However, such coupling is equivalent to that appearing in Eq. (3.7) modulo a surface term (see Bettoni et al. 2012). Moreover, as argued in Bettoni & Liberati (2013), the action given in Eq. (3.7) is a subcase of the Horndeski one, which constitutes the most general scalar-tensor theory giving rise to second-order field equations. Indeed, the coupling term $\tilde{G}^{\mu\nu}\,\nabla_\mu\varphi\nabla_\nu\varphi$ itself is proportional to a term of the Horndeski Lagrangian. Note also that the coupling hereby considered is written in terms of a real scalar field for simplicity. However, the NMC in Eq. (3.6) can be easily generalised to a complex scalar field as $\tilde{G}^{\mu\nu}\nabla_\mu\varphi\nabla_\nu\varphi^\dagger$.

The model's field equations are found by varying the Jordan frame total action given by Eq. (3.7) to the physical metric $\tilde{g}_{\mu\nu}$ (see Appendix (A) for the complete derivation):

$$\frac{1}{8\pi G}\widetilde{G}_{\mu\nu} = T^{\text{bar}}_{\mu\nu} + T^{\text{DM}}_{\mu\nu} + \epsilon L^2 T^{\text{NMC}}_{\mu\nu}, \tag{3.8}$$

where:

$$\begin{aligned}
T^{\text{bar}}_{\mu\nu} &= (\rho + p)u_\mu u_\nu + \widetilde{g}_{\mu\nu}p;\\
T^{\varphi}_{\mu\nu} &= \nabla_\mu\varphi\nabla_\nu\varphi - \frac{1}{2}\widetilde{g}_{\mu\nu}\widetilde{g}^{\alpha\beta}\partial_\alpha\varphi\partial_\beta\varphi - \widetilde{g}_{\mu\nu}V(\varphi);\\
T^{\text{NMC}}_{\mu\nu} &= \widetilde{g}_{\mu\nu}\widetilde{G}_{\alpha\beta}\nabla^\alpha\varphi\nabla^\beta\varphi + \widetilde{R}_{\mu\nu}\widetilde{g}_{\alpha\beta}\nabla^\alpha\varphi\nabla^\beta\varphi - R\nabla_\mu\varphi\nabla_\nu\varphi\\
&+ 2\widetilde{g}_{\sigma\mu}\nabla_\alpha\nabla^\sigma\left(\nabla^\alpha\varphi\nabla_\nu\varphi\right) - \Box\left(\nabla_\mu\varphi\nabla_\nu\varphi\right) - \widetilde{g}_{\mu\nu}\nabla_\alpha\nabla_\beta\left(\nabla^\alpha\varphi\nabla^\beta\varphi\right)\\
&+ \left(\widetilde{g}_{\mu\nu}\Box - \nabla_\mu\nabla_\nu\right)\left(\nabla^\alpha\varphi\nabla_\alpha\varphi\right),
\end{aligned}$$

Here, $\Box = \nabla^\alpha\nabla_\alpha$ denotes the d'Alembert operator. By varying the total action in Eq. (3.7) to the DM scalar field φ, one obtains the scalar field equation of motion, which reads as

$$\Box\varphi + V'(\varphi) + 2\epsilon L^2\widetilde{G}^{\mu\nu}\partial_\mu\varphi\partial_\nu\varphi = 0. \tag{3.9}$$

Appendix (B) contains the complete derivation of Eq. (3.9). If the NMC is absent (i.e. $\epsilon = 0$) and $V(\varphi) = -1/2m^2\varphi^2$, with m being the mass of the particle associated with the field φ, the standard Klein-Gordon equation is retrieved.

3.1.3 Physical origin of the NMC

The NMC in Eq. (3.7) arises when the lengthscale L is comparable with the local curvature scale. However, one may ask: what is the physical origin of L? Indeed, there are a plethora of dynamical mechanisms that could easily result in DM spontaneously developing an effective characteristic lengthscale in galactic haloes. One such process is DM phase transitions happening in virialised structures, i.e., the lengthscale L could be tied with DM's collective behaviour. For instance, as previously mentioned in Sec. (2.2.4), BECs develop a coherence lengthscale called healing length. As a result, BECs may indeed develop an NMC with gravity (e.g., Bettoni et al. 2011; Bettoni & Liberati 2015). DM could also develop a macroscopic characteristic length phenomenologically. The same physical process making DM depart from a pressureless dust equation of state (EoS) in galaxies could also be responsible for the emergence of L. Finally, DM could develop a characteristic lengthscale when considering a fluid description instead of scalar field DM. Under this framework, the mean free path of the fluid constituents could indeed reasonably be comparable with the curvature scale (e.g., Bettoni et al. 2011). The NMC lengthscale would then naturally stem from the averaging procedure associated with the fluid description of matter. However, the precise physical origin of the coupling scalelength L in Eq. (3.7) is yet to be pinpointed. Since the focus of this work is to test the phenomenology of this model, an agnostic approach will be adopted in this regard.

Before continuing, an important remark is in order: the NMC DM model considered here does not consist of a fundamental theory of modified gravity. It does not consist of a scalar-tensor theory, and although the usual coincidence of physical and gravitational metric was relaxed, GR still holds. Thus, the NMC lengthscale L is not a new fundamental constant of nature. It is instead assumed to be a coherence lengthscale dynamically developed by DM in galactic haloes. Hence, the expectation is that it will show some dependence on the characteristics of the single DM haloes.

3.1.4 NMC DM in the Newtonian limit

Investigations of gravitational dynamics at the level of galaxies are best performed in the Newtonian limit of the theory, which is recovered by taking the weak field limit of the gravitational interaction. This is a useful approximation to describe low-density and small-velocity physical systems such as galaxies. As shown in Bettoni et al. (2014) and detailed in Appendix (C), the NMC considered in Eq. (3.7) leads to the following modified version of the Poisson equation:

$$\nabla^2\Phi = 4\pi G\,[(\rho + \rho_{\rm bar}) - \epsilon\, L^2\, \nabla^2\rho], \tag{3.10}$$

where Φ is the Newtonian potential, and $\rho_{\rm bar}$ and ρ are the baryon and DM mass densities respectively. Such modified Poisson equation implies that the source for gravity is not just the total matter density in itself but also the spatial inhomogeneities in the DM distribution. Remarkably, the same formal modification can be obtained starting directly from a cosmological fluid description (see

Bettoni & Liberati 2015), albeit in this case, there is no fundamental reason to couple the fluid directly to the Einstein tensor — and indeed, it is necessary to couple separately the fluid to the Ricci scalar and/or Ricci tensor to get the same kind of modification, as in Bettoni et al. (2014). It is also worth reporting that the same form of modified Poisson equation can be derived in Born–Infeld gravity (e.g., Beltran Jimenez et al. 2018).

3.1.5 Constraining the NMC with gravitational waves

The NMC here considered is of Horndeski type and leads to a local modification of the speed of gravity to the speed of light. Ivanov & Liberati (2020) tested this NMC using the joint detection of GW170817 and its electromagnetic counterpart GRB170817A (Abbott et al. 2017a,b). In this analysis, the NMC is assumed to emerge via a Bose–Einstein condensation in virialised structures. When it is not in the condensate phase, the DM scalar field is assumed to oscillate in order to behave as pressureless CDM in a cosmological setting (as, e.g., in Turner 1983). Since there is no complete mathematical theory of condensation in curved spacetimes, there is no *a priori* knowledge on how strong the gravitational field needs to be in order for the condensation to occur — is DM in the condensate phase only inside galactic halos or also inside cluster halos? This uncertainty is parametrised by introducing a free parameter $\beta \equiv \tilde{L}/(\alpha\xi)$ in the analysis, with $\tilde{L}$ being the NMC lenghtscale on cluster scales (kept as a free parameter), ξ being the healing length of the condensate and $\alpha = \left(\bar{\rho}_{cl}/\bar{\rho}_{gh}\right)^{-1/2} R_{h,g}/R_{h,cl} \sim 0.1$ being an empirical constant taking into account the fact that a BEC in the whole cluster would have a different healing length than a BEC in a galaxy (with $\bar{\rho}_{cl} = 3 \times 10^{-24}$ kg/m^5 and $R_{h,cl} = 1.2 \times 10^{23}$ m being the assumed typical total average density and virial radius of clusters and $\bar{\rho}_{gh} = 10^{-23}$ kg/m^3 and $R_{h,g} = 200kpc = 6 \times 10^{21}$ m being the same thing for galaxies). In order to parametrise the field oscillations (which could be damped by the NMC when DM is in the condensate phase), two other free parameters are introduced — $\gamma_1 = \frac{m_{\text{eff,gal}}}{m}$ and $\gamma_2 = \frac{m_{\text{eff,cl}}}{m}$, with m being the mass scale of the DM field and m_{eff} being an effective mass related to the effective period of dampened oscillations in galaxies ($m_{\text{eff,gal}}$) or clusters ($m_{\text{eff,cl}}$). In total, this model has five free parameters: $\beta, \gamma_1, \gamma_2$, the mass scale of the condensate m and the galactic NMC lengthscale L.

The dominant effect on γ-ray bursts' (GRBs) time delay to the corresponding gravitational wave (GW) signal may be assumed to come from three primary sources: the Milky Way DM halo, the host galaxy halo and, eventually, from the halos of clusters between Earth and the event. Moreover, it is assumed that GWs and GRBs pass through the centre of each halo and that a Burkert profile describes their internal structure. Under these assumptions, the authors obtain a relative difference between the speed of gravity c_g and the speed of light $\Delta c_g \equiv \frac{c_g - c}{c}$ given by

$$\Delta c_g(r) = \frac{\rho_{0,g} L^2}{4 M_p^2 m^2 r_{0,g}^2} F\left(\frac{r}{r_{0,g}}\right).$$

Here, $\rho_{0,g} = 3 \times 10^{-22}$ kg m^{-3} and $r_{0,g} = 15$ kpc are assumed typical values for the Burkert's galactic halo profile core density and radius, M_p is the reduced Planck mass given by $M_p \equiv 1/\sqrt{8\pi G} = 2.4 \times 10^{27}$eV and $F(x)$ is a function given by

$$F(x) := \frac{\left(1 + 2x + 3x^2\right)^2}{(1+x)^3\left(1+x^2\right)^3}.$$

The total time lag between electromagnetic and GWs can be written as an integral over the line of sight:

$$\Delta t = 2 \int_0^{\ell/2} \mathrm{d}r \Delta c_g(r),$$

with $\ell = 40$ Mpc being the distance between the source and the observer. Accounting for the contribution of both the field's time gradients ($\Delta t_{g,osc}, \Delta t_{cl,osc}$, dominated by the possible oscillation of the field) and spatial gradients ($\Delta t_{cl}, \Delta t_g$) in both clusters and galaxies, the overall arrival time delay formula reads as

$$\begin{aligned}\Delta t_{tot} &= \Delta t_g + \Delta t_{g,osc} + \Delta t_{cl} + \Delta t_{cl,osc} \\ &= \frac{\rho_{0,g} L^2}{4 M_p^2 m^2 r_{0,g}} F\left(\frac{r_{\mathrm{max},g}}{r_{0,g}}\right) + 16\pi G R_{h,g} \bar{\rho}_{gh} \gamma_1^2 L^2 \\ &+ \frac{N \alpha^2 \beta^2 \rho_{0,cl} L^2}{4 M_p^2 m^2 r_{0,cl}} F\left(\frac{r_{\mathrm{max},cl}}{r_{0,cl}}\right) + 4\pi G \ell \bar{\rho}_{cl} \alpha^2 \beta^2 \gamma_2^2 L^2,\end{aligned}$$

with N being the number of clusters between Earth and the source. With no oscillations anywhere in the condensate phase (i.e., $\{\beta = 0, \gamma_1 = 0\}$ or $\{\beta = 1, \gamma_1 = 0, \gamma_2 = 0\}$), the gradients are far too small to affect significantly the arrival time difference between GWs and GRBs. The retrieved constraints are $m \gtrsim 10^{-24}$eV and $1/L \gtrsim 10^{-28}$eV. Instead, in the case of undamped field oscillations (either in the galactic halo, the cluster one or both), $\{\beta = 0, \gamma_1 = 1\}$,$\{\beta = 1, \gamma_1 = 1, \gamma_2 = 0\}$,$\{\beta = 1, \gamma_1 = 0, \gamma_2 = 1\}$ and $\{\beta = 1, \gamma_1 = 1, \gamma_2 = 1\}$. In this case, the inferred constraints are $m \gtrsim 10^{-21}$eV and $1/L \gtrsim 10^{-25}$eV. All in all, the analysis proves that the constraint does not depend on whether the condensation happens only inside galaxy halos or also within cluster halos. However, it depends strongly on whether the scalar field oscillates or whether the NMC suppresses the oscillations. These constraints were obtained at an order of magnitude level, yet this analysis shows a promising avenue to constrain NMC DM properties.

As an initial endeavour in investigating the phenomenology of the NMC DM model, it is essential to characterise the properties of self-gravitating DM structures anticipated by this theoretical framework. This will be the focal point of the upcoming Section.

3.2 Self-gravitating equilibria of DM halos

3.2.1 Fluid approximation

As a first step in studying the NMC DM model's phenomenology, it is crucial to characterise NMC DM haloes and their self-gravitating equilibria. As this analysis is focused on assessing the features of virialised NMC DM structures, baryons will be neglected. Hence, in this Section, the density term ρ will always refer to the DM density.

The self-gravitating equilibria of DM halos can be specified in the fluid approximation (Teyssier et al. 1997, Subramanian et al. 2000, Lapi & Cavaliere 2011, Nadler et al. 2018) via the continuity, Euler (or Jeans, in this context), and Poisson equations:

$$\begin{cases} \partial_t \rho + \nabla \cdot (\rho \mathbf{v}) = 0, \\ \partial_t \mathbf{v} + (\mathbf{v} \cdot \nabla) \mathbf{v} + \dfrac{1}{\rho} \nabla p = -\nabla \Phi, \\ \nabla^2 \Phi = 4\pi G \, (\rho - \epsilon \, L^2 \, \nabla^2 \rho). \end{cases} \tag{3.11}$$

Here, $\mathbf{v}$ is the bulk velocity. The pressure $p = \rho \, \sigma_r^2$ does not represent the relativistic pressure $p \approx 0$ adopted for DM in a cosmological context. However, it is instead the pressure dynamically generated by the random motions of the DM particles in approximate virial equilibrium within the gravitational potential. Such pressure is usually specified in terms of a radial velocity dispersion σ_r^2 or, more generally, of an anisotropic stress tensor σ_{ij}^2. Finally, the last equation in the system of Eqs. (3.11) is the modified Poisson equation given by Eq. (3.10). As it will be clear, a negative polarity $\epsilon = -1$ is required to obtain physically acceptable DM density distributions, whereas L will be closely related to the DM core radius. Note that NMC terms do not appear in the Euler equation since they are found to be sub-leading in the non-relativistic limit (i.e., expansion in $1/c^2$; see Bettoni et al. 2014).

To close the system of Eqs. (3.11), the pressure must be related to the density via a certain EoS. The EoS adopted here originates from the gravitational assembly of DM halos via accretion and mergers from the cosmic web. This EoS stems from the progressive stratification of DM's pseudo-entropy $K \equiv p/\rho^{5/3}$, or equivalently of the coarse-grained phase-space density $\rho/\sigma_r^3 \propto K^{-3/2}$, in terms of a simple power-law profile $K(r) \propto r^{\alpha}$. Although the physical origin of this scale-free behaviour is not fully understood (see Nadler et al. 2018; Arora & Williams 2020), $N-$body simulations (Peirani et al. 2006; Navarro et al. 2010; Ludlow et al. 2011; Gao et al. 2012; Nolting et al. 2016; Butsky et al. 2016) have shown this to approximately hold over more than three orders of magnitude in radius within virialised halos, with power-law index $\alpha \approx 1.25 - 1.3$. Such values are indeed expected based on simple self-similar arguments (see Bertschinger 1985; Lapi & Cavaliere 2009, 2011; Nadler et al. 2018) and also broadly consistent with observations (see Lapi

& Cavaliere 2009; Chae 2014; Munari et al. 2014). On this basis, but to keep some degree of generality, the following EoS parametrisation is adopted:

$$p(\rho, r) = \lambda\, \rho^{\Gamma}\, r^{\alpha} = \rho_\alpha\, \sigma_\alpha^2 \left(\frac{\rho}{\rho_\alpha}\right)^{\Gamma} \left(\frac{r}{r_\alpha}\right)^{\alpha} , \tag{3.12}$$

where r_α is a reference radius, ρ_α is defined as $\rho_\alpha \equiv \rho(r_\alpha)$ and $\sigma_\alpha^2 \equiv \sigma_r^2(r_\alpha)$. Here the fiducial values $\Gamma \approx \frac{5}{3}$ and $\alpha \approx 1.3$ will be adopted. Some authors (e.g., Schmidt et al. 2008; Hansen et al. 2010) have claimed that it is the quantity $\rho/\sigma_r^{\epsilon} \propto r^{-\zeta}$ with $\epsilon \lesssim 3$ to feature a powerlaw behavior. However in the parametrization of Eq. (3.12) hereby considered this just amounts to take $\alpha = \frac{2}{3}\,\zeta$ and $\Gamma = 1 + \frac{2}{\epsilon}$.

Under static ($\mathbf{v} = 0$), spherically symmetric, and isotropic conditions (see Sec. (3.3) for a generalisation), the Eqs. (3.11) becomes:

$$\begin{cases} \dfrac{1}{\rho}\dfrac{\mathrm{d}p}{\mathrm{d}r} = -\dfrac{\mathrm{d}\Phi}{\mathrm{d}r} , \\[2ex] \dfrac{1}{r^2}\dfrac{\mathrm{d}}{\mathrm{d}r}\left(r^2\,\dfrac{\mathrm{d}\Phi}{\mathrm{d}r}\right) = 4\pi G \left[\rho - \epsilon\, L^2\, \dfrac{1}{r^2}\dfrac{\mathrm{d}}{\mathrm{d}r}\left(r^2\,\dfrac{\mathrm{d}\rho}{\mathrm{d}r}\right)\right] , \end{cases} \tag{3.13}$$

supplemented with the trivial mass conservation constraint $\mathcal{M}(t)$ =const, where

$$\mathcal{M} \equiv 4\pi \int_0^{\infty} \mathrm{d}r\, r^2\, \rho(r) , \tag{3.14}$$

is the total mass $\mathcal{M}$ of the DM halo.

3.2.2 The fundamental equation and its solutions

It is convenient to introduce normalized variables $\bar{r} \equiv r/r_\alpha$, $\bar{\rho} \equiv \rho/\rho_\alpha$ and define the quantities $\kappa \equiv 4\pi G\, \rho_\alpha\, r_\alpha^2/\sigma_\alpha^2$ and $\eta \equiv \epsilon\, L^2/r_\alpha^2$. To understand the physical meaning of κ, one can choose $r_\alpha = r_{\max}$ to be the point at which the circular velocity $v_c^2(r) \equiv G\,M(<r)/r$ peaks at a value $v_c^2(r_{\max}) = 4\pi\rho(r_{\max})\, r_{\max}^2$, so that $\kappa = v_c^2(r_{\max})/\sigma^2(r_{\max})$ is seen to compare the estimate $\sigma^2(r_{\max})$ for the random kinetic energy with that $v_c^2(r_{\max})$ for the gravitational potential.

Eliminating $\mathrm{d}\Phi/\mathrm{d}r$ from Eqs. (3.13) and using the EoS Eq. (3.12) yields the following fundamental equation for the density

$$\bar{\rho}'' + \frac{(\Gamma-2)\,\dfrac{\bar{\rho}'^2}{\bar{\rho}} + \dfrac{\alpha\,(2\Gamma-1)+2\,\Gamma}{\Gamma}\,\dfrac{\bar{\rho}'}{\bar{r}} + \dfrac{\alpha\,(\alpha+1)}{\Gamma}\,\dfrac{\bar{\rho}}{\bar{r}^2} - 2\,\eta\,\kappa\,\dfrac{\bar{\rho}^{2-\Gamma}\,\bar{\rho}'}{\Gamma\,\bar{r}^{\alpha+1}} + \kappa\,\dfrac{\bar{\rho}^{3-\Gamma}}{\Gamma\,\bar{r}^{\alpha}}}{1 - \eta\,\kappa\,\dfrac{\bar{\rho}^{2-\Gamma}}{\Gamma\,\bar{r}^{\alpha}}} = 0 , \tag{3.15}$$

while the mass conservation constraint now reads $\mathcal{M} = \rho_\alpha\, r_\alpha^3\, f_{\mathcal{M}}$ in terms of the shape factor $f_{\mathcal{M}} = 4\pi \int_0^{\infty} \mathrm{d}\bar{r}\, \bar{r}^2\, \bar{\rho}(\bar{r})$. The solution space of such an equation

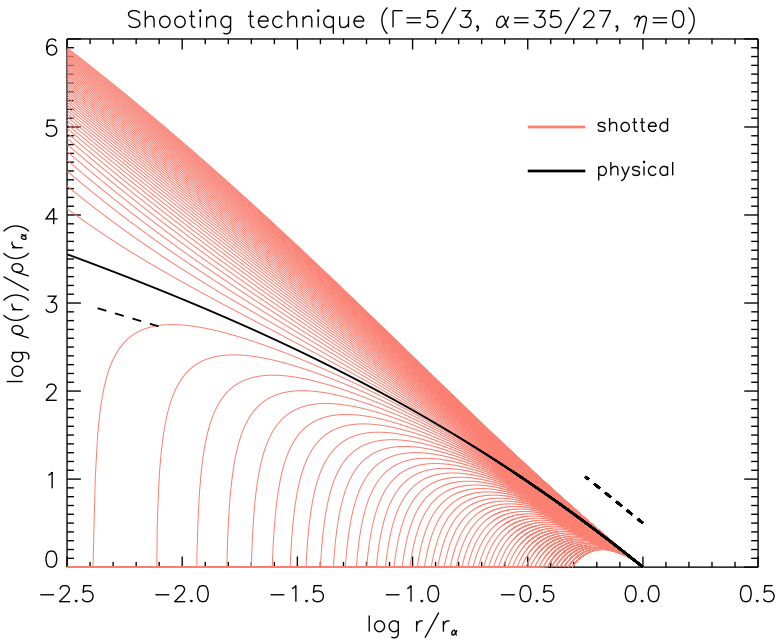

Figure 3.1: Example aimed at illustrating the shooting technique adopted to solve the fundamental Eq. (3.15) and to find the physically acceptable solutions. Radial coordinates and density profile values are normalised to the reference radius r_α where the logarithmic slope $\gamma \equiv -\frac{\mathrm{d}\log\rho}{\mathrm{d}\log r}$ of the profile is $\gamma_\alpha = \frac{2-\alpha}{2-\Gamma}$. The differential equation is integrated inward of r_α with boundary condition $\rho(r_\alpha) = \rho_\alpha$ and $\rho'(r_\alpha) = -\gamma_\alpha \frac{\rho_\alpha}{r_\alpha}$. Red lines show shot solutions for different values of the constant κ appearing in Eq. (3.15). The black line is the only physical profile for $\kappa = \kappa_{\Gamma,\alpha}$ (for $\kappa > \kappa_{\Gamma,\alpha}$ shot solutions are below the physical profile, while for $\kappa < \kappa_{\Gamma,\alpha}$ are above). The two dashed lines indicate the asymptotic slope $\gamma_0 = \frac{\alpha}{\Gamma}$ in the inner region and the slope γ_α at $r = r_\alpha$. This example considers the minimally-coupled case $\eta = 0$, and EoS parameters $\Gamma = \frac{5}{3}$ and $\alpha = \alpha_{\rm crit} = \frac{35}{27}$, yielding $\kappa_{\Gamma,\alpha} \approx 2.5$, $\gamma_0 = \frac{7}{9}$ and $\gamma_\alpha = \frac{19}{9}$.

is rather rich. For $\Gamma = \frac{5}{3}$ and $\eta = 0$ it has been quite extensively studied in the literature to describe the radial structure of standard ΛCDM halos (see Williams et al. 2004; Hansen 2004; Austin et al. 2005; Dehnen & McLaughlin 2005; Lapi & Cavaliere 2009). A generalised form of this equation with a generic Γ and featuring the addition of the NMC will be used.

It is now convenient to look for power-law behaviours $\bar{\rho} \simeq \bar{r}^{-\gamma}$ to understand the general features of the solutions. Substituting in the fundamental equation yields

$$\Gamma\,(\Gamma-1)\left(\gamma-\frac{\alpha}{\Gamma}\right)\left(\gamma-\frac{\alpha+1}{\Gamma-1}\right)-\eta\,\kappa\,\frac{\gamma\,(\gamma-1)}{\bar{r}^{\gamma\,(2-\Gamma)+\alpha}}=-\frac{\kappa}{\bar{r}^{\gamma\,(2-\Gamma)+\alpha-2}}\,. \tag{3.16}$$

Focusing first on the minimally coupled case ($\eta = 0$), it is evident that trivial power-law solutions with slope $\gamma = \gamma_\alpha \equiv \frac{2-\alpha}{2-\Gamma}$ are admitted, implying $\kappa = \kappa_{\rm PL} \equiv$

$2\,\frac{(\Gamma-\alpha)\,(\alpha+4-3\Gamma)}{(2-\Gamma)^2}$. These values are not physically acceptable at small and large radii since the gravitational force and mass would diverge. However, they provide the behaviour of any solution at intermediate radii. It is now numerically convenient to choose r_α as the reference radius where the logarithmic slope of the density is $-\gamma_\alpha$. Then, one can integrate inward and outward to find general solutions. In terms of the normalised variables, this corresponds to setting the boundary conditions as $\bar{\rho}(1) = 1$ and $\bar{\rho}'(1) = -\gamma_\alpha$. When integrating inward of r_α, it is found that the density profile features a physically acceptable behaviour only for a specific value of $\kappa = \kappa_{\Gamma,\alpha}$, somewhat different from the $\kappa_{\rm PL}$ defined above. In particular, for such value $\kappa_{\Gamma,\alpha}$ the profile asymptotes for $\bar{r} \ll 1$ to $\bar{\rho} \propto \bar{r}^{-\gamma_0}$ with $\gamma_0 \equiv \frac{\alpha}{\Gamma}$, consistently with the power counting in Eq. (3.16). For $\kappa > \kappa_{\Gamma,\alpha}$, the profile has wiggles (i.e., change of sign in the second derivative) and steepens toward the centre, implying a diverging gravitational force. In contrast, for $\kappa < \kappa_{\Gamma,\alpha}$, the profile develops a central hole. The optimal value $\kappa_{\Gamma,\alpha}$ can be found by a shooting technique, i.e., automatically solving inward the differential equation with different slopes $-\gamma_\alpha$ at r_α until the desired, physical inner asymptotic behaviour is found. Fig. (3.1) depicts the results achieved with this technique.

Fig. (3.2) illustrates the resulting full density profiles for three different values of α. The outer behaviour of the profile turns out to be physical only for $\alpha \leq \alpha_{\rm crit} \equiv \frac{\Gamma(5\Gamma-6)}{3\Gamma-2}$. The outer slope is too flat to imply a diverging mass for $\alpha > \alpha_{\rm crit}$. For $\alpha < \alpha_{\rm crit}$ the solution $\bar{\rho} \propto \bar{r}^{-\gamma_\infty}$ attains a slope $\gamma_\infty \equiv \frac{\alpha+1}{\Gamma-1}$ at a finite large radius before an outer cutoff. For $\alpha = \alpha_{\rm crit}$ the cutoff is pushed to infinity and the slope $\gamma_{\infty,\rm crit} \equiv \frac{5\Gamma+2}{3\Gamma-2}$ is attained only asymptotically for $\bar{r} \to \infty$, consistently with the power-counting from Eq. (3.16). Correspondingly, the intermediate and inner slopes read $\gamma_{\alpha,\rm crit} \equiv \frac{5\Gamma-2}{3\Gamma-2}$ and $\gamma_{0,\rm crit} \equiv \frac{5\Gamma-6}{3\Gamma-2}$, respectively. These different behaviors are illustrated in Fig. (3.2) for the fiducial value $\Gamma = \frac{5}{3}$. In such a case, the power-law solutions have $\gamma_\alpha = 6 - 3\,\alpha$ and $\kappa_{\rm PL} = 6\,(5 - 3\,\alpha)\,(\alpha - 1)$, while the physical solutions feature an inner slope $\gamma_0 = \frac{3\,\alpha}{5}$ and an outer slope $\gamma_\infty = \frac{3\,(1+\alpha)}{2}$. In the inset of Fig. (3.2), the values of $\kappa_{\alpha,\Gamma}$ are reported as a function of α. For $\alpha = \alpha_{\rm crit} = \frac{35}{27}$ one gets $\gamma_{0,\rm crit} \equiv \frac{7}{9}$, $\gamma_{\alpha,\rm crit} = \frac{19}{9}$, $\gamma_{\infty,\rm crit} = \frac{31}{9}$, and $\kappa_{\alpha,\Gamma} = \frac{200}{81} \approx 2.5$.

When including the NMC $\eta \equiv \epsilon\,\frac{L^2}{r_\alpha^2}$, the solution space changes appreciably. First, ϵ (hence η) must be negative. Otherwise, the inner profile diverges at a finite radius. Then, for any negative value of η, there is again an optimal value of $\kappa = \kappa_{\Gamma,\alpha,\eta}$ such that the inner profile is physical, with limiting central slope $\gamma_0 = 0$ (i.e., a core). This again follows the power counting in Eq. (3.16) since the second term on the left-hand side dominates the behaviour for small $\bar{r} \ll 1$. Other solutions with κ smaller or larger than $\kappa_{\Gamma,\alpha,\eta}$ are not physically acceptable. Indeed, they feature non-monotonic behaviours with the density first flattening and then steepening toward a central slope $\gamma_0 = 1$, or they develop a central hole. As for the outer behaviour, the profile has a cutoff at a finite radius $\mathcal{R}$ setting the effective halo boundary, which is smaller for more negative values of η. The physically acceptable profiles for different η and the related values of the constant $\kappa_{\Gamma,\alpha,\eta}$ are illustrated in Fig. (3.4). The corresponding distributions of mass, circular velocity and velocity dispersion for a few values of the NMC η are also depicted in Fig. (3.3).

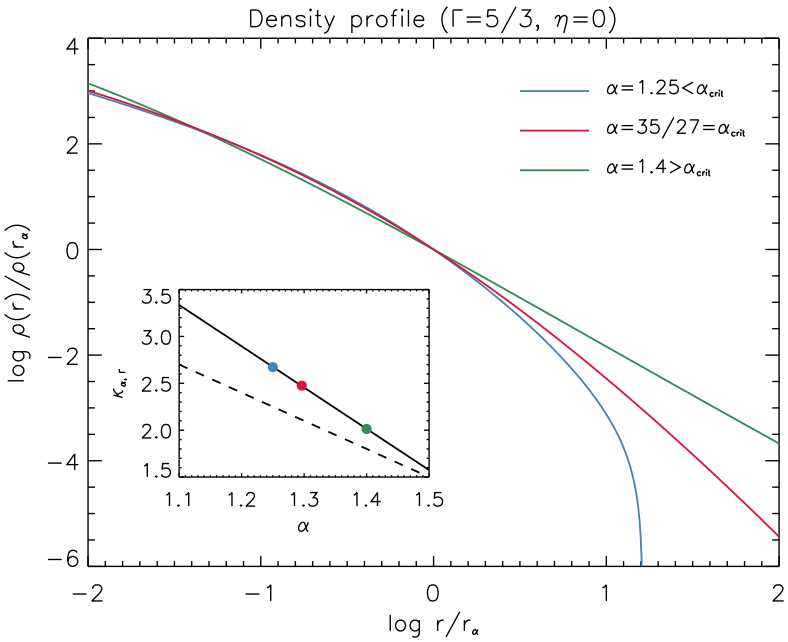

Figure 3.2: Examples aimed at showing the outer behaviour of the density profiles from solving the fundamental Eq. (3.15). The illustrated profiles refer to the minimally coupled case ($\eta = 0$) with EoS parameter $\Gamma = \frac{5}{3}$ and three different values of α. The red line corresponds to $\alpha = \frac{35}{27} = \alpha_{\rm crit}$, for which the density asymptotes to a slope $\gamma_\infty = \frac{\alpha+1}{\Gamma-1} \approx \frac{31}{9}$. The blue line refers to $\alpha = 1.25 < \alpha_{\rm crit}$, for which the slope γ_∞ is attained at a finite radius before a cutoff. Finally, the green line refers to $\alpha = 1.4 > \alpha_{\rm crit}$, for which the outer slope is unphysical, as it would lead to a diverging mass. The inset reports the dependence of the constant $\kappa_{\Gamma,\alpha}$ on α for the full solutions (coloured dots and solid black line) and for the pure power-law solutions (dashed black line).

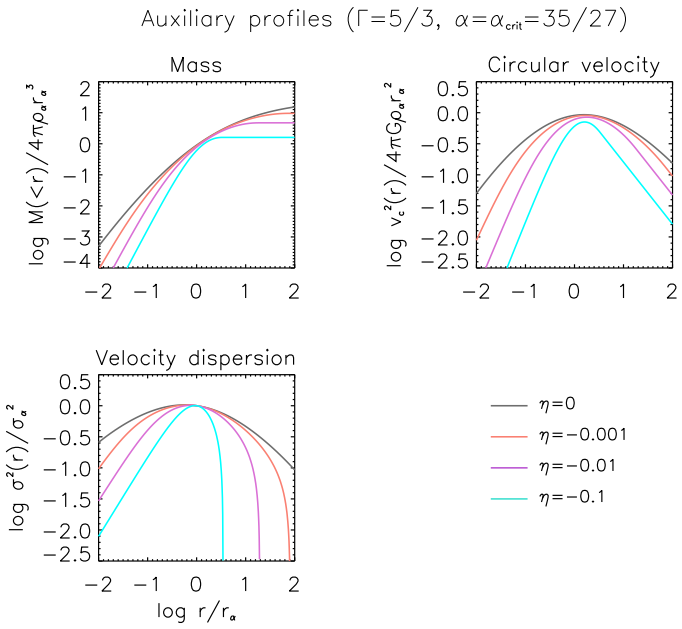

Figure 3.3: Profiles of mass (top left panel), circular velocity (top right panel) and velocity dispersion (bottom left panel) corresponding to a few of the density profiles illustrated in Fig. (3.2), with EoS parameters $\Gamma = \frac{5}{3}$ and $\alpha = \alpha_{\rm crit} = \frac{35}{27}$. Several values for the NMC are represented: $\eta = 0$ (black), -0.001 (orange), -0.01 (magenta), -0.1 (cyan).

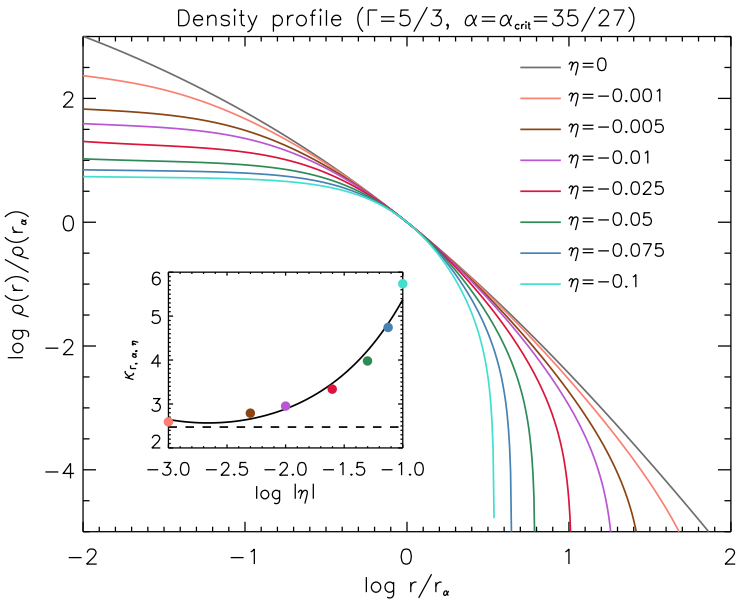

Figure 3.4: Density profiles for EoS parameters $\Gamma = \frac{5}{3}$ and $\alpha = \alpha_{\rm crit} = \frac{35}{27}$ and for different values of the NMC $\eta = 0$ (grey), -0.001 (orange), -0.005 (brown), -0.01 (magenta), -0.025 (red), -0.05 (green), -0.075 (blue), -0.1 (cyan). The inset reports the corresponding values of the constant $\kappa_{\Gamma,\alpha,\eta}$ for the physical solutions as a function of η (coloured dots and solid line) and for the $\eta = 0$ case (dashed black line).

3.2.3 NMC DM density profiles VS other literature profiles

It is now interesting to compare the shape of the NMC DM physical solutions to some classic literature density profiles, characterised by different analytic expressions and numbers of parameters commonly adopted to fit simulations or observations. To this purpose, it is convenient to use a radial coordinate $\hat{r} \equiv r/r_{-2}$ normalised to the radius r_{-2} where the logarithmic density slope $\frac{\mathrm{d}\log\rho}{\mathrm{d}\log r} = -2$. and to rescale the density profile $\hat{\rho} \equiv \rho/\rho(r_{-2})$ accordingly. Specifically, the following density profiles will be considered.

- $\alpha\beta\gamma$ profiles

  The $\alpha\beta\gamma$ profiles (Zhao 1996) are a family of density profiles described by three parameters, featuring the shape

  $$\hat{\rho}(\hat{r}) = \hat{r}^{-\tau}\left(\frac{1+w}{1+w\,\hat{r}^{\omega}}\right)^{\xi}, \tag{3.17}$$

  where the three parameters τ, ω, ξ describe respectively the central slope, the middle curvature and the outer decline of the density run, while $w \equiv -\frac{2-\tau}{(2-\tau-\omega\,\xi)}$. Familiar empirical profiles are recovered for specific values of the triplet (τ, ω, ξ). Plummer's profile (Plummer 1911) corresponds to $(0, 2, 5/2)$, Jaffe's (Jaffe 1983) to (2,1,2), and Hernquist's (Hernquist 1990) to $(1, 1, 3)$. The standard NFW profile is obtained for the parameter triple $(1, 1, 2)$. For a generalisation with a different inner slope, often referred to as gNFW, the parameters $(\tau, 1, 3-\tau)$ apply (Mamon et al. 2019; for a more complex cored version see also Read et al. 2016). It is worth mentioning that recently Freundlich et al. (2020) have considered a $\alpha\beta\gamma$ profile (referred also as Zhao–Dekel model) with parameters $(\tau, \frac{1}{2}, 7-2\tau)$, that can provide good fits to the density profiles from both $N-$body, DM-only and hydrodynamical simulations including baryonic effects.

- Sersic–Einasto profile

  The Sersic–Einasto profile (see An & Zhao 2013) is defined as

  $$\hat{\rho}(\hat{r}) = \hat{r}^{-\tau}\, e^{-u\,(\hat{r}^{\omega}-1)}, \tag{3.18}$$

  where τ is the inner density slope, ω is a shape parameter and $u \equiv \frac{(2-\tau)}{\omega}$. The classic cored Einasto shape (Sérsic 1963; Sérsic 1963; Prugniel & Simien 1997; Graham et al. 2006; also Lazar et al. 2020 for a more complex analytical expression) is recovered for $\tau = 0$. N-body simulations in the standard ΛCDM model are usually well described by the parameter values $\omega \approx 0.15-0.2$ and $\tau \approx 0$ (although values $\tau \lesssim 0.8$ are not ruled out given the resolution of current simulations).

- Soliton profile

The soliton profile features the shape (see Schive et al. 2014a,b)

$$\hat{\rho}(\hat{r}) = \left(\frac{1 + \omega/\hat{r}_c^2}{1 + \omega\, \hat{r}^2/\hat{r}_c^2} \right)^8 , \tag{3.19}$$

where the normalized core radius reads $\hat{r}_c = \sqrt{7\,\omega}$. In numerical simulations of ψDM (see Sec. (2.2.3)), halos are described by a combination of this solitonic profile with $\omega \approx 0.091$ in the inner region and of an NFW profile in the outskirts.

- BEC DM profile

  The profile followed by an interacting BEC (see Sec. (2.2.4)) in the Thomas–Fermi limit reads

$$\hat{\rho}(\hat{r}) = \frac{1}{\hat{r}} \frac{\sin\left(\pi\, \hat{r}/\hat{R}\right)}{\sin\left(\pi/\hat{R}\right)} , \tag{3.20}$$

  where the normalized halo boundary is defined by the equality $\pi/\hat{R} + \tan\left(\pi/\hat{R}\right) = 0$. Incidentally, note that such a profile corresponds to the solution of Eq. (3.16) for $\Gamma = 2$ and $\alpha = \eta = 0$.

- Burkert profile

  The Burkert profile given by Eq. (1.5) can be rewritten as

$$\hat{\rho}(\hat{r}) = \frac{(1 + \hat{r}_c)\,(1 + \hat{r}_c^2)}{(\hat{r} + \hat{r}_c)\,(\hat{r}^2 + \hat{r}_c^2)} , \tag{3.21}$$

  where $\hat{r}_c$ is the normalised core radius, defined by the nonlinear algebraic equation $2\,\hat{r}_c^3 + \hat{r}_c^2 - 1 = 0$.

A comparison between the shape of the NMC DM solutions to a few of the above profiles is detailed in Fig. (3.5), where, for definiteness, $\Gamma = \frac{5}{3}$ and $\alpha = \alpha_{\rm crit} = \frac{35}{27}$ are adopted. First, it is evident that the NMC DM density run for $\eta = 0$ describes quite well the NFW and Einasto profiles commonly used to fit N-body simulations in the standard ΛCDM cosmology. For $-0.1 < \eta < -0.01$, the NMC DM solutions develop a core and the shape out to few/several r_{-2} is remarkably close to the Burkert profile, commonly exploited to fit observations of dwarf galaxies. There is a progressive deviation from the Burkert profile at larger distances since the latter has been designed to have a limiting slope close to the NFW one. In contrast, the NMC DM profiles get truncated at a finite radius $\mathcal{R}$. However, this is not a concern for an appreciable range of η values since the truncation occurs at radii much beyond r_{-2} that are scantily, if at all, probed by observations (see also Sec. (3.2.4)). The NMC DM solutions have the remarkable property of reproducing the Burkert shape in the inner region and over an extended radial range outward of r_{-2}. For comparison, other models,

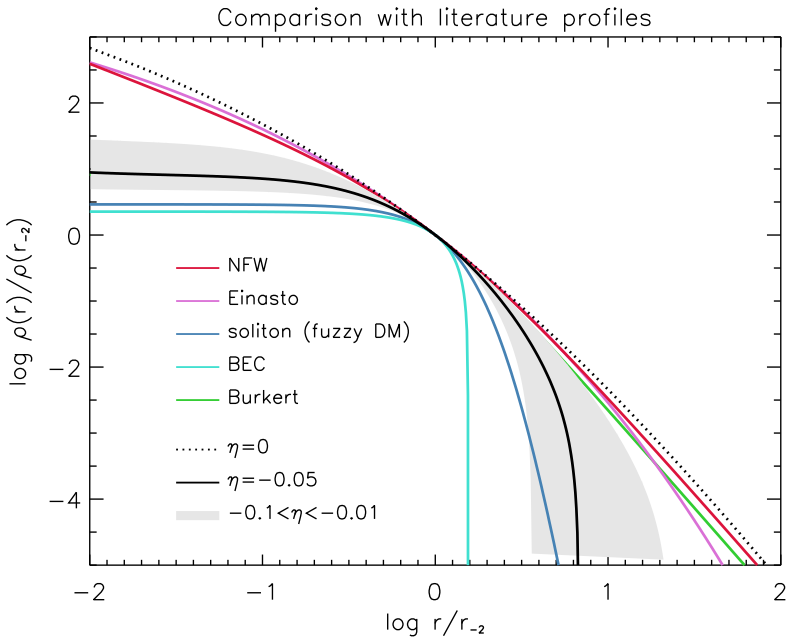

Figure 3.5: Comparison of NMC density distributions with classic literature profiles: NFW (red line), Einasto (magenta line), ψDM (blue line), BEC DM (cyan line), and Burkert (green line). The dot black line refers to $\eta = 0$, the solid black line is for $\eta = -0.05$, and the grey-shaded area illustrates the region covered by η in the range from -0.1 (lower envelope) to -0.01 (upper envelope). The radial coordinate and the density profiles have been normalised to the radius r_{-2} where the logarithmic density slope $\frac{\mathrm{d}\log\rho}{\mathrm{d}\log r} = -2$.

such as those based on BEC DM, predict a cored density profile with appreciable deviations from the Burkert shape. Such deviations are expressed in a prominent cutoff or steep decline outside the core. Note that the NMC DM solutions for $\eta = -0.05$ can be reasonably described by a $\alpha\beta\gamma$ model (cf. Eq. (3.17) with parameters $(\tau, \omega, \xi) = (0, \frac{3}{2}, \frac{5}{2})$, or by a Sersic–Einasto model (cf. Eq. (3.18) with parameters $(\tau, \omega) = (0, \frac{3}{4})$ up to several r_{-2} before the final cutoff.

3.2.4 Comparison with dwarf galaxies rotation curves

The NMC mass distributions are now compared with observed galaxy RCs. Since baryons are not included in this part of the analysis, fits will focus on dwarf, strongly DM-dominated galaxies. Specifically, the co-added RC built by Lapi et al. (2018) is considered. This RC is based on the high-quality measurements of about 20 dwarf galaxies with $I-$band magnitude $M_I \gtrsim -18.5$ from the original sample by Persic et al. (1996). The sample features an average disc lengthscale $R_e \lesssim 1.5$ kpc, disc mass $M_\star \lesssim 10^9\, M_\odot$ and halo mass $\mathcal{M} \lesssim 10^{11}\, M_\odot$. The co-added RC is well-measured to a galactocentric distance of about 7 kpc. Fits to the measured RC with the NFW and Burkert profile are obtained by exploiting a Levenberg–Marquardt least-squares minimisation routine. The measured RC is fitted with the NFW and Burkert profile and the NMC DM physical solutions for different values of the NMC parameter η. The outcomes of this procedure are illustrated in Fig. (3.6).

As it is well known, the NFW fit (equivalent to the NMC DM solution with $\eta = 0$) struggles to fit the measured dwarf galaxy RCs, yielding a reduced $\chi^2 \approx 4$. On the other hand, the Burkert profile performs much better, providing a good fit with a reduced $\chi^2 \approx 0.58$. The NMC solution for $\eta \approx -0.05$ provides a fit of quality comparable to the Burkert one, yielding practically the same reduced $\chi^2 \approx 0.61$. The current data are compatible within 3σ with any value of η ranging from -0.1 to -0.01. Accurate determinations of the co-added RC out to 10 kpc or beyond would be necessary to determine the NMC parameter η to a good level of precision. Interestingly, one can also see from Fig. (3.6) that there is a tendency to favour values of η slightly less negative than -0.05, which is what is to be expected in dwarf galaxies with halo masses $\mathcal{M} \lesssim 10^{11}\, M_\odot$ based on universal scaling arguments (see Sec. (3.2.5) and in particular Eq. (3.25)).

A best-fit value of the core radius is retrieved from the fit with $\eta \approx -0.05$ (or equivalently from the Burkert one). The inferred core radius value amounts to $r_0 \approx 2.9 \pm 0.1$ kpc, which is about twice the average disc lengthscale of the systems in the considered sample. Such value is remarkably consistent with the empirical yet still puzzling relationship between core radius and disc scale length as determined by Donato & Salucci (2004).

The choice of the NMC hereby exploited is relatively simple if compared, for example, to the one considered in Bruneton et al. (2009), leading to a MONDian phenomenology on galactic scales. From this perspective, the relatively good performance of such a simple NMC model in reproducing the measured RCs is valuable and far from trivial.

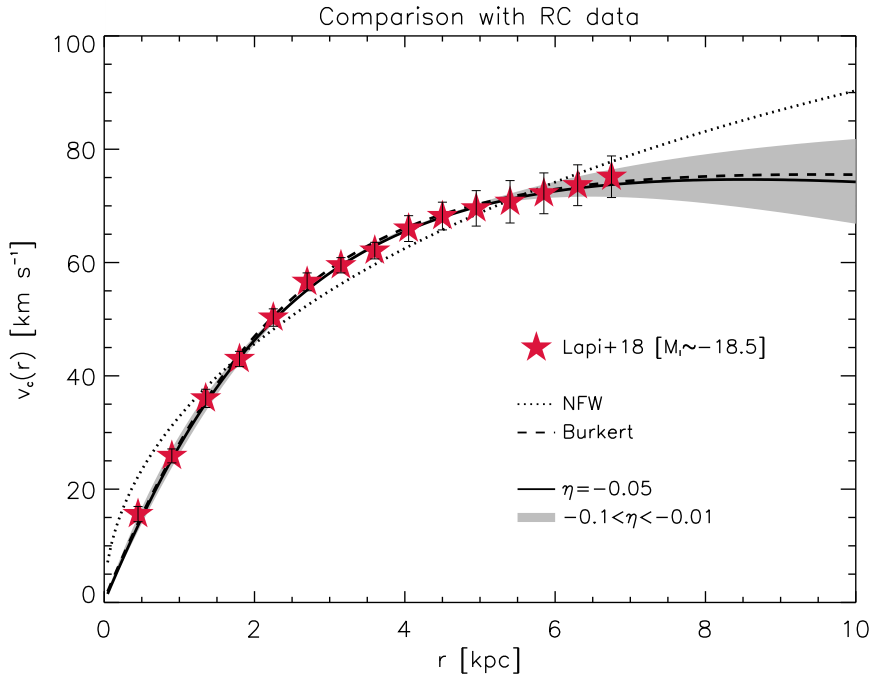

Figure 3.6: Comparison of NMC halo mass distributions with observed dwarf galaxy RCs. Data points (red stars; Lapi et al. 2018) refer to the co-added RCs of about 20 dwarf galaxies with I-band magnitude $M_I \gtrsim -18.5$, extracted from the original sample by Persic et al. (1996). The solid line illustrates the fit via the NMC DM physical solution with NMC parameter $\eta \approx -0.05$, while the shaded grey area shows the effect of changing η in the range from -0.1 to -0.01. For comparison, the dashed line illustrates the fit with the Burkert profile and the dotted line with the NFW profile.

3.2.5 Universal Core Surface Density

It has been well established observationally that, at least for dwarf galaxies with halo masses $\mathcal{M} \lesssim 10^{11}\,M_\odot$, the product of the core density and core radius (i.e., a sort of core surface density) is an approximately universal constant with values $\rho_0\, r_0 \approx 75^{+55}_{-45}\,M_\odot\ \mathrm{pc}^{-2}$ among different galaxies (Salucci & Burkert 2000; Burkert 2015; see Fig. (3.7)). This somewhat unexpected property poses a serious challenge to any theoretical model of core formation (e.g., Deng et al. 2018; Burkert 2020). Can NMC DM halos be consistent with such a remarkable scaling law?

Adopting for definiteness $\Gamma = \frac{5}{3}$ and $\alpha = \alpha_{\rm crit} = \frac{35}{27}$, the physical solutions of Eq. (3.15) subject to the boundary conditions $\rho(r_\alpha) = \rho_\alpha$ and $\rho'(r_\alpha) = -\gamma_\alpha \frac{\rho_\alpha}{r_\alpha}$ are computed for several values of the NMC parameter η. Using the obtained normalised profiles, one can fit as a function of $|\eta| = \frac{L^2}{r_\alpha^2}$ in the range $-0.1 \lesssim \eta \lesssim -0.01$ the following relations involving the normalised boundary radius $\mathcal{R}$, the core radius r_0, the core density ρ_0 and the mass shape factor $f_\mathcal{M}$ defined below Eq. (3.15):

$$\frac{\mathcal{R}}{r_\alpha} \simeq 0.8\,|\eta|^{-0.7}\,, \qquad f_\mathcal{M} \simeq 9.1\,|\eta|^{-0.4}\,, \qquad \frac{\rho_0}{\rho_\alpha} \simeq 0.9\,|\eta|^{-0.8}\,, \qquad \frac{r_0}{r_\alpha} \simeq 1.6\,|\eta|^{0.5}\,. \tag{3.22}$$

The above scaling is then combined with the expression for the total mass $\mathcal{M} = f_\mathcal{M}\,\rho_\alpha\, r_\alpha^3$ and with the definition of the virial radius $\mathcal{R} = (3\,\mathcal{M}/4\pi\Delta_{\rm vir}\,\rho_{\rm c}\,E_z)^{1/3} \approx 120\,E_z^{-1/3}\,(\mathcal{M}/10^{11}\ M_\odot)^{1/3}$ (see Sec. (1.3.2)). Here $\rho_{\rm c} \approx 2.8\times 10^{11}\,h^2\,M_\odot\ \mathrm{Mpc}^{-3}$ is the critical density, $E_z \equiv \Omega_M\,(1+z)^3 + \Omega_\Lambda$ takes into account the formation redshift z of the halo, and $\Delta_{\rm vir}$ is the nonlinear threshold for virialization, with values around 100 at $z \approx 0$ and increasing toward 180 for $z \gtrsim 1$. Eventually, the following relations are derived:

$$r_0 \simeq 1.6\,L\,, \qquad r_\alpha \simeq 1.1\,L^{0.6}\,\mathcal{R}^{0.4} \qquad \rho_0 \simeq 0.3\,\Delta_{\rm vir}\,\rho_{\rm c}\,E_z \left(\frac{\mathcal{R}}{L}\right)^{2.1} = \rho_\alpha \left(\frac{\mathcal{R}}{L}\right)^{0.6}\,. \tag{3.23}$$

Interestingly, the core radius r_0 is proportional, with a coefficient of order 1, to the NMC lengthscale L.

A relation between the core radius r_0 (or L) and the halo mass $\mathcal{M}$ is needed to proceed further. Such relation is thought not to be fundamental but rather to stem from two other relationships involving the baryonic mass: (i) the relation between the stellar (disc) mass and the halo mass (e.g., Moster et al. 2013), which is known to be originated by baryonic processes related to galaxy formation; (ii) the relation between the core radius r_0 and the disc scalelength (in turn related to the stellar mass; e.g., Donato & Salucci 2004), which is instead still not completely understood. In this part of the analysis, the baryonic component is not included, and thus, one cannot infer the $r_0 - \mathcal{M}$ relation from first principles. However, one can adopt the outcome $r_0 \approx 4.5\,(\mathcal{M}/10^{11}\,M_\odot)^{0.6}$ kpc from the dynamical modelling study by Salucci et al. 2007, and see what this implies for the core surface density. Specifically, from Eqs. (3.23) the following result is obtained:

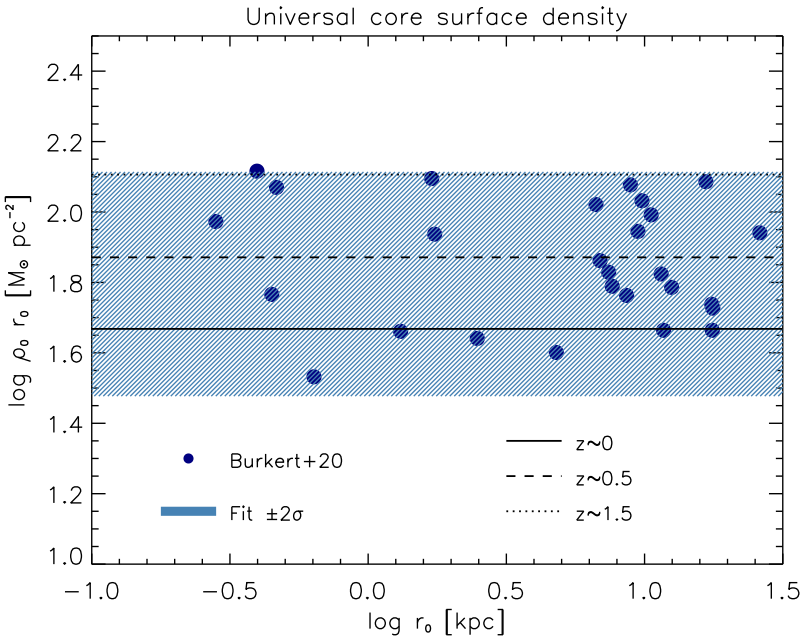

Figure 3.7: Core surface density $\rho_0 \times r_0$ as a function of the core radius r_0. Data points from Burkert (2020) are well fitted by the universal value $75^{+55}_{-45}\, M_\odot\ \mathrm{pc}^{-2}$ (blue shaded area). The black lines illustrate the prediction for NMC DM halos for three different halo formation redshifts $z \approx 0$ (solid), 0.5 (dashed), and 1.5 (dotted).

$$\Sigma_0 \equiv \rho_0 \times r_0 \approx 50 \left(\frac{\Delta_{\rm vir}}{100}\right) E_z^{0.3}\, M_\odot\, \mathrm{pc}^{-2}\,. \tag{3.24}$$

This result is independent of the halo mass or the core radius and weakly dependent on formation redshift. Fig. (3.7) depicts the above for three values of the formation redshift $z \approx 0, 0.5, 1.5$, finding it remarkably consistent with the average observed relation and its scatter. This is a relevant result: the universality of the core surface density has proven highly challenging to alternative DM models, even for those barely consistent with the $r_0 - \mathcal{M}$ relation assumed here. For example, as pointed out by Burkert (2020), ψDM can reproduce the $r_0 - \mathcal{M}$ relation, albeit with some (uncertain) hypothesis on core formation redshift. However, such a model is considerably out of track regarding the core surface density scaling since it robustly predicts $\rho_0 \propto r_0^{-4}$. The same issue concerns many other DM models inspired by particle physics, as extensively discussed, e.g., by Deng et al. (2018).

As an aside, from Eqs. (3.7) and the adopted $r_0 - \mathcal{M}$ relation, one can also derive three other interesting scaling laws. First, the dependence of η on halo mass reads

$$|\eta| \approx 0.04 \left(\frac{\mathcal{M}}{10^{11}\, M_\odot}\right)^{0.35} E_z^{0.3}\,. \tag{3.25}$$

This relation confirms that values of the NMC in the range $\eta = -0.1$ to -0.01 cover the typical mass range of dwarf galaxies. The dependence of η on halo

mass/formation redshift will induce slightly different shapes in the profiles, implying a weak violation of self-similarity. Though challenging, it will be interesting to look for such behaviours in real data (see Sec. (3.2.4)). Second, it may be interesting to derive the dependence on the coupling, hence on mass, of the inner logarithmic slope $\gamma_{0.1}$ measured at a reference radius of $r \approx 0.1\, r_{-2} \sim$ a few per cent of $\mathcal{R}$. The scaling $|\gamma_{0.1}| \simeq 0.035\, |\eta|^{-0.55}$ is obtained, and after Eq. (3.25) it translates into the following mass-dependence:

$$|\gamma_{0.1}| \simeq 0.2 \left(\frac{\mathcal{M}}{10^{11}\, M_\odot} \right)^{-0.2} E_z^{-0.16} \,. \tag{3.26}$$

This relation implies a slight tendency for less massive halos to have flatter profiles at a fixed radius in the inner region (note that asymptotically, at the centre, all the NMC DM density profiles are flat). Yet the presence of baryons, neglected in this analysis, could alter this scaling. In future work, it would be interesting to assess the entity of such baryonic impact in halos of different masses and how the outcome compares with the results from ΛCDM hydrodynamical simulations including feedback effects (e.g., Tollet et al. 2016; Freundlich et al. 2020), that show a non-trivial mass dependence for the halo inner shape.

Finally, one can compute the halo concentration as $c_\alpha \equiv \frac{\mathcal{R}}{r_\alpha}$ (using $\frac{\mathcal{R}}{r_{-2}}$ yields similar result), which turns out to be

$$c_\alpha \simeq 10 \left(\frac{\mathcal{M}}{10^{11}\, M_\odot} \right)^{-0.15} E_z^{-0.2} \,, \tag{3.27}$$

in broad agreement and slightly smaller than the outcome of N-body, DM-only simulations in the standard ΛCDM cosmology (e.g., Bullock et al. 2001; Macciò et al. 2007).

3.3 Anisotropic conditions

This section will discuss the self-gravitating equilibria of NMC DM halos when anisotropic conditions apply. One can include these conditions in our treatment by modifying the second of Eqs. (3.13) as

$$\frac{1}{\rho} \frac{\mathrm{d}p}{\mathrm{d}r} + 2\beta \frac{\sigma_r^2}{r} = -\frac{\mathrm{d}\Phi}{\mathrm{d}r} \,, \tag{3.28}$$

where $\beta \equiv 1 - \frac{\sigma_\theta^2}{\sigma_r^2}$ is the Binney (1978) anisotropy parameter in terms of the tangential and radial velocity dispersions σ_θ and σ_r, respectively. N-body simulations suggest $\beta(r)$ to increase from central values $\beta_0 \lesssim 0$, meaning near isotropy, to outer values $\beta \gtrsim 0.5$, meaning progressive prevalence of radial motions. This overall trend can be physically understood in terms of efficient dynamical relaxation processes toward the inner regions, which tend to enforce closely isotropic conditions, while in the outskirts, the infall energy of accreting matter is more easily converted by phase mixing into radial random motions (see Lapi & Cavaliere

2011 for details). Specifically, simulations suggest the effective linear expression (e.g., Hansen & Moore 2006)

$$\beta(r) \simeq \beta_0 + \beta_1 \left[\gamma(r) - \gamma_0\right] = \beta_0 - \beta_1 \gamma_0 - \beta_1 \, r \, \frac{\rho'}{\rho} \,, \tag{3.29}$$

in terms of the logarithmic density slope $\gamma(r) \equiv -\frac{\mathrm{d}\log\rho}{\mathrm{d}\log r}$, with $\gamma_0 \equiv \gamma(0)$ being a value yet to be determined, $\beta_0 \lesssim 0$ and $\beta_1 \approx 0.2$.

Adopting Eq. (3.29) and following the same derivation of the main text, the fundamental Eq. (3.15) now reads

$$\begin{aligned} &\left[1 - \eta\,\kappa\,\frac{\bar{\rho}^{2-\Gamma}}{(\Gamma - 2\beta_1)\,\bar{r}^{\alpha}}\right]\bar{\rho}'' + (\Gamma - 2)\,\frac{\bar{\rho}'^2}{\bar{\rho}} + \\ &+ \frac{\alpha\,(2\Gamma - 1) + 2\,\Gamma + 2(\Gamma - 1)\beta_0 - 2[\alpha + 2 + (\Gamma - 1)\gamma_0]\beta_1}{\Gamma - 2\beta_1}\,\frac{\bar{\rho}'}{\bar{r}} + \\ &+ \frac{[\alpha + 1]\,[\alpha + 2(\beta_0 - \beta_1\gamma_0)]}{\Gamma - 2\beta_1}\,\frac{\bar{\rho}}{\bar{r}^2} - 2\,\eta\,\kappa\,\frac{\bar{\rho}^{2-\Gamma}\,\bar{\rho}'}{(\Gamma - 2\beta_1)\,\bar{r}^{\alpha+1}} + \kappa\,\frac{\bar{\rho}^{3-\Gamma}}{(\Gamma - 2\beta_1)\,\bar{r}^{\alpha}} = 0 \,, \end{aligned} \tag{3.30}$$

Looking for power-law behaviors $\bar{\rho} \simeq \bar{r}^{-\gamma}$ one obtains

$$\Gamma\,(\Gamma - 1)\left[\gamma - \frac{\alpha + 2\beta_0}{\Gamma} - 2\frac{\beta_1}{\Gamma}\,(\gamma - \gamma_0)\right]\left[\gamma - \frac{\alpha + 1}{\Gamma - 1}\right] - \eta\,\kappa\,\frac{\gamma\,(\gamma - 1)}{\bar{r}^{\gamma\,(2-\Gamma)+\alpha}} = -\frac{\kappa}{\bar{r}^{\gamma\,(2-\Gamma)+\alpha-2}} \,, \tag{3.31}$$

which, remarkably, allows to determine the central slope γ_0 self-consistently.

In fact, for minimally coupled halos ($\eta = 0$), the anisotropic solutions feature a modified inner slope $\gamma_0 = \frac{\alpha+2\beta_0}{\Gamma}$ to the isotropic case, while retaining the same slopes at intermediate radii $\gamma_\alpha = \frac{2-\alpha}{2-\Gamma}$ and in the outer region $\gamma_\infty = \frac{\alpha+1}{\Gamma-1}$. As mentioned above, $\beta_0 \approx 0$ so that the changes are minor (if any, $\beta_0 \lesssim 0$ so that the inner profile is flattened a bit). In addition, the critical solution is characterised by a value $\alpha_{\rm crit} = \frac{\Gamma\,(5\Gamma-6)+2\beta_0\,(\Gamma-1)\,(\Gamma-2)}{3\Gamma-2}$; in particular, $\alpha_{\rm crit} = \frac{35-4\beta_0}{27}$ holds for for $\Gamma = \frac{5}{3}$. The corresponding inner, intermediate and outer slopes read $\gamma_{0,\rm crit} = \frac{5\Gamma-6+2\beta_0\Gamma}{3\Gamma-2}$, $\gamma_{\alpha,\rm crit} = \frac{5\Gamma-2+2\beta_0\,(\Gamma-1)}{3\Gamma-2}$, and $\gamma_{\infty,\rm crit} = \frac{5\Gamma+2+2\beta_0\,(\Gamma-2)}{3\Gamma-2}$, respectively.

For NMC halos, an inner core with $\gamma_0 \approx 0$ is always enforced by the second term in Eq. (3.31) so that the variations to the isotropic case are minor and limited to the outermost regions. Fig. (3.8) represents how the NMC density profile with $\eta = -0.05$, $\Gamma = \frac{5}{3}$ and $\alpha = \frac{35-4\beta_0}{27} = \alpha_{\rm crit}$ is affected by anisotropies. For realistic values $-0.1 \lesssim \beta_0 \lesssim 0.1$ and $\beta_0 \approx 0.2$, the profile is marginally affected in the inner region and at intermediate radii. At the same time, it tends to extend toward slightly larger radii (i.e., the cutoff moves outward) due to the progressive prevalence of radial anisotropy in the halo outskirts. Such an effect, though minor, is more pronounced for larger (more positive) β_0.

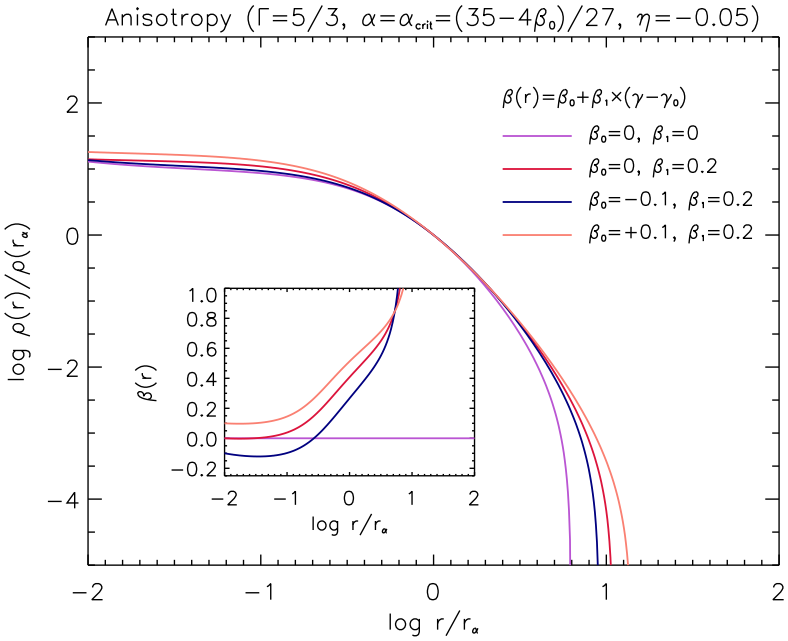

Figure 3.8: Effects of realistic anisotropic conditions on the minimally-coupled density profile with $\eta = -0.05$ with EoS parameters $\Gamma = \frac{5}{3}$ and $\alpha = \frac{35-4\beta_0}{27} = \alpha_{\rm crit}$. Anisotropy profiles are described by the expression $\beta(r) = \beta_0 + \beta_1 (\gamma - \gamma_0)$, and are illustrated in the inset. The purple line refers to the reference profile in isotropic conditions with $\beta_0 = \beta_1 = 0$, the red line to $\beta_0 = 0$ and $\beta_1 = 0.2$, the blue line to $\beta_0 = -0.1$ and $\beta_1 = 0.2$, and the orange line to $\beta_0 = +0.1$ and $\beta_1 = 0.2$.

3.4 NMC DM in spiral galaxies

The analysis in Sec. (3.1.1) shows how Eq. (3.10) gives rise to some exciting features for strongly DM-dominated systems in self-gravitating equilibria. The NMC helps develop an inner core in DM density profiles, enforcing a shape closely following the Burkert one out to several core scale radii (see Sec. (3.2.3) and Sec. (3.2.2)). Moreover, NMC DM-dominated halos are consistent with the core-column density relation, i.e., with the observed universality of the product between the core radius r_0 and the core density ρ_0 observed for dwarf galaxies (see Sec. (3.2.5)). However, the NMC hypothesis still needs to be tested in galaxies with different velocities at the optical radius, where the contribution of the baryonic component to the dynamics can be substantial. This section will show how the NMC DM model can provide accurate fits of spiral galaxies' RCs and how such a model can adequately account for the RAR, with an in-depth comparison to other standard-lore DM halo density profiles.

3.4.1 Rotation Curve fitting of spiral galaxies

The NMC DM will be used to mass-model stacked RCs of local spiral galaxies with different velocities at the optical radius and related properties. The inferred results will be then compared with fits obtained from the standard Newtonian case for two other classic DM halo shapes, namely the NFW profile of Eq. (1.4) and the phenomenological Burkert profile of Eq. (1.5).

This analysis relies on the samples of stacked RCs collected by Persic et al. (1996) for normal spirals divided in 11 average velocity bins, by Dehghani et al. (2020) for low surface brightness (LSB) spirals divided in 5 average velocity bins and by Karukes & Salucci (2017) for low-luminosity dwarfs. These stacked RCs are built by co-adding high-quality individual RCs of thousands of galaxies with similar velocities at the optical radius and related properties. For each galaxy, the co-addition is performed after normalising velocities and radii to reference scales, which are typically the galactic optical radius $r_{\rm opt}$ and the optical circular velocity $v_{\rm opt} \equiv v(r_{\rm opt})$. Further details on this procedure can be found in Lapi et al. (2018). The average properties of the sample of stacked RCs hereby considered are listed in Tab. (3.1).

Stacked RCs are mass-modelled as the sum of a baryonic (disc) component $v^2_{\rm d}(r) = G\,M_{\rm d}(<r)/r$ plus a DM contribution $v^2_{\rm DM}(r) = G\,M_{\rm DM}(<r)/r$, with $M_{\rm d}(<r)$ and $M_{\rm DM}(<r)$ the cumulative disc and DM mass, respectively. The overall velocity model plainly reads as $v^2_{\rm tot}(r) = v^2_{\rm d}(r) + v^2_{\rm DM}(r)$. The distribution followed by baryonic matter is modelled as a razor-thin exponential disc (Freeman 1970) with an exponential surface density

$$\Sigma_{\rm d}(r) = \Sigma_0 \exp\left(-r/r_{\rm d}\right) ;$$

here $\Sigma_0 = M_{\rm d}/2\pi\, r^2_{\rm d}$ is the central value in terms of the total disc mass $M_{\rm d} = M_{\rm d}(<\infty)$ and of the disc scale-length $r_{\rm d} \approx r_{\rm opt}/3.2$. The related contribution to the RC

is given by (e.g., Binney & Tremaine 1987)

$$v_{\rm d}^2(r) = \frac{G\,M_{\rm d}}{r_{\rm d}}\,2\,y^2\,[I_0(y)K_0(y) - I_1(y)K_1(y)]\ , \tag{3.32}$$

where $y \equiv r/(2\,r_{\rm d})$, while $I_{0,1}(\cdot)$ and $K_{0,1}(\cdot)$ are modified Bessel functions. Contributions from a gaseous disc are negligible and largely unconstrained. Hence, only the stellar disc is included in the present mass-modelling. In the fits' radial range, $r \lesssim r_{\rm opt}$, such contributions are of minor importance and can be neglected.

Three different models are then considered to describe DM's contribution to the total RC of each galaxy. Two are based on standard Newtonian gravity but differ in the DM profile shape: NFW or Burkert, whereas the other is the NMC DM model. This analysis assumes that the NMC DM model is based on the NFW profile while including a perturbative correction to the dynamics via the NMC term appearing in Eq. (3.10).

- NFW profile

  The velocity profile predicted by the NFW model can be written in terms of the halo virial mass $M_{\rm v}$ and the halo concentration, defined in terms of the halo virial radius $r_{\rm v} \approx 260\,(M_{\rm v}/10^{12}\,M_\odot)^{1/3}$ (see Sec. (1.3.4)):

  $$v_{\rm DM}^2(r) = \frac{GM_{\rm v}}{r_{\rm v}}\,\frac{g(c)}{s}\,\left[\ln(1+c\,s) - \frac{c\,s}{1+c\,s}\right]\ . \tag{3.33}$$

  Once again, $g(c) \equiv [\ln(1+c) - c/(1+c)]^{-1}$ and $s \equiv r/r_{\rm v}$. The overall galaxy RC can be specified in three parameters: the halo mass $M_{\rm v}$, the halo concentration c and the disc mass $M_{\rm d}$.

- NMC model

  In spherical symmetry, Eq. (3.10) implies that the total gravitational acceleration writes

  $$g_{\rm tot}(r) = -\frac{G\,M(<r)}{r^2} + 4\pi\,G\,\epsilon L^2\,\frac{{\rm d}\rho}{{\rm d}r}, \tag{3.34}$$

  where $M(<r)$ is the total mass enclosed in the radius r. The first term is the usual Newtonian acceleration, and the second is the additional contribution from the NMC. The related RCs $v_{\rm tot}^2(r) = |g_{\rm tot}(r)|\,r$ of spiral galaxies predicted in this framework will differ from the standard Newtonian case.

  In this analysis, the NMC is treated as a perturbative correction to the dynamics predicted by the standard NFW profile. Here, the perturbative parameter is the term L^2/r_s^2, which, as it will be shortly manifest, is always small for the range of masses probed in our study. Plugging Eq. (1.4) in Eq. (3.34) one eventually obtains the RC

  $$v_{\rm DM}^2(r) = \frac{GM_{\rm v}}{r_{\rm v}}\,\frac{g(c)}{s}\,\left[\ln(1+c\,s) - \frac{c\,s}{1+c\,s} + \frac{\epsilon L^2}{r_s^2}\,\frac{1+3\,c\,s}{(1+c\,s)^3}\right]\ . \tag{3.35}$$

It is clear that, in the minimally-coupled case, one exactly re-obtains the NFW RC. The overall RC model has four free parameters: the halo concentration c, the halo virial mass $M_{\rm v}$, the NMC lengthscale L, and the disc mass $M_{\rm d}$.

- Burkert profile

  The phenomenological Burkert profile predicts an RC that writes as (see Salucci & Burkert 2000):

$$v^2_{\rm DM}(r) = \frac{4\,GM_0}{r}\left\{\ln\left(1+\frac{r}{r_0}\right) - \tan^{-1}\left(\frac{r}{r_0}\right) + \frac{1}{2}\ln\left[1+\left(\frac{r}{r_0}\right)^2\right]\right\}, \qquad (3.36)$$

  where r_0 is the core scale radius, and $M_0 = 1.6\,\rho_0\,r_0^3$. It is customary to describe the total Burkert's RC in terms of three parameters: the core radius r_0, the core mass M_0, and the ratio $\kappa \equiv v^2_{\rm d}(r_{\rm opt})/v^2_{\rm tot}(r_{\rm opt})$ of the disc to the total velocity at the optical radius.

Fits to the stacked RC data with the aforementioned mass models are obtained using the `emcee` python package for Bayesian Monte Carlo Markov Chain (MCMC) parameter estimation (see Foreman-Mackey et al. 2013). The outcomes concerning all velocity bins for each of the galaxy types (normal spirals, LSBs and dwarfs) are represented in Tab. (3.2), Tab. (3.3) and Tab. (3.4). The results on the estimated virial masses are consistent for the three profiles. The complete sample of the corresponding RCs is shown in Appendix (D). In this Section, only three exemplary bins (one for each kind of spiral galaxy considered in the analysis) are shown in Fig. (3.9), Fig. (3.10) and Fig. (3.11).

Bin 5 from the Persic et al. (1996) sample is considered in Fig. (3.9). The results on the estimated virial mass are consistent for the three profiles. The disc mass is consistent between the NMC and Burkert models, while for the NFW model, only a relatively loose upper limit can be derived. All in all, the NMC model curve performs appreciably better in terms of reduced $\chi^2_{\rm red} \approx 0.6$ to the Burkert $\chi^2_{\rm red} \approx 22.5$ and to the pure NFW model $\chi^2_{\rm red} \approx 11$, as can also be appreciated graphically. The estimated value of the NMC lengthscale is around 0.2 kpc, roughly corresponding to a sixtieth of r_s. Fits of the NFW and NMC models are also performed by imposing the concentration parameter of the halo to satisfy the relation with the virial mass by Dutton & Macciò (2014). Both fits are not appreciably altered, but the posterior distribution of the fitted parameters in the NMC model is still consistent and somewhat narrowed.

Fig. (3.10) refers to Bin 5 in the sample of LSB galaxies by Dehghani et al. (2020). In this case, the Burkert model yields a reduced $\chi^2_{\rm red} \approx 11$, the NFW fit yields $\chi^2_{\rm red} \approx 3$ and the NMC model performs better yielding $\chi^2_{\rm red} \approx 1.411$. As expected, the disc mass in all the fits is poorly constrained since these LSB galaxies have a significantly extended disc mass distribution relative to the region probed by the RC.

Finally, in Fig. (3.11), the dwarf galaxy bin is analysed. Since it was initially designed on purpose, it is not surprising that, in this case, the Burkert profile yields the best description of the RC with a reduced $\chi^2_{\rm red} \approx 0.8$. However, the

NMC model performs decently with $\chi^2_{\rm red} \approx 4$, and substantially better than the NFW profile for which $\chi^2_{\rm red} \approx 14$. Note that such galaxies are strongly DM dominated in the region probed by the RC. Hence, the disc mass is vanishingly small and/or unconstrained by all models.

An interesting result is that the NMC model predicts higher values of the lengthscale L in DM halos of higher virial masses — see Fig. (3.12). This trend is well reproduced by the scaling $L(M_v) \propto M_v^{0.8}$, broadly consistent with the findings for DM-dominated dwarf galaxies detailed in Sec. (3.2.5).

As can be seen by looking at the overall results listed in Appendix (D) and recapped in Tab. (3.2), Tab. (3.3) and Tab. (3.4), the NMC model yields RC fits that are always superior to the pure NFW one and in several instances comparable or even better than the Burkert model. Furthermore, Tab. (3.4) contains the results of performing an F-test to compare the NFW and the NMC models. Such test suggests that the addition of the parameter L effectively improves the fits for the majority of the bins.

Two caveats are in order here. First, the Burkert profile is phenomenological and has been designed specifically to fit the RC of dwarf galaxies. Contrariwise, the NMC DM model is derived theoretically from first principles (though in a specific scenario), so the fact that its performances on RC fitting for different kinds of galaxies improves substantially over the pure NFW shape is encouraging.

Table 3.1: Samples considered for the analysis of stacked RCs: PSS stands for the sample of normal spirals by Persic et al. (1996), LSB stands for the sample of low surface brightness spirals from Dehghani et al. (2020), and Dw for the sample of dwarfs by Karukes & Salucci (2017). For each bin, the optical radius $r_{\rm opt}$ and optical velocities $v_{\rm opt}$ are reported.

Sample/Bin	$r_{\rm opt}$ [kpc]	$v_{\rm opt}$ [km s^{-1}]
PSS 1	4.6	75
PSS 2	5.7	104
PSS 3	6.5	116
PSS 4	7.6	135
PSS 5	8.9	154
PSS 6	10.1	169
PSS 7	11.5	185
PSS 8	13.5	205
PSS 9	15.3	225
PSS 10	18.	243
PSS 11	22.7	279
LSB 1	5.5	44
LSB 2	6.9	73
LSB 3	11.8	101
LSB 4	14.5	141
LSB 5	25.3	206
Dw	2.5	40

Table 3.2: Results of the MCMC parameter estimation from the fits to the stacked RCs when using the Burkert profile.

Sample/Bin	$\log r_0$ [kpc]	$\log \rho_0$ [$M_\odot$ kpc^{-3}]	$\kappa \equiv v_d^2(r_{opt})/v_{tot}^2(r_{opt})$	χ^2_{red}
PSS 1	0.596 ± 0.049	7.609 ± 0.080	$0.113^{+0.046}_{-0.039}$	0.210
PSS 2	0.790 ± 0.050	$7.486^{+0.062}_{-0.069}$	$0.249^{+0.028}_{-0.024}$	0.436
PSS 3	$0.696^{+0.066}_{-0.060}$	$7.638^{+0.094}_{-0.13}$	$0.314^{+0.057}_{-0.036}$	0.477
PSS 4	$0.796^{+0.073}_{-0.062}$	$7.556^{+0.093}_{-0.13}$	$0.376^{+0.058}_{-0.033}$	0.589
PSS 5	$1.175^{+0.060}_{-0.076}$	7.038 ± 0.071	$0.556^{+0.020}_{-0.018}$	22.466
PSS 6	$1.179^{+0.047}_{-0.053}$	7.058 ± 0.050	0.545 ± 0.011	1.290
PSS 7	$1.297^{+0.077}_{-0.11}$	6.892 ± 0.098	$0.632^{+0.023}_{-0.020}$	0.686
PSS 8	$3.15^{+1.2}_{-0.64}$	$6.301^{+0.032}_{-0.053}$	0.791 ± 0.011	3.851
PSS 9	$1.517^{+0.093}_{-0.17}$	6.65 ± 0.12	$0.722^{+0.022}_{-0.018}$	1.525
PSS 10	$2.26^{+0.35}_{-0.54}$	$6.167^{+0.046}_{-0.11}$	$0.836^{+0.015}_{-0.011}$	2.279
PSS 11	$1.963^{+0.095}_{-0.76}$	$6.30^{+0.24}_{-0.43}$	$0.823^{+0.055}_{-0.024}$	2.279
LSB 1	$0.664^{+0.062}_{-0.099}$	$7.03^{+0.16}_{-0.12}$	$0.151^{+0.077}_{-0.088}$	0.971
LSB 2	$1.259^{+0.076}_{-0.16}$	6.601 ± 0.074	0.534 ± 0.027	3.710
LSB 3	$1.272^{+0.062}_{-0.079}$	6.536 ± 0.076	$0.518^{+0.032}_{-0.030}$	0.370
LSB 4	$3.28^{+1.7}_{-0.65}$	$5.911^{+0.047}_{-0.075}$	0.750 ± 0.018	4.882
LSB 5	0.751 ± 0.018	$8.019^{+0.058}_{-0.036}$	$0.071^{+0.018}_{-0.070}$	12.268
Dw	$0.358^{+0.027}_{-0.032}$	7.563 ± 0.045	0.055 ± 0.025	0.760

Table 3.3: Results of the MCMC parameter estimation from the fits to the stacked RCs when using the NFW profile.

Sample/Bin	c	$\log M_{\rm d}$ [$M_\odot$]	$\log M_{\rm v}$ [$M_\odot$]	$\chi^2_{\rm red}$
PSS 1	$6.43^{+1.2}_{-0.78}$	6.8 ± 1.0	$12.17^{+0.13}_{-0.29}$	4.265
PSS 2	$7.4^{+2.5}_{-1.5}$	$8.67^{+0.61}_{-0.082}$	$12.45^{+0.15}_{-0.43}$	3.931
PSS 3	5.4 ± 1.7	$9.728^{+0.062}_{-0.034}$	$12.75^{+0.23}_{-0.57}$	5.730
PSS 4	$6.4^{+2.2}_{-1.9}$	$9.980^{+0.063}_{-0.036}$	$12.66^{+0.16}_{-0.49}$	4.542
PSS 5	22.71 ± 0.75	4.3 ± 2.5	11.779 ± 0.029	10.913
PSS 6	$10.2^{+2.0}_{-1.7}$	$10.208^{+0.098}_{-0.062}$	$12.347^{+0.067}_{-0.18}$	1.166
PSS 7	$9.0^{+4.3}_{-2.7}$	$10.54^{+0.10}_{-0.053}$	$12.435^{+0.038}_{-0.41}$	2.470
PSS 8	$26.2^{+1.9}_{-1.7}$	$10.19^{+0.28}_{-0.091}$	$11.939^{+0.039}_{-0.034}$	1.281
PSS 9	$15.0^{+5.4}_{-3.8}$	$10.79^{+0.17}_{-0.073}$	$12.186^{+0.032}_{-0.13}$	1.392
PSS 10	$29.1^{+2.6}_{-2.2}$	$10.47^{+0.33}_{-0.081}$	$12.091^{+0.042}_{-0.036}$	1.109
PSS 11	$18.6^{+7.1}_{-4.8}$	$11.19^{+0.17}_{-0.10}$	$12.233^{+0.046}_{-0.080}$	0.531
LSB 1	$3.51^{+0.67}_{-1.3}$	$7.94^{+0.61}_{-0.28}$	$11.63^{+0.25}_{-0.37}$	4.335
LSB 2	11.27 ± 0.68	4.4 ± 2.5	$11.229^{+0.043}_{-0.052}$	0.456
LSB 3	$3.85^{+0.84}_{-1.8}$	$9.901^{+0.096}_{-0.037}$	$12.28^{+0.22}_{-0.42}$	6.382
LSB 4	$12.7^{+2.0}_{-1.5}$	$10.31^{+0.11}_{-0.074}$	11.514 ± 0.061	1.502
LSB 5	23.5 ± 1.1	5.1 ± 2.9	12.065 ± 0.022	2.564
Dw	$4.42^{+0.97}_{-0.70}$	$3.3^{+1.7}_{-2.7}$	$11.85^{+0.17}_{-0.35}$	14.519

Table 3.4: Results of the MCMC parameter estimation from the fits to the stacked RCs when using the NMC profile. In addition to the fit parameter estimates, the F-ratio between the NFW and NMC models calculated as in Eq. (11.50) of Bevington & Robinson (2003), i.e. $F = (\chi^2_{\rm NFW} - \chi^2_{\rm NMC})/\chi^2_{\rm NMC,red}$ is reported. Values of F are reported alongside the associated p-values. Here, the null hypothesis is $L = 0$.

Sample/Bin	c	$\log M_{\rm d}$ [$M_\odot$]	$\log M_{\rm v}$ [$M_\odot$]	L [kpc]	$\chi^2_{\rm red}$	F	p-value
PSS 1	$9.14^{+1.0}_{-0.84}$	$6.2^{+1.0}_{-1.9}$	$11.71^{+0.10}_{-0.15}$	$0.254^{+0.016}_{-0.012}$	1.742	25.6	10^{-4}
PSS 2	$13.7^{+2.4}_{-0.68}$	$7.9^{+1.3}_{-1.6}$	$11.712^{+0.043}_{-0.16}$	0.4645 ± 0.0084	0.803	67.2	$< 10^{-5}$
PSS 3	$22.1^{+2.0}_{-0.42}$	7.0 ± 1.7	$11.470^{+0.026}_{-0.057}$	0.5192 ± 0.0067	0.511	174.6	$< 10^{-5}$
PSS 4	$23.7^{+2.3}_{-0.32}$	7.1 ± 1.8	$11.615^{+0.023}_{-0.054}$	0.6011 ± 0.0091	0.786	82.2	$< 10^{-5}$
PSS 5	$13.6^{+3.3}_{-4.3}$	$9.95^{+0.27}_{-0.047}$	$12.018^{+0.069}_{-0.20}$	$0.208^{+0.024}_{-0.035}$	0.615	285.7	$< 10^{-5}$
PSS 6	14.2 ± 2.9	$10.01^{+0.27}_{-0.077}$	$12.122^{+0.053}_{-0.14}$	$0.314^{+0.097}_{-0.040}$	1.098	2.0	0.2
PSS 7	$32.7^{+1.4}_{-1.2}$	$6.9^{+1.5}_{-2.3}$	11.802 ± 0.025	0.915 ± 0.013	1.088	22.6	$2 \cdot 10^{-4}$
PSS 8	32.5 ± 1.4	6.0 ± 2.3	11.937 ± 0.026	$0.443^{+0.065}_{-0.042}$	0.591	20.9	$3 \cdot 10^{-4}$
PSS 9	$31.2^{+1.8}_{-1.1}$	6.4 ± 2.5	12.076 ± 0.026	$0.733^{+0.063}_{-0.042}$	0.854	11.7	$3.5 \cdot 10^{-3}$
PSS 10	44.4 ± 1.6	6.9 ± 1.7	12.043 ± 0.017	1.439 ± 0.030	1.139	0.6	0.5
PSS 11	$42.4^{+2.3}_{-2.6}$	7.1 ± 1.8	12.251 ± 0.025	1.858 ± 0.093	0.952	-	-
LSB 1	$6.05^{+1.0}_{-0.88}$	5.2 ± 1.9	$11.07^{+0.11}_{-0.19}$	$0.280^{+0.010}_{-0.013}$	1.980	21.2	$3 \cdot 10^{-4}$
LSB 2	$12.98^{+0.87}_{-0.65}$	5.4 ± 2.0	$11.123^{+0.038}_{-0.051}$	$0.415^{+0.011}_{-0.013}$	1.512	-	-
LSB 3	$9.4^{+1.7}_{-2.1}$	$9.29^{+0.45}_{-0.17}$	$11.620^{+0.054}_{-0.085}$	$0.350^{+0.042}_{-0.028}$	0.923	101.5	$< 10^{-5}$
LSB 4	$23.7^{+1.2}_{-1.0}$	6.1 ± 2.3	$11.516^{+0.029}_{-0.026}$	$0.746^{+0.012}_{-0.014}$	1.352	2.9	0.1
LSB 5	26.9 ± 1.3	$7.2^{+1.6}_{-2.5}$	12.020 ± 0.022	1.551 ± 0.048	1.411	14.9	10^{-3}
Dw	8.32 ± 0.63	$3.3^{+1.3}_{-3.3}$	$10.988^{+0.083}_{-0.11}$	0.2259 ± 0.0043	3.987	45.9	$< 10^{-5}$

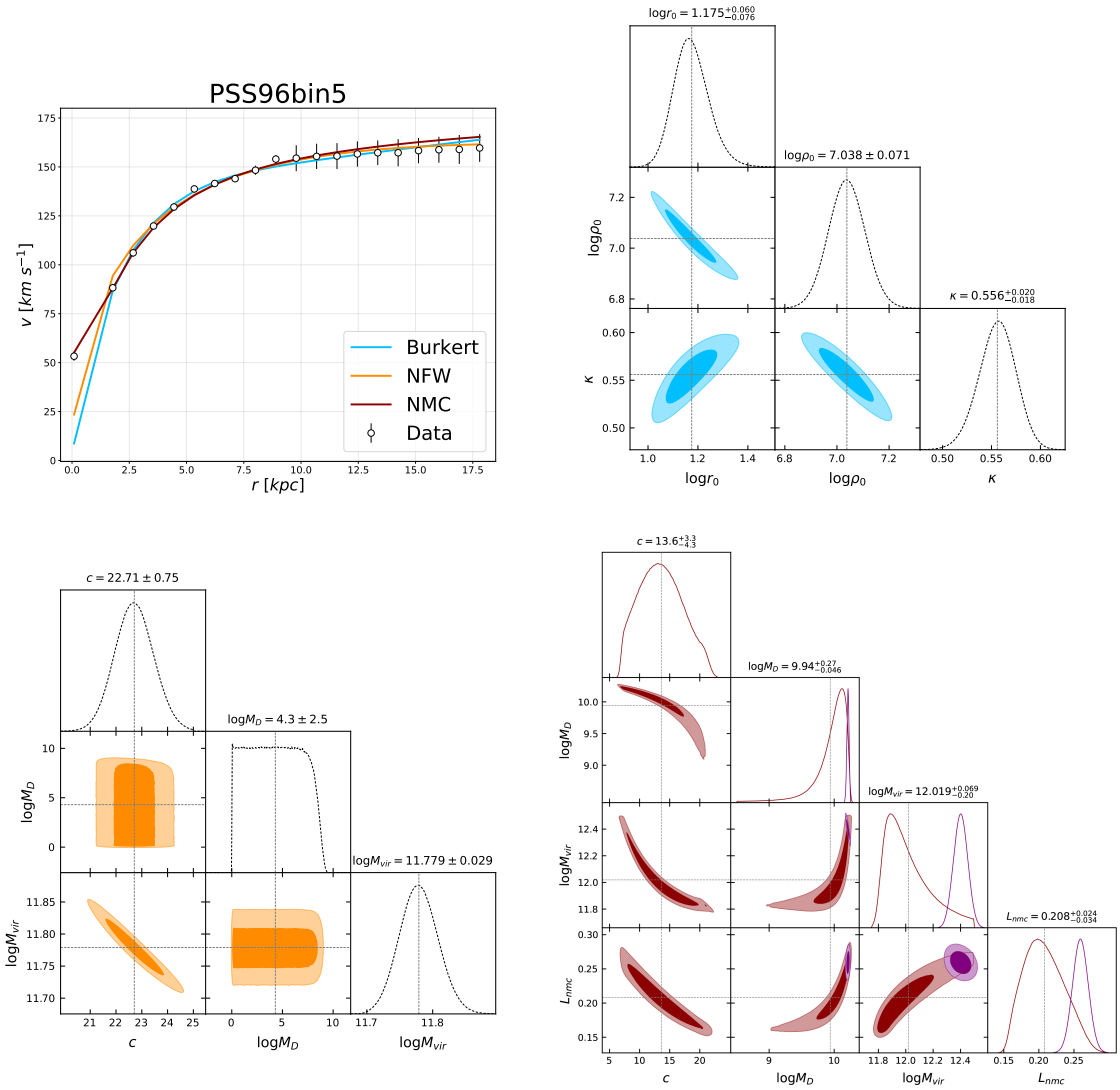

Figure 3.9: Analysis of the stacked RC for bin 5 of the spiral galaxy sample by Persic et al. (1996). The top left panel illustrates the RC curve data (open symbols) and the best-fit model for the Burkert (cyan line), NFW (orange line) and NMC profile (red line). The outcomes of the Bayesian MCMC parameter estimation are shown as corner plots for the Burkert profile (top right panel), for the NFW profile (bottom left) and for the NMC model (bottom right, with purple contours representing the posterior when the halo concentration is constrained by the relation of Dutton & Macciò 2014 given by Eq. (3.44)).

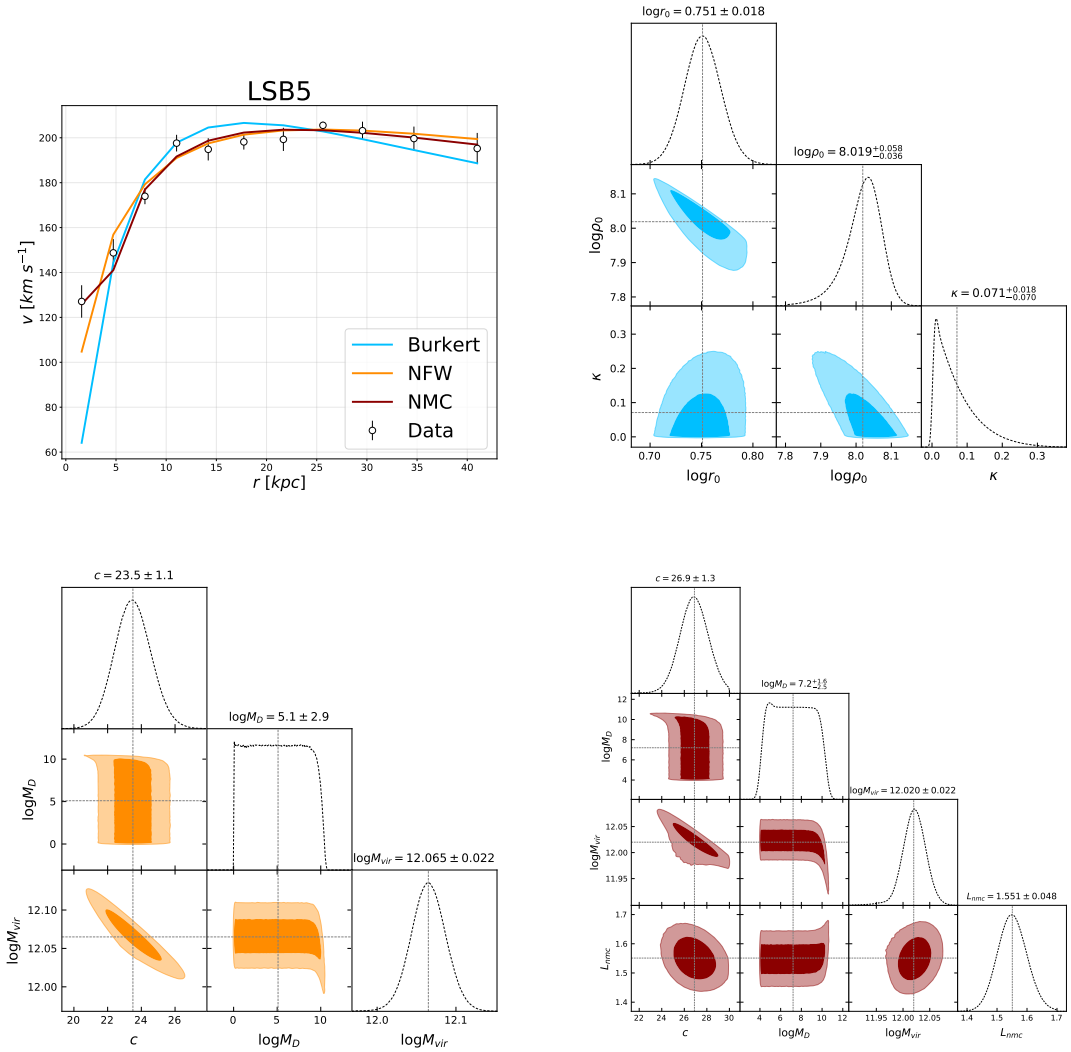

Figure 3.10: The same of Fig. (3.9) for the bin 5 of LSB galaxies by Dehghani et al. (2020).

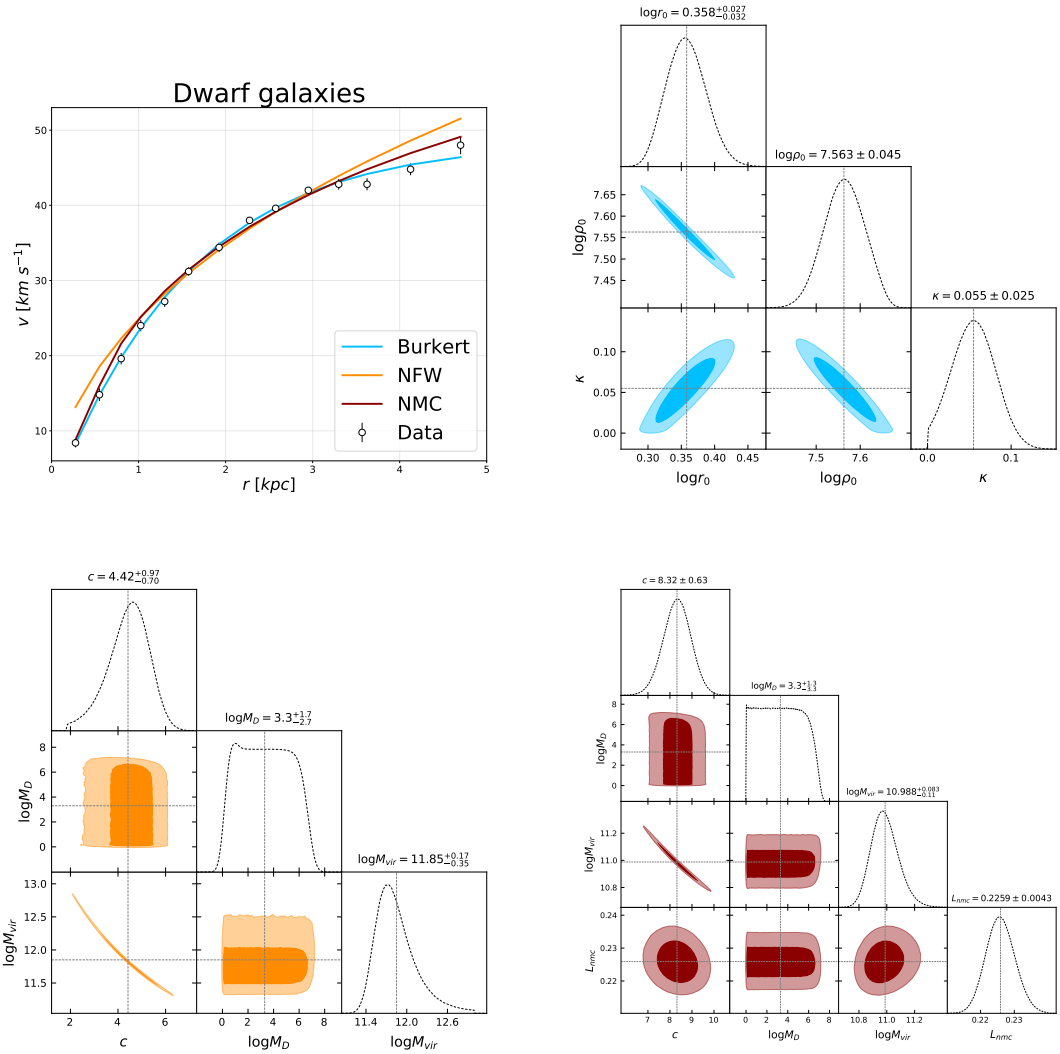

Figure 3.11: The same of Fig. (3.9) for the dwarf galaxies by Karukes & Salucci (2017).

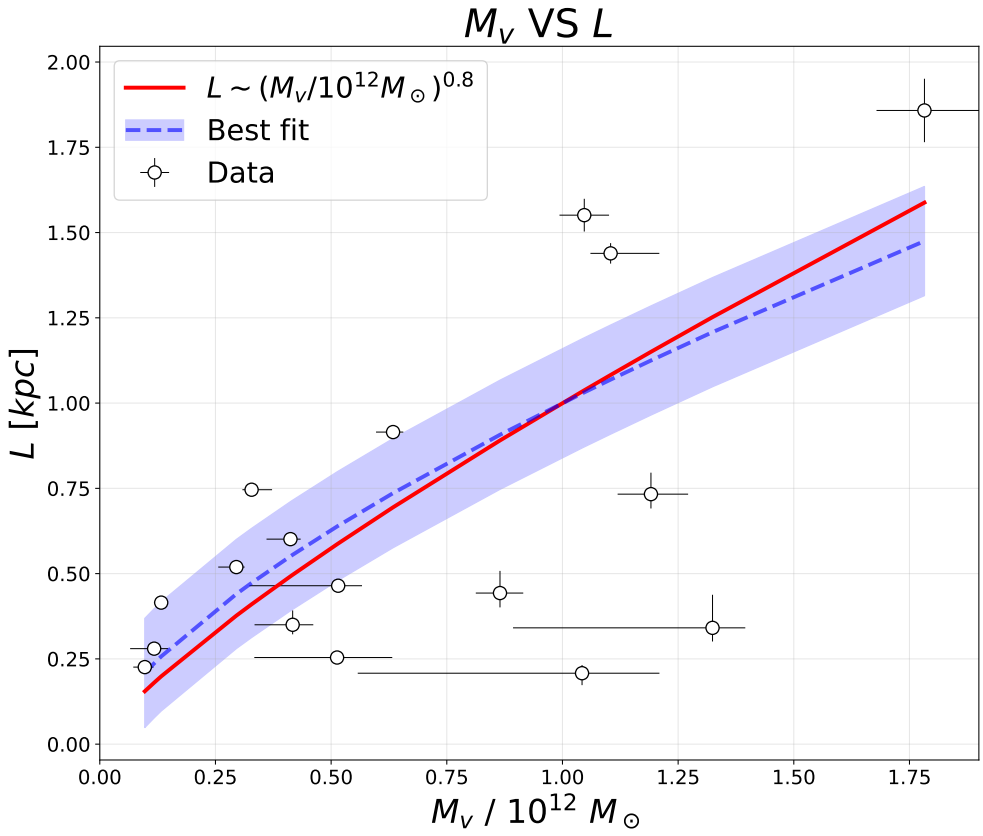

Figure 3.12: Scaling between L and M_v found in the RC fit analysis. The blue dashed line represents the best fit of data to a simple power function, resulting in a slope $m_{best} = (0.67 \pm 0.16)$ (the shaded area represents a one-sigma confidence interval). The red solid line instead represents the generalisation to baryonic-rich objects of the scaling $L \propto M_v^{0.8}$ found in the DM-dominated dwarf galaxies regime (see Sec. (3.2.4)).

3.4.2 Testing the NMC with the RAR

As discussed in Sec. (1.4.5), the RAR subsumes and generalises a plethora of well-known dynamical laws of galaxies describing the interplay between DM and baryons. For with $\hat{g} = 0$, the fitting function found in Lelli et al. (2017) given by Eq. (1.6) accurately represents the RAR for spiral and irregulars, while the additive term depending on $\hat{g}$ describes the flattening of the RAR in the typical acceleration regime proper of dwarf spheroidal galaxies. The aim is to determine whether the NMC model can adequately reproduce the RAR and whether it can do so with NMC lengthscale values consistent with those derived in Sec. (3.4.1) from the analysis of stacked RC data. The RAR is a local scaling law that combines data at different radii in galaxies with different masses, which feature different contributions of stellar disc and bulge, gas and DM. The problem is hence approached via a semi-empirical method. The first step is to build up mock RCs of galaxies with different properties and then to sample them to derive the total and baryonic accelerations and construct the RAR.

- DM mass

  The first step consists of drawing a vast number of total DM halo masses $M_{\rm v}$ within the range $8 < \log(M_{\rm v}/M_\odot) < 13.3$ according to the local halo mass function (a uniform sampling does not impact appreciably the outcomes).

- Stellar mass

  The stellar mass is then derived and associated with each galaxy by using the relation found by Behroozi et al. (2013) through an abundance matching technique:

$$\log M_\star = \log(\epsilon M_1) + f\left[\log\left(\frac{M_{\rm v}}{M_1}\right)\right] - f(0), \tag{3.37}$$

$$f(x) = -\log(10^{\alpha x}+1) + \delta\frac{\log[1+\exp(x)]^\gamma}{1+\exp(10^{-x})},$$

  with $\log M_1 = 11.514$ being a characteristic halo mass, and parameters $\log\epsilon = -1.777, \alpha = -1.412, \delta = 3.508, \gamma = 0.316$, while allowing for a log-normal scatter of 0.25 dex.

- Gas mass

  The gas mass is then determined by exploiting the relation found with the stellar mass by Papastergis et al. (2012) and Peeples et al. (2014):

$$\log\left(\frac{M_{\rm HI}}{M_\star}\right) = -0.43\log\left(\frac{M_\star}{M_\odot}\right) + 3.75, \tag{3.38}$$

  allowing a lognormal scatter of 0.15 dex. Note that, in this analysis, there is the implicit assumption that in local galaxies the majority of the interstellar

medium consists of atomic hydrogen HI and that both the ionised and the molecular components are minor (see Papastergis et al. 2012; Saintonge et al. 2011). The total gas mass is $M_{\rm gas} \approx 1.33\, M_{\rm HI}$ to account for the contribution of He.

- Stellar and gas radial distributions

  The gaseous and the stellar components are assumed to be distributed in a razor-thin exponential disc. The stellar disc half-mass radius is determined from the stellar mass via the relation by Shen et al. (2003)

$$\log\left(\frac{R_{\rm e}}{\rm kpc}\right) = \frac{1}{2.47}\left(\log\left(\frac{\rm M_\star}{M_\odot}\right) - 7.79\right). \tag{3.39}$$

  applying for $M_\star < 10^9 M_\odot$, and that by Lange et al. (2015)

$$R_{\rm e} = 0.13\left(\frac{M_\star}{M_\odot}\right)^{0.14}\left(1.0 + \frac{M_\star}{14.03\cdot 10^{10}\rm M_\odot}\right)^{0.77}\ \rm kpc \tag{3.40}$$

  for $M_\star \geq 10^9\, M_\odot$. $R_{\rm d} \approx R_e/1.678$ gives the stellar disc lengthscale. The allowed lognormal scatter for both these relations amounts to 0.1 dex. The gas distribution lengthscale is taken as $R_{\rm gas} = 2\, R_{\rm d}$.

- Bulge mass

  The galactic bulge mass is determined using the relation with the stellar mass by Gadotti (2009) and Moran et al. (2012):

$$\frac{M_{\rm B}}{M_\star} = \frac{\log\left(M^\star/M_\odot\right) - 9.5}{4.2}, \tag{3.41}$$

  with a lognormal scatter of 0.1 dex. The implied bulge-to-total mass ratio is $\sim 30\%$ for Milky-Way-like galaxies. The bulge is assumed to be present only if $M_\star \geq 3\times 10^9 M_\odot$.

- Bulge radial distribution

  The bulge mass is assumed to be radially distributed according to a Hernquist profile (Hernquist 1990)

$$\rho(r) = \frac{M_{\rm B} R_{1/4}}{2\pi r\left(R + R_{1/4}\right)^3}, \tag{3.42}$$

  where $R_{1/4}$ is the radius at which the enclosed bulge mass is a quarter of its total value. The half-mass radius $R_{1/2} = (1+\sqrt{2})R_{1/4}$ is gauged based on the scaling relation with the bulge mass by Gadotti (2009)

$$\log\left(\frac{R_{1/2}}{\rm kpc}\right) = 0.30\log\left(\frac{M_{\rm B}}{M_\odot}\right) - 3.124, \tag{3.43}$$

with a lognormal scatter of 0.1 dex.

- DM radial distribution

  The DM mass is radially distributed according to various profiles to test their performance on the RAR. For the NFW and the NMC models, Eq. (3.33) is used. The concentration parameter c is determined according to the relation with the halo mass from Dutton & Macciò (2014)

$$\log c = 0.905 - 0.101 \log \left(M_{\rm v} / 10^{12} h^{-1} M_{\odot} \right) , \tag{3.44}$$

  with a lognormal scatter of 0.11 dex.

  For the Burkert model, Eq. (3.36) is used by setting the core radius r_0 from two conditions: (i) the mass within the virial radius must match $M_{\rm v}$; (ii) the core radius and core density must satisfy the universal core surface density relation $\rho_0 \times r_0 \approx 75\, M_{\odot}\ {\rm pc}^{-2}$ discussed in Sec. (3.2.5), with a scatter of 0.2 dex (see, e.g., Salucci & Burkert 2000; Donato et al. 2009; Burkert 2015, 2020).

  Finally, we consider a profile emerging from hydrodynamical simulations by Di Cintio et al. (2014), which considers DM responses to baryonic effects (including stellar feedback). Such a profile is essentially a generalised version of the NFW one featuring the following shape:

$$\rho(r) = \frac{\rho_s}{(r/r_{\rm s})^{\gamma} \left[1 + (r/r_{\rm s})^{\alpha} \right]^{(\beta-\gamma)/\alpha}} . \tag{3.45}$$

  with shape parameters linked to the stellar-to-halo mass ratio $X \equiv M_{\star}/M_{\rm v}$ (see also Stinson et al. 2013) as

$$\begin{aligned} \alpha &= 2.94 - \log \left[\left(10^{X+2.33} \right)^{-1.08} + \left(10^{X+2.33} \right)^{2.29} \right] , \\ \beta &= 4.23 + 1.34X + 0.26X^2 , \\ \gamma &= -0.06 + \log \left[\left(10^{X+2.56} \right)^{-0.68} + \left(10^{X+2.56} \right) \right] . \end{aligned} \tag{3.46}$$

- Building up the mock RC

  All the mass components and the associated radial distribution $M_i(< R)$ have now been specified for any galaxy of given virial mass $M_{\rm v}$. The corresponding RCs can thus be easily determined from $v_i^2(R) = G\, M_i(< R)/R$. The only exception consists in the NMC model, for which the DM velocity has an additional term $v_{\rm DM}^2(r) = G\, M_{\rm DM}(< r)/r - \epsilon\, L^2\, r\, 4\pi\, G\, {\rm d}\rho/{\rm d}r$. Finally, the overall mock RC is the sum of all the different contributions $v_{\rm tot}^2 = \sum_i v_i^2$.

  Fig. (3.13) illustrates four representative mock RCs for galaxies with different halo masses $M_{\rm v}$, highlighting the diverse behaviour when assuming the NFW, the Burkert, the Di Cintio (DC+14) or the NMC halo profiles. As for the baryonic components, in moving toward smaller halo masses, the inner contribution due to the bulge component becomes less prominent,

while the gas contribution progressively increases to become even more dominant over the stellar disc. As for the DM models, the halo shapes are different, with the Burkert profile yielding overall higher velocities in lower-mass galaxies. The mock RCs are compared to the stacked empirical RCs considered in Sec. (3.4.1) to test their realism. The outcome is shown in Fig. (3.14), highlighting the compatibility between the mock curves and empirical, stacked ones.

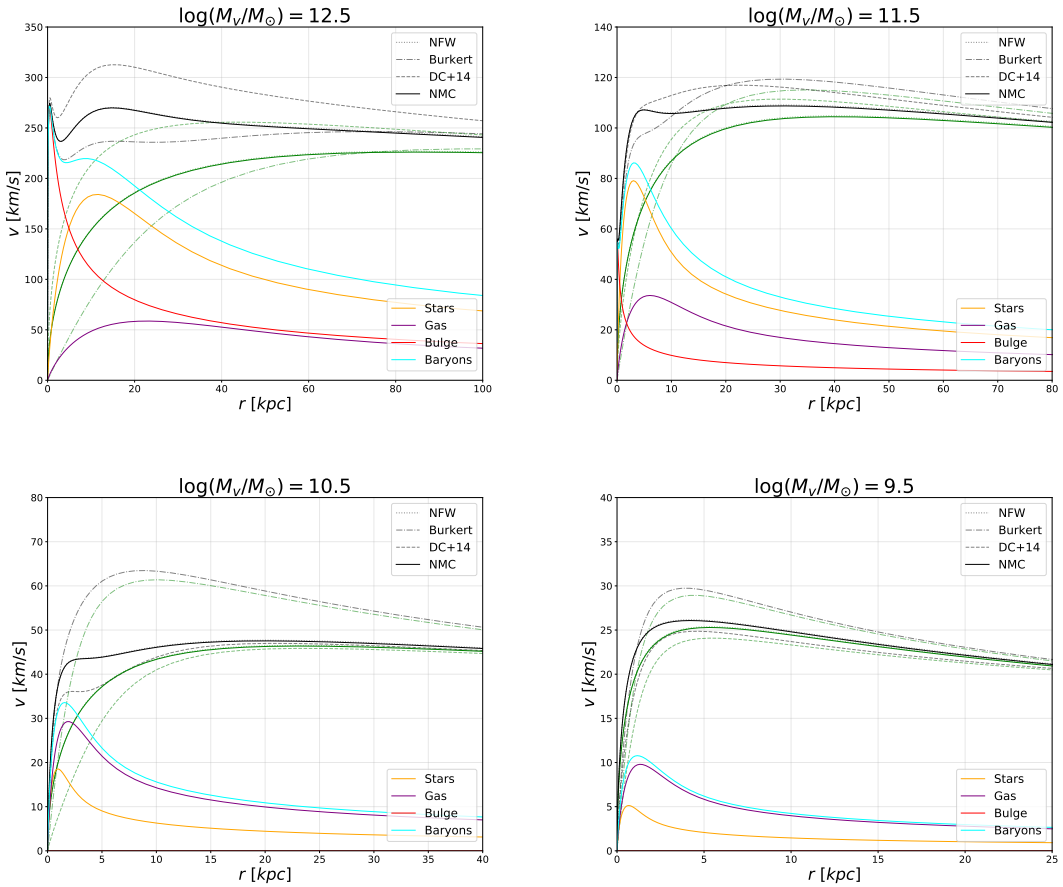

Figure 3.13: Four representative mock RCs for different DM halo masses. In each panel, the contributions from the stellar disc (orange), gas disc (purple), bulge (red), overall baryons=bulge+stars+gas (cyan), DM halo (green), and total (black) are shown. For the green and black colours, dotted lines refer to the NFW profile, dot-dashed lines to the Burkert profile, dashed lines to the DC+14 profile, and solid lines to the NMC profile.

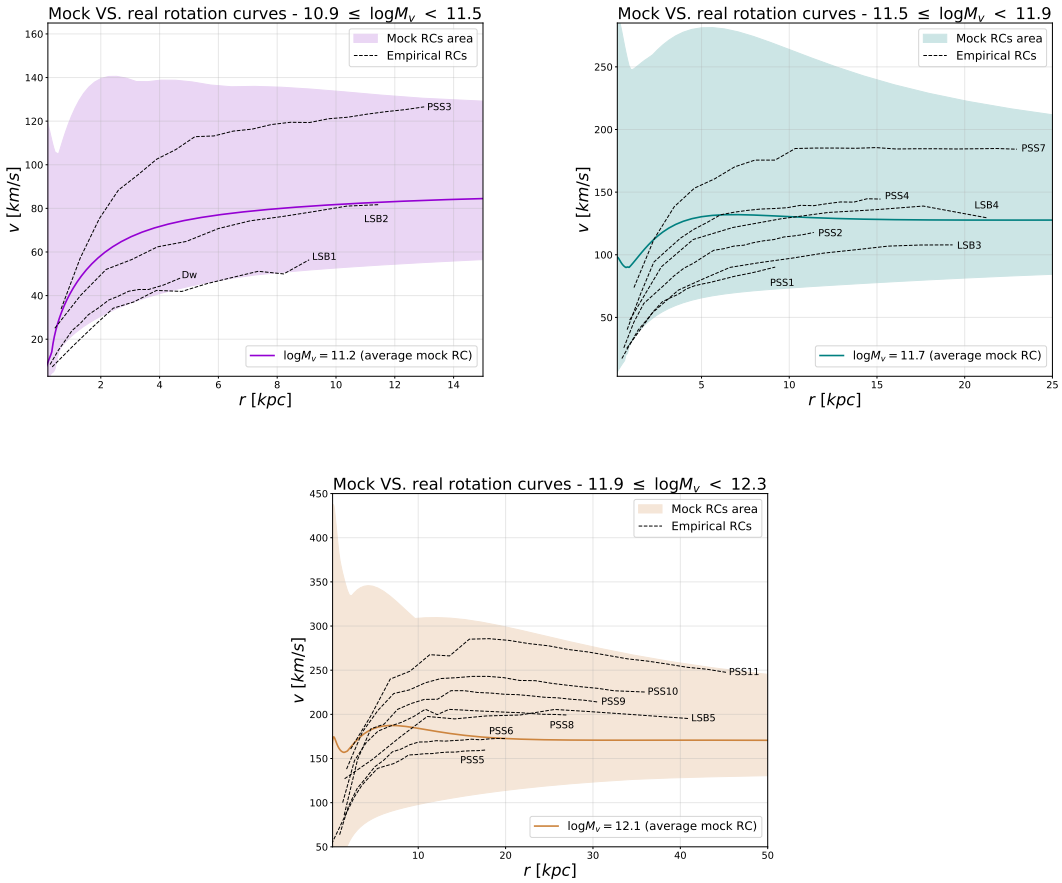

Figure 3.14: Comparison between mock RCs with the empirical stacked RCs utilised in Sec. (3.4.1). The stacked RCs (dashed black lines) are divided into three virial mass bins, and for each of these bins, 10^3 mock curves varying in the range outlined by the shaded area were generated, with the average mock RC plotted as a solid line.

Once the mock RC for each mock galaxy has been characterised, the gravitational acceleration is computed following

$$|g_j(r)| = \frac{v_j^2(r)}{r}, \tag{3.47}$$

the index j = bar, tot specifies the baryonic contribution or the total value, including DM. The RAR is then constructed by binning the mock galaxy sample in $g_{\rm bar}$ and extracting the average values and standard deviation of $g_{\rm tot}$. For a fair comparison with the data, the sampled portion of the RC is restricted to twice the optical radius of each mock galaxy. It is clear that this procedure includes in a given bin of $g_{\rm bar}$ objects with different halo masses and at different radii; e.g., an object can display a low baryonic acceleration either because it has a small halo mass or because its RC is sampled at large radii.

Fig. (3.15) illustrates the results on the RAR for the DM models listed above (color-coded). For comparison, a black line with a shaded area is reported, representing the determination by Lelli et al. (2017) as in Eq. (1.6). Grey squares represent binned data for spirals and irregulars, and individual data for dwarf spheroidal galaxies are highlighted with diamonds (filled symbols are for more secure determinations). There is a substantial agreement of the RAR for all the DM models at high baryonic accelerations. Such a regime is mainly dominated by the contribution at small radii in high-mass galaxies, where the total gravitational acceleration is dominated by baryons, implying $g_{\rm tot} \approx g_{\rm bar}$ irrespective of the specific DM profile. However, a marked difference among the RAR for different DM models sets in toward lower baryonic accelerations. Such a regime is dominated by the behaviour at small/intermediate radii in intermediate and low-mass galaxies, where the total baryon acceleration $g_{\rm bar}$ is dominated by the stellar disc. The total gravitational acceleration is instead contributed by both the disc and the halo $g_{\rm tot} \approx g_{\rm DM} + g_{\rm bar}$. Thus, depending on the DM model, most of the contribution to $g_{\rm tot}$ may come from the disc enforcing a behaviour of the RAR similar to the high acceleration regime or from the DM enforcing an upward deviation of the RAR.

All in all, both the RAR associated with the Di Cintio and the Burkert models tend to appreciably deviate downward, to the point of becoming inconsistent with the measured RAR (especially in dSph) for $g_{\rm bar} \lesssim 10^{-11}$ m s^{-2}. Contrariwise, the RAR of the NFW model displays the opposite behaviour, with the corresponding curve flattening and progressively saturating to values slightly above the observed RAR, though still consistent with the upper outliers. Nevertheless, one must keep in mind that the NFW model suffers from poor performances in fitting the individual RCs of many dwarf spheroidals (e.g., de Blok 2010) and the stacked dwarf galaxy RCs analysed here. Finally, the NMC model can reproduce the average measured RAR when extrapolating to smaller masses, assuming the dependence $L(M_{\rm v}) \propto M_{\rm v}^{0.8}$ found from the RC analysis of Sec. (3.4.1). Thus, such RAR follows a profile intermediate between the NFW and the cored ones. Remarkably, the NMC one is the only model that, in this analysis, can simultaneously reproduce the RAR and decently fits the stacked RC of spirals, LSBs and dwarf galaxies.

The prediction on the RAR for the MOND framework is also illustrated for

reference. This may be derived from the relation $\mu(x)\, g_{\rm tot} = g_{\rm bar}$ where the simple interpolating function $\mu(x) = x/(1+x)$ with $x \equiv g_{\rm tot}/a_0$ and $a_0 \sim 1.2 \times 10^{-10}$ m s^{-2} is generally adopted (e.g., Famaey & Binney 2005, Zhao & Famaey 2006; see Sec. (2.2.6)). The MOND outcome is close to the measured RAR at high acceleration, while it lacks the progressive flattening at low $g_{\rm bar}$. However, some authors pointed out that this simple parameterisation of MOND is not accurate because of the EFE (see Sec. (2.2.6)). One can account for the EFE by modifying the interpolating function to read $\mu(x) = (x/1 + x + e)\,[1 + (2+e)\,e/x(1+e)]$, with $e = g_{\rm ext}/a_0$ being the strength of the effect to the MOND acceleration scale (as in Timberlake et al. 2021). This parameter was estimated to be around $e \approx 0.033$ by Chae et al. (2020) and Chae et al. (2021) from the analysis of individual galaxy RCs (Desmond et al. 2018). The RAR from MOND theory including the EFE deviates downward at low accelerations and can account for some of the bottom outliers. However, to reproduce the observed RAR for the bulk of the galaxies would require negative values of e, which is not supported by observational estimates and known to be theoretically unfeasible in the MOND framework (see Chae et al. 2020).

Fig. (3.16) represents the RAR expected from the NMC model for different values of the NMC lengthscale L/r_s. Plainly, for vanishing L/r_s, the NFW outcome is recovered. For L/r_s progressively increasing, the NMC model spans the dispersion of the outliers in the RAR at low baryonic accelerations.

In conclusion, the outcomes of this session illustrate that the NMC DM predicts an interesting galactic-scale phenomenology. By considering the NMC as a perturbation acting upon the NFW profile, this model faithfully replicates the RCs of various late-type galaxies. NMC DM also predicts a simple power-law correlation between the virial mass of structures and the NMC's lengthscale L. This scaling allows to reproduce the RAR down to the regime probed by dwarf spheroidal galaxies.

However, how well does this model perform when applied to highly massive structures such as galaxy clusters? Are these structures compliant with the observed relationship between the NMC's lengthscale and the virial mass of haloes? The following section will provide a definitive response to these inquiries.

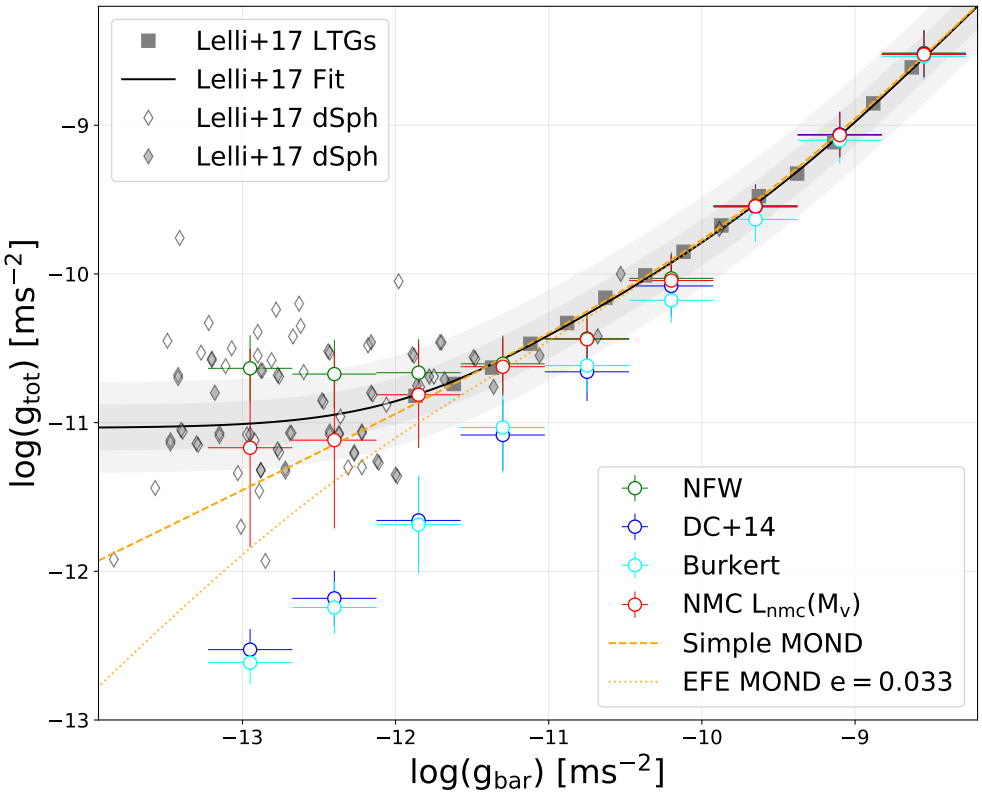

Figure 3.15: The Radial Acceleration Relation (or RAR). The solid black line with shades illustrates the average results and its 2σ and 3σ variance from the analysis of the SPARC database by Lelli et al. (2017). In particular, grey squares refer to the binned outcome for normal spiral galaxies and diamonds to measurements in individual dwarf spheroidal (filled symbols are more secure determinations). Such dwarf spheroidals have large error bars not displayed in this plot for visual clarity. Thus, the extension of the fit line through this cloud is much less certain than for the LTGs. The coloured circles illustrate the prediction from our empirical modelling of RCs when adopting different halo profiles: NFW (green), Di Cintio (blue), Burkert (cyan) and NMC with a mass-dependent scaling for the coupling lengthscale L (red; see text for details). For reference, the MOND expectations without (dashed orange) and with (dotted orange) the external field effect (to the value $e = +0.033$ estimated in Chae et al. 2020) is displayed.

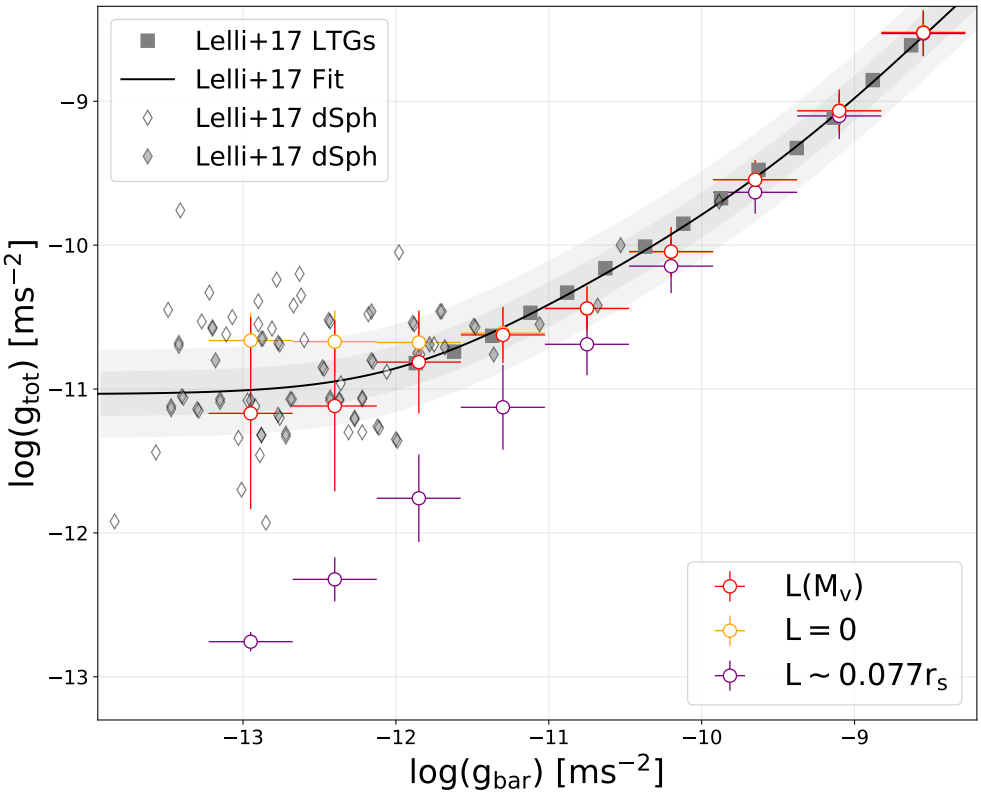

Figure 3.16: The RAR for the NMC model, with different coupling lengthscales L/r_s. As expected, setting the coupling length to zero (orange) amounts to recover the RAR reproduced by the NFW model. The RAR for $L/r_s \sim 0.077$ is also displayed, i.e. the average value obtained from the RC analysis of large spiral galaxies (purple). Intermediate values for L/r_s describe RARs that will lie between these two extremes. For reference, the RAR obtained assuming a mass-dependent scaling for the coupling lengthscale L as in Fig. (3.15) is also reported (red).

3.5 NMC DM and Galaxy Clusters

This section collects tests of the NMC DM model on the scales of galaxy clusters. The aim is to assess its capability to fit the pressure profiles of these massive structures and to determine if the scale relation predicted by the NMC DM model retrieved in Sec. (3.4.1) is also satisfied in these regimes.

The thermal pressure profiles[2] of galaxy clusters are defined as functions of the gravitational potential in play. In the framework of the NMC DM model, this reads as

$$P^{\rm th}(R) = P^{\rm th}(0) - 1.8\mu m_{\rm p}\int_0^R n_{\rm e}(r)\left[\frac{GM_{\rm DM}(r)}{r^2} - 4\pi\, G\,\epsilon L^2\,\frac{{\rm d}\rho}{{\rm d}r}\right]{\rm d}r. \tag{3.48}$$

Here, the electron density (ED) profile is modelled through the Vikhlinin profile (Vikhlinin et al., 2006)

$$\frac{n_e(r)}{n_0} = \frac{(r/r_c)^{-\alpha/2}[1+(r/r_s)^{\gamma}]^{-\eta/(2\gamma)}}{[1+(r/r_c)^2]^{(3/2)\beta-\alpha/4}}. \tag{3.49}$$

Here, $\beta \equiv \mu m_{\rm p}\sigma^2/k_{\rm b}T_{\rm gas}$ is the ratio of the specific energy in galaxies to the specific energy in the hot gas, with μ being the mean molecular weight, $m_{\rm p}$ being the mass of the proton, σ being the one-dimensional velocity dispersion, and $T_{\rm gas}$ is the temperature of the intracluster medium (ICM); whereas the additional term describes a change of slope by η near the radius r_s, and the parameter γ controls the width of the transition region and r_c is the core radius of the gas distribution.

This analysis exploits the same perturbative approach of Sec. (3.4) (i.e., the NMC is treated as a perturbation acting over the standard NFW profile). Here, the NFW profile will be expressed in terms of the halo virial mass M_{500} (i.e., the mass value at which the interior mean density is 500 times the critical density of the Universe) and the corresponding halo concentration $c \equiv r_{500}/r_s$, with $r_{500} \approx 260\left(M_{500}/10^{12}M_{\odot}\right)^{1/3}$. The DM mass profile in Eq. (3.48) will then coincide with the NFW mass distribution and, identically to Sec. (3.4), the term $\frac{{\rm d}\rho}{{\rm d}r}$ will be the gradient of the NFW density profile. Again, in this analysis, the perturbative parameter is L/r_s, a quantity always small for the range of masses hereby probed, as the results will show.

3.5.1 The X-COP Galaxy Clusters Sample

This analysis relies on data from the XMM-Newton Cluster Outskirts Project [3] (X-COP) data products (see Eckert et al. 2017; Ghirardini et al. 2018; Ettori et al. 2019; Eckert et al. 2019; Ghirardini et al. 2019). This sample consists of 12 clusters with well-observed X-ray emission and high signal-to-noise ratio in

[2]Here the gas density $n_{\rm gas}(r) \approx 1.826\, n_e(r)$ is the sum of the electron and proton number densities, μ is the mean molecular weight in a.m.u., and m_p is the proton mass.

[3]The datasets are publicly available at the following link: https://dominiqueeckert.wixsite.com/xcop/about-x-cop

the Planck Sunyaev–Zel'dovich (SZ) survey (Ade et al. 2016). X-COP data provide information about the ICM temperature and pressure in a wide radial range, from 0.2 to 2 Mpc.

The methodology adopted here is equivalent to the one earlier implemented in Haridasu et al. (2022). To constrain the NMC lengthscale (L) alongside the parameters of the mass profile (Θ_M) and the electron density (Θ_e), a joint likelihood $\mathcal{L}$ is considered, and it is written as

$$\mathcal{L} = \mathcal{L}_{\rm P_X} + \mathcal{L}_{\rm P_{SZ}} + \mathcal{L}_{\rm ED}, \tag{3.50}$$

where the pressure is computed through Eq. (3.48) and the electron density is modelled as in Eq. (3.49). Here, the first term accounts for the likelihood corresponding to the X-ray temperature P_X data, the second term denotes the likelihood for the co-varying SZ pressure data and the last term in Eq. (3.50) accounts for the modelled electron density data. Alongside these primary parameters of the model, this analysis also includes an additional intrinsic scatter $\Sigma_{\rm P,int}$ following the approach in Ghirardini et al. (2018) and Ettori et al. (2019)[4].

A Bayesian analysis through MCMC sampling is exploited to achieve the desired results. To perform the chains' analysis and plot the contours, the `emcee` package and the `GetDist` package (Lewis 2019) are used. Priors are assumed to be flat and uniform on all the parameters $\Theta_e = \{n_0, \alpha, \beta, \epsilon, r_{\rm c}, r_{\rm s}\}$, $\Theta_{\rm M} = \{M_{500}, c\}$ and the NMC characteristic lengthscale L in the MCMC analysis. A model comparison through the Bayesian evidence $\mathcal{B}$ (Trotta 2008, 2017; Heavens et al. 2017b) is also performed using the `MCEvidence` package (Heavens et al. 2017a)[5]. Comparing the Bayesian evidence, one can assess the preference for a given model $\mathcal{M}_1(\Theta_1)$ over the base model (i.e., the NFW model). Also, the Bayesian evidence is contrasted on the Jeffrey's scale (Jeffreys 1961), where $\Delta \log(\mathcal{B}) < 2.5$ and $\Delta \log(\mathcal{B}) > 5$ imply either a weak or a strong preference for the extended model, respectively.

3.5.2 Fitting Galaxy Clusters pressure profiles

The results of the MCMC parameter estimation are reported in Tab. (3.6) and the respective statistical comparison in Tab. (3.5). The reduced chi-squared ($\chi^2_{\rm red}$) values in Tab. (3.5) indicate that for the majority of the clusters, the NMC DM model generally describes the data comparably and often even better than the NFW model. Nevertheless, a remark is in order: the NMC lengthscale L value is partially guided by data availability at the innermost radii, and X-COP cluster pressure profiles are not well characterised in these regions. This lack of data at small radii relaxes the constraints on the higher end of the possible values for L, and it is ultimately responsible for the production of a hole-like feature (corresponding to low or negative values of pressure) observed in this analysis for a certain fraction of the cluster pressure profiles at inner radii. However, these features could be erased by adding one or more data points at inner radii for the pressure profiles. Unfortunately, such data are not available for the X-COP cluster

[4]For a more in-depth discussion on the mild differences between the approach hereby exploited and the analysis performed in Ettori et al. (2019) refer to Haridasu et al. (2022).

[5]See the online documentation.

sample. In light of this, values of the NMC lengthscale L obtained in this analysis for clusters exhibiting a hole in their pressure profiles should be interpreted as upper bounds on the actual values of L. The NMC DM model does not modify the estimation of pressure profiles in the cluster's outskirts. This essentially implies that the results presented here are not degenerate with any additional physics that can potentially affect the pressure profile estimation at outer radii, such as non-thermal pressure support, which, for example, could be important for cluster A2319 (Eckert et al. 2019). The last column of Tab. (3.5) shows estimates of the Bayesian evidence $\Delta_{\mathcal{B}}$ exploited to compare the two models further, assuming standard NFW to be the base model. The NMC DM model is preferred for half of the clusters in the sample, and likewise, it is mildly disfavored by the other half (up to the more striking case of RXC1825, for which $\Delta_{\mathcal{B}} = -3.53$).

Tab. (3.6) reports the concentration c_{500} and virial mass M_{500} values from the MCMC analysis for the NFW and the NMC DM models. Estimates for these values from the two models are always compatible within the displayed uncertainties, except for cluster RXC1825's concentration (slightly larger in the NMC framework than the NFW case) and M_{500} (conversely slightly smaller in the NMC case). Despite this compatibility, the NMC model predicts concentration values systematically larger than the NFW ones. Tab. (3.6) also features the MCMC estimations for the NMC lengthscale L. Overall, these values of L exceed by two orders of magnitude on average the same values obtained for spiral galaxies in Sec. (3.4.1). This result is remarkably consistent with the increasing trend observed for spiral galaxies in Gandolfi et al. (2022a) between the mass of DM halos and the L associated with them.

Fig. (3.17) and Fig. (3.18) show two exemplificative profiles (clusters A644 and A2142) obtained with the MCMC analysis, alongside the posterior contour plots for M_{500}, c and L (all the other pressure profiles and contour plots are displayed in Appendix (E)). As in the other clusters, both the NFW and the NMC DM models provide a good description of the general trend of the data. However, the NMC DM model can better fit the clusters whose data at the innermost radii are tracing a flattening in the shape of the pressure profiles. Such flattening seems to arise right within the area in which the NMC effect is active (i.e., within a distance of L from the centre of the dark haloes, represented as a blue shaded area in both Fig. (3.17) and Fig. (3.18)). As mentioned, such an NMC effect should be read with caution, given the limitation of the temperature data available in the innermost regions of the cluster.

Fig. (3.19) shows the one-dimensional posterior distribution of the L parameter from the MCMC analysis for the X-COP cluster sample. Consistently with the galactic dark halos analysed in Sec. (3.4.1), L has different values in different halos, depending on their characteristics (particularly their virial mass). Some halos (e.g., RXC1825 or A85) show a one-dimensional posterior converging towards $L = 0$, suggesting that the DM density profile for these halos may have a cuspy shape, well reproduced by the NFW model. In other halos (e.g., A2319 and A2255), the NMC produces typical lengthscale capable of reaching fractions of Mpc. These values are likely to be slightly overestimated since, as previously discussed, some of these clusters exhibit an NMC DM pressure profile featuring a central hole.

Table 3.5: Reduced χ^2 from the MCMC parameter estimation for both the NFW and NMC DM models alongside the Bayesian evidence $\Delta_{\mathcal{B}}$ in favour of the NMC DM model.

Cluster	z	$\chi^2_{\rm red,NFW}$	$\chi^2_{\rm red,NMC}$	$\Delta_{\mathcal{B}}$
A85	0.0555	2.9	2.7	-0.89
A644	0.0704	2.4	2.2	0.11
A1644	0.0473	3.9	3.4	1.01
A1759	0.0622	1.7	1.6	1.34
A2029	0.0773	1.6	1.6	-0.15
A2142	0.0909	3.3	3.3	-1.32
A2255	0.0809	6.7	1.8	2.64
A2319	0.0557	7.8	7.1	2.05
A3158	0.0597	2.3	2.1	2.81
A3266	0.0589	6.7	6.8	-1.89
RXC1825	0.0650	3.3	6.1	-3.53
ZW1215	0.0766	0.97	0.86	-0.81

Despite this, the peak of such a one-dimensional posterior is far from $L = 0$, indicating that the shape of the density profile of these dark halos could be less cuspy and different from that of the NFW profile. As can be seen in the right panel of Fig. (3.17), the non-zero values for L are essentially accompanied by a mild positive correlation with M_{500} and subsequently a non-Gaussian degeneracy with the concentration c. Also, for all the clusters that have a non-zero posterior for the L, no correlation with the M_{500} parameter is observed as in the case of A2142, shown in the right panel of Fig. (3.18). In this context, clusters A2255 and A2319 show a slightly larger value of the lengthscale L in the posteriors. Note that a solid bi-modal behaviour is found for the clusters A2255 and RXC1825. For these clusters, the maximum posterior region is selected. As can also be seen from the corresponding Bayesian evidence in favour of the NMC DM model, the clusters A3158, A2319, and A2255 show a moderate preference ($\Delta_{\mathcal{B}} \gtrsim 2$), owing to the slightly larger values of L. As seen in Fig. (E.1), this evidence in favour of the NMC DM in these three clusters is essentially driven by the improvement of the fit accounting for the innermost data point in the X-ray pressure observations. On the contrary, the cluster RXC1825 prefers the standard NFW scenario at a similar level of Bayesian evidence.

Table 3.6: Results of the MCMC parameter estimation for the NFW models and the NMC DM model.

Cluster	$c_{500,\mathrm{GR}}$	$M_{500,\mathrm{GR}}/(10^{14}M_\odot)$	$c_{500,\mathrm{NMC}}$	$M_{500,\mathrm{NMC}}/(10^{14}M_\odot)$	L [kpc]
A85	$2.0^{+0.1}_{-0.1}$	$6.2^{+0.2}_{-0.3}$	2.0 ± 0.2	$6.2^{+0.3}_{-0.3}$	12^{+6}_{-10}
A644	5^{+1}_{-2}	4.6 ± 0.4	$6.2^{+1.0}_{-1.7}$	4.6 ± 0.4	26^{+11}_{-4}
A1644	$1.1^{+0.2}_{-0.4}$	$3.2^{+0.3}_{-0.4}$	$1.4^{+0.3}_{-0.5}$	$3.3^{+0.3}_{-0.3}$	27^{+9}_{-3}
A1759	3.0 ± 0.2	$4.7^{+0.2}_{-0.3}$	$3.4^{+0.3}_{-0.3}$	$4.6^{+0.2}_{-0.2}$	20^{+7}_{-3}
A2029	$3.3^{+0.2}_{-0.3}$	7.7 ± 0.4	$3.6^{+0.3}_{-0.5}$	7.5 ± 0.4	28^{+15}_{-7}
A2142	$2.3^{+0.2}_{-0.2}$	8.4 ± 0.4	$2.4^{+0.2}_{-0.3}$	8.4 ± 0.4	17.3^{+7}_{-15}
A2255	$1.6^{+0.4}_{-0.9}$	4.7 ± 0.4	$2.3^{+0.3}_{-0.7}$	4.8 ± 0.3	109^{+11}_{-8}
A2319	$3.8^{+0.4}_{-0.6}$	7.4 ± 0.2	$4.6^{+0.6}_{-0.8}$	7.4 ± 0.2	60^{+17}_{-5}
A3158	$2.0^{+0.3}_{-0.4}$	$4.0^{+0.3}_{-0.3}$	$2.6^{+0.4}_{-0.4}$	4.0 ± 0.2	36^{+6}_{-3}
A3266	$1.7^{+0.2}_{-0.2}$	6.6 ± 0.2	1.7 ± 0.2	$6.5^{+0.3}_{-0.3}$	15^{+5}_{-13}
RXC1825	$2.6^{+0.4}_{-0.4}$	$4.1^{+0.3}_{-0.3}$	$4.0^{+0.5}_{-0.9}$	3.5 ± 0.3	9^{+3}_{-8}
ZW1215	$1.5^{+0.2}_{-0.3}$	7.1 ± 0.7	$1.6^{+0.2}_{-0.3}$	7.0 ± 0.6	22^{+9}_{-19}

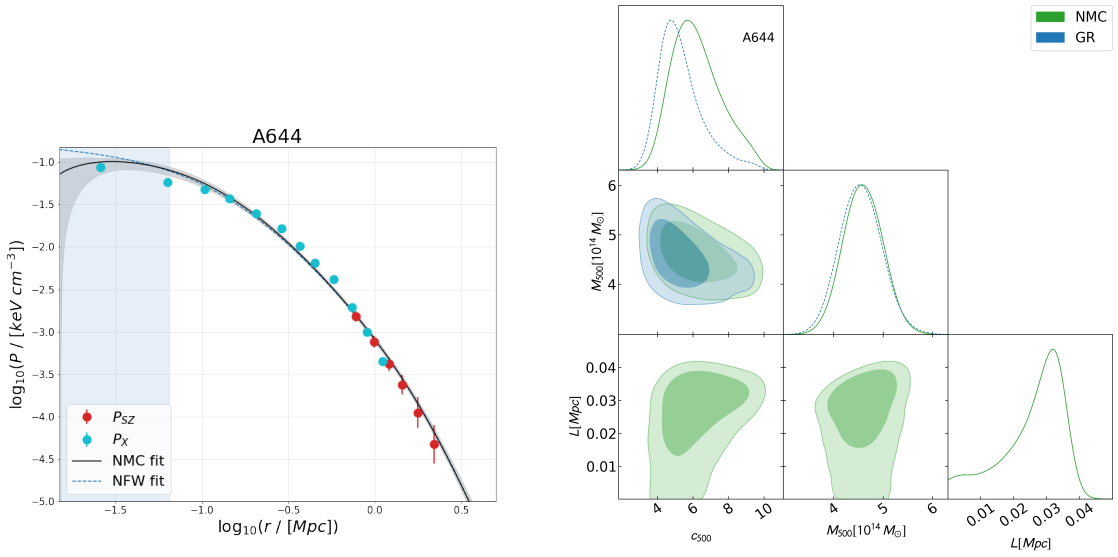

Figure 3.17: Left: Pressure profile and related contour plots for the A644 cluster. Data are displayed as red dots (SZ effect data) and cyan dots (data from the temperature profile by X-ray measurements). The black, solid lines represent the Bayesian MCMC best fit for the NMC DM model, with the grey contour representing the 68 % confidence interval around the best-fit line. The dashed blue line represents instead the NFW best fit. The blue shaded area in the profile represents the region of the dark halo within which the NMC is active, i.e. an area that extends from the centre of the halo up until L. Right: The green contours represent the NMC DM model, while the blue contours represent the NFW fit.

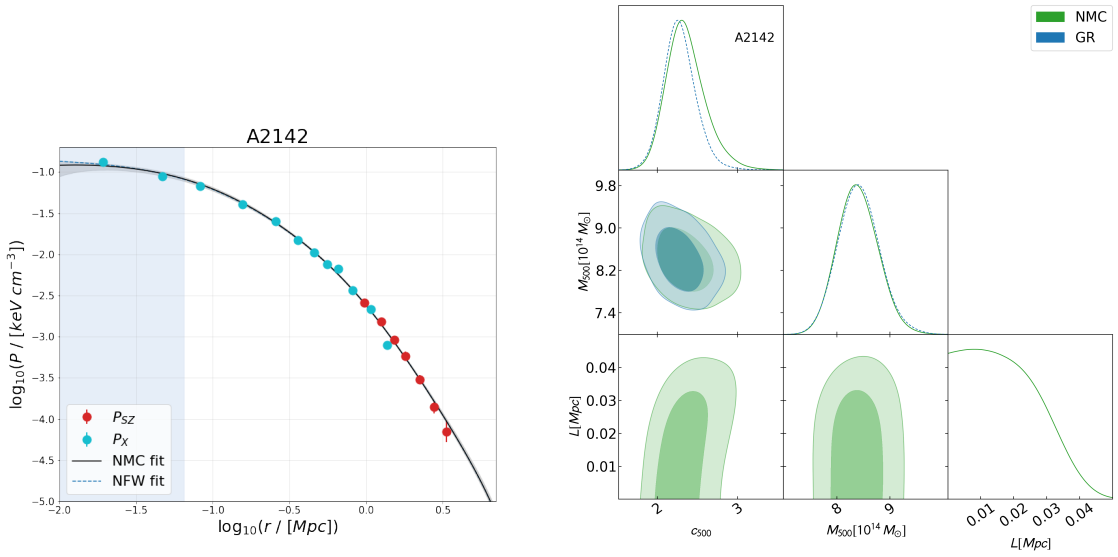

Figure 3.18: Same as Fig. (3.17) but for the A2142 cluster.

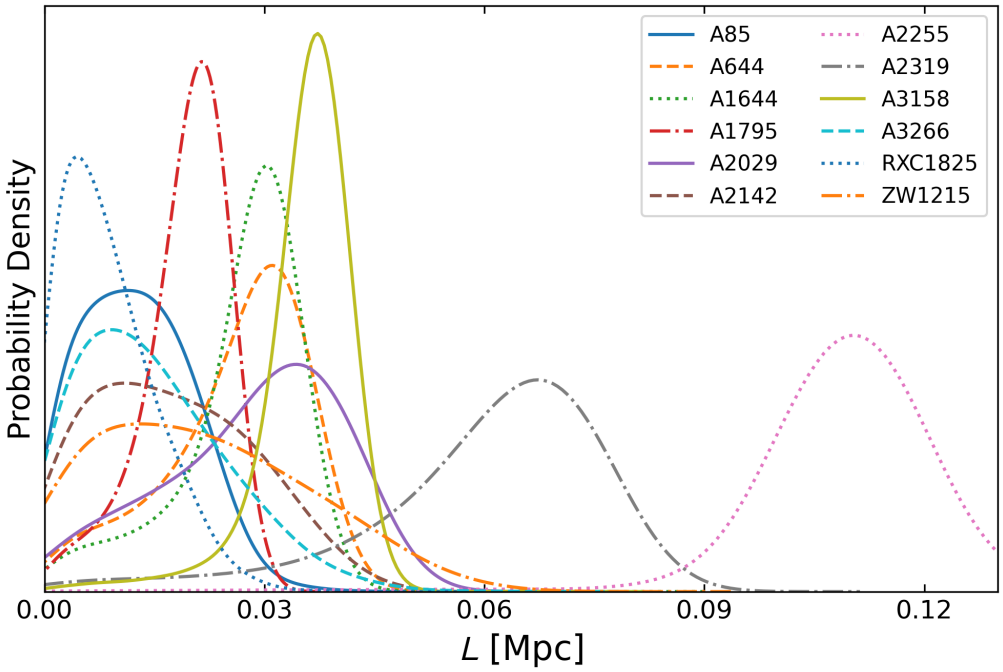

Figure 3.19: The one-dimensional posterior distribution for the lengthscale parameter L as retrieved in the Bayesian MCMC analysis.

3.5.3 The virial mass VS non-minimal coupling lengthscale in clusters

This section aims to investigate the relation between the NMC lengthscale L and the dark halo virial mass M_{500} observed as a result of the analysis. This relationship is an important feature of the NMC DM model, which, as stated in Sec. (3.1.3), is not to be considered a modified theory of gravity. Therefore, L should not be considered a new proposed fundamental constant of nature. The observed relationship between L and M_{500} shows that L indeed does not have a universal value and depends on at least one property of the dark haloes under consideration, as shown in Sec. (3.4.1) for galactic dark halos where such a relationship was described with a simple power-law. Here, the validity of this relation is investigated up to the virial mass ranges typical of galaxy clusters. The present analysis results are shown in Fig. (3.20). Here, the virial masses of the spiral galaxies of Sec. (3.4.1) and their errors are rescaled from M_{200} to M_{500} to homogenise the results. Remarkably, the X-COP clusters data points derived by the MCMC analysis seemingly agree with the power-law trend of the L - M_{500} relationship observed in Sec. (3.4.1). An MCMC fit is performed using the model $\log_{10} L = a \log_{10}(bM_{500})$ to fit both galactic and clusters data simultaneously, obtaining as parameter values $a = 0.542 \pm 0.005$ and $b = 0.807 \pm 0.005$. The slope a found in this analysis is compatible with the slope (0.7 ± 0.2) found in Sec. (3.4.1) by fitting a similar power-law to galaxies only. The best-fit line is shown in Fig. (3.20) as a solid black line with a grey shaded area representing a one-sigma confidence limit of the fit. In the same figure, a grey dotted line shows the relation $L = M_{200}^{0.8}$,

which is the one retrieved for galactic haloes and it was adopted as a reference relation to study the capacity of the NMC DM model in reproducing the RAR. In the galactic virial mass regime, the two power-laws are consistent within a one-sigma confidence limit, and their slopes are compatible within the errors. The updated scaling law retrieved in the present analysis translates into an average variation of the RAR to the one computed in Sec. (3.4.2) by a mere 0.33%, with the average of such variation being taken for every radial acceleration bin in which the RAR is computed (spanning from a minimum variation of 0.004% to 1.4% among all the bins). Such variation is well within the errors associated with the RAR computed for every single bin of radial acceleration. The RAR's minimum and maximum percentage relative uncertainties are 0.67% and 3.27%, respectively, and the average one is 1.85%. One can thus conclude that the updated L - M_{500} relation retrieved here, albeit different from the one considered in Sec. (3.4.2), can still reproduce the RAR in the galactic dark haloes mass regime. That being said, from Fig. (3.20), it is possible to appreciate the significant difference between the two power-laws when approaching the cluster dark halo mass regime. This discrepancy essentially constitutes an improvement over the previous analysis, which utilised only galaxies to assess the same relation. As previously mentioned, values for L could be slightly overestimated for some clusters. Hence, the real best-fit power-law could be even less steep than what is found in the present analysis. Moreover, considering a galaxy cluster dataset that probes the innermost regions of the halo could help reduce the scatter in the L - M_{500} relation.

3.5.4 Scatter in the virial mass VS concentration relation

Fig. (3.21) depicts the correlation between concentration c and M_{500} values inferred from the MCMC analysis hereby exploited against the relationship between c_{200} and M_{200} of dark halos found in Dutton & Macciò (2014) and given by Eq. (3.44). To make this comparison, the value of the virial mass M_{500} of the clusters is rescaled to M_{200}, recalculating the corresponding concentrations accordingly. Then, an MCMC fit is performed to find the best-fit power law that best describes the data obtained by exploiting the NFW and NMC DM models. In both these cases, there is some visible difference between the best-fit power laws and the relationship found in Dutton & Macciò (2014). This discrepancy is appreciable at least up to the cluster mass regime, where both the best-fit power laws of the NFW and NMC DM model intersect the report of Dutton & Macciò (2014). No essential differences can be identified between the two models since the corresponding data have a somewhat similar scatter around the Dutton & Macciò (2014) relation. This fact is expected following the previous examination of the tabulated results of the MCMC analysis performed here. Fig. (3.21) can provide interesting qualitative hints on this framework's expected concentrations of sub-haloes in galaxy clusters. As argued in Meneghetti et al. (2020), ΛCDM could be at variance with the observed density and compactness of DM sub-haloes in galaxy clusters. From the analysis conducted here, the NMC DM model predicts galaxy-sized DM sub-structures in clusters featuring overall higher concentrations associated with lower halo mass values to the standard CDM paradigm. However, only future analysis relying on high-quality data and exploiting a larger sample of galaxy clusters could confirm this prediction. In this context, the observed tensions at galaxy cluster scales present a promising way to further test the NMC dark matter scenario and its phenomenology.

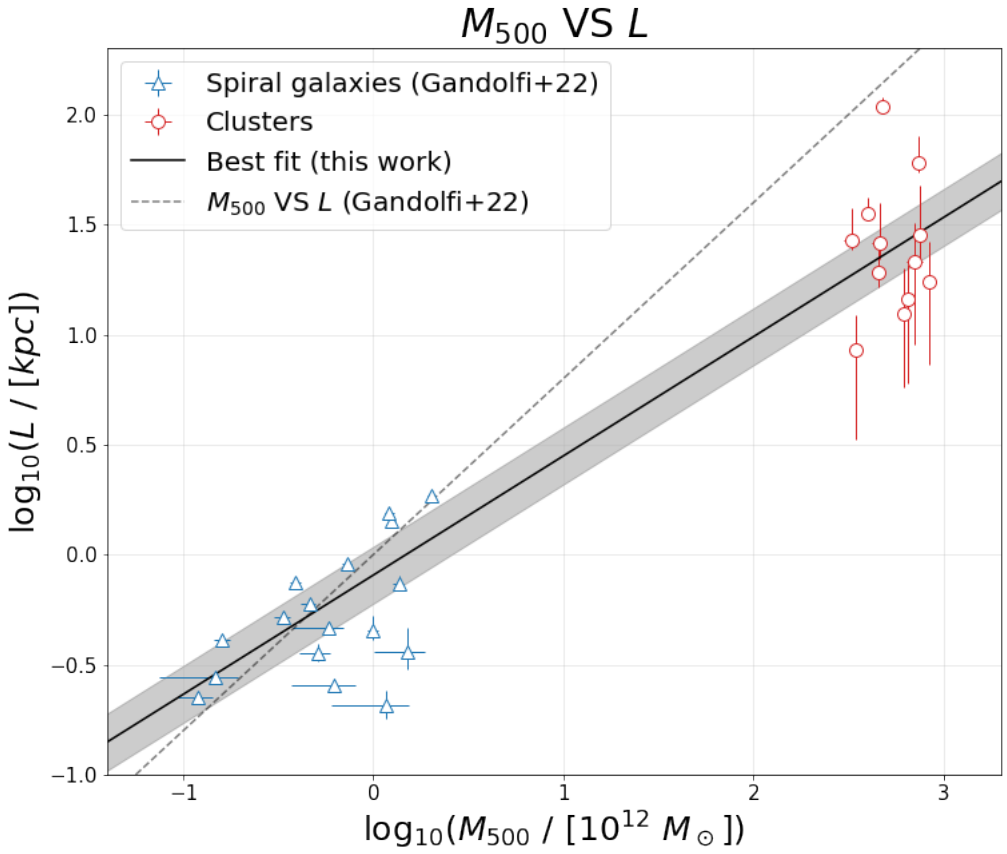

Figure 3.20: Virial mass (M_{500}) vs. L relation. Blue triangles are the same spiral galaxies data utilised in Sec. (3.4.1). Red circles represent the X-COP cluster measurements found in the Bayesian MCMC analysis hereby exploited. The best-fit power-law coincides with the black solid line, whereas the shaded grey area represents a one-sigma confidence interval. The grey dashed line represents the M_{500} VS L relation found in Sec. (3.4.1) and exploited in Sec. (3.4.2) to obtain the results therein. Note that the virial masses of spirals and their errors are rescaled to M_{500} (i.e., a mass at which the interior mean density is 500 times the critical density of the Universe) since they were originally computed as M_{200} (i.e., a mass at which the interior mean density is 200 times the critical density of the Universe).

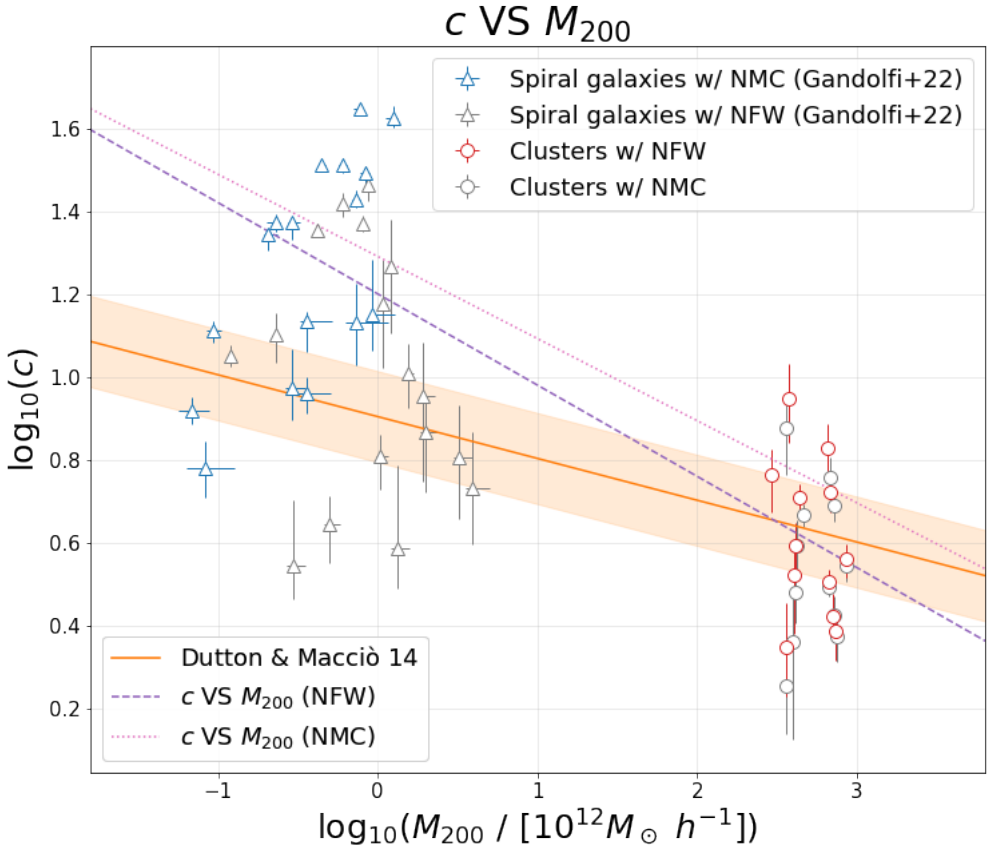

Figure 3.21: Concentration VS virial mass relation. Grey triangles and grey circles are spiral galaxies analysed in Sec. (3.4.1), and X-COP clusters' data were obtained with the NFW model. Blue triangles and red circles represent the retrieved values assuming the NMC DM model. The orange solid line represents the relation by Dutton & Macciò (2014) featuring a lognormal scatter of 0.11 dex represented by the orange area around the line. The purple dashed line and the pink dashed lines represent the c_{200} VS M_{200} relations, respectively, found for the NFW model and the NMC DM model. Note that the cluster virial masses (M_{500}) and their errors have been downscaled to M_{200} to make them comparable to the Dutton & Macciò (2014) relation.

3.6 Conclusions and future perspectives

3.6.1 NMC DM's key results

In this Chapter, I introduced a model that involves a non-minimal coupling (NMC) between cold dark matter (CDM) and gravity originally proposed in Bruneton et al. (2009); Bettoni et al. (2014); Bettoni & Liberati (2015). On cosmological scales, this model reduces to a standard CDM scenario. However, when examining galactic or galaxy cluster scales, the NMC enhances our understanding of DM and resolves some of the issues that the CDM paradigm faces on these scales. Here, I recap the primary findings of this analysis.

- NMC DM haloes exhibit internal structures characterised by cored profiles, resembling the Burkert phenomenological profile up to the typical scale radii probed by observations (Sec. (3.2.3));
- These cores align with the observed constancy of core surface density in dwarf galaxies detailed in Salucci & Burkert (2000) and Burkert (2015) (Sec. (3.2.5));
- The NMC DM model consistently provides better fits to the stacked RCs of late-type galaxies, spanning from dwarfs to massive spirals, compared to the NFW profile in terms of reduced chi-square values. These fits are always comparable to the Burkert profile ones and always return realistic values for the DM haloes' concentrations and virial masses (Sec. (3.2.4), Sec. (3.4.1));
- The analysis of RCs reveals a scaling relationship between the scale length associated with NMC and the virial mass of DM haloes, approximated by a simple power-law (Sec. (3.4.1));
- The model effectively describes the thermal pressure profiles of galaxy clusters, affirming a correlation between the NMC scale length (L) and the virial mass of DM haloes, extending beyond the range of virial masses subtended by galactic structures (Sec. (3.5.2));
- The mass scaling derived from fitting galaxy RCs and analysing pressure profiles of galaxy clusters reproduces the Radial Acceleration Relation (RAR in galaxies, even for dwarf spheroidals (Sec. (3.5.3)).

In summary, the NMC DM model discussed here is a straightforward and theoretically motivated model that addresses long-standing issues within the CDM paradigm. This model depends on a single free parameter, the NMC lengthscale (L). Such lengthscale exhibits a simple scaling law with the halo's virial mass, approximable by a power-law. Finally, this model is not necessarily a modified gravity theory since several possible physical mechanisms could easily explain the emergence of this NMC in virialised structures (see Sec. (3.1.3)).

3.6.2 Future perspectives

The future developments of the NMC DM model encompass various aspects, which are elaborated below.

- The NMC DM model could be further tested to fit the projected velocity dispersion profiles of dwarf spheroidal galaxies, assessing if the NMC is active and, if so, checking whether the inferred values of L comply with the observed power-law trend with the virial mass of DM haloes and if these galaxies comply with the RAR;
- One could test the capability of the NMC DM model to reproduce Milky Way's RC built with high-precision astrometric data from GAIA (Chrobáková et al. 2020; Wang et al. 2023). Indeed, this analysis could tighten even further the constraints on the NMC lengthscale L. Knowing the value of L for our galaxy could also provide hints if the NMC could be constrained with Solar System tests;
- After a theoretical development, the effects of the NMC on strong gravitational lensing effects could be tested empirically, e.g., by assessing if NMC DM haloes may reproduce the observed Einstein radii of known lenses (e.g., Shevchuk et al. 2023);
- The current static investigation could be expanded to include dynamic conditions. This will involve the incorporation of the NMC within full N-body numerical simulations to understand the role of this effect in structure formation. As conjectured in Bettoni et al. (2012), a repulsive NMC would generate a pressure term for the DM component able to reduce the growth of structures at galactic scales. By quantifying the dependence of this suppression on model parameters, it may be possible to obtain new constraints for NMC DM from comparisons between simulations and observational data;
- To further validate the NMC DM analysis on cluster scales, a potential future step would involve using data from well-characterised galaxy clusters at smaller radii. This could include data from collaborations such as CLASH (Cluster Lensing and Supernova survey with Hubble; Umetsu et al. 2016). These observations would probe the regions where the influence of the NMC is particularly significant, greatly enhancing the constraints on the lengthscale L derived from the X-COP clusters analysis;
- Colliding galaxy clusters could serve as promising systems for studying the NMC DM model, similar to what has been done, e.g., in SIDM scenarios (Kahlhoefer et al. 2014). In the NMC model, the total gravitational potential given by Eq. (3.10) depends on the Laplacian of the DM density. Hence, the effects of the NMC could be particularly pronounced in regions where the density of DM changes significantly, e.g., due to the merger of the haloes. Moreover, the repulsive nature of the NMC could be relevant at the collision interface, potentially slowing down the merger process;

- If a repulsive NMC of this kind was active also on large cosmological scales, it could produce a DE-like effect. Bettoni et al. (2012) shows that a DM fluid forming BECs at suitably late cosmological time and developing an NMC with gravity would behave as the superposition of two fluids: one standard pressureless dust plus a fluid that behaves like a cosmological constant term. A first step in this sense would be to study the Strong Energy Condition for the total SET appearing in Eq. (3.8) to asses if the NMC can source a repulsive effect counteracting the attractive pull of matter. Subsequently, it would be interesting to constrain such cosmological NMC utilising type Ia SN data, CMB's first-peak angular scale, BAO's temperature spectrum measurements and estimates of the Universe's age inferred from cosmic chronometers and globular clusters;
- Once the phenomenology of the model is soundly characterised and enough data are collected, an interesting extension of this work would involve pinpointing the exact mechanism that gives rise to this NMC between DM and gravity. Such a physical mechanism should be able to explain the observed power-law relationship between the NMC length scale L and the virial mass of structures.

The model introduced in this Chapter is a possible addition to the alternative DM scenarios detailed in Sec. (2.2). Yet, beyond the creation and assessment of novel models, it is equally crucial to formulate techniques for distinguishing among established paradigms, particularly with state-of-the-art observations from instruments like the James Webb Space Telescope. This is precisely the objective of the upcoming Chapter.

Chapter 4

Dark Matter Astroparticle Constraints with JWST

4.1 Understanding dark matter through JWST high-z observations

Equipped with an unprecedented mix of sensitivity and resolution, the James Webb Space Telescope (JWST) could revolutionise our knowledge of the high-redshift ($z > 6$) Universe and, ultimately, the nature of the dark Universe itself. Its primary imager, called Near Infrared Camera (NIRCam), has a resolution reaching 0.07 arcsec at 2 microns and, observing in the near-infrared part of the spectrum, covers wavelengths longward than the Hubble Space Telescope's (HST) cutoff. In its first year of activity, JWST was able to peek into the early Universe by identifying a population of galaxies at redshift $z > 11$ (Naidu et al. 2022a,b; Castellano et al. 2022; Adams et al. 2023; Donnan et al. 2023; Morishita & Stiavelli 2023; Finkelstein et al. 2023; Atek et al. 2023a,b; Yan et al. 2023; Rodighiero et al. 2023). These early observations, partially complemented by Near Infrared Spectrograph (NIRSpec) ones, confirmed the presence of galaxies up to $z \sim 13.20$ (Robertson et al. 2023). And surprisingly, some of these galaxies discovered at high-z by JWST seemingly call into question the current cosmological model — ΛCDM.

4.1.1 Are JWST high-z observations in tension with ΛCDM?

During its first year of activity, JWST has shown its capabilities to question what we know about the formation of cosmic structures. Indeed, some high-redshift galaxy candidates discovered by JWST have raised concerns about their consistency with galaxy formation in the standard ΛCDM cosmological model, showing unexpectedly high stellar masses (Boylan-Kolchin 2023; Labbé et al. 2023). In the standard ΛCDM picture, the available baryonic reservoir of the host DM halo sets limits to the stellar mass of a galaxy; thus, the mass function of DM haloes imposes an absolute upper limit on the number density and stellar mass density expected at any redshift. The recent literature discusses how the most massive galaxy candidates in JWST observations at $z \sim 7 - 10$ lie at the edge of the mass

limits predicted by the ΛCDM paradigm (e.g., Boylan-Kolchin 2023). This tension could indicate a critical unresolved issue on how galaxies form at early times in ΛCDM. Some authors took this as proof that the ΛCDM paradigm possibly needs to be rewritten, and the presence of such massive objects so early in the Universe's history could hint at new physics beyond this standard framework (e.g., Dolgov 2023; Deliduman et al. 2023; Gupta 2023; Adil et al. 2023). However, before radically rewriting part of the known physics, an essential step is to ask how reliable these early estimates carried out by JWST are.

On the one hand, JWST has opened an unprecedented window into a previously unknown part of the Universe. This offers new, exciting possibilities — but also calls for some caution. The most successful tool for identifying ultra-high-redshift candidates and inferring their properties (such as their stellar mass and star formation rates) is photometric template fitting, a technique in which one or more codes are used to compare a series of model spectral templates against the observed photometry. From this comparison, the redshift and properties of the observed galaxies are inferred from the best-fit models (either under a frequentist chi-squared minimisation or a Bayesian likelihood approach). Most of these models consist of synthetic templates derived from local Universe conditions, either theoretically disallowed or observationally disproven for galaxies at ultra-high redshift. For example, many current stellar population templates return ages surpassing the age of the Universe at $z \sim 12$ (Brammer et al. 2008), while, at those redshifts, the stellar population cannot be more than a few hundred Myr old. Moreover, a central assumption common to all current templates is a universal stellar IMF, assumed to coincide with the current Milky Way one. A proper choice of the IMF may be crucial to understanding the properties of galaxies. In fact, the light emitted by a galaxy is dominated by the most massive stars, which comprise only a tiny fraction of the stellar mass — the IMF is therefore necessary to infer the contribution of the remaining stellar population from that high-mass tail. The IMF should depend upon several properties of star-forming molecular clouds, including gas temperature and metallicity, quantities varying wildly as we delve into the early Universe, favouring bottom-lighter IMFs (Steinhardt et al. 2023). Moreover, none of the local strong-line metallicity calibrations seems to provide a good prediction of the observed metallicities at $z > 7.5$ (Curti et al. 2023). Hence, new templates for the photometric analysis of high-z galaxies must be developed to derive their physical properties accurately (this was recently done in Larson et al. 2022 and Steinhardt et al. 2023).

Furthermore, preliminary photometry of many JWST high-redshift galaxy candidates is carried out on NIRCam data, sometimes complemented where available by Mid-Infrared Instrument (MIRI) observations. This process, therefore, samples only a part of the near/mid-infrared emission of each galaxy and could make some of their properties unconstrained and unreliable. For example, the reddening of a galaxy can be determined by a degeneracy between its redshift and its dust content, which absorbs starlight in the UV/visible band, reprocessing and re-emitting it in the far infrared/sub-mm part of the spectrum. In order to break these degeneracies, it is thus necessary to adopt a multiband observational approach, sampling the spectral energy distribution (SED) of galaxies in bands

ranging beyond near/mid-infrared and constraining their properties properly. Working in synergy with other facilities such as the Atacama Large Millimeter Array (ALMA), JWST has demonstrated its importance in characterising objects from the early Universe (e.g., Bakx et al. 2023; Fujimoto et al. 2023).

Another technique that ensures a precise determination of the physical characteristics of galaxies is spectroscopy. Indeed, spectroscopic observations of some photometric high-z massive early galaxies found with JWST that seemed to defy the ΛCDM paradigm revealed that these objects were, in fact, lower-redshift contaminants (e.g., Kocevski et al. 2023; Arrabal Haro et al. 2023). All this shows the potential of JWST to test the current cosmological model and our knowledge about the dark Universe and cosmic structure formation. However, it demonstrates also that to carry out this investigation, a detailed knowledge of the possible issues and systematics of data analysis and what the best observation strategies are is essential.

While the nature of high-redshift galaxies ranging from the end of the epoch of reionisation up to earlier cosmic times begins to be carefully determined, it is possible to formulate constraints on how JWST high-z observations targeting faint galaxies can broaden our knowledge of the astroparticle characteristics of DM. In the following sections, I will show a method to constrain the properties of DM based on the analysis of the cosmic star-formation rate (cSFR) density of high-redshift galaxies, discussing the impact of JWST observations on such constraints. As will be shown, JWST could discriminate and possibly rule out various alternative DM models to the pure CDM picture as the ones detailed in Sec. (2.2).

4.2 DM constraints from the cosmic SFR density at high redshift

This section will discuss the constraints to DM that can be derived from recent observations of the cSFR density at high redshift (e.g., Oesch et al. 2018; Bouwens et al. 2021, 2022; Harikane et al. 2023). This observable crucially depends on the number density of ultra-faint galaxies, which tend to live within small DM halos, especially at high redshifts. Thus, their numbers can constrain the low-mass end shapes of the HMF and the power spectrum, which is sensitive to the microscopic properties of the DM particles. With respect to other probes of DM exploited in the literature, the cSFR density is a very basic astrophysical quantity that suffers less from observational, systematic and modelling uncertainties. The work detailed in this Section was originally presented in Gandolfi et al. (2022b).

4.2.1 UV luminosity function from HST and JWST

To begin with, the recent determinations of the UV luminosity functions by Oesch et al. (2018) and Bouwens et al. (2021) out to redshift $z \sim 10$ and UV magnitudes $M_{\rm UV} \lesssim -17$ are considered. Fig. (4.1) illustrates the binned luminosity functions (filled circles) at ≈ 1600 Å in the relevant redshift range $z \sim 6-10$ (colour-coded),

together with the corresponding continuous Schechter function rendition (solid lines) in the form

$$\frac{\mathrm{d}N}{\mathrm{d}M_{\mathrm{UV}}\,\mathrm{d}V} = \phi^{\star}\,\frac{\ln(10)}{2.5}\,10^{-0.4\,(M_{\mathrm{UV}}-M^{\star}_{\mathrm{UV}})\,(\alpha+1)} \times e^{-10^{-0.4\,(M_{\mathrm{UV}}-M^{\star}_{\mathrm{UV}})}}. \tag{4.1}$$

The evolution with redshift of the parameters entering Eq. (4.1) is characterised according to the expressions by Bouwens et al. (2021, 2022). Toward high z, these yield a steepening faint end-slope $\alpha \approx -1.95 - 0.11\,(z-6)$, an approximately constant characteristic magnitude $M^{\star}_{\mathrm{UV}} \approx -21.04 - 0.05\,(z-6)$ and an appreciably decreasing normalization $\phi^{\star} \approx 3.8 \times 10^{-4-0.35\,(z-6)-0.027\,(z-6)^2}$ Mpc^{-3}. Fig. (4.1) depicts the intrinsic luminosity functions after correction for dust extinction (dotted lines), which have been computed exploiting the relation between extinction, the slope of the UV spectrum, and observed UV magnitude by Meurer et al. (1999); Bouwens et al. (2014). The effects of dust extinction on the UV luminosity function are minor for $M_{\mathrm{UV}} \gtrsim -17$ and will be irrelevant for this analysis. The intrinsic UV luminosity can be related to the physical SFR of galaxies. In particular, for a Chabrier IMF, age $\gtrsim 10^8$ years, and appreciably sub-solar metallicity the relation $\log \mathrm{SFR}\,[\mathrm{M}_{\odot}\,\mathrm{yr}^{-1}] \approx -0.4\,(M_{\mathrm{UV}}+18.5)$ holds (see Kennicutt & Evans 2012; Madau & Dickinson 2014; Cai et al. 2014; Robertson et al. 2015; Finkelstein et al. 2019). The related values are reported on the top axis in Fig. (4.1).

Fig. (4.1) also contains two other datasets. The first one (open circles) is from Bouwens et al. (2022), which has been able to estimate the luminosity function down to $M_{\mathrm{UV}} \approx -12.5$ by exploiting gravitational lensed galaxies in the Hubble Frontier Field clusters. However, the sample is characterised by a paucity of detected sources, resulting in considerable statistical uncertainties. Moreover, possible systematics in the lensing reconstruction and completeness issues do not yet allow one to draw firm conclusions on the shape of the luminosity function at such ultra-faint magnitudes. The second set of data (filled squares) involves the early results from JWST by Harikane et al. (2023), which have provided an estimate of the luminosity function at $z \gtrsim 12$, though with relatively low statistics. Interestingly, at $z \sim 12$, the shape of the luminosity function is roughly consistent with the lower redshift estimates, though its evolution in normalisation considerably slows down. More data are needed to confirm such a trend, which could be very relevant for the astroparticle constraints of this analysis, as it will become clear shortly.

From the intrinsic UV luminosity functions, the cosmic SFR density can be computed as

$$\rho_{\mathrm{SFR}}(z) = \int_{-\infty}^{\min[M^{\mathrm{obs}}_{\mathrm{UV}},M^{\mathrm{lim}}_{\mathrm{UV}}]} \mathrm{d}M_{\mathrm{UV}}\,\frac{\mathrm{d}N}{\mathrm{d}M_{\mathrm{UV}}\,\mathrm{d}V}\,\mathrm{SFR}\,, \tag{4.2}$$

where $M^{\mathrm{obs}}_{\mathrm{UV}}$ is the faintest limit probed by observations (e.g., $M_{\mathrm{UV}} \approx -13$ for Bouwens et al. (2022), or ≈ -17 for Harikane et al. (2023)), and $M^{\mathrm{lim}}_{\mathrm{UV}}$ represents a limiting magnitude down to which the luminosity function is steeply increasing. Hence, here, the SFR density contributed by magnitudes $M_{\mathrm{UV}} \gtrsim M^{\mathrm{lim}}_{\mathrm{UV}}$ fainter than such a limit is negligible. The quantity $M^{\mathrm{lim}}_{\mathrm{UV}}$ is somewhat uncertain: as mentioned

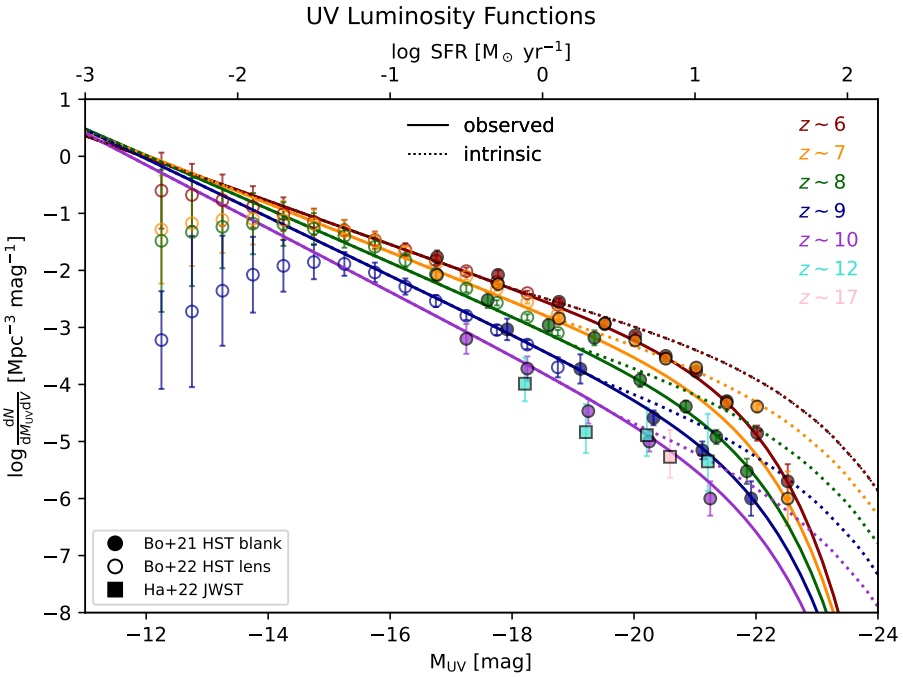

Figure 4.1: The UV luminosity functions at redshifts $z \sim 6$ (red), $z \sim 7$ (orange), $z \sim 8$ (green), $z \sim 9$ (blue), $z \sim 10$ (magenta), $z \sim 12$ (cyan) and $z \sim 17$ (pink). Data points are from Oesch et al. (2018) and Bouwens et al. (2021) (filled circles), Bouwens et al. (2022) (empty circles), and Harikane et al. (2023) (squares). Coloured lines illustrate Schechter fits to the blank-field measurements from Bouwens et al. (2021): solid lines refer to the observed luminosity functions, while dotted lines to the intrinsic ones, after correction for dust extinction via the UV continuum slope according to the procedure by Bouwens et al. (2014).

above, the most recent and stringent constraints are from the analysis by Bouwens et al. (2022), which rules out the presence of a turnover in the luminosity function brightward of $M_{\rm UV} \sim -15.5$. The data by Bouwens et al. (2022) seem to suggest a possible flattening of the luminosity function for $M_{\rm UV} \gtrsim -15$, but the large errors and the systematic uncertainties due to the paucity of sources as well as incompleteness issues do not allow to make robust conclusions. Thus, in the following, there will not be any attempt to model the detailed shape of any possible bending. The extrapolation of the steep Schechter fits to the data by Bouwens et al. (2021) with a sharp limit at $M_{\rm UV}^{\rm lim}$ [1] will instead be used.

The rationale is that at magnitudes fainter than $M_{\rm UV}^{\rm lim}$, the luminosity function flattens or even bends downwards because the galaxy formation process becomes inefficient and/or because the power spectrum is cut off due to the microscopic nature of DM. Such a magnitude limit is connected to two parameters describing these effects: a threshold halo mass $M_{\rm H}^{\rm GF}$ below which galaxy formation is hindered because of various processes, like photo-suppression by the intense UV background or inefficiency in atomic cooling by the low temperature and metallicity of small halos at high redshift (see Efstathiou (1992); Sobacchi & Mesinger (2013); Finkelstein et al. (2019)); and astroparticle properties X specific of a given DM scenario (e.g., WDM mass), that characterises the suppression of the power spectrum at small scales.

4.2.2 Halo mass function and abundance matching

Here, three common non-standard DM scenarios alternative to CDM are considered: WDM, ψDM, and SIDM (see Sec. (2.2)). In all these scenarios, the number of small-mass halos is reduced relative to CDM. This is best specified in terms of the HMF, which can be conveniently written in terms of the CDM one as

$$\frac{{\rm d}N}{{\rm d}M_{\rm H}\,{\rm d}V} = \frac{{\rm d}N_{\rm CDM}}{{\rm d}M_{\rm H}\,{\rm d}V}\left[1+\left(\frac{M_{\rm H}^{\rm cut}}{M_{\rm H}}\right)^{\beta}\right]^{-\gamma}\,, \tag{4.3}$$

where $M_{\rm H}$ is the DM halo mass, β and γ are shape parameters, and $M_{\rm H}^{\rm cut}$ is a cutoff halo mass. The CDM halo mass function is computed by exploiting the Python `COLOSSUS` package Diemer (2018) and the fitting formula by Tinker et al. (2008) for virial masses. The parameters (β, γ) in Eq. (4.3) are instead derived from fits to the outcomes of numerical simulations in the considered DM scenarios. The related values of such parameters and the literature works from which these are taken (Schneider et al. 2012; Schive et al. 2016; Huo et al. 2018) are reported in Tab. (4.1). In order to derive robust constraints on different DM scenarios based on the HMF, it is essential to rely on the results from detailed simulations (as done here) and not on semi-analytic derivations based on the excursion set formalism,

[1] In fact, one can easily adopt a smooth bending of the luminosity function and set instead the upper limit of integration in Eq. (4.2) just to $M_{\rm UV}^{\rm obs}$. E.g., Bouwens et al. (2022) empirically suggest to multiply Eq. (4.1) by a factor $10^{0.4\,(\alpha+1)/2\times(M_{\rm UV}+16)^2/(M_{\rm UV}^{\rm lim}+16)}$ for $M_{\rm UV} \gtrsim -16$. In the computation of the cosmic SFR, this produces practically indistinguishable results from our simple treatment.

Table 4.1: Parameters describing the ratio of the HMF for different DM scenarios relative to the standard CDM in terms of the expression $[1+(M_{\rm H}^{\rm cut}/M_{\rm H})^{\beta}]^{-\gamma}$, where $M_{\rm H}$ is the halo mass and $M_{\rm H}^{\rm cut}$ is a characteristic cutoff scale. The values of the parameters (β, γ), extracted from fits to the outcomes of numerical simulations in the considered DM scenarios, are taken from the literature studies referenced in the last column.

Scenario	β	γ	Ref.
WDM	1.0	1.16	Schneider et al. (2012)
ψDM	1.1	2.2	Schive et al. (2016)
SIDM	1.0	1.34	Huo et al. (2018)

whose outcomes on the shape of the mass function for masses $M_{\rm H} \lesssim M_{\rm H}^{\rm cut}$ are rather sensitive to several assumptions (e.g., the filter function used in deriving the mass variance from the power spectrum, the mass-dependence in the collapse barrier, etc.; see Schneider et al. 2013; Lapi & Danese 2015; May & Springel 2023).

In the WDM model, the cutoff mass $M_{\rm H}^{\rm cut}$ is determined by free streaming effects (Schneider et al. 2012; see Sec. (2.2.2) and reads $M_{\rm H}^{\rm cut} \approx 1.9\times10^{10}$ $\mathrm{M}_\odot\,(m_X/\mathrm{keV})^{-3.33}$, where m_X indicates the particle's mass. However, note that this cutoff (or *half-mode*) mass is substantially larger by factors of a few 10^3 than the mass related to the typical scalelength for the diffusion of WDM particles out of primordial perturbations, i.e., the free streaming mass. In ψDM, $M_{\rm H}^{\rm cut} \approx 1.6\times10^{10}$ $\mathrm{M}_\odot\ (m_X/10^{-22}\,\mathrm{eV})^{-1.33}$ is related to the coherent behaviour of the particles with mass m_X (Schive et al. 2016). In the SIDM scenario, $M_{\rm H}^{\rm cut} \approx 7\times10^{7}$ $\mathrm{M}_\odot\,(T_X/\mathrm{keV})^{-3}$ can be linked to the visible sector temperature T_X when kinetic decoupling of the DM particles takes place (Huo et al. 2018).

Fig. (4.2) illustrates the HMF in the different DM scenarios at a reference redshift $z \approx 10$ to highlight the dependence on the particle property. For WDM, it is seen that the HMF progressively flattens to that in standard CDM (black line). Such deviation occurs at smaller halo masses for higher WDM particle masses m_X, and the CDM behaviour is recovered for $m_X \to \infty$. In the other DM scenarios the behaviour is similar. Yet, the HMF's shape past the low-mass end flattening can be appreciably different. For example, in the ψDM scenario, the HMF is strongly suppressed for small masses and bends downward rather than flattening, implying a solid reduction or even an absence of low-mass halos.

It is crucial to characterise the relationship between UV magnitudes and halo masses. To do so, a standard abundance matching technique (Aversa et al. 2015; Moster et al. 2018; Cristofari & Ostriker 2019; Behroozi et al. 2019) can be exploited, i.e., matching the cumulative number densities in galaxies and halos according to the expression

$$\int_{M_{\rm H}}^{+\infty} \mathrm{d}M'_{\rm H}\,\frac{\mathrm{d}N}{\mathrm{d}M'_{\rm H}\,\mathrm{d}V}(M'_{\rm H}, z|X) = \int_{-\infty}^{M_{\rm UV}} \mathrm{d}M'_{\rm UV}\,\frac{\mathrm{d}N}{\mathrm{d}M'_{\rm UV}\,\mathrm{d}V},(M'_{\rm UV}, z) \qquad (4.4)$$

which implicitly defines a one-to-one monotonic relationship $M_{\rm UV}(M_{\rm H}, z|X)$. Here the quantity X stands for the specific property of the DM scenario that de-

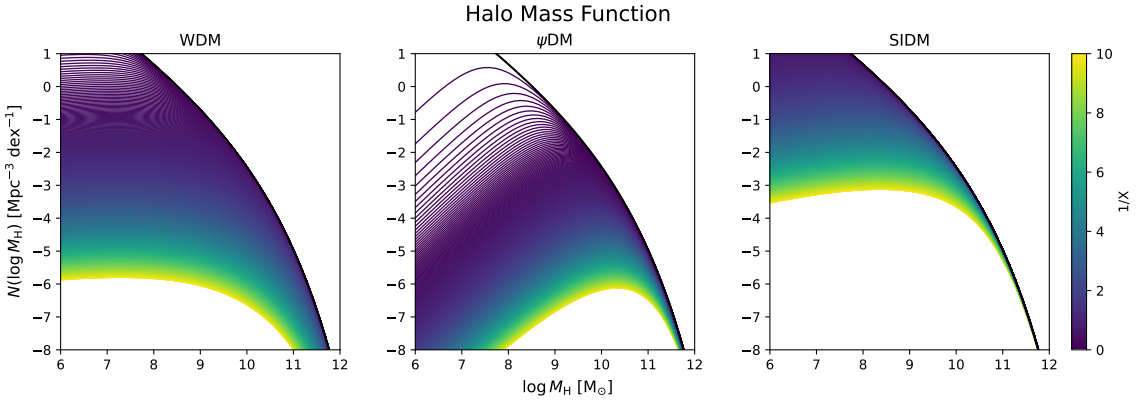

Figure 4.2: HMF at a reference redshift $z \approx 10$ in different DM scenarios: WDM (left panel), ψDM (middle panel) and SIDM (right panel). The colorbar refers to values of keV/m_X for WDM, 10^{-22} eV/m_X for ψDM and keV/T_X for SIDM. In all panels, the black line refers to the standard CDM scenario.

termines the behaviour of the HMF for $M_{\rm H} \lesssim M_{\rm H}^{\rm cut}$: particle mass m_X in keV for WDM and in 10^{-22} eV for ψDM, and kinetic temperature T_X in keV for SIDM. Fig. (4.3) shows the outcome of this procedure at a reference redshift $z \approx 10$ in the different DM scenarios, highlighting its dependence on the particle property. Focusing on WDM as a representative case, it is seen that the $M_{\rm UV}(M_{\rm H}, z|m_x)$ relation progressively flattens toward small $M_{\rm H}$ to the standard CDM case, and especially so for smaller m_X. At the other end, the relation becomes indistinguishable from CDM's for particle masses $m_X \gtrsim$ some keVs. At a given particle mass, the relation $M_{\rm H}(M_{\rm UV}, z|m_X)$ barely depends on redshift $z \gtrsim 6$. This is because the cosmic evolution of the UV luminosity function and the halo mass function mirror each other (see discussion by Bouwens et al. 2021). In the other DM scenarios, the behaviour of the $M_{\rm UV}(M_{\rm H}, z|X)$ relation is similar, but its shape for small halo masses is appreciably different. In the ψDM scenario, for example, the relation flattens abruptly, reflecting the paucity of small halos in the HMF (see Fig. (4.2)).

The rationale is now to compute the cosmic SFR density $\rho_{\rm SFR}(z)$ according to Eq. (4.2) by integrating the luminosity function down to a magnitude limit $M_{\rm UV}^{\rm lim}(M_{\rm H}^{\rm GF}, z|X)$. This limiting magnitude depends on two parameters, namely the minimum halo mass for galaxy formation $M_{\rm H}^{\rm GF}$ and the astroparticle properties X of a given DM scenario. The aim is to estimate these quantities by comparing $\rho_{\rm SFR}(z)$ with the observational determinations.

4.2.3 Bayesian analysis

The descriptions provided in Sec. (4.2.2) highlight that the limiting UV magnitude $M_{\rm UV}^{\rm lim}$ depends on two parameters: the limiting halo mass for galaxy formation $M_{\rm H}^{\rm GF}$, and a quantity X specific to the DM scenario. Such quantity coincides with the particle mass m_X in units of keV for WDM, the particle mass m_X in units of 10^{-22} eV for ψDM, and the temperature of kinetic decoupling T_X in units of keV for SIDM. These two parameters effectively encompass various effects determining

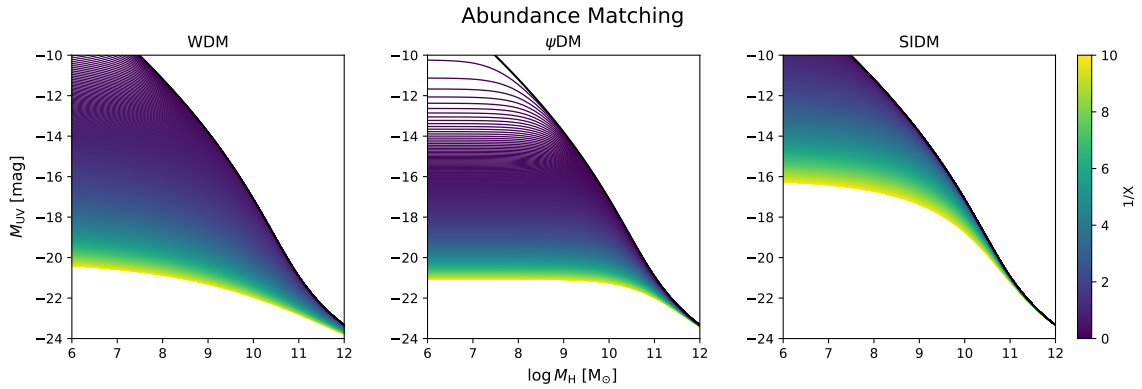

Figure 4.3: Relationship between the UV magnitude $M_{\rm UV}$ and the halo mass $M_{\rm H}$ at a reference redshift $z \approx 10$, derived from the abundance matching of the observed UV luminosity function and the HMF in different DM scenarios: WDM (left panel), ψDM (middle panel) and SIDM (right panel). The colorbar refers to values of keV/m_X for WDM, 10^{-22} eV/m_X for ψDM and keV/T_X for SIDM. In all panels, the black line refers to the standard CDM scenario.

$M_{\rm UV}^{\rm lim}$. Such effects are related to the efficiency of galaxy formation processes in small halos and the suppression in the number of low-mass halos due to the microscopic nature of DM. An added value of the empirical approach pursued here, which relies on extrapolation of the observed UV luminosity functions down to $M_{\rm UV}^{\rm lim}$, is that no further parameter is needed to predict the cosmic SFR density (besides the underlying assumption of an IMF, that in any case marginally affects the astroparticle constraints, as shown by Lapi et al. 2022).

A Bayesian MCMC framework is exploited to estimate the two parameters described above, relying on the Python package `emcee`. For large values of X, all the outcomes of the non-standard scenarios converge toward CDM. Hence, it is convenient to look for an estimate of $1/X$ instead of X to have a fitting parameter varying in a compact domain. This analysis exploits a standard Gaussian likelihood $\mathcal{L}(\theta) \equiv -\sum_i \chi_i^2(\theta)/2$, where $\theta = \{M_{\rm H}^{\rm GF}, 1/X\}$ is the vector of parameters, and the summation is over different datasets. The corresponding $\chi_i^2 = \sum_j [\mathcal{M}(z_j,\theta) - \mathcal{D}(z_j)]^2/\sigma_{\mathcal{D}}^2(z_j)$ is obtained by comparing the empirical model expectations $\mathcal{M}(z_j,\theta)$ to the data $\mathcal{D}(z_j)$ with their uncertainties $\sigma_{\mathcal{D}}^2(z_j)$, summing over the different redshifts z_j of the data points. Specifically, the overall data sample is constituted by robust measurements of the cosmic SFR density (see summary in Table 4.2) from UV luminosity function data from HST (Bouwens et al. 2022), UV luminosity function early data from JWST (Harikane et al. 2023), GRB counts data from Fermi (Kistler et al. 2009) and (sub)mm luminosity function data from ALMA (Gruppioni et al. 2020). The minimum observational magnitude limit $M_{\rm UV}^{\rm obs}$ of the different datasets is considered in the computation of the cSFR density.

Flat priors $\pi(\theta)$ are adopted on the parameters within the ranges $\log M_{\rm H}^{\rm GF}[M_\odot] \in [6, 11]$, and $1/X \in [0, 10]$. The posterior distribution $\mathcal{P}(\theta) \propto \mathcal{L}(\theta)\,\pi(\theta)$ is then sampled by running `emcee` with 10^4 steps and 200 walkers. Each walker is initialised with a random position uniformly sampled from the (flat) priors. After checking

Table 4.2: Overview of the estimate for the cSFR density considered in the Bayesian analysis of this work. Values and uncertainties refer to log SFR [$M_\odot$ yr^{-1}]. UV Luminosity Function (LF) HST data are from Oesch et al. (2018); Bouwens et al. (2021, 2022), UV LF JWST data from Harikane et al. (2023), GRB counts data from Kistler et al. (2009) and ALMA (sub)mm LF data from Gruppioni et al. (2020).

Data	Redshifts	Values	Uncertainties
UV LF [HST]	$\{3.8, 4.9, 5.9, 6.8, 7.9, 8.9, 10.4\}$	$\{-1.14, -1.4, -1.66, -1.85, -2.05, -2.61, -3.13\}$	$\{0.08, 0.07, 0.05, 0.06, 0.11, 0.11, 0.35\}$
UV LF [JWST]	$\{\sim 9, \sim 12, \sim 17\}$	$\{-2.90, -3.61, \lesssim -3.94\}$	$\{0.17, 0.27, 0.31\}$
GRB counts [Fermi]	$\{4.49, 5.49, 6.49, 7.74\}$	$\{-1.138, -1.423, -1.262, -1.508\}$	$\{0.184, 0.289, 0.359, 0.517\}$
(sub)mm LF [ALMA]	$\{4.00, 5.25\}$	$\{-1.218, -1.252\}$	$\{0.219, 0.612\}$

the auto-correlation time, the first 20% of the flattened chain is removed to ensure the burn-in. The typical acceptance fractions of the various runs are $30 - 40\%$.

4.2.4 Results and discussion

Firstly, the analysis is carried out in the standard CDM scenario. The result is shown by the grey contours/lines in Fig (4.4), Fig (4.5) and Fig (4.6). In the CDM model, the UV limiting magnitude $M_{\rm UV}^{\rm lim}$ depends by construction only on the threshold minimum halo mass for galaxy formation. The marginalised constraint on the latter is found to be $\log M_{\rm H}^{GF}[M_\odot] \approx 9.4^{+0.2\,(+0.4)}_{-0.1\,(-0.4)}$, a value which is reasonably close to the photo-suppression mass expected by the intense UV background during reionisation (e.g., Finkelstein et al. 2019). The corresponding limiting magnitude at $z \sim 10$ is around $M_{\rm UV}^{\rm lim} \approx -14.7$.

The situation differs in the other DM scenarios since the limiting UV magnitude can also depend on the DM astroparticle property X. The results for WDM are illustrated by the red lines/contours in Fig. (4.4). There is an evident degeneracy between the WDM mass m_X and the threshold halo mass $M_{\rm H}^{\rm GF}$ for galaxy formation. In fact, the exact value for the limiting UV magnitude $M_{\rm UV}^{\rm lim}$ can be obtained with smaller $M_{\rm H}^{\rm GF}$ and smaller m_X (see Fig. 4.3). This is because lowering $M_{\rm H}^{\rm GF}$ extends the HMF toward smaller masses; thus, more halos are available for hosting galaxies. Instead, decreasing m_X progressively flattens the shape of the HMF, reducing the number of halos and offsetting the previous effect. Such a situation is possible if m_X is not too low. Otherwise, the reduction in the halo number is so drastic that it cannot be compensated by reasonable values of $M_{\rm H}^{\rm GF}$. Note the minimally acceptable $M_{\rm H}^{\rm GF}$ could be around $10^{7-8}\,M_\odot$, because below

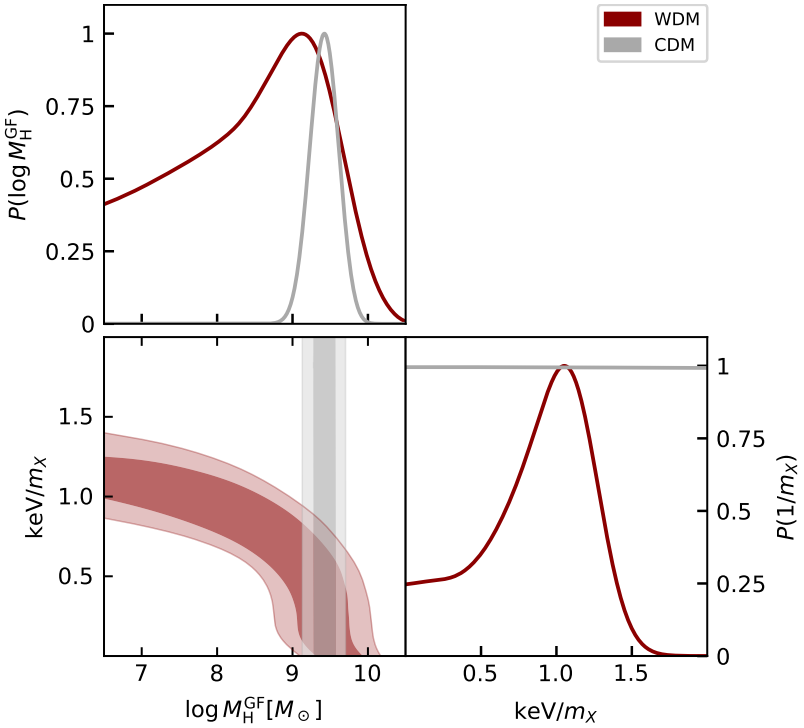

Figure 4.4: MCMC posterior distributions in the WDM scenario (red contours and lines), for the threshold halo mass for galaxy formation $M_{\rm H}^{\rm GF}$, and the inverse of the DM particle's mass keV/m_X. For reference, the outcomes in the standard CDM scenario are also reported (grey contours and lines). The contours show 68% and 95% confidence intervals, and the marginalised distributions are in arbitrary units (normalised to 1 at their maximum value).

these masses atomic cooling becomes inefficient. A hard limit is further set by minihalos of $10^6\,M_\odot$, where the first (pop-III) stars are thought to form.

The marginalized constraints for WDM turns out to be $\log M_{\rm H}^{GF}[M_\odot] \approx 7.6^{+2.2\,(+2.3)}_{-0.9\,(-3.3)}$ and $m_X \approx 1.2^{+0.3\,(11.3)}_{-0.4\,(-0.5)}$ keV, corresponding to a UV limiting magnitude $M_{\rm UV}^{\rm lim} \approx -13.3$. There is a clear peak in the posterior for the WDM mass around the keV scale, which is interesting because such a value has often been invoked to solve small-scale issues of CDM (see Sec. (2.2.2)). However, larger values of $m_X \gtrsim$ a few keVs that produce outcomes practically indistinguishable for CDM are still well allowed (within 2σ) by the current estimates of the cSFR density.

The situation for ψDM and SIDM is somewhat similar to WDM. The main difference resides in the behaviour of the HMF at small masses, which induces a different shape in the relationship between $M_{\rm H}$ and $M_{\rm UV}$, affecting the marginalised constraints.

ψDM's results are illustrated in Fig. (4.5), and only an upper limit of the threshold halo mass for galaxy formation $\log M_{\rm H}^{GF}[M_\odot] < 7.9\,(< 9.3)$ can be provided. However, the particle mass is constrained to $m_X \approx 3.7^{+1.8\,(+12.9.3)}_{-0.4\,(-0.5)} \times 10^{-22}$ eV, corresponding to a UV limiting magnitude $M_{\rm UV}^{\rm lim} \approx -14.6$ at $z \sim 10$. In the SIDM scenario, whose results are illustrated in Fig. (4.5), the marginalised constraints

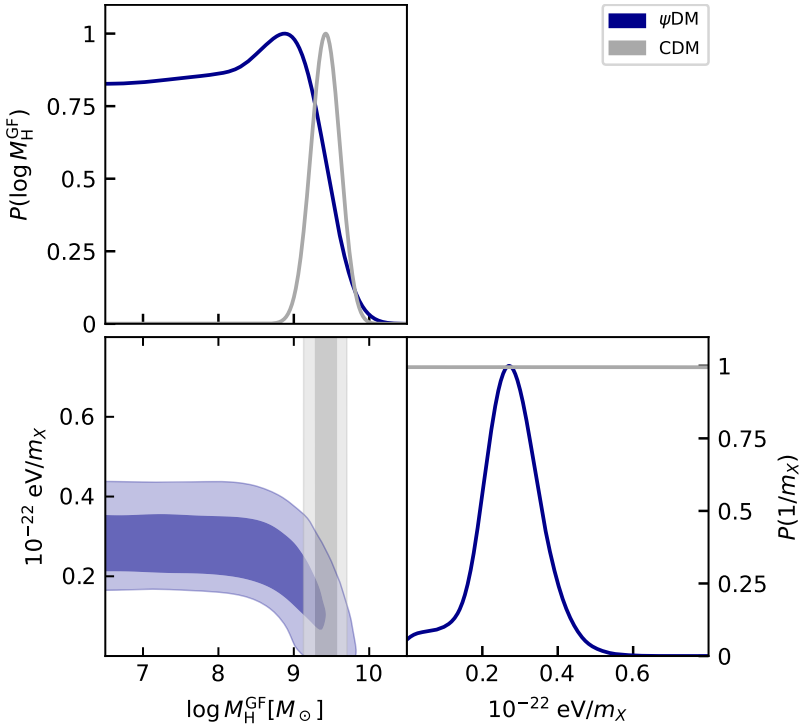

Figure 4.5: MCMC posterior distributions in the ψDM scenario (blue contours and lines) for the threshold halo mass for galaxy formation $M_{\rm H}^{\rm GF}$ and the inverse of the DM particle's mass 10^{-22} eV/m_X. For reference, the outcomes in the standard CDM scenario are also reported (grey contours and lines). The contours show 68% and 95% confidence intervals, and the marginalised distributions are in arbitrary units (normalised to 1 at their maximum value).

read $\log M_{\rm H}^{GF}[M_\odot] \approx 7.6^{+2.2\,(+2.3)}_{-1.1\,(-3.2)}$ and $T_X \approx 0.21^{+0.04\,(+1.8)}_{-0.06\,(-0.07)}$ keV, corresponding to a UV limiting magnitude $M_{\rm UV}^{\rm lim} \approx -13.7$ at $z \sim 10$. The overall marginalised constraints are summarised in Tab. (4.3).

Fig. (4.7) illustrates the performance of the best-fits on the observed cSFR density. All DM scenarios (coloured lines) reproduce comparably well with the available data. This is also highlighted by the 95% credible interval from sampling the posterior distribution, which is shown only in the WDM case for clarity (red shaded area). In terms of projection on this observable, different DM scenarios are consistent with each other, approximately within 2σ.

A quantitative model comparison analysis via the Bayes information criterion (Schwarz 1978; Liddle 2004) is performed, which is defined as BIC$\equiv -2\ln\mathcal{L}_{\rm max} + N_{\rm par}\ln N_{\rm data}$ in terms of the maximum likelihood estimate $\mathcal{L}_{\rm max}$, of the number of parameters $N_{\rm par}$, and the number of data points $N_{\rm data}$. The BIC comes from approximating the Bayes factor, which gives the posterior odds of one model against another, presuming that the models are equally favoured *a priori*. DIC, instead, is an indicator that may be less sensitive to priors (Spiegelhalter et al. 2002). It is defined as DIC$\equiv -2\log\mathcal{L}(\bar{\theta}) + 2\,p_D$, where the overbar denotes the mean and the effective number of parameters p_D is estimated as $p_D \approx -2\overline{\log\mathcal{L}(\theta)} - 2\log\mathcal{L}(\bar{\theta})$. Note that what matters is only the relative value of the BIC or the DIC

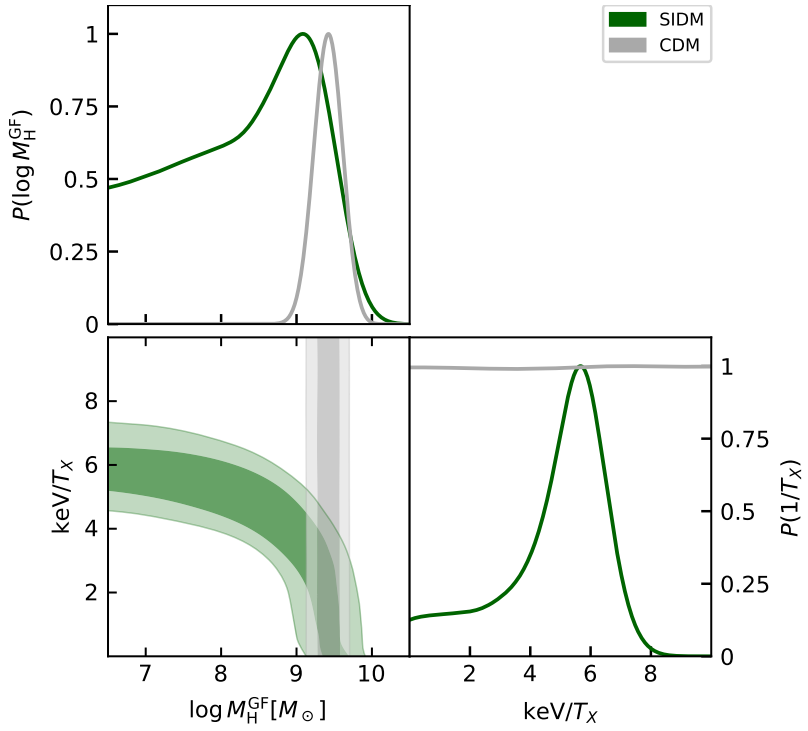

Figure 4.6: MCMC posterior distributions in the SIDM scenario (green contours and lines), for the threshold halo mass for galaxy formation $M_{\rm H}^{\rm GF}$, and the inverse of the DM kinetic temperature at decoupling keV/T_X. For reference, the outcomes in the standard CDM scenario are also reported (grey contours and lines). The contours show 68% and 95% confidence intervals, and the marginalised distributions are in arbitrary units (normalised to 1 at their maximum value).

Table 4.3: Marginalised posterior estimates (featuring the mean, 68% and 95% confidence limits) of the parameters from the MCMC analysis for the different DM scenarios considered (WDM, ψDM, and SIDM). Specifically, $M_{\rm H}^{\rm GF}$ is the threshold halo mass for galaxy formation, while the astroparticle quantity X in the third column stands for particle mass m_X in keV for WDM, particle mass m_X in 10^{-22} eV for ψDM, and kinetic temperature T_X in keV for SIDM. The last two columns refer to the value of the Bayes information criterion (BIC) and the Deviance information criterion (DIC) for model comparison (see Sec. (4.2.4)). The top half of the Table refers to the current constraints on the cSFR density, while the bottom half refers to the forecasts for JWST observations extended down to UV magnitude $M_{\rm UV} \approx -13$ (see Sec. (4.2.5)).

Scenario	M_H^{GF}	X	BIC	DIC
CDM	$9.4^{+0.2\,(+0.4)}_{-0.1\,(-0.4)}$	–	≈ 31	≈ 13
WDM	$7.6^{+2.2\,(+2.3)}_{-0.9\,(-3.3)}$	$1.2^{+0.3\,(+11.3)}_{-0.4\,(-0.5)}$	≈ 33	≈ 14
ψDM	$< 7.9\,(< 9.3)$	$3.7^{+1.8\,(+12.9)}_{-0.9\,(-1.4)}$	≈ 33	≈ 14
SIDM	$7.6^{+2.2\,(+2.3)}_{-1.1\,(-3.2)}$	$0.21^{+0.04\,(+1.8)}_{-0.06\,(-0.07)}$	≈ 33	≈ 14
CDM + JWST forecast	$< 7.2\,(< 8.5)$	–	≈ 89	≈ 130
WDM + JWST forecast	$< 6.6\,(< 8.2)$	$> 1.8\,(> 1.2)$	≈ 87	≈ 125
ψDM + JWST forecast	$6.2^{+1.3}_{-1.3}\,(< 8.2)$	$> 17.3\,(> 12)$	≈ 92	≈ 135
SIDM + JWST forecast	$< 6.8\,(< 8.3)$	$> 0.4\,(> 0.3)$	≈ 89	≈ 130

among different models. In particular, a difference larger than 10 indicates robust evidence favouring the model with the smaller value. The values of the BIC and the DIC (for the different DM scenarios) are reported in Tab. (4.3) and do not suggest clear evidence in favour of one scenario over the others or the standard CDM.

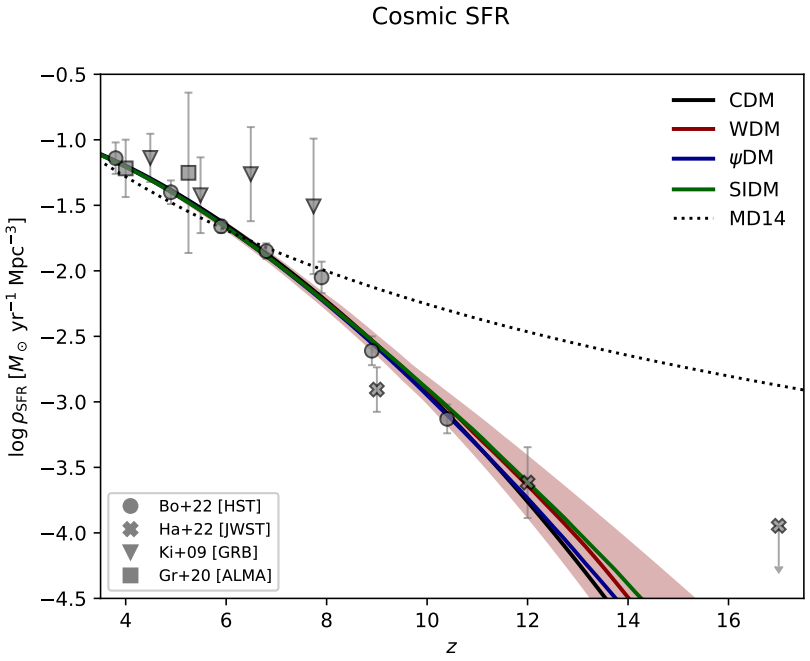

Figure 4.7: The cosmic SFR density as a function of redshift. UV HST data from Oesch et al. (2018); Bouwens et al. (2021) are represented by circles, UV JWST data from Harikane et al. (2023) by crosses, Fermi GRB data from Kistler et al. (2009) by inverse triangles and (sub)mm ALMA data from Gruppioni et al. (2020) by squares. Lines illustrate the best fits from the MCMC analysis in various DM scenarios: CDM (black), WDM (red), ψDM (blue), and SIDM (green). For clarity, the typical 2σ credible interval from sampling the posterior distribution is shown only in the WDM scenario as a red-shaded area. For reference, the dotted line is the classic fitting formula gauged at $z \lesssim 6$ by Madau & Dickinson (2014).

4.2.5 Forecasts for JWST

As mentioned in Sec. (4.2) and shown in Fig. (4.1), the early data from JWST at $z \sim 12$ seems to indicate a slowing down in the evolution of the UV luminosity function to lower $z \lesssim 10$. The effect is also evident in the cSFR density of Fig. (4.7) since the JWST data (crosses) at $z \sim 9-12$ are around the same values as the HST ones (circles). Yet, the former refer to a UV luminosity function integrated down to $M_{\rm UV}^{\rm obs} \approx -17$ while the latter refers to $M_{\rm UV}^{\rm obs} \approx -13$.

Besides the possible issues related to systematics and completeness effects in the early JWST observations that future campaigns will clear, one can ask:

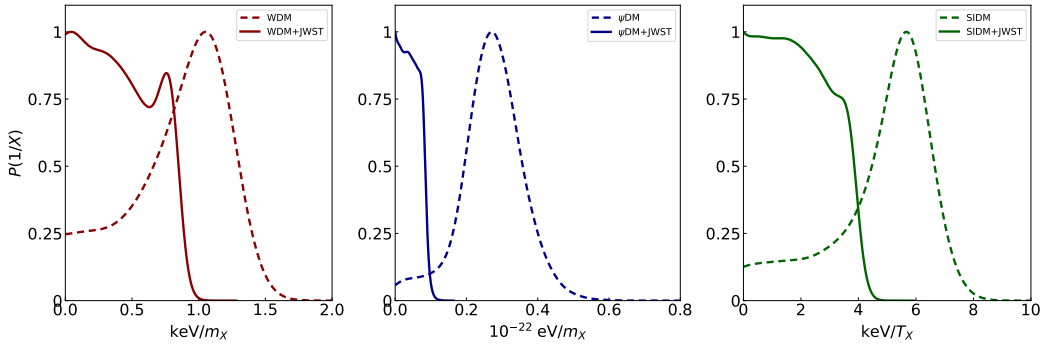

Figure 4.8: Forecasts of the marginalised posteriors on the WDM mass (left panel), ψDM mass (middle panel) and SIDM kinetic temperature at decoupling (right panel) based on prospective data at $z \gtrsim 10$ from JWST (solid lines). For reference, the dashed lines illustrate the current constraints from Fig. (4.4), Fig. (4.5), and Fig. (4.6). The marginalised distributions are in arbitrary units (normalised to 1 at their maximum value).

what if the JWST data is confirmed and extended to ultra-faint magnitudes? The following procedure details how one can make a sound and conservative forecast based on the derived astroparticle constraints. The current cSFR density estimate from JWST by Harikane et al. (2023) at $z \gtrsim 9$ is scaled up by 0.4 dex to reflect the same increase in $\rho_{\rm SFR}$ of the HST data by Bouwens et al. (2022) when integrating the luminosity function from $M_{\rm UV}^{\rm obs} \approx -17$ to $M_{\rm UV}^{\rm obs} \approx -13$. A relative uncertainty is assigned to the JWST data comparable to the HST one by Bouwens et al. (2022).

Fig. (4.8) illustrates the marginalised posteriors on the astroparticle quantities in the WDM, ψDM and SIDM scenarios. The appreciably higher values of the cSFR density implied from the putative JWST data tend to go in tension with the suppression of the power spectrum at small scales in non-CDM scenarios, erasing the bell-shaped posterior still allowed by the current data. As a consequence, rather stringent lower limits on the astroparticle quantities can be derived: WDM mass $m_X \gtrsim 1.8\,(1.2)$ keV, ψDM mass $m_X \gtrsim 17.3\,(12) \times 10^{-22}$ eV, and SIDM kinetic temperature $T_X > 0.4\,(0.3)$ keV. These lower bounds would be competitive with current literature constraints that tend to exclude part of the parameter space in non-CDM models. However, the independent and basic nature of the cSFR density observable may provide constraints less affected by systematics and model-dependent interpretations.

Finally, note from Tab. (4.3) that the fit to the forecasted JWST data will require a pretty low galaxy formation threshold $M_{\rm H}^{\rm GF}$ in CDM (and even more extreme values in the other scenarios). Nonetheless, the upper bounds at 2σ remain consistent with the atomic cooling limit. Hence, the forecasted JWST data should not present an insurmountable astrophysical challenge for CDM. This analysis highlights how upcoming ultra-faint galaxy surveys in the (pre)reionisation era will probe the microscopic nature of the elusive DM particles.

4.3 Conclusions and future prospects

The method detailed in this Chapter allows to obtain astroparticle constraints for DM models as WDM, ψDM and SIDM benefitting from high-z observations by JWST. However, this analysis based on cSFR density represents only one piece of the information that high-z JWST observations can offer on the nature of DM. High-redshift ($z \geq 6$) measurements of the stellar mass functions and the associated stellar mass density can be used further to constrain DM scenarios (Dayal & Giri 2023). Even the galaxy correlation function at small scales of faint objects probed by JWST can be an informative tool in this sense (Maio & Viel 2023). Galaxy CO emission investigated by JWST in synergy with ALMA and other arrays (e.g., VLA or NOEMA) can be used to constrain DM's astroparticle properties. In fact, the DM particle mass indirectly determines the timescale for complete molecule formation in galaxies — smaller particle masses involve galaxies featuring poorer number statistics and lower molecular content (Maio & Viel 2023). Finally, further insights on DM particle properties may come from the observations of the hypothetical Population III stars or even dark stars (e.g., Ilie et al. 2023). At slightly lower redshifts, JWST Cycle 2 observations will be used to resolve and constrain the stellar emission of a sample of 16 massive galaxies between $4 < z < 5$ to constrain their stellar mass content (proposal 3954; PI Lelli). ALMA high-quality [CII] data of these sources indicate regularly rotating disks, and by synergising these observations with the upcoming JWST ones, it will be possible to study the RCs of galaxies belonging to a previously inaccessible epoch.

Of course, there is room to improve and expand the analysis detailed in this Chapter. Some future developments include:

- Refining the analysis by updating the data considering even more recent estimates of the UV luminosity function's faint-end yielded by JWST observations (e.g., Leung et al. 2023; Pérez-González et al. 2023);
- Extending this analysis by including new DM models and modified gravity theories and comparing the obtained cSFR density with CDM predictions. In principle, any DM or modified gravity paradigm that predicts a suppression in the low-mass end of the halo mass function could be constrained by this type of analysis;
- Computing and including completeness corrections for the datasets considered in the analysis;
- Extending the samples of known high-z galaxy candidates and, conversely, confirming their nature robustly.

Ultimately, the bounds on DM particle masses inferred with this method could informatively be cross-correlated with the astroparticle constraints that come from Lyman-α forest observations (Viel et al. 2013; Iršič et al. 2017b,a; Villasenor et al. 2023), γ-ray bursts (de Souza et al. 2013; Lapi et al. 2017), cosmic reionisation (Barkana et al. 2001; Lapi & Danese 2015; Dayal et al. 2017; Lapi et al. 2017; Carucci & Corasaniti 2019; Lapi et al. 2022), high-z galaxies counts (Pacucci et al.

2013; Schultz et al. 2014; Menci et al. 2016; Corasaniti et al. 2017), gravitational lensing (Vegetti et al. 2018; Ritondale et al. 2019), integrated 21 cm data (Carucci et al. 2015; Chatterjee et al. 2019; Rudakovskyi et al. 2020), γ-ray emission (Bringmann et al. 2017; Grand & White 2022), fossil records of the Local Group (Weisz et al. 2014), dwarf galaxy profiles and scaling relations (Weisz & Boylan-Kolchin 2017; Calabrese & Spergel 2016; Burkert 2020), and Milky Way satellite galaxies (Kennedy et al. 2014; Horiuchi et al. 2014; Lovell et al. 2016; Newton et al. 2021) or a combination of these (Nadler et al. 2021; Enzi et al. 2021).

Chapter 5

Conclusions and future prospects

The results obtained within this thesis are multiple. Chapter 3 presents a model in which DM is dynamically non-minimally coupled with gravity (as in Bettoni et al. 2014), testing it against various observables from the scales of dwarf galaxies up to those of galaxy clusters. All in all, this model has shown a rich and interesting phenomenology capable of solving long-standing problems of the CDM paradigm. This effort led to the developing of an analysis pipeline that ultimately allows testing the phenomenology of any DM model or modified gravity theory predicting deviations to a pure ΛCDM picture in galactic dynamics or galaxy clusters' pressure profiles shapes. Indeed, such pipeline has already been used to test the *DM in Fractional Gravity* paradigm (see Sec. (5.1) where I briefly summarise the model's gist and the main results obtained so far).

In Chapter 4, I detailed a possible method based on cutting-edge JWST high-z observations to constrain the astroparticle properties of DM. The forecasts retrieved in this Chapter show how the upcoming faint galaxy surveys carried out with this exceptional instrument could discriminate between alternative DM models and the pure CDM picture. In this sense, a detailed analysis of the existing deep JWST surveys is essential to find and characterise high-z and faint galaxies, improving the data on which this method is based. On the other hand, determining the nature of faint objects like high-z galaxies is highly non-trivial. To best constrain these objects' properties, it is then necessary to develop the best strategies to obtain new observations complementing and strengthening existing ones.

In these concluding sections, I will summarise the work already carried out and in progress on both these fronts, detailing the successes achieved and the challenges still awaiting. This Chapter is based on the discoveries presented in Benetti et al. (2023a); Benetti et al. (2023b); Benetti et al. (2023c) (Sec. (5.1)) and Bisigello et al. (2023) (Sec. (5.2)), as well as future JWST proposals (Sec. (5.3)).

5.1 Fractional Gravity

A first and illustrative application of the analysis pipeline developed for the NMC DM framework pertains to the Fractional Gravity DM model, recently discussed in Benetti et al. (2023a); Benetti et al. (2023b); Benetti et al. (2023c). This model shares

some common characteristics with modified gravity models (Calcagni 2013; Varieschi 2020; Giusti et al. 2020; Giusti 2020; Varieschi 2021; Calcagni & Varieschi 2022; Borjon-Espejel et al. 2022; García-Aspeitia et al. 2022), yet it fundamentally differs on several key aspects. The central, underlying concept is that DM within galaxies originates fractional gravity, where a modified Poisson equation determines the gravitational potential associated with a given DM density distribution. Such equation incorporates fractional derivatives, representing derivatives of non-integer type, intending to represent non-local effects that may be needed to solve small-scale problems in galactic dynamics:

$$(-\Delta)^s \Phi(r) = -4\pi G \ell^{2-2s} \rho(r), \tag{5.1}$$

where $(-\Delta)^s$ being the fractional Laplacian, $s \in [1, 3/2]$ is a fractional index and ℓ is a fractional lengthscale. The general solution of this equation reads

$$\Phi_s(r) = -\frac{\sqrt{\pi} G \ell^{2-2s} \Gamma\left(\frac{3}{2} - s\right)}{4^{s-3/2}(2s-1)\Gamma(s)} \frac{\mathcal{J}_s^\rho(r)}{r},$$

with Γ representing the Euler Gamma function and

$$\mathcal{J}_s^\rho(r) = \int_0^\infty \mathrm{d}r' r' \rho(r') \left[(r + r')^{2s-1} - |r - r'|^{2s-1} \right].$$

Fractional gravity is not necessarily meant to be an *ab initio* theory but may constitute an effective description for a whole class of models implying non-local effects in the gravitational behaviour of DM (e.g., quantum entanglement between DM particles). Similarly to the perturbative approach adopted for NMC DM, a standard NFW density distribution is substantially altered to the Newtonian case by fractional gravity. Instead, baryons are assumed to originate standard gravity, though feeling the overall gravitational potential of the system.

Thanks to the analysis pipeline described in Sec. (3.1), it was possible to relatively quickly test the phenomenology of this model against astrophysical observations from galaxies to clusters, as done with NMC DM. Specifically, in Benetti et al. (2023a), Benetti et al. (2023b) and Benetti et al. (2023c), we achieved the key results listed below.

- Fractional gravity predicts an effective density distribution which is flatter in the inner region to the true NFW one, offering a straightforward solution to the core-cusp problem of CDM without altering the NFW density profile indicated by N-body simulations (but rather altering the dynamics it produces), see Fig. (5.1a) and Fig. (5.1b);

- This model provides accurate fits[1] to the stacked RCs and projected velocity dispersion profiles of late-type galaxies with different properties, from high/low surface-brightness systems to dwarf irregular and dwarf spheroidal galaxies (i.e., low-mass systems where the effect of fractional gravity are expected to be particularly relevant and in which the effect of

[1]For the quantitative analysis see Benetti et al. (2023a).

baryonic feedbacks is largely subdominant), with the fits performing in most instances significantly better than the standard Newtonian gravity, see an example in Fig. (5.1c);

- Fractional gravity reproduces to reasonable accuracy the observed shape and scatter of the RAR over an extended range of galaxy accelerations; see Fig. (5.2);
- The fractional gravity framework properly accounts for the universal core surface density and the scaling relation between the core radius of the DM component and the disc lengthscale;
- This model performs remarkably well[2] in modelling the ICM profiles for the X-COP galaxy cluster sample;
- Fractional gravity predicts a relationship between the concentration of the DM profile and the halo mass still consistent with the expectations of N-body simulations in the ΛCDM framework;
- Fractional gravity predicts a weakening of its effects toward more massive systems and a consistent scaling of the fractional gravity parameters from dwarf galaxies to massive clusters, see Fig. (5.3).

In the future we will develop a relativistic extension of this model, while parallel testing its phenomenology with the Milky Way RC and assess its effects on gravitational lensing. All in all, these findings imply that fractional gravity can substantially alleviate the small-scale issues of the standard CDM paradigm while remaining successful on large cosmological scales. These results demonstrate how the analysis pipeline developed in this thesis can efficiently test alternative DM scenarios or modified gravity frameworks.

In conclusion, a question arises: is there a relationship between Fractional Gravity and the NMC DM model detailed in Chapter 3? Before proceeding further, let us take a moment to examine possible analogies between the two frameworks. Both these models predict a galaxy-scale DM phenomenology compliant with observations, producing cored profiles agreeing with the observed cored-surface density relationship, capable of reproducing the RCs of dwarf galaxies as well as massive spirals' and adequately describing the empirical tight relationships between DM and baryons in these galaxies. Additionally, both frameworks predict similar scaling between the coupling/fractional lengthscale and the haloes' virial masses. In particularly massive structures, both paradigms tend to recover a pure CDM picture. Could there be a relationship between NMC DM and Fractional Gravity, perhaps with the first model as a special case of the second? In this scenario, the coherent behaviour of DM responsible for the dynamic development of the NMC would be an approximation of a broader non-local behaviour of the DM (parameterised by Fractional Gravity), which leads the dark particles to probe a substantial part of the halo's potential wells unconventionally, with each particle

[2]For the quantitative analysis see Benetti et al. (2023b).

feeling the overall distribution of the other particles (and thus the potential) in its entirety (or almost). However, where does this non-locality stem from? Future work will solve this question, but some hints bring us towards the quantum world. On the one hand, DM could develop a dynamical NMC with gravity by condensing in BECs, i.e., macroscopic quantum states. Conversely, the non-local "bond beyond distance" showcased by DM particles in Fractional Gravity could be related to quantum particle entanglement. Both frameworks rely on a hypothetical quantum nature of the DM particles capable of manifesting inside haloes. While this is a promising avenue to pursue, only future in-depth studies on the topic will provide a definitive answer to the common origin of these paradigms. A key step to this end involves formulating a relativistic extension of Fractional Gravity. This step would allow us not only to understand the fundamental physics behind this model better but also to test it in relativistic regimes, e.g., by studying the propagation of GWs and their electromagnetic counterparts in this framework or to evaluate whether fractional effects can take on a DE role as on a cosmological scale, as may happen in the case of NMC DM.

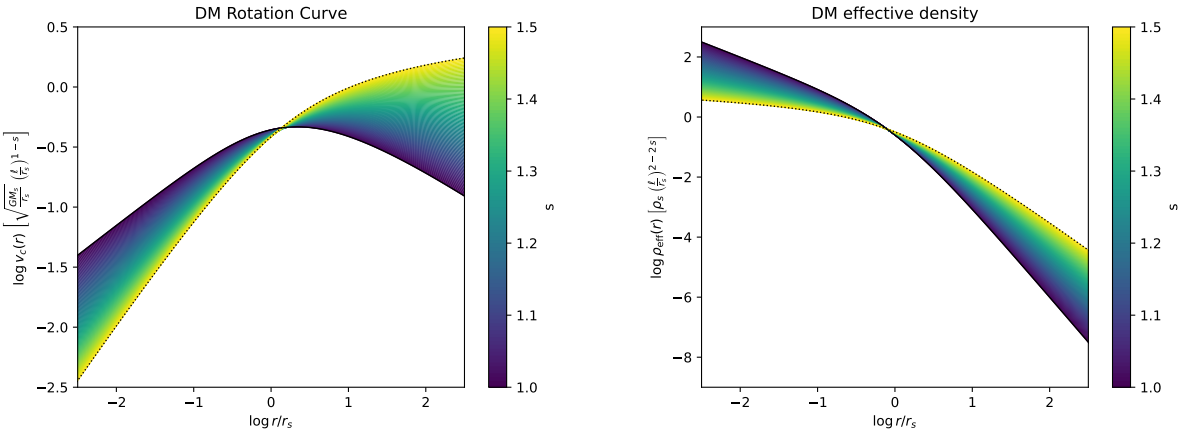

(a) (b)

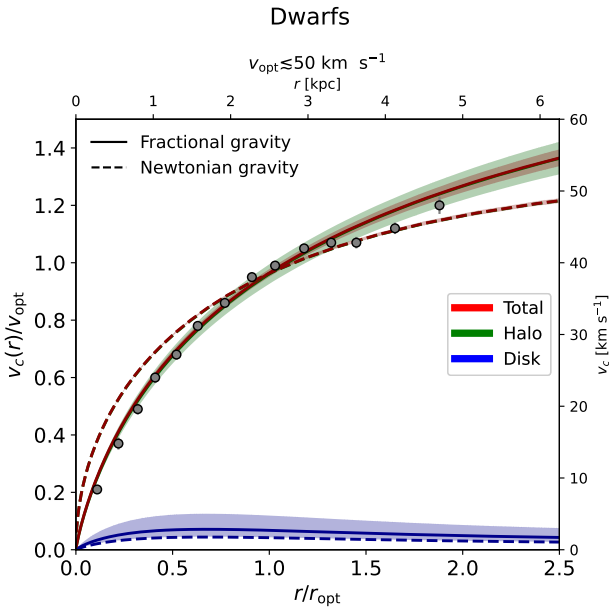

(c)

Figure 5.1: DM RC (Fig. (5.1a)) and effective density (Fig. (5.1b)) for different values of the fractional parameter s (color-coded). For reference, the dotted line refers to the maximal value $s = 3/2$. Fig. (5.1c) shows the fit to the stacked RC for the dwarf galaxy sample considered in Benetti et al. (2023a) (filled circles) with Newtonian (dashed lines) and Fractional Gravity (solid lines). Red lines refer to the total rotation curve, blue lines to the disc component, and green lines to the halo component. For the fractional case, the shaded areas illustrate the 1σ credible intervals from sampling the posterior distribution.

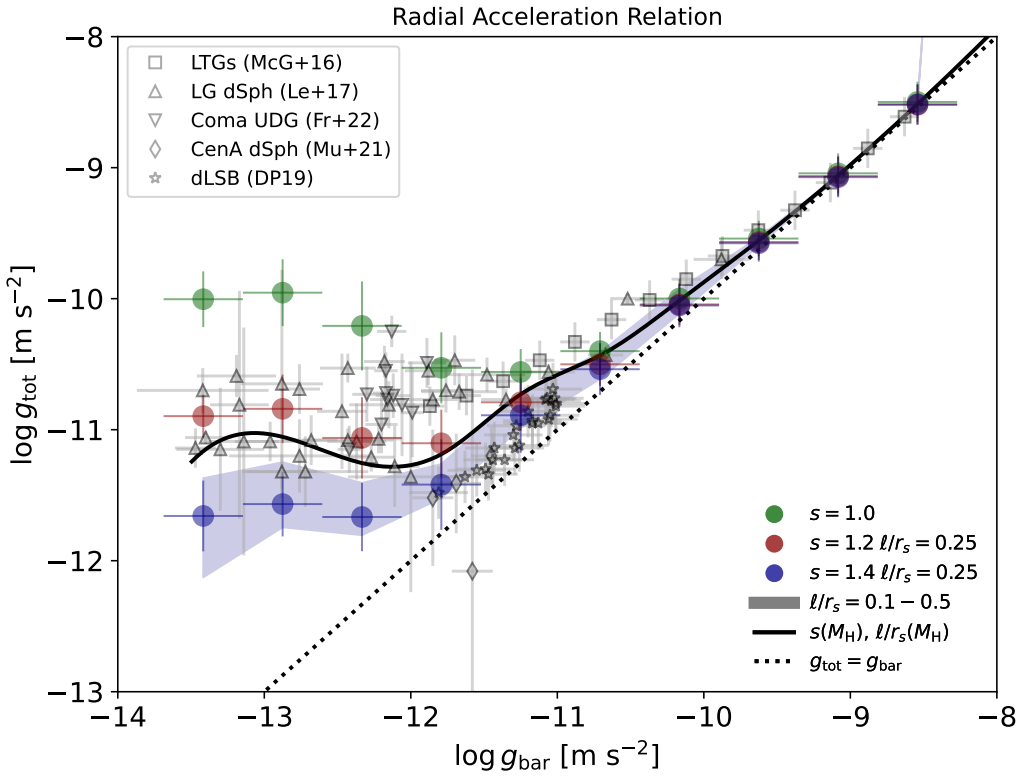

Figure 5.2: The radial acceleration relation (RAR) in Fractional Gravity. Green circles illustrate the outcome for $s = 1$ (independent of ℓ and corresponding to Newtonian gravity), red circles for $s = 1.2$ and $\ell/r_s = 0.25$, and blue circles for $s = 1.4$ and $\ell/r_s = 0.25$. The red and blue shaded areas show the effect of varying ℓ/r_s in the range $0.1 - 0.5$. Finally, the black curve is on adopting a halo mass-dependence in s and ℓ/r_s as emerging from the analysis of stacked rotation curve of Benetti et al. (2023a) (see Fig. 5.3). For reference, the dotted black line displays the one-to-one relation $g_{tot} = g_{bar}$. Data for spiral galaxies (binned) are from McGaugh et al. (2016) (squares), for Local Group dwarf spheroidal from Lelli et al. (2017) (triangles), for Coma Cluster Ultra Diffuse Galaxies from Freundlich et al. 2022 (reversed triangles), for Centaurus A dwarf spheroidals from Müller et al. 2022 (diamonds), and for dwarf LSB with $g_{bar}(0.4 \lesssim r/R_{opt} \lesssim 1) < -11$ from Di Paolo et al. 2019 (stars).

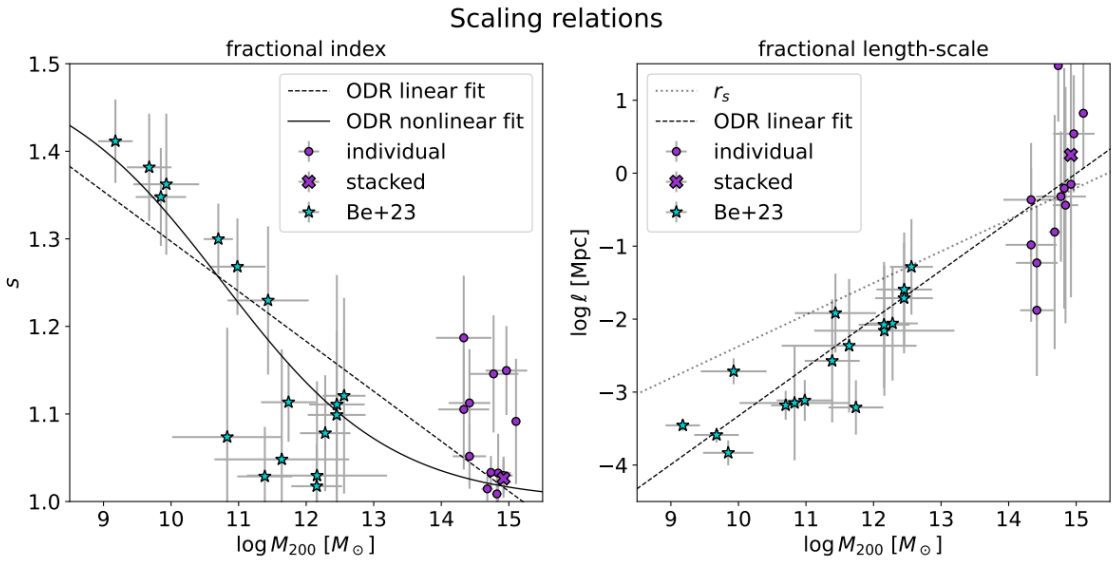

Figure 5.3: Scaling relations in fractional gravity from galaxies to clusters: fractional index s (left) and lengthscale ℓ (right) vs. DM mass M_{200}. Magenta circles refer to the individual X-COP galaxy clusters analysed in Benetti et al. (2023b). In contrast, magenta crosses represent the stacked cluster sample from the same work, while cyan stars refer to the stacked RCs of galaxies from Benetti et al. (2023a). Dashed lines display an orthogonal distance regression (ODR) algorithm linear fit to the overall data, while a solid line in the left panel shows a nonlinear ODR fit with limiting values 1 and 1.5 from large to small masses, and a dotted line in the right panel illustrates the scale radius rs of the NFW profile.

5.2 Searching for high-z galaxies in the CEERS field

As shown earlier, the search for high-z galaxies can be deeply entangled with understanding the nature of DM. Reddened high-z galaxies may be selected in photometric catalogues through a colour-based selection (e.g., Hainline et al. 2020) or, similarly, as *dropouts* at short wavelengths, relying on the large break in the continuum flux corresponding to the 912 Å Lyman limit from neutral hydrogen absorption in the line-of-sight. In Bisigello et al. (2023), we applied this latter technique on four out of ten CEERS NIRCam pointings in the Extended Groth Strip (EGS) field relying on the catalogue by Finkelstein et al. (2023), which uses the co-added F277W+F356W image as detection image. Galaxies were selected to have a S/N > 3 in the F444W filter and a S/N < 2 in every filter equal or below 2 μm both for JWST and the available archival HST observations in the EGS field, with a further magnitude cut [F444W] < 29 mag. Moreover, we checked that the selected galaxies had a S/N < 2 in the co-added F115W+F150W+F200W band images and subsequently fitted the photometric points with the code `Bagpipes` (Carnall et al. 2018). This selection is ideal for identifying very dusty (i.e., with an absorption index $A_V > 1$ mag) galaxies with stellar masses between 10^6 to $10^{10} M_\odot$ at $z < 5$, more massive dusty galaxies at $z = 5 - 18$ and galaxies at $z > 18$ due

to the Lyman absorption, independently of their dust extinction. The obtained sample of F200W-dropouts contains no strong candidates at $z > 6.5$, and instead, it consists almost completely ($\sim 81\%$) of $z < 2$ low-mass galaxies, with a median stellar mass of $10^{7.3} M_{\odot}$. These galaxies show an exceptional dust extinction with a median value of $A_V = 4.9$ mag, which is unexpected given their low stellar mass. The remaining galaxies, which are at $z < 6.5$, show similar large dust extinction ($A_V > 1$), but they are generally more massive ($> 10^{7.5} M_{\odot}$). However, as seen by the sample redshift distribution in Fig. (5.4b), 93/133 objects show multiple solutions that have a probability larger than 10% of being high-z galaxies, showing multiple peaks in the redshift posterior. Hence, we will characterise these objects with further observations (e.g., exploiting MIRI coverage were available) while checking for other high-z candidates in the other NIRCam CEERS pointings. Alongside this analysis, I will investigate the presence of additional objects not included in the catalogue by Finkelstein et al. (2023). This procedure will involve the creation of a catalogue of the CEERS field using the F444W one as detection image and applying the selection criteria detailed in Bisigello et al. (2023). In the four pointing examined in Bisigello et al. (2023), nine additional sources were found with this technique. These sources were absent in the catalogue based on the F277W+F356W co-added image, as they are faint in one or both bands. Yet, since four of these sources are detected only in the F444W filter, we did not attempt to derive any physical property for them. However, there is still to see what hides in the other CEERS NIRCam pointings.

5.3 DM astroparticle constraints from the abundance of high-z galaxies

The observed high density of galaxies measured at high redshifts can place stringent constraints on DM particle masses in different frameworks (e.g., de Vega & Sanchez 2010; Menci et al. 2016; Shirasaki et al. 2021). The argument is straightforward: for a given limiting magnitude and redshift, the cumulative galaxy number density should be smaller than the whole halo mass function within a specific DM scenario, i.e., the observed number of galaxies should not exceed the number of haloes predicted by a specific theory. Hence:

$$\phi_{\rm obs} \equiv \int_{L_{\rm cut}}^{\infty} {\rm d}L \frac{{\rm d}n_{\rm gal}}{{\rm d}L} \leq \int_{M_{\rm min}}^{M_{\rm max}} {\rm d}M \frac{{\rm d}n}{{\rm d}M}, \tag{5.2}$$

where $L_{\rm cut}$ is the luminosity corresponding to the limiting magnitude, ${\rm d}n_{\rm gal}/{\rm d}L$ is the galaxy luminosity function. Since the shape of the halo mass function in a specific scenario depends on the DM particle mass, constraining the abundance of galaxies at high-redshifts (i.e., where the differences between CDM and alternative DM scenarios are more visible) can constrain the DM particle mass (see Fig. (5.5)). In the future, I will, therefore, deal with quantitatively establishing what constraints deep JWST surveys can have on the astroparticle properties of DM in terms of high-z galaxies abundances. To do this, one needs to design specific spectroscopic observations aimed at confirming with the least possible error the

presence of galaxies at a particular redshift, and on the other hand, there is the need for studies aimed at characterising the completeness of the reference surveys[3]. This method has been successfully applied to constrain the WDM particle mass relying on data from the Hubble Frontier Field clusters (Menci et al. 2016). However, it is yet to be applied to JWST observations, and it constitute a possible strategy for a future JWST proposal.

[3]One could also not account for completeness with the price of obtaining looser astroparticle constraints.

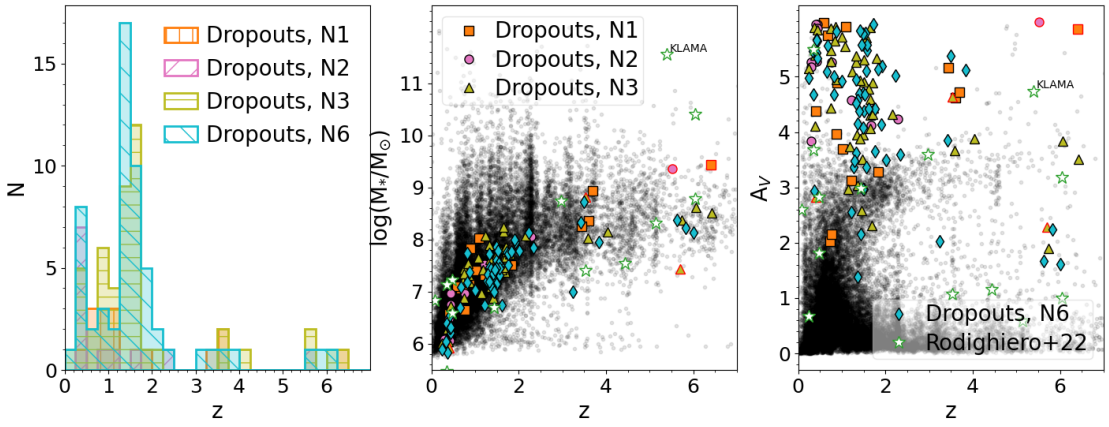

(a)

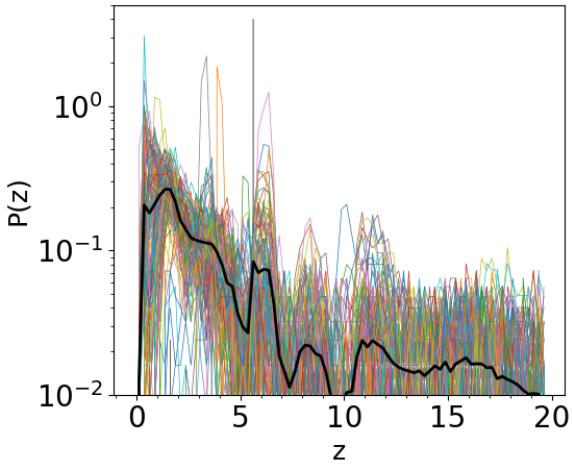

(b)

Figure 5.4: Fig. (5.4a): Redshift distribution, redshift vs stellar mass and redshift vs $A(V)$ for F200W-dropouts in the four CEERS pointings (colour points) and for the entire sample in the NIRCam2 pointing (small black dots). Points with a red edge are objects in the F200W-dropout sample not found in the catalogue by Finkelstein et al. (2023) based on photometry derived using the Kron radius. The sample of F200W-dropouts by Rodighiero et al. 2023 (green empty stars). Fig. (5.4b): Redshift probability distributions $P(z)$ of the entire F200W dropout sample of Bisigello et al. (2023) (coloured line) and average $P(z)$ (black thick solid line).

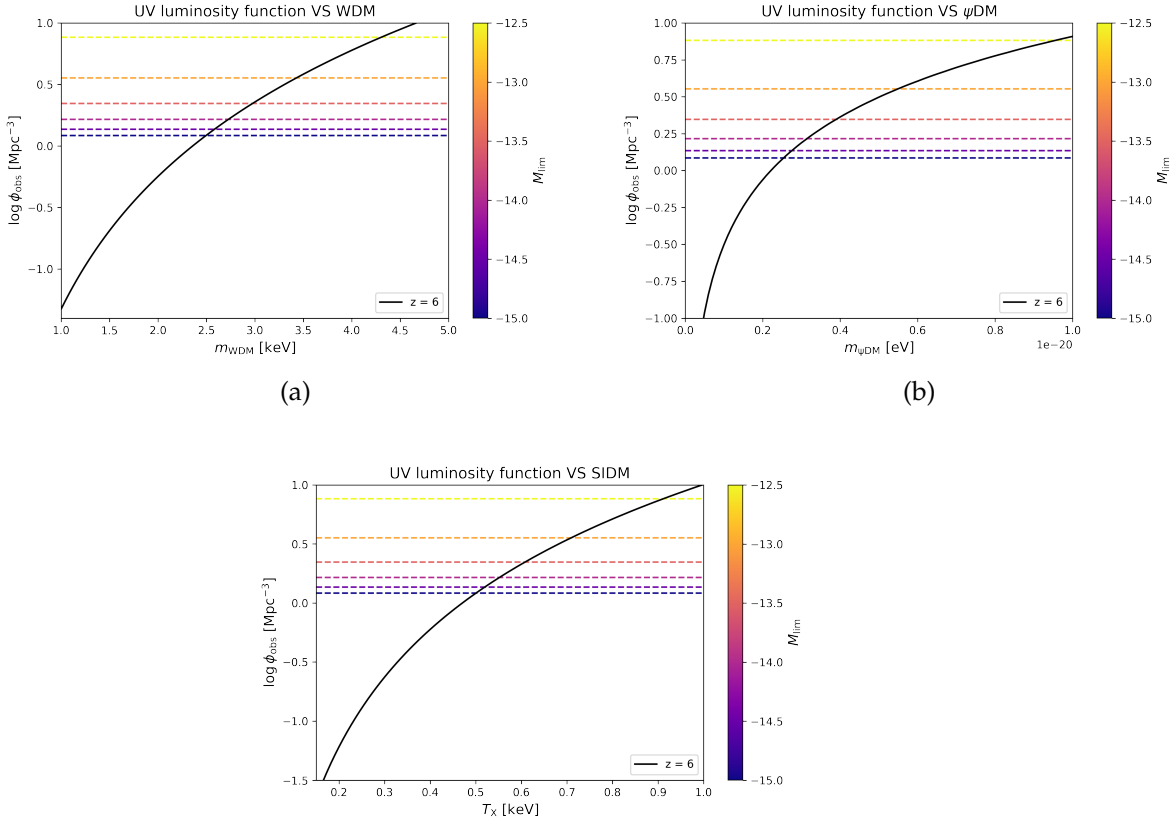

Figure 5.5: Lower limits of WDM (Fig.(5.5a)), ψDM (Fig.(5.5b)) and SIDM (Fig.(5.5c)) masses or temperatures obtained from the UV luminosity function of galaxies (given by Eq. (4.1)) at $z = 6$. The dashed horizontal lines represent different lower bounds of the UV luminosity function at $z = 6$, showing how the excluded space of particle masses or temperatures can broaden with deeper observations. The solid lines show the maximum number density of DM halos as a function of WDM, ψDM and SIDM masses or temperatures based on the HMF given by Eq. (4.3) with the values specified in Tab. (4.1). Assuming a one-to-one correspondence of DM halos and faint galaxies, one can exclude the alternative DM models if the maximum number density of DM halos becomes smaller than the observed galaxy abundance.

Appendix A

Varying the NMC DM relativistic action

In the Jordan frame, the NMC DM model's relativistic action reads as

$$S = S_{\rm EH}\left[\widetilde{g}_{\mu\nu}\right] + S_{\rm bar}\left[\widetilde{g}_{\mu\nu}, \psi\right] + S_{\rm DF}\left[\widetilde{g}_{\mu\nu}, \varphi\right] + S_{\rm NMC}\left[\widetilde{g}_{\mu\nu}, \varphi\right],$$

where $\widetilde{g}_{\mu\nu}$ represent the physical metric, linked to the gravitational metric via a disformal transformation of the kind $\widetilde{g}_{\mu\nu} = g_{\mu\nu} + h_{\mu\nu}$, with $h_{\mu\nu} \propto \nabla_\mu\varphi\nabla_\nu\varphi$. The action $S_{\rm EH}\left[\widetilde{g}_{\mu\nu}\right]$ is the standard Einstein–Hilbert action given by:

$$S_{\rm EH}\left[\widetilde{g}_{\mu\nu}\right] = \kappa \int {\rm d}^4x\sqrt{-\widetilde{g}}R,$$

with $\kappa = 1/(16\pi G)$ in natural units.

Baryons are encoded by the (real) scalar field ψ, and their action is represented by $S_{\rm bar}$. Here, baryons are assumed to be described by a perfect fluid with a pressure p_b and energy density ρ_b with the following stress-energy tensor (SET):

$$T^{\rm bar}_{\mu\nu} = (\rho_b + p_b)u_\mu u_\nu + \widetilde{g}_{\mu\nu}p_b.$$

The baryonic action term can be obtained from $T^{\rm bar}_{\mu\nu} = -2/\sqrt{-\widetilde{g}}\delta S_{\rm bar}$.

The DM action $S_{\rm DF}\left[\widetilde{g}_{\mu\nu}, \varphi\right]$ reads as:

$$S_{\rm DM}\left[\widetilde{g}_{\mu\nu}, \varphi\right] = \int d^4x\sqrt{-\tilde{g}}\mathcal{L}_\varphi,$$

with $\mathcal{L}_\varphi$ being the standard lagrangian of a scalar field, namely

$$\mathcal{L}_\varphi = \frac{1}{2}\widetilde{g}^{\mu\nu}\partial_\mu\varphi\,\partial_\nu\varphi - V(\varphi).$$

Finally, the NMC part of the action reads as

$$S_{\rm NMC}\left[\widetilde{g}_{\mu\nu}, \varphi\right] = \epsilon L^2 \int {\rm d}^4x\sqrt{-\tilde{g}}\widetilde{G}^{\mu\nu}\partial_\mu\varphi\partial_\nu\varphi.$$

In order to find the (modified) Einstein equation, one varies the action as follows:

$$\delta S = \int d^4x \left[\delta S_{\rm EH}\left[\widetilde{g}_{\mu\nu}\right] + \delta S_{\rm bar}\left[\widetilde{g}_{\mu\nu}, \psi\right] + \delta S_{\rm DF}\left[\widetilde{g}_{\mu\nu}, \varphi\right] + \delta S_{\rm NMC}\left[\widetilde{g}_{\mu\nu}, \varphi\right]\right].$$

I hereby discuss the variation of each one of the single terms appearing in the action above.

Variation of the Einstein–Hilbert action: the first of the three terms in the expression above gives the usual Einstein tensor. The variation reads as

$$\delta S_{\rm EH}\left[\widetilde{g}_{\mu\nu}\right] = \frac{1}{16\pi G}\int d^4x \left(\delta\sqrt{-\widetilde{g}}R + \sqrt{-\widetilde{g}}\delta R\right).$$

In order to express the variation of the metric determinant $\delta\sqrt{-\widetilde{g}}$ one is required to consider the Jacobi formula for the differentiation of a determinant:

$$\delta\widetilde{g} = \delta\det\left(\widetilde{g}_{\alpha\beta}\right) = \widetilde{g}\widetilde{g}^{\alpha\beta}\delta\widetilde{g}_{\alpha\beta}.$$

Hence, the following is obtained:

$$\begin{aligned}\delta\sqrt{-\widetilde{g}} &= -\frac{1}{2\sqrt{-\widetilde{g}}}\delta\widetilde{g} = -\frac{1}{2\sqrt{-\widetilde{g}}}\widetilde{g}\widetilde{g}^{\alpha\beta}\delta\widetilde{g}_{\alpha\beta} = \frac{1}{2\sqrt{-\widetilde{g}}}(-\widetilde{g})\widetilde{g}^{\alpha\beta}\delta\widetilde{g}_{\alpha\beta} = \\ &= \frac{1}{2\sqrt{-\widetilde{g}}}\left(\sqrt{-\widetilde{g}}\right)^2\widetilde{g}^{\alpha\beta}\delta\widetilde{g}_{\alpha\beta}.\end{aligned}$$

One can now take advantage of the following relation:

$$\delta(\widetilde{g}^{\alpha\beta}\widetilde{g}_{\alpha\beta}) = \delta\widetilde{g}^{\alpha\beta}\widetilde{g}_{\alpha\beta} + \widetilde{g}^{\alpha\beta}\delta\widetilde{g}_{\alpha\beta} = 0.$$

The variation of the metric determinant can now be expressed as a function of the variation of the inverse of the metric:

$$\delta\sqrt{-\widetilde{g}} = -\frac{1}{2}\sqrt{-\widetilde{g}}\widetilde{g}_{\alpha\beta}\delta\widetilde{g}^{\alpha\beta}.$$

Plugging the above relation in the Einstein–Hillbert's action variation and collecting the common $\sqrt{-\widetilde{g}}$ we obtain:

$$\boxed{\frac{\delta S_{\rm EH}\left[\widetilde{g}_{\mu\nu}\right]}{\delta\widetilde{g}^{\alpha\beta}} = \kappa\int d^4x\sqrt{-\widetilde{g}}\left(-\frac{1}{2}\widetilde{g}_{\alpha\beta}R + \widetilde{R}_{\alpha\beta}\right) = \kappa\int d^4x\sqrt{-\widetilde{g}}\widetilde{G}_{\alpha\beta},}$$

since $\delta R = R_{\alpha\beta}\delta\widetilde{g}^{\alpha\beta}$.

Variation of the DM action: varying the DM scalar field action one gets:

$$\delta S_{\rm DM}\left[\widetilde{g}_{\mu\nu},\varphi\right]=\int d^4x\delta(\sqrt{-\widetilde{g}}\mathcal{L}_\varphi)=\int d^4x\;\delta\left[-\frac{1}{2}\sqrt{-\widetilde{g}}\widetilde{g}^{\mu\nu}\partial_\mu\varphi\partial_\nu\varphi-\sqrt{-\widetilde{g}}V(\varphi)\right]=$$
$$=\int d^4x\;\left[-\frac{1}{2}\delta\sqrt{-\widetilde{g}}\widetilde{g}^{\mu\nu}\partial_\mu\varphi\partial_\nu\varphi-\frac{1}{2}\sqrt{-\widetilde{g}}\delta\widetilde{g}^{\mu\nu}\partial_\mu\varphi\partial_\nu\varphi-\delta\sqrt{-\widetilde{g}}V(\varphi)\right]=$$
$$=\int d^4x\;\frac{1}{2}\sqrt{-\widetilde{g}}\left[\frac{1}{2}\widetilde{g}_{\alpha\beta}\widetilde{g}^{\mu\nu}\partial_\mu\varphi\partial_\nu\varphi\delta\widetilde{g}^{\alpha\beta}-\delta\widetilde{g}^{\mu\nu}\partial_\mu\varphi\partial_\nu\varphi-\widetilde{g}_{\alpha\beta}\delta\widetilde{g}^{\alpha\beta}V(\varphi)\right].$$

Here, one can drop variations of terms independent of the metric. Hence:

$$\frac{\delta S_{\rm DM}\left[\widetilde{g}_{\mu\nu},\varphi\right]}{\delta\widetilde{g}^{\alpha\beta}}=\int d^4x\;\frac{1}{2}\sqrt{-\widetilde{g}}\left[-\frac{1}{2}\widetilde{g}_{\alpha\beta}\widetilde{g}^{\mu\nu}\partial_\mu\varphi\partial_\nu\varphi+\partial_\alpha\varphi\partial_\beta\varphi+\widetilde{g}_{\alpha\beta}V(\varphi)\right],$$

and thus:

$$T^{\varphi}_{\mu\nu}=\nabla_\mu\varphi\nabla_\nu\varphi-\frac{1}{2}\widetilde{g}_{\mu\nu}\widetilde{g}^{\alpha\beta}\partial_\alpha\varphi\partial_\beta\varphi-\widetilde{g}_{\mu\nu}V(\varphi).$$

Variation of the NMC action: the variation of the NMC term reads as

$$\delta S_{\rm NMC}\left[\widetilde{g}_{\mu\nu},\varphi\right]=\epsilon L^2\int d^4x\,\sqrt{-\widetilde{g}}\left\{\frac{1}{2}\,\delta\widetilde{R}_{\alpha\beta}\,\partial^\alpha\varphi\partial^\beta\varphi+\frac{1}{2}\,\partial^\alpha\varphi\partial^\beta\varphi\left[R\,g_{\mu\alpha}g_{\nu\beta}-g_{\mu\nu}\widetilde{R}_{\alpha\beta}\right.\right.$$
$$\left.\left.-\widetilde{G}_{\mu\nu}g_{\alpha\beta}\right]\delta\widetilde{g}^{\mu\nu}\right\}.$$

To simplify calculations, I will consider a small perturbative tensor $\varepsilon_{\mu\nu}$ mapping the metric in $\widetilde{g}_{\mu\nu}\to\widetilde{g}_{\mu\nu}+\varepsilon_{\mu\nu}$. One can then expand all the relevant quantities at order $O(\varepsilon^2)$:

$$\widetilde{g}^{\mu\nu}\to\widetilde{g}^{\mu\nu}-\varepsilon^{\mu\nu};$$
$$\sqrt{-\widetilde{g}}\to\sqrt{-\widetilde{g}}\left(1+\frac{1}{2}\widetilde{g}^{\mu\nu}\varepsilon_{\mu\nu}\right);$$
$$\Gamma^\mu_{\nu\rho}\to\Gamma^\mu_{\nu\rho}+Z^\mu_{\nu\rho},\ \text{with}\ \ Z^\sigma_{\nu\rho}=\frac{1}{2}\widetilde{g}^{\sigma\alpha}\left(\nabla_\nu\varepsilon_{\alpha\rho}+\nabla_\rho\varepsilon_{\alpha\nu}-\nabla_\alpha\varepsilon_{\nu\rho}\right);$$
$$\widetilde{R}_{\mu\nu}\to\widetilde{R}_{\mu\nu}+\nabla_\sigma Z^\sigma_{\mu\nu}-\nabla_\mu Z^\sigma_{\nu\sigma};$$
$$R\to R+\nabla_\sigma Z^\sigma{}_{\mu\nu}\widetilde{g}^{\mu\nu}-\nabla_\mu Z^\sigma_{\nu\sigma}\widetilde{g}^{\mu\nu}-\widetilde{R}^{\mu\nu}\varepsilon_{\mu\nu}.$$

The NMC action term can then be expanded at linear order in ϵ:

$$S_{\rm NMC}\left[\widetilde{g}_{\mu\nu},\varphi\right]=\int d^4x\sqrt{-g}\left\{\frac{1}{2}\left[\widetilde{g}^{\mu\nu}\widetilde{G}_{\alpha\beta}\nabla^\alpha\varphi\nabla^\beta\varphi+\widetilde{R}^{\mu\nu}\widetilde{g}_{a\beta}\nabla^\alpha\varphi\nabla^\beta\varphi+\right.\right.$$
$$\left.\left.-R\nabla^\mu\varphi\nabla^v\varphi\right]\varepsilon_{\mu\nu}+\left[\nabla_\sigma Z^\sigma_{\mu\nu}-\nabla_\mu Z^\sigma_{\sigma\nu}-\frac{1}{2}\widetilde{g}_{\mu\nu}\left(\nabla_\sigma Z^\sigma_{\alpha\beta}\widetilde{g}^{\alpha\beta}-\nabla_\alpha Z^\sigma_{\sigma\beta}\widetilde{g}^{\alpha\beta}\right)\right]\nabla^\mu\varphi\nabla^v\varphi\right\}.$$

One can then proceed to rewrite the following terms:

$$\nabla_\sigma Z^\sigma_{\mu\nu}\nabla^\mu\varphi\nabla^\nu\varphi = \left[\widetilde{g}^{\sigma\mu}\nabla_\alpha\nabla_\sigma\left(\nabla^\alpha\varphi\nabla^\nu\varphi\right) - \frac{1}{2}\Box\left(\nabla^\mu\varphi\nabla^\nu\varphi\right)\right]\varepsilon_{\mu\nu} + \text{boundary};$$

$$\nabla_\mu Z^\sigma_{\sigma\nu}\nabla^\mu\varphi\nabla^\nu\varphi = \frac{1}{2}\widetilde{g}^{\mu\nu}\nabla_\alpha\nabla_\beta\left(\nabla^\alpha\varphi\nabla^\beta\varphi\right)\varepsilon_{\mu\nu} + \text{boundary};$$

$$\widetilde{g}^{\alpha\beta}\nabla_\sigma Z^\sigma_{\alpha\beta}\nabla^\mu\varphi\nabla_\mu\varphi = \frac{1}{2}\left(2\nabla^\mu\nabla^v - \widetilde{g}^{\mu\nu}\Box\right)\left(\nabla^\alpha\varphi\nabla_\alpha\varphi\right)\varepsilon_{\mu v} + \text{boundary};$$

$$\widetilde{g}^{\alpha\beta}\nabla_a Z^\sigma_{\sigma\beta}\nabla^\mu\varphi\nabla_\mu\varphi = \frac{1}{2}\widetilde{g}^{\mu\nu}\Box\left(\nabla^\alpha\varphi\nabla_\alpha\varphi\right)\varepsilon_{\mu\nu} + \text{boundary}.$$

Plugging these terms into the variation of the NMC action term yields the NMC stress-energy tensor, which reads as

$$\begin{aligned}T^{\text{NMC}}_{\mu\nu} &= \widetilde{g}_{\mu\nu}\widetilde{G}_{\alpha\beta}\nabla^\alpha\varphi\nabla^\beta\varphi + \widetilde{R}_{\mu\nu}\widetilde{g}_{\alpha\beta}\nabla^\alpha\varphi\nabla^\beta\varphi - R\nabla_\mu\varphi\nabla_\nu\varphi\\ &+ 2\widetilde{g}_{\sigma\mu}\nabla_\alpha\nabla^\sigma\left(\nabla^\alpha\varphi\nabla_\nu\varphi\right) - \Box\left(\nabla_\mu\varphi\nabla_\nu\varphi\right) - \widetilde{g}_{\mu\nu}\nabla_\alpha\nabla_\beta\left(\nabla^\alpha\varphi\nabla^\beta\varphi\right)\\ &+ \left(\widetilde{g}_{\mu\nu}\Box - \nabla_\mu\nabla_\nu\right)\left(\nabla^\alpha\varphi\nabla_\alpha\varphi\right).\end{aligned}$$

Eventually, the Einstein equation comprehensive of the NMC can be written as:

$$\boxed{\frac{1}{8\pi G}\widetilde{G}_{\alpha\beta} = T^{\text{bar}}_{\alpha\beta} + T^{\varphi}_{\alpha\beta} + T^{\text{NMC}}_{\alpha\beta}.} \tag{A.1}$$

Notice that the effective SET $T^{\text{NMC}}_{\alpha\beta}$ has a somewhat non-standard expression since it depends on the curvature.

Appendix B

Deriving the DM scalar field equation of motion

To obtain the DM scalar field φ equation of motion, one can vary the model's action to the DM scalar field φ. Both the Einstein–Hilbert term and the baryons term do not give any contribution in this sense, as well as any term depending on $\sqrt{-\widetilde{g}}$. Indeed, all these terms do not depend on the scalar field φ. Instead, the DM term and the NMC term will give the following contributions:

$$\delta S\left[\widetilde{g}_{\mu\nu},\varphi\right]=\int \mathrm{d}^4\sqrt{-\widetilde{g}}\left[\frac{1}{2}\widetilde{g}^{\mu\nu}\left(\partial_\mu\delta\varphi\partial_\nu\varphi+\partial_\mu\varphi\partial_\nu\delta\varphi\right)-V'(\varphi)\delta\varphi+\right.$$
$$\left.+\epsilon L^2\left(\widetilde{G}^{\mu\nu}\partial_\mu\delta\varphi\partial_\nu\varphi+\widetilde{G}^{\mu\nu}\partial_\mu\varphi\partial_\nu\delta\varphi\right)\right].$$

Now, thanks to the fact that the variation and partial derivatives can commute, one can write that:

$$\frac{1}{2}\widetilde{g}^{\mu\nu}\left(\partial_\mu\delta\varphi\partial_\nu\varphi+\partial_\mu\varphi\partial_\nu\delta\varphi\right)=\widetilde{g}^{\mu\nu}\partial_\mu\delta\varphi\partial_\nu\varphi,$$
$$\epsilon L^2\left(\widetilde{G}^{\mu\nu}\partial_\mu\delta\varphi\partial_\nu\varphi+\widetilde{G}^{\mu\nu}\partial_\mu\varphi\partial_\nu\delta\varphi\right)=2\epsilon L^2\left(\widetilde{G}^{\mu\nu}\partial_\mu\delta\varphi\partial_\nu\varphi\right).$$

Moreover, the following equalities can be established:

$$\nabla_\mu(g_{\mu\nu}\delta\varphi\partial_\nu\varphi)=\nabla_\mu g^{\mu\nu}\delta\varphi\partial_\nu\varphi+g^{\mu\nu}\nabla_\mu\delta\varphi\partial_\nu\varphi+g^{\mu\nu}\delta\varphi\nabla_\mu\partial_\nu\varphi=$$
$$=\nabla_\mu g^{\mu\nu}\delta\varphi\partial_\nu\varphi+g^{\mu\nu}\partial_\mu\delta\varphi\partial_\nu\varphi+g^{\mu\nu}\delta\varphi\partial_\mu\partial_\nu\varphi=$$
$$=g^{\mu\nu}\partial_\mu\delta\varphi\partial_\nu\varphi+g^{\mu\nu}\delta\varphi\partial_\mu\partial_\nu\varphi,$$

Here, I made use of the fact that partial derivatives can replace covariant derivatives if they are applied to a scalar field. Moreover, I dropped the term depending on $\nabla_\mu g^{\mu\nu}$ under the assumption that the connection is metric (i.e. $\nabla_\mu g^{\mu\nu}=0$). Hence:

$$g^{\mu\nu}\partial_\mu\delta\varphi\partial_\nu\varphi=\nabla_\mu(g_{\mu\nu}\delta\varphi\partial_\nu\varphi)-g^{\mu\nu}\delta\varphi\partial_\mu\partial_\nu\varphi.$$

Similarly, one can write the following:

$$\begin{aligned}\nabla_\mu(G_{\mu\nu}\delta\varphi\partial_\nu\varphi) &= \nabla_\mu G^{\mu\nu}\delta\varphi\partial_\nu\varphi + G^{\mu\nu}\nabla_\mu\delta\varphi\partial_\nu\varphi + G^{\mu\nu}\delta\varphi\nabla_\mu\partial_\nu\varphi = \\ &= \nabla_\mu G^{\mu\nu}\delta\varphi\partial_\nu\varphi + G^{\mu\nu}\partial_\mu\delta\varphi\partial_\nu\varphi + G^{\mu\nu}\delta\varphi\partial_\mu\partial_\nu\varphi = \\ &= G^{\mu\nu}\partial_\mu\delta\varphi\partial_\nu\varphi + G^{\mu\nu}\delta\varphi\partial_\mu\partial_\nu\varphi.\end{aligned}$$

Since the Einstein tensor is divergenceless, i.e. $\nabla_\mu G^{\mu\nu} = 0$, one obtains:

$$G^{\mu\nu}\partial_\mu\delta\varphi\partial_\nu\varphi = \nabla_\mu(G_{\mu\nu}\delta\varphi\partial_\nu\varphi) - G^{\mu\nu}\delta\varphi\partial_\mu\partial_\nu\varphi.$$

By plugging these results into the variation of the action, one obtains the following expression:

$$\frac{\delta S\left[\widetilde{g}_{\mu\nu},\varphi\right]}{\delta\varphi} = \int \mathrm{d}^4\sqrt{-\widetilde{g}}\left(-\widetilde{g}^{\mu\nu}\partial_\mu\partial_\nu\varphi - V'(\varphi) - 2\epsilon L^2\widetilde{G}^{\mu\nu}\partial_\mu\varphi\partial_\nu\varphi\right).$$

Notice that in the above expression, all the terms in the form $\nabla_\mu A^\mu$, with A^μ being a generic vector, have been dropped. In fact, the integration of these terms yields a null boundary term.

Eventually, the variation of the overall model's action to the scalar field φ leads to the following equation of motion:

$$\boxed{\Box\varphi + V'(\varphi) + 2\epsilon L^2\widetilde{G}^{\mu\nu}\partial_\mu\varphi\partial_\nu\varphi = 0.} \tag{B.1}$$

If the non-minimal coupling is absent (i.e. $\epsilon = 0$) and $V(\varphi) = -\frac{1}{2}m^2\varphi^2$, with m being the mass of the particle associated to the field φ, the standard Klein-Gordon equation is retrieved.

Appendix C

Newtonian limit of NMC DM

The Newtonian regime is achieved when the gravitational interaction is approximated in the limit of weak fields. This approximation is relevant for physical systems with low density and slow velocities, making it especially suitable for studying gravitational dynamics on a galactic scale. To this pro, the metric is expanded as $\widetilde{g}_{\mu\nu} \to \eta_{\mu\nu} + h_{\mu\nu}$, with $\eta_{\mu\nu}$ being the Minkowski metric tensor and $h_{\mu\nu}$ representing a small perturbation over it. Then, defining

$$\bar{h}_{\mu\nu} = h_{\mu\nu} - \frac{1}{2}\eta_{\mu\nu}h \quad \to \quad h_{\mu\nu} = \bar{h}_{\mu\nu} - \frac{1}{2}\eta_{\mu\nu}\bar{h},$$

and making use of the transverse gauge $\partial^\mu \bar{h}_{\mu\nu} = 0$, at first order one obtains

$$G^{(1)}_{\mu\nu} \equiv -\frac{1}{2}\Box\bar{h}_{\mu\nu}.$$

This means that, under the approximation hereby considered, the modified Einstein equation Eq. (A.1) becomes

$$-\frac{1}{2}\Box\bar{h}_{\mu\nu} = \frac{8\pi G_N}{c^4}T_{\mu\nu} \quad \to \quad \Box\bar{h}_{\mu\nu} = -\frac{16\pi G_N}{c^4}\left[T^{\phi}_{\mu\nu} + \epsilon T^{NMC}_{\mu\nu}\right].$$

For the h_{00} component of the perturbation tensor it holds that

$$\Box h_{00} = \frac{1}{2}\left(\Box\bar{h}_{00} + \Box\bar{h}_{11} + \Box\bar{h}_{22} + \Box\bar{h}_{33}\right).$$

Knowing that in weak gravity $h_{00} = -2/c^2\Phi$, with Φ being the Newtonian gravitational potential, one eventually gets

$$\Box\Phi = -\frac{c^4}{4}\left(\Box\bar{h}_{00} + \Box\bar{h}_{11} + \Box\bar{h}_{22} + \Box\bar{h}_{33}\right) = \frac{4\pi G}{c^2}(T_{00} + T_{11} + T_{22} + T_{33}), \tag{C.1}$$

with T_{ij} being the total effective SET appearing in Eq. (3.8). When inserted in the linearised Einstein equations, such SET has to be taken at zeroth order in h in the metric expansion. This will mean that covariant derivatives will be reduced to partial derivatives, and the metric tensor will coincide with the flat, Minkowski one $\eta_{\mu\nu}$. Furthermore, the curvature terms in Eq. (3.8) will vanish.

While for simplicity, the NMC formalism was until now presented in terms of a real scalar field, the coupling can be easily generalized to a complex scalar field as $\widetilde{G}^{\mu\nu}\nabla_\mu\varphi\nabla_\nu\varphi^\dagger$. Considering a complex scalar field renders it possible to adopt the Madelung (1926) representation so that the scalar field can be represented as a fluid (see also Sec. (2.2.4)). In the Madelung approximation, the field is split into two real components: a modulus ρ representing the probability density associated with the field and a phase θ, reading as $\varphi = \sqrt{\rho}e^{i\theta}$. Under this approximation, the scalar field's SET can be rewritten as (see Bettoni et al. 2014)

$$T^{\phi}_{\mu\nu} = \nabla_\mu\phi^\dagger\nabla_\nu\phi + \nabla_\mu\phi\nabla_\nu\phi^\dagger - g_{\mu\nu}\left(g^{\alpha\beta}\nabla_\alpha\phi^\dagger\nabla_\beta\phi + V(\phi)\right).$$

In the weak field limit, this expression changes to

$$T_{\mu\nu} = \rho u_\mu u_\nu - \eta_{\mu\nu}\left(\rho\frac{c^2+u^2}{2} + V(\phi)\right) + \frac{\hbar^2}{m^2}\partial_\mu\sqrt{\rho}\partial_\nu\sqrt{\rho}, \tag{C.2}$$

with the 4-vector[1] $u^\mu = \hbar/m\nabla^\mu\theta$. In this regime, the NMC SET instead becomes

$$\begin{aligned} T^{NMC}_{\mu\nu} =& L^2\partial_\mu\partial^\alpha\left(\frac{\hbar^2}{m^2}\partial_\alpha\sqrt{\rho}\partial_\nu\sqrt{\rho} + \rho u_\alpha u_\nu\right) \\ &- \frac{L^2}{2}\Box\left(\frac{\hbar^2}{m^2}\partial_\mu\sqrt{\rho}\partial_\nu\sqrt{\rho} + \rho u_\mu u_\nu\right) \\ &- \frac{L^2}{2}\eta_{\mu\nu}\partial^\alpha\partial^\beta\left(\frac{\hbar^2}{m^2}\partial_\alpha\sqrt{\rho}\partial_\beta\sqrt{\rho} + \rho u_\alpha u_\beta\right) \\ &+ \frac{L^2}{2}\left(\eta_{\mu\nu}\Box - \partial_\mu\partial_\nu\right)\left(\frac{\hbar^2}{m^2}\partial^\alpha\sqrt{\rho}\partial_\alpha\sqrt{\rho} + \rho u^2\right). \end{aligned} \tag{C.3}$$

In the left hand size of the linearised Einstein equations Eq. (C.1), the highest-order term in c is of order zero, and it will have to match the right hand side of the equation when sending $c \to +\infty$. In the non-relativistic limit, one has that $u^0 \to c$ and $\vec{u} \to \vec{v}$ (i.e., the 3-velocity of the fluid), and this dramatically reduces the number of terms that are relevant in the weak field limit. In fact, the highest order possible terms in c in both Eq. (C.2) and Eq. (C.3) are of order c^2. Hence, the only terms surviving in the Newtonian limit when $c \to +\infty$ are the ones of zero order, while the rest will go to zero.

By computing these terms and opening the box terms as a composition of time plus spatial derivatives, the following Poisson equation is eventually retrieved:

$$\boxed{\nabla^2\Phi = 4\pi G\left(\rho - \epsilon L^2\nabla^2\rho\right).}$$

From this equation, it is clear that the contribution to the gravitational potential by DM is determined not only by the DM density itself but also by its inhomogeneities.

[1]Note that the norm of this 4-vector is $u_\mu u^\mu = -c^2$. Hence, it cannot be considered a real velocity associated with the fluid. Such a four-velocity can indeed be obtained by defining the vector $v^\mu \equiv u^\mu/\sqrt{-u_\alpha u^\alpha}$, which has the right norm.

Appendix D

Stacked Rotation Curve fits

This Appendix contains the fits to stacked RCs for the whole galaxy samples presented in Sec. (3.4.1) (see Tab. (3.1)).

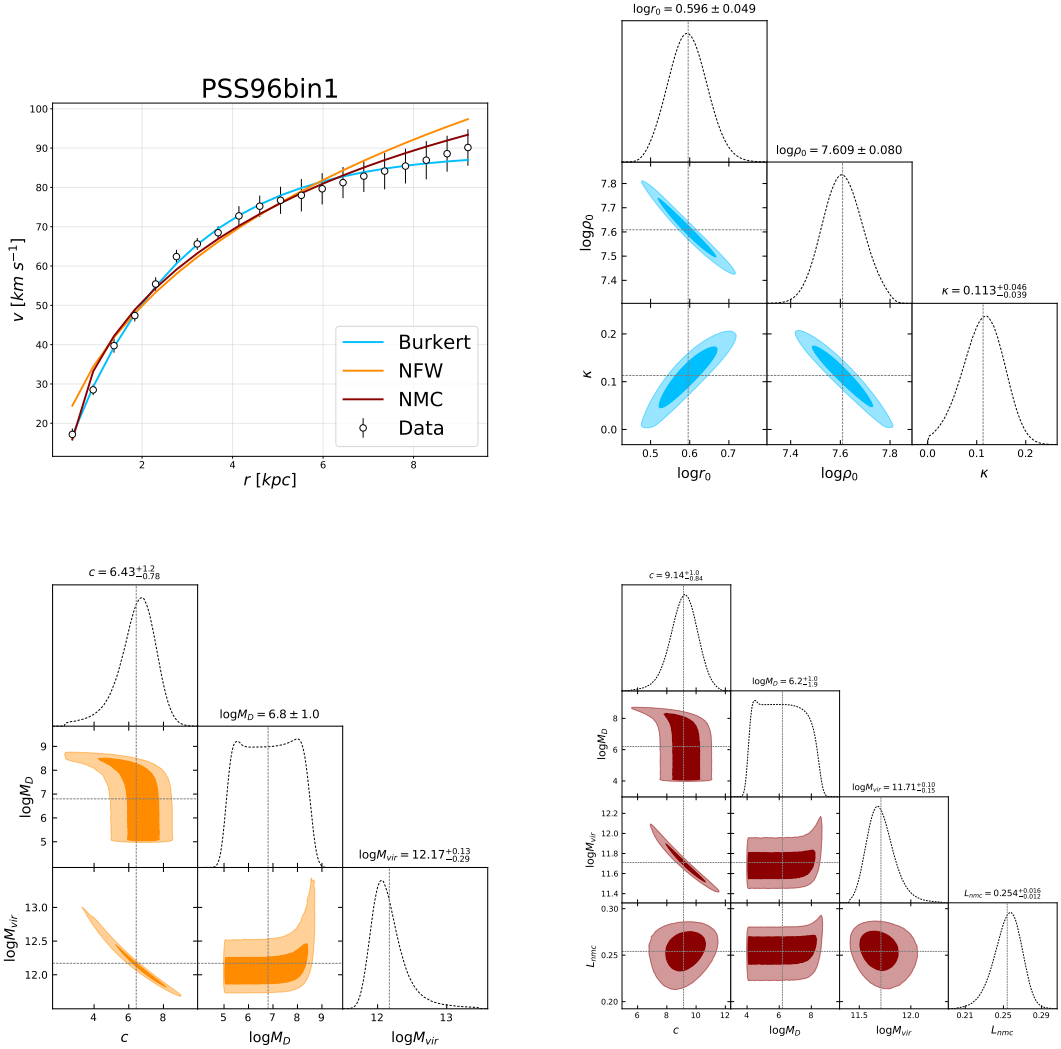

Figure D.1: Bin 1 of Persic & Salucci (1995).

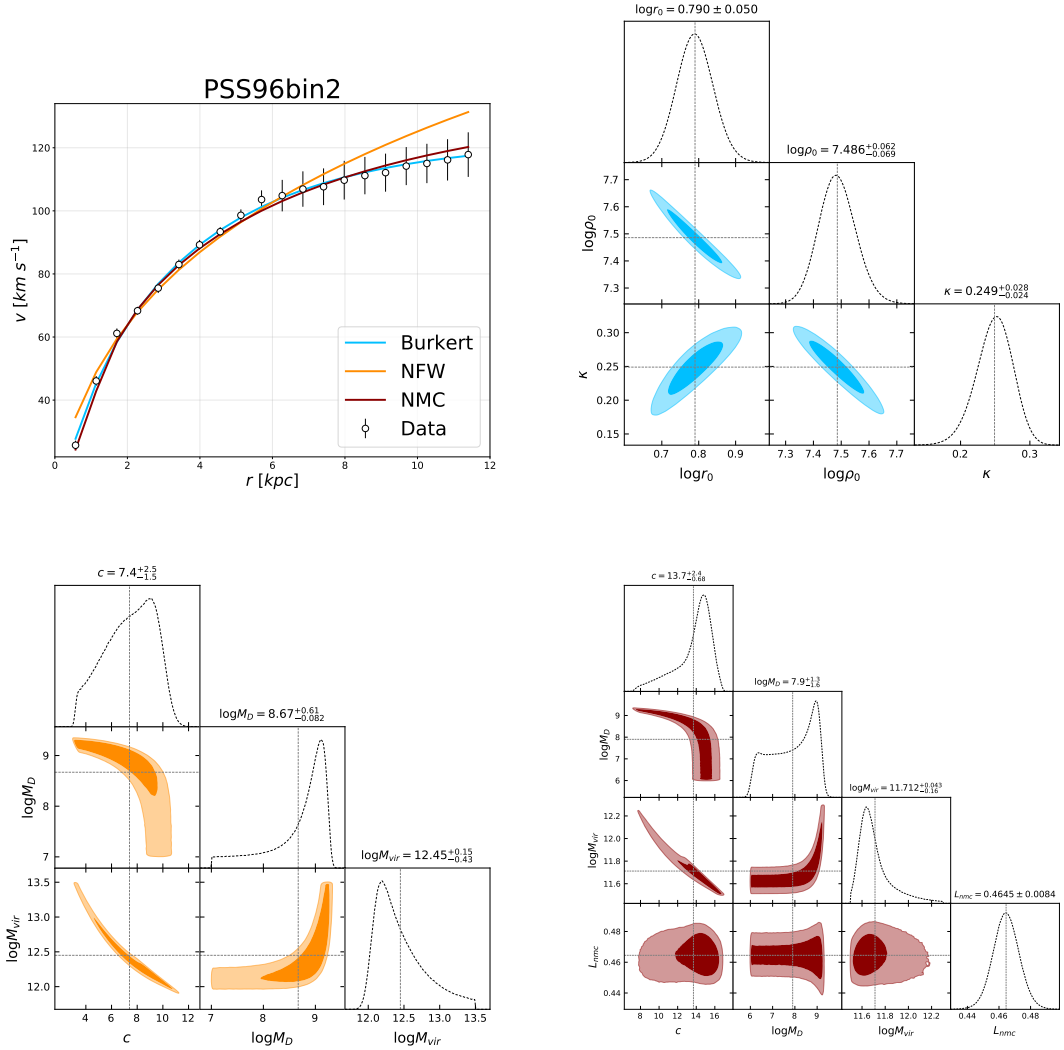

Figure D.2: Bin 2 of Persic & Salucci (1995).

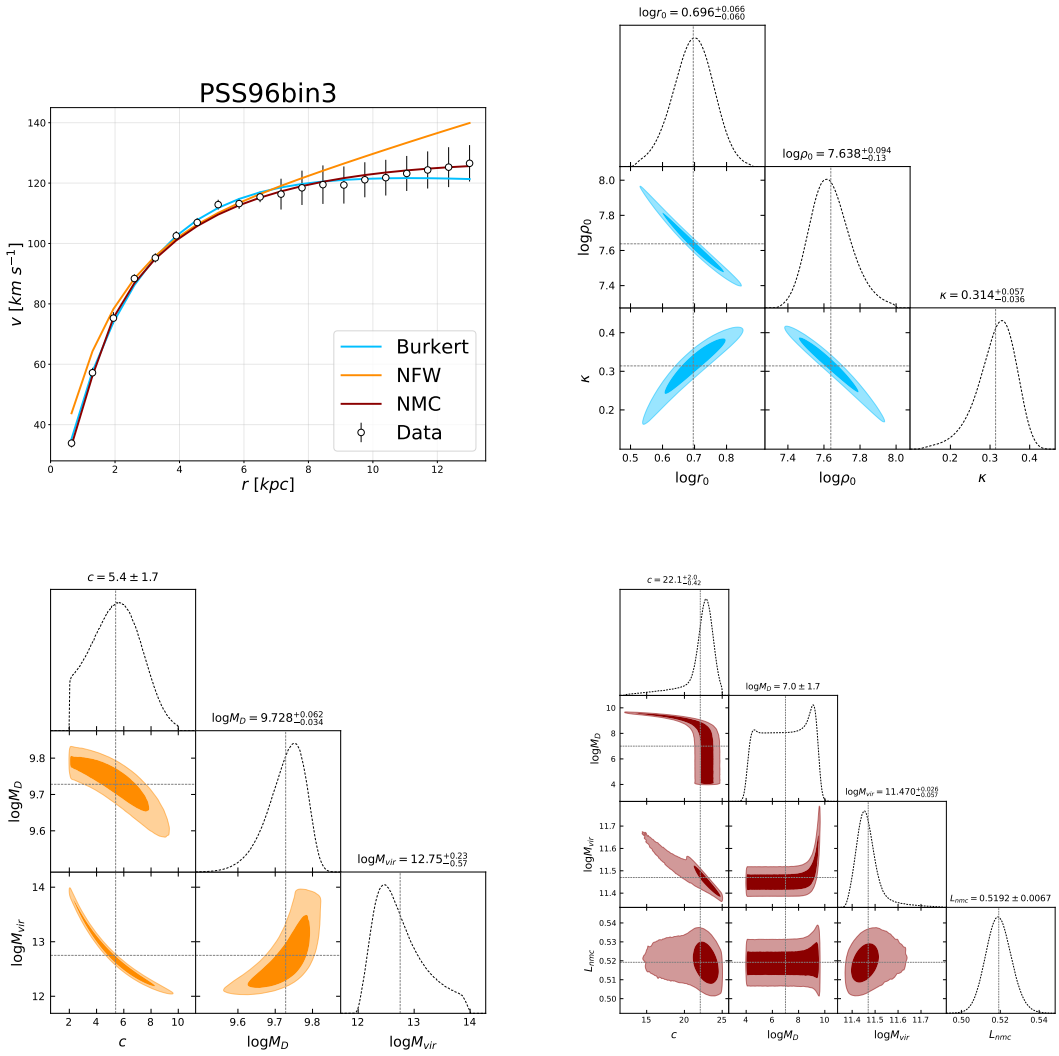

Figure D.3: Bin 3 of Persic & Salucci (1995).

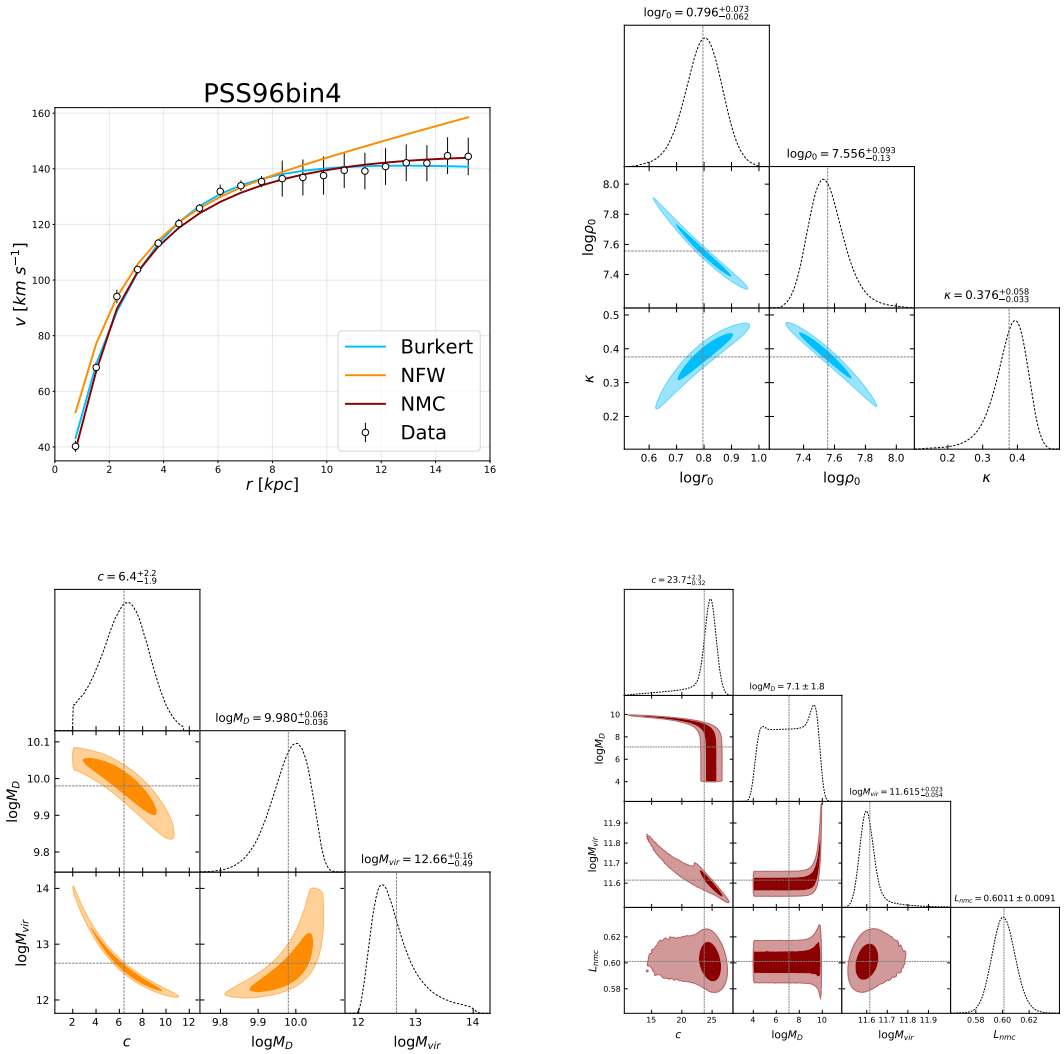

Figure D.4: Bin 4 of Persic & Salucci (1995).

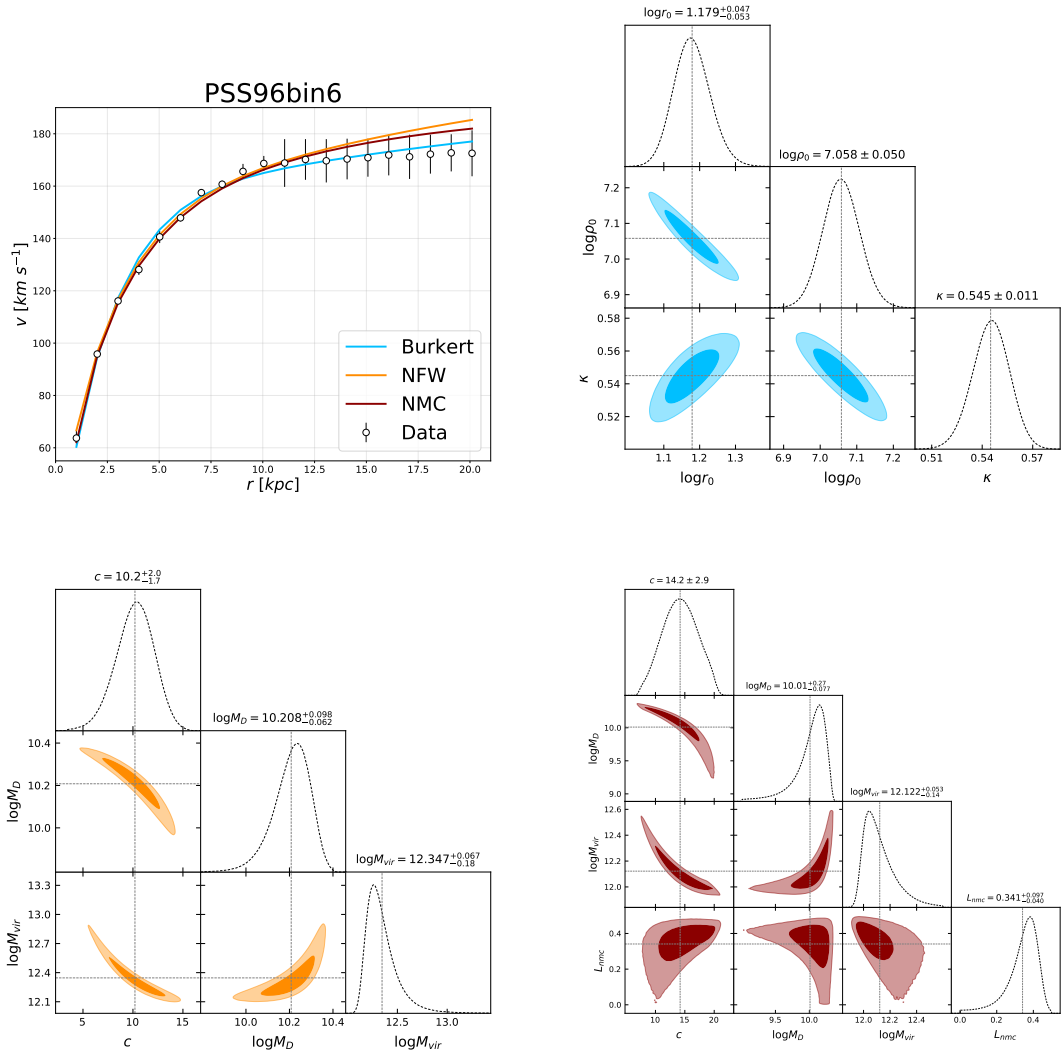

Figure D.5: Bin 6 of Persic & Salucci (1995).

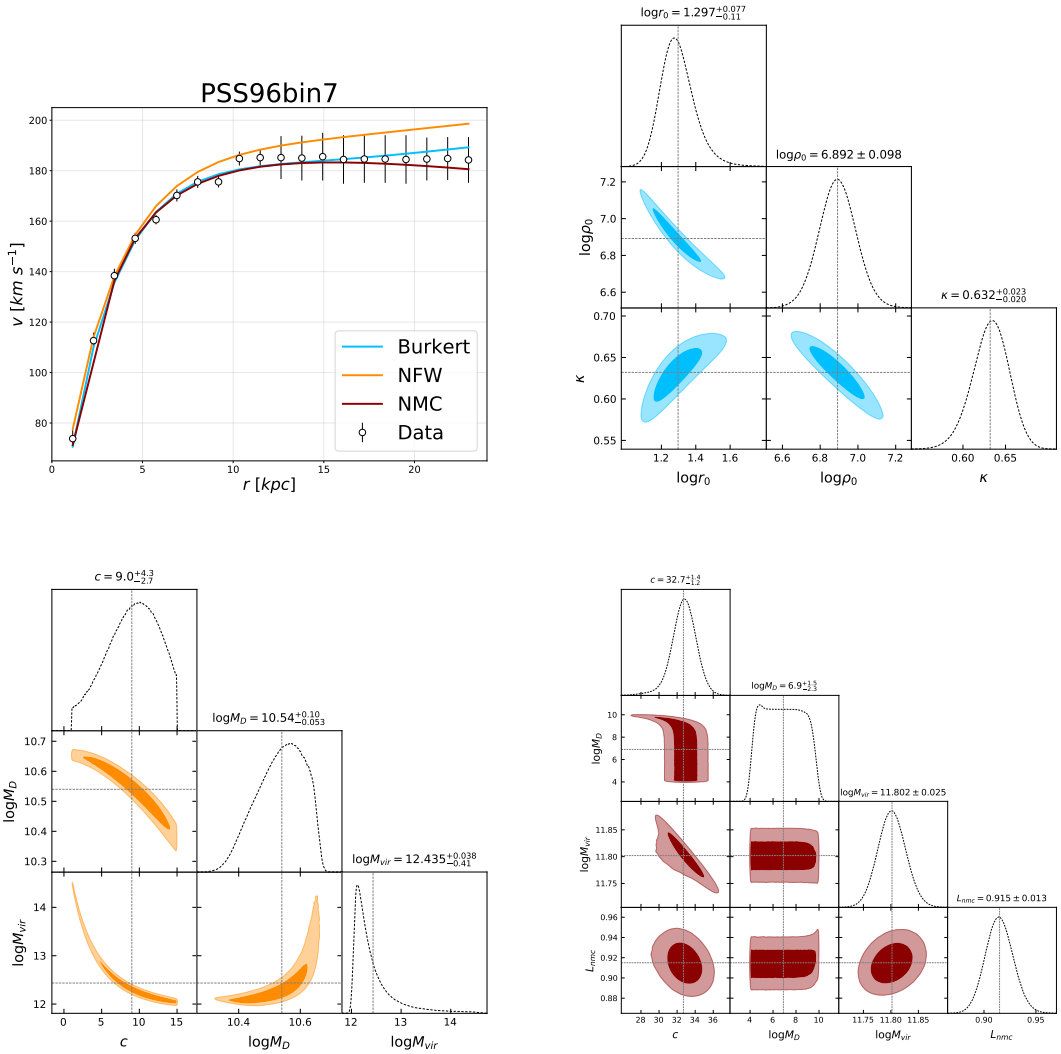

Figure D.6: Bin 7 of Persic & Salucci (1995).

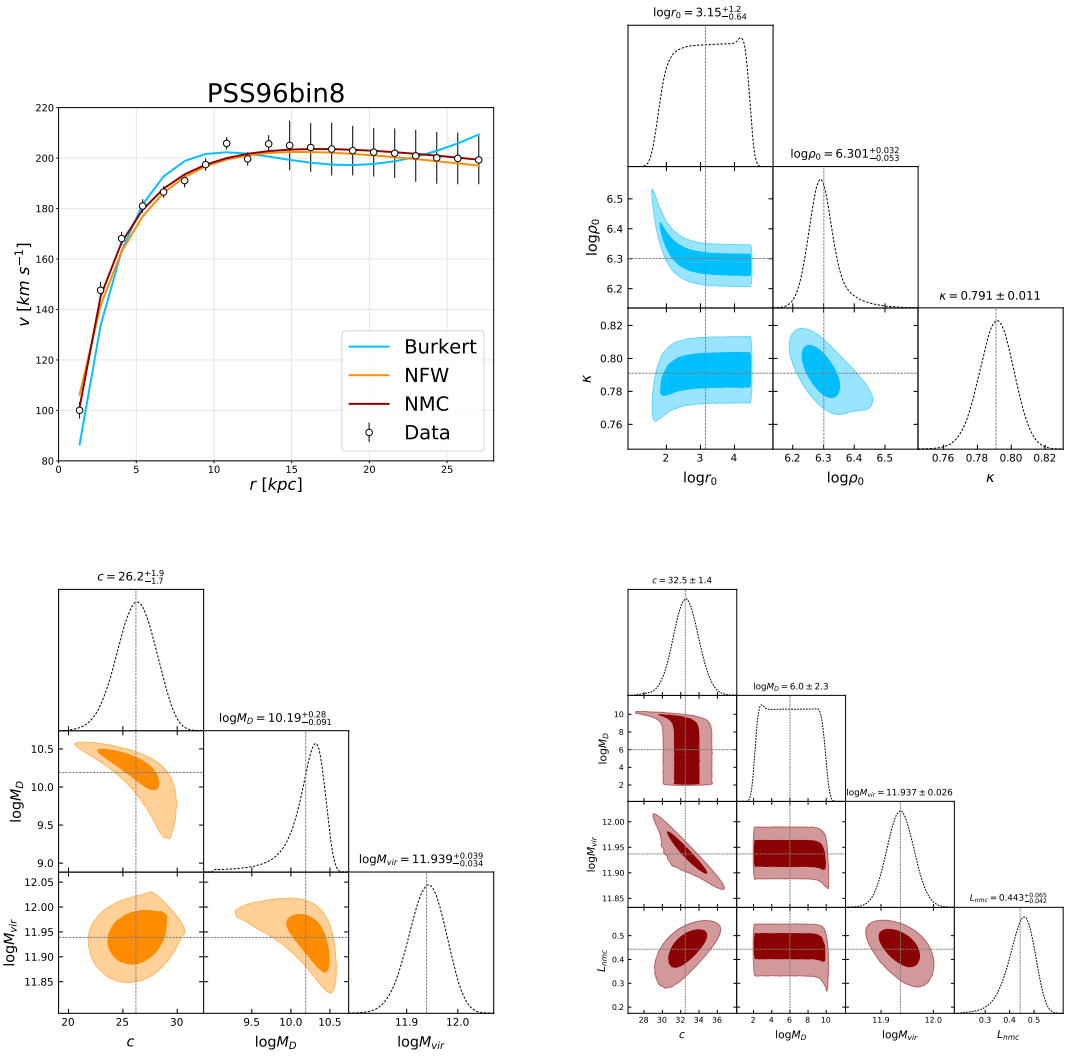

Figure D.7: Bin 8 of Persic & Salucci (1995).

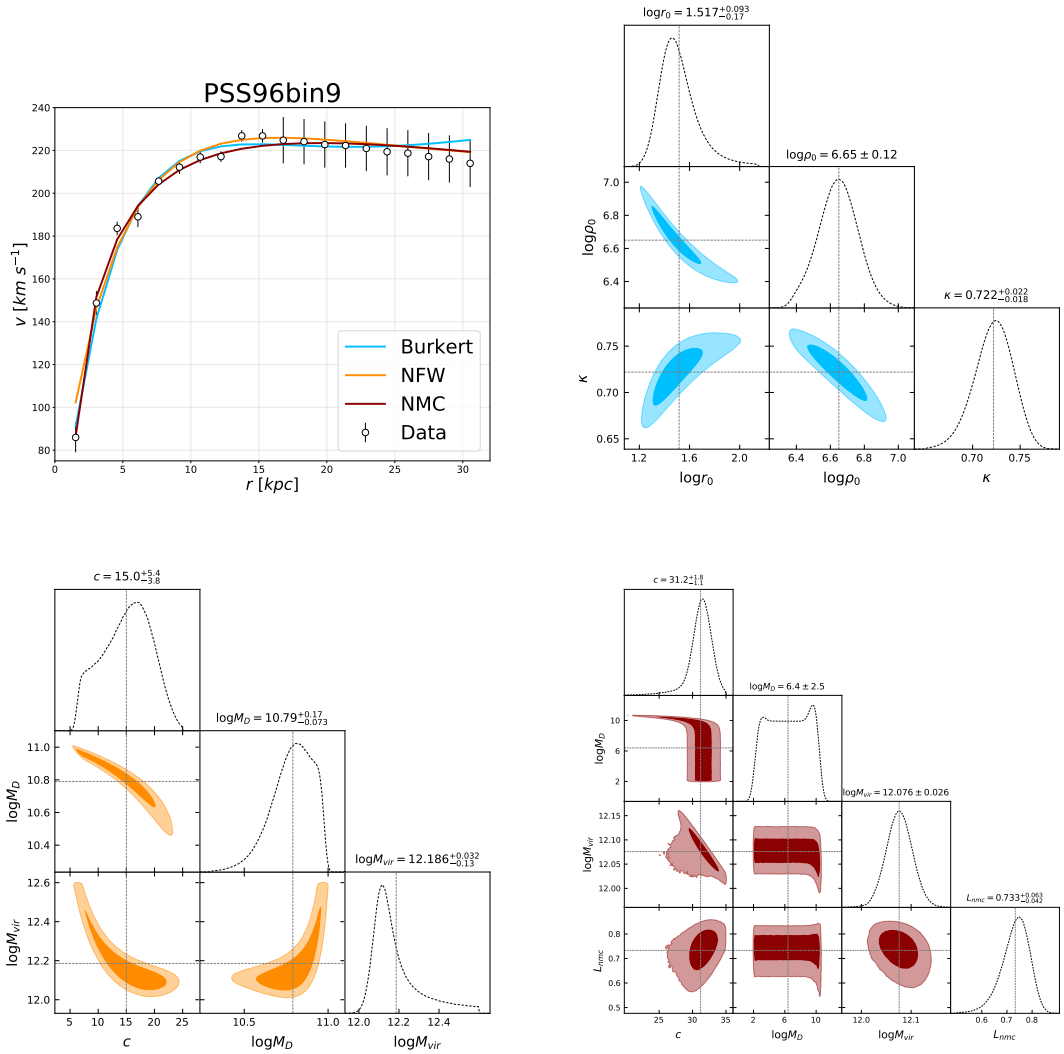

Figure D.8: Bin 9 of Persic & Salucci (1995).

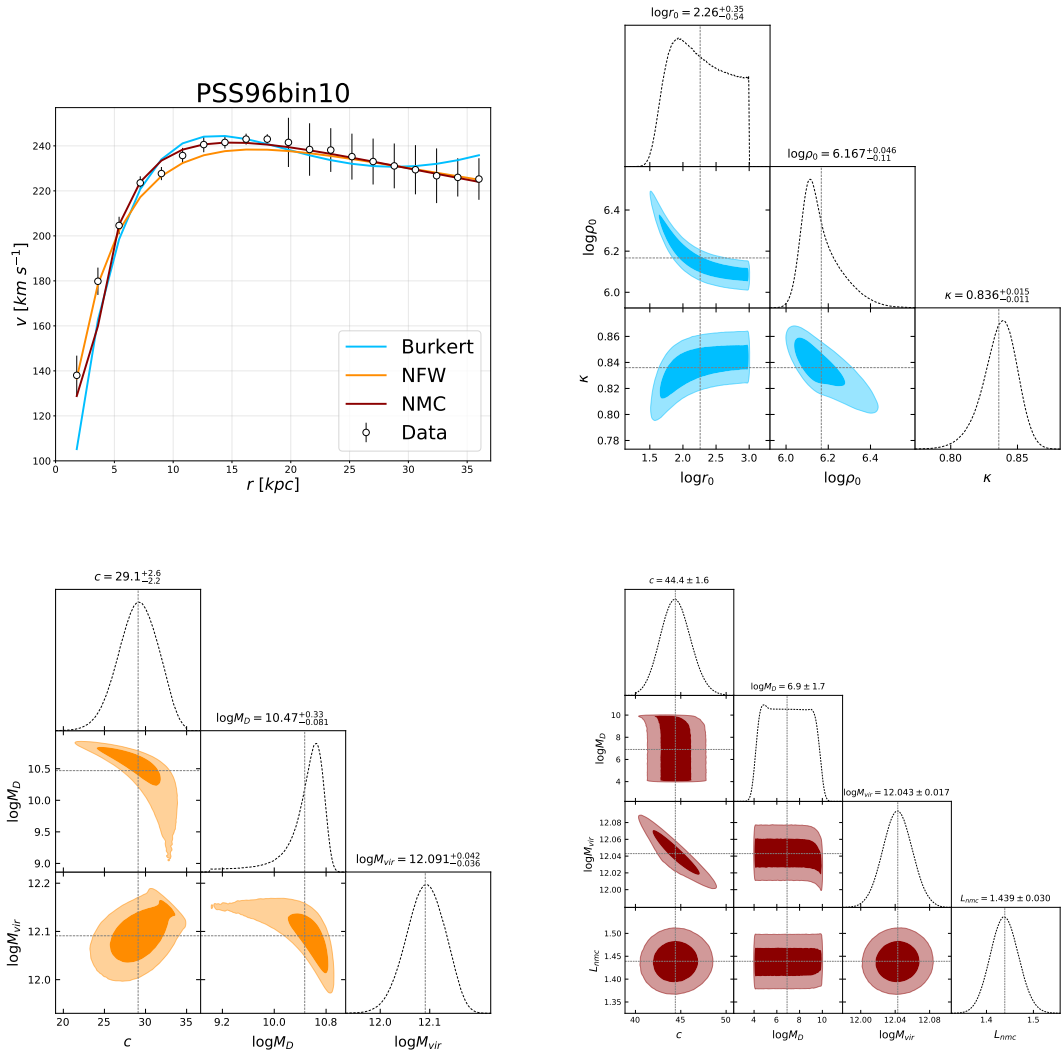

Figure D.9: Bin 10 of Persic & Salucci (1995).

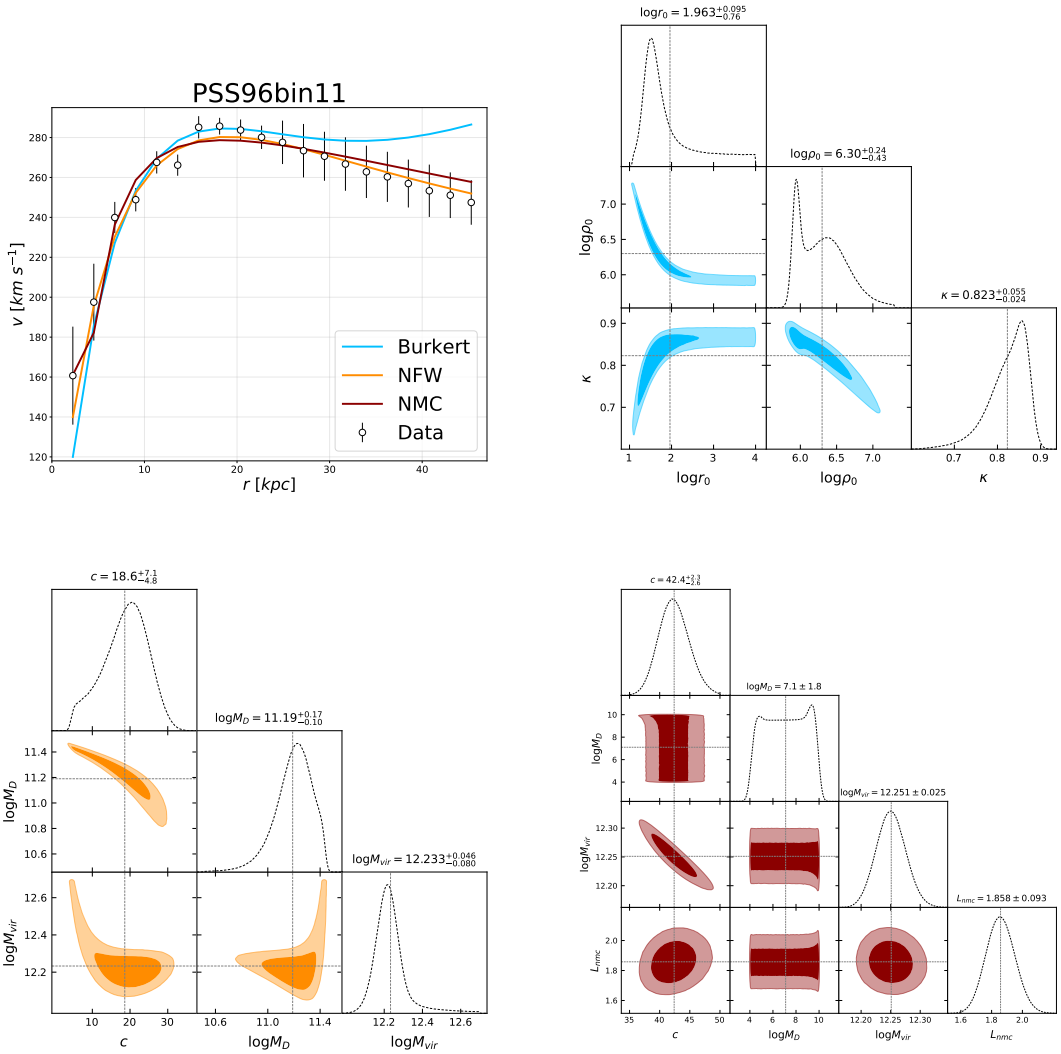

Figure D.10: Bin 11 of Persic & Salucci (1995).

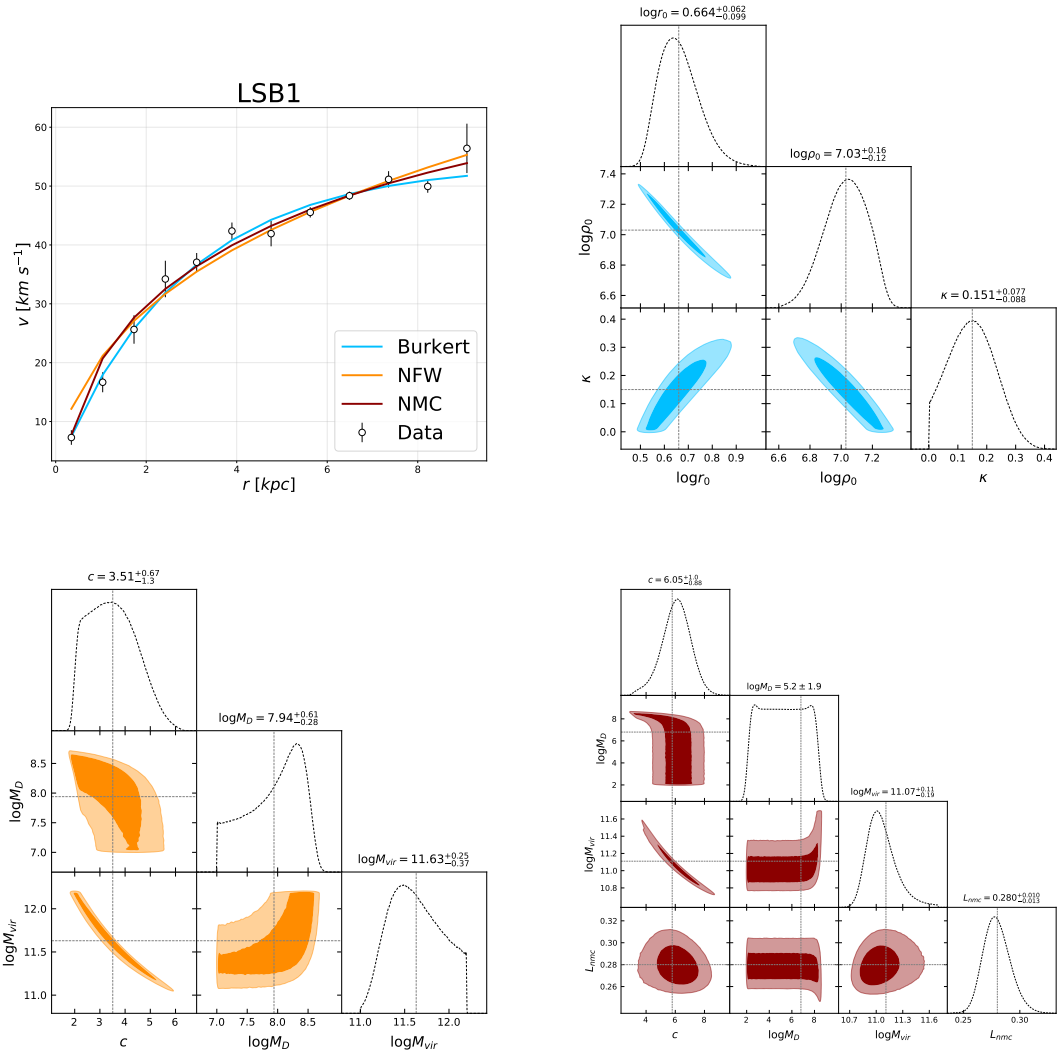

Figure D.11: Bin 1 of LSB galaxies of Dehghani et al. (2020).

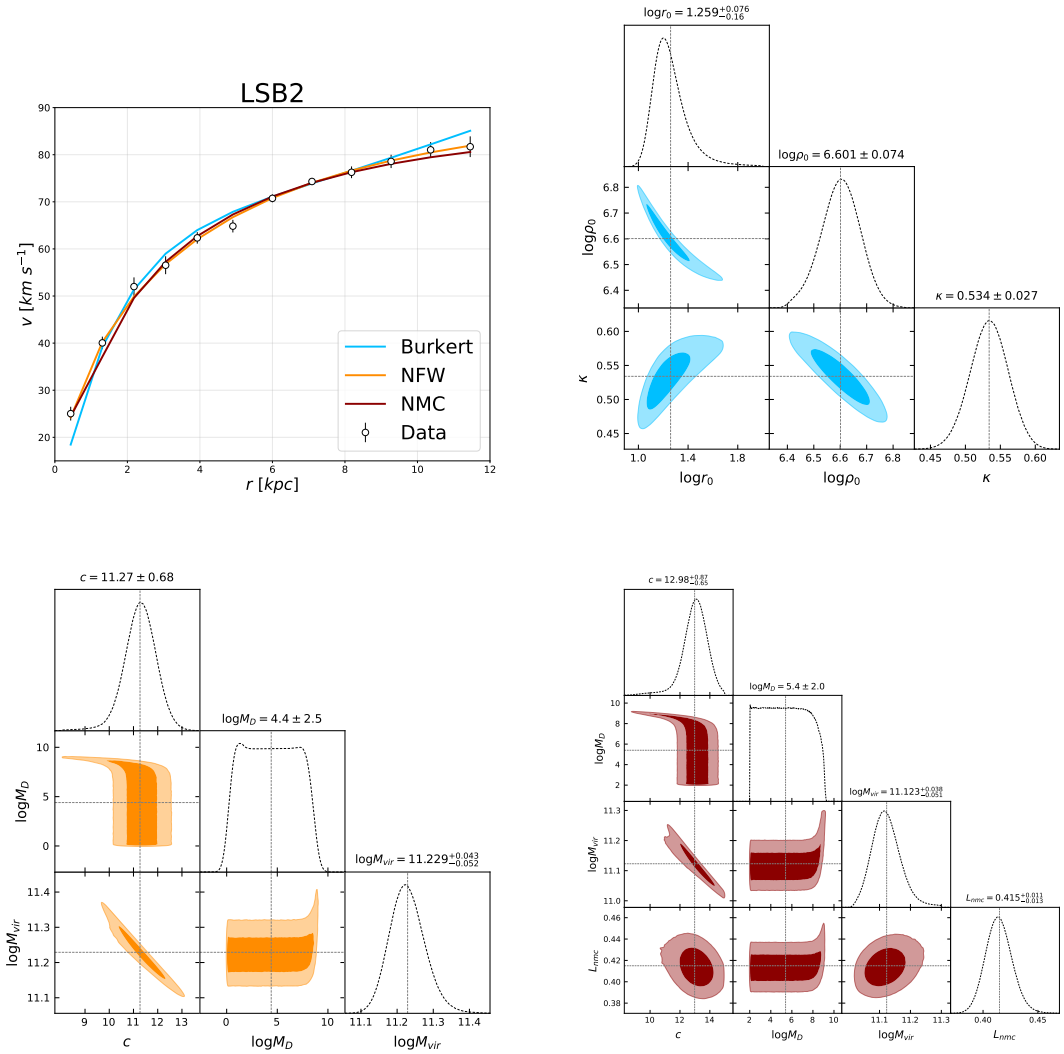

Figure D.12: Bin 2 of LSB galaxies of Dehghani et al. (2020).

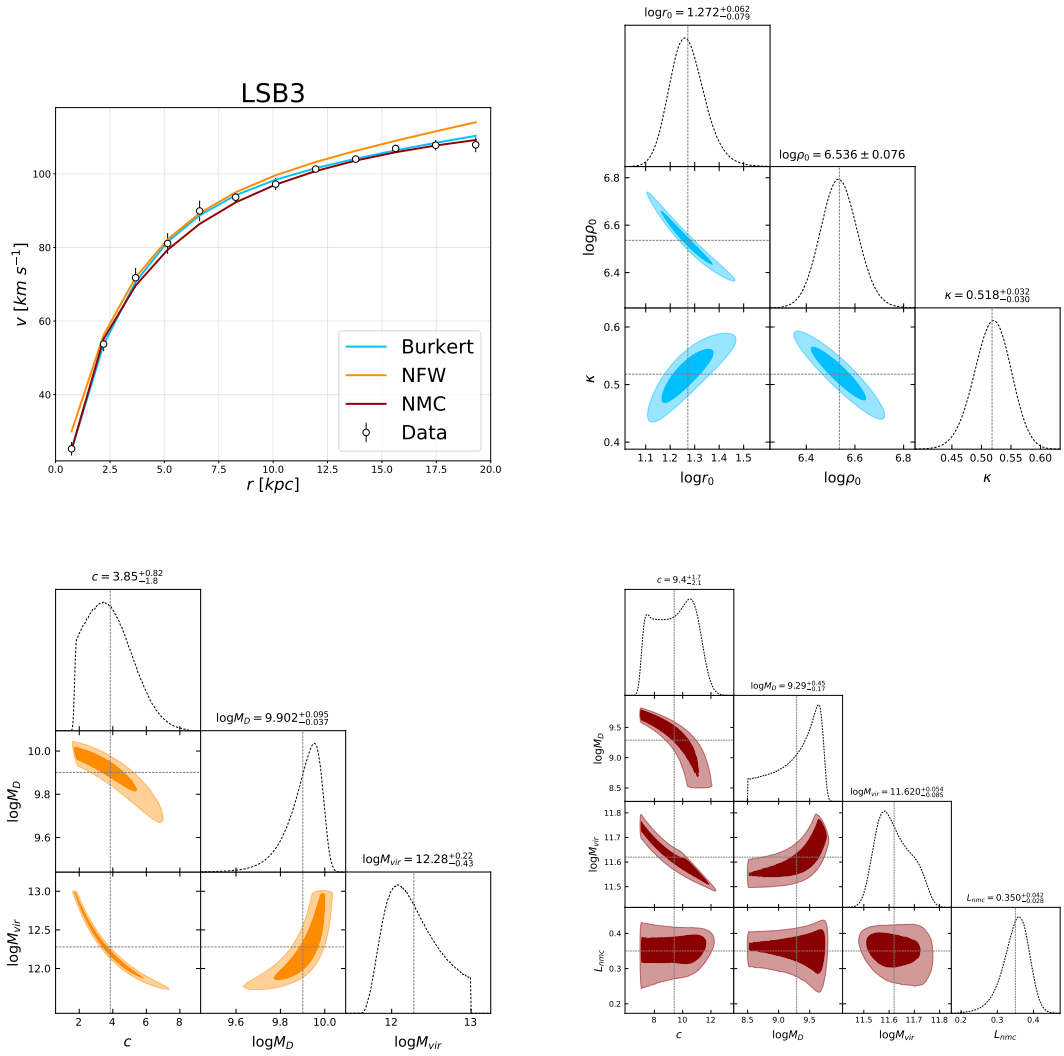

Figure D.13: Bin 3 of LSB galaxies of Dehghani et al. (2020).

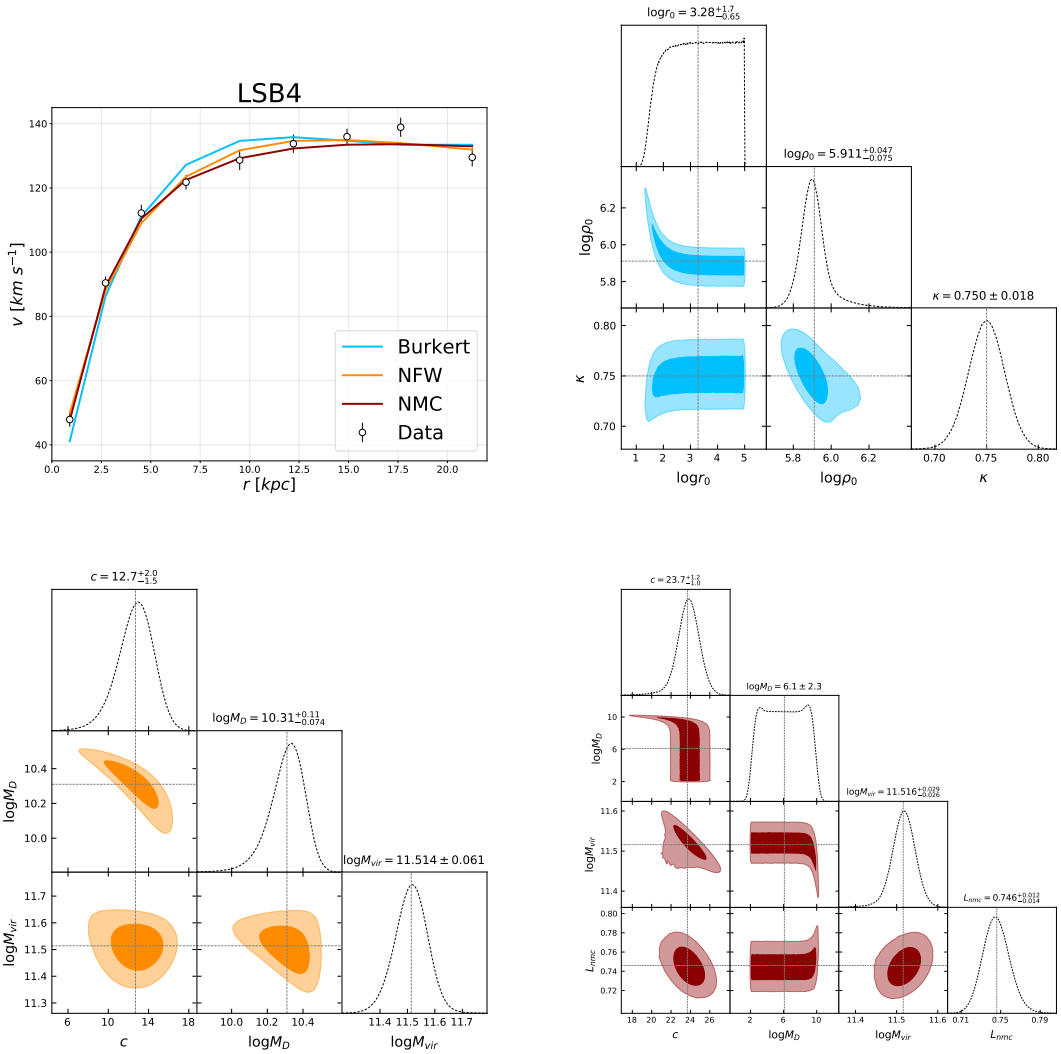

Figure D.14: Bin 4 of LSB galaxies of Dehghani et al. (2020).

Appendix E

Pressure profiles of the X-COP clusters

This Appendix contains the pressure profiles reconstructed for the NFW and NMC DM cases for each of the 12 clusters alongside the complete contour plots as in Sec. (3.5.2).

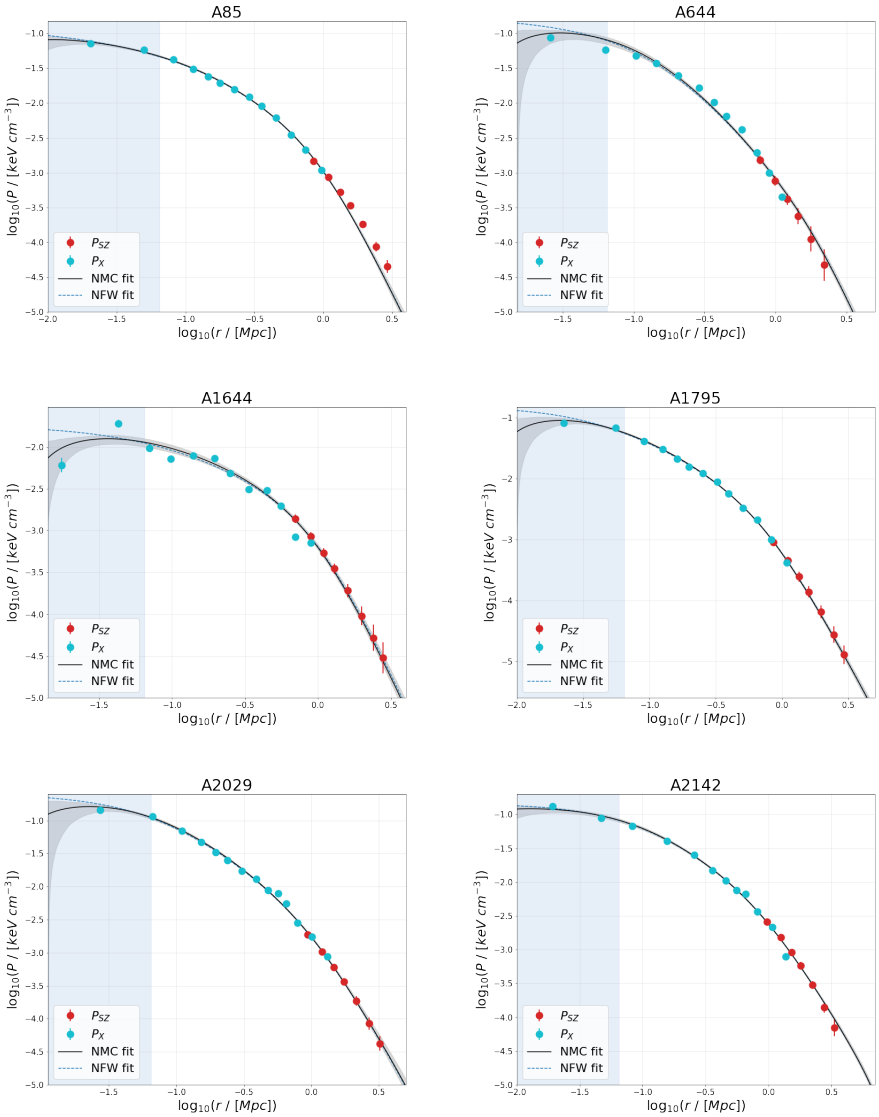

Figure E.1: Comparison of the pressure profiles for the NMC DM model (solid lines) against those of the NFW model (dashed grey lines) for all the 12 clusters in the X-COP compilation.

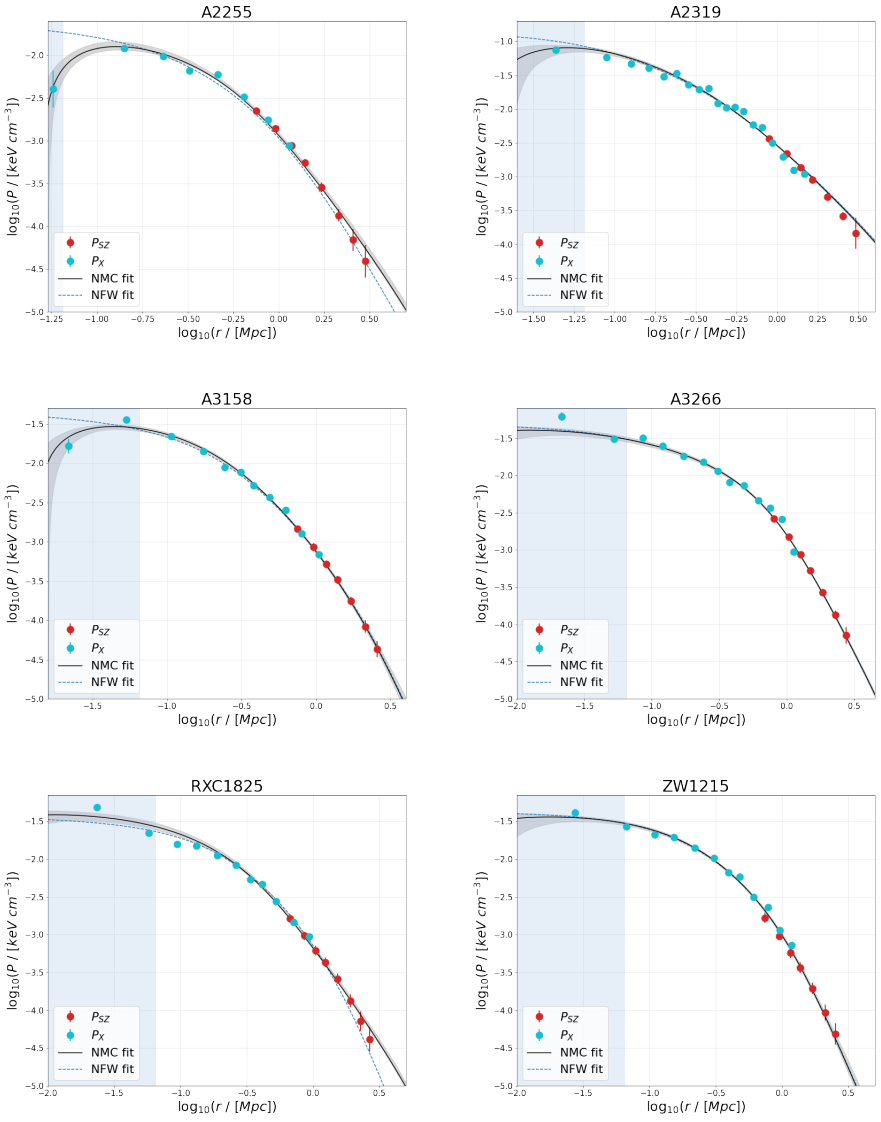

Figure E.2: Continuation of Fig. (E.1).

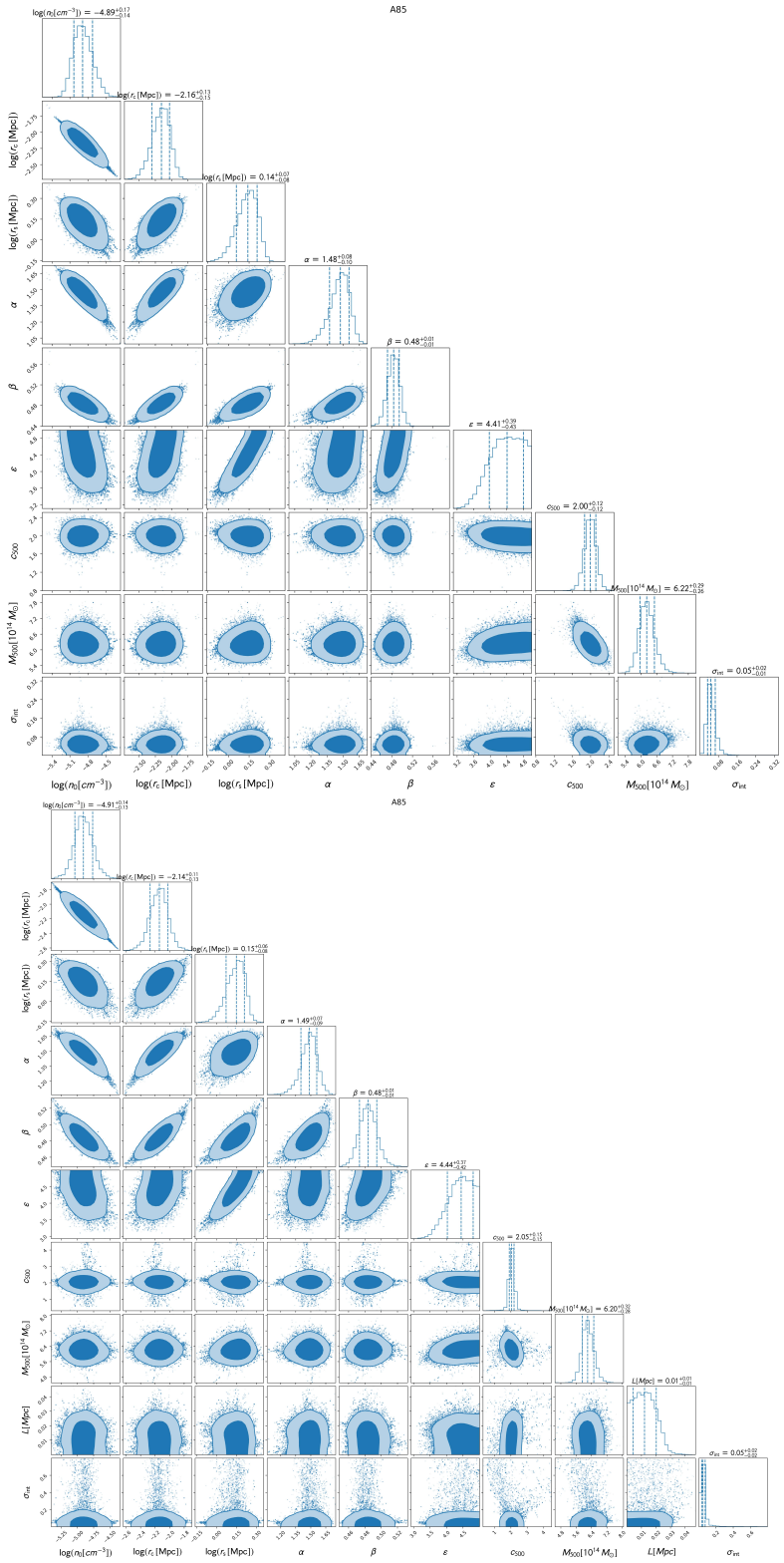

Figure E.3: A85 contour plots for the NFW pressure profile (top) and NMC DM pressure profile (bottom).

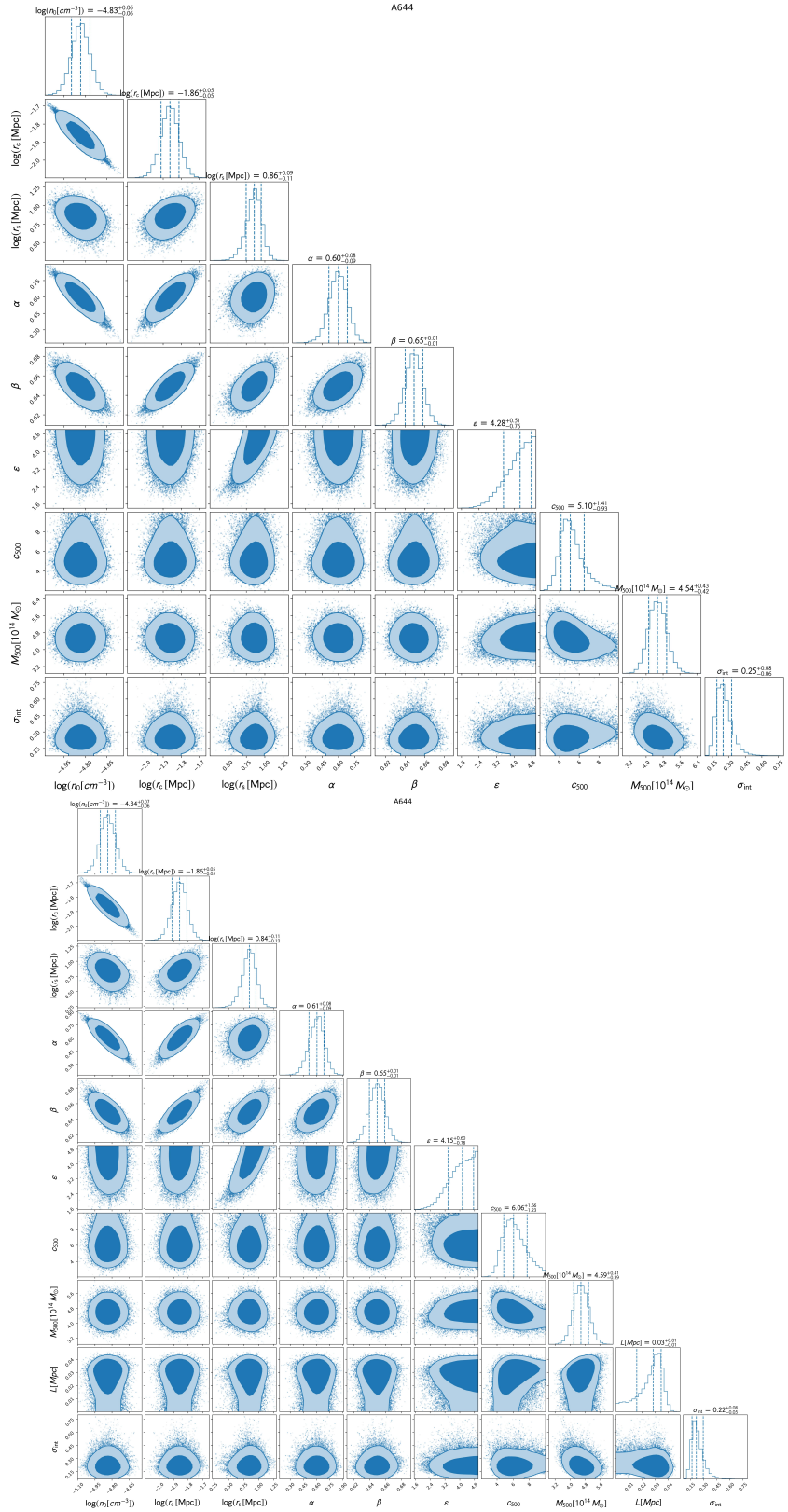

Figure E.4: A644 contour plots for the NFW pressure profile (top) and NMC DM pressure profile (bottom).

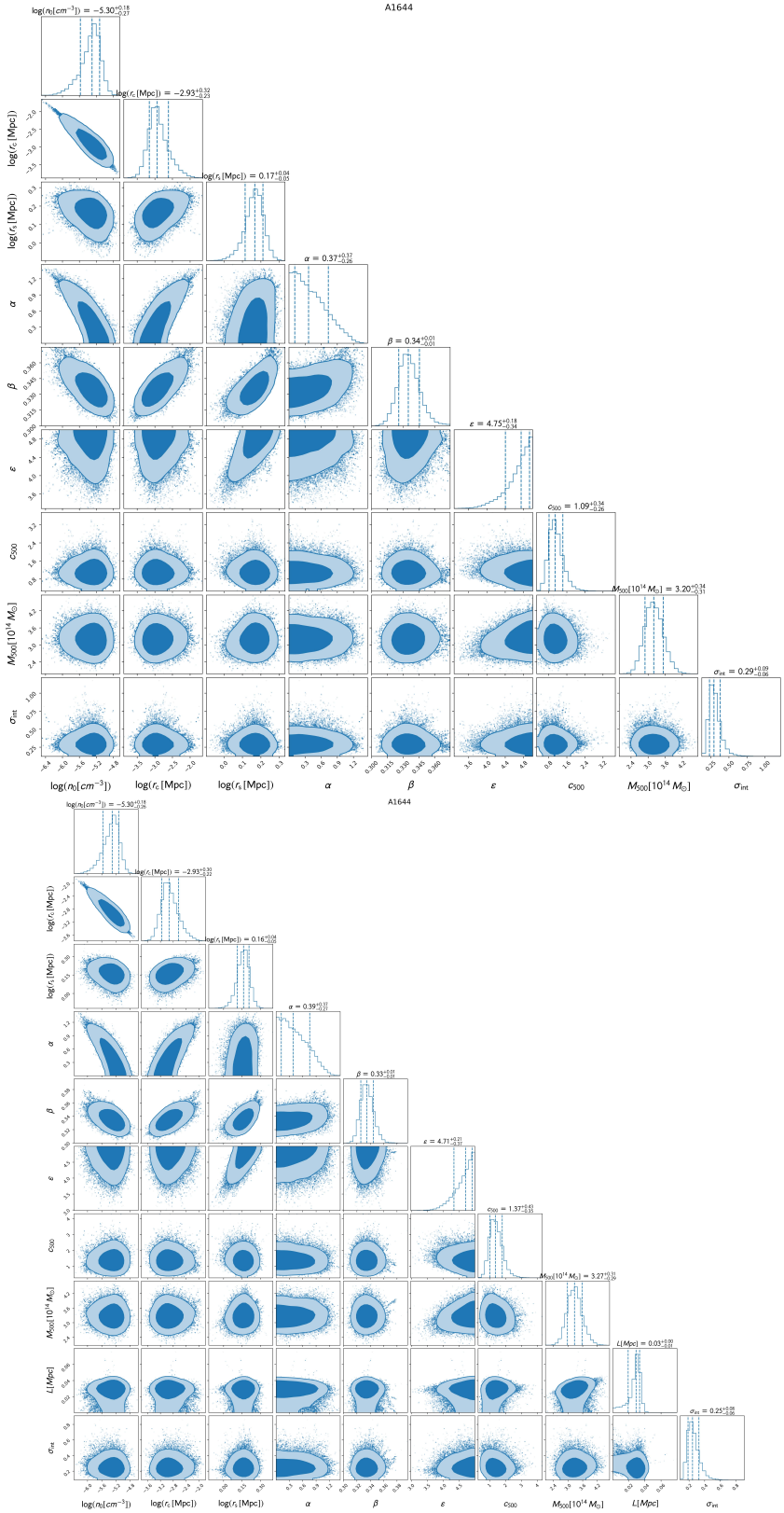

Figure E.5: A1644 contour plots for the NFW pressure profile (top) and NMC DM pressure profile (bottom).

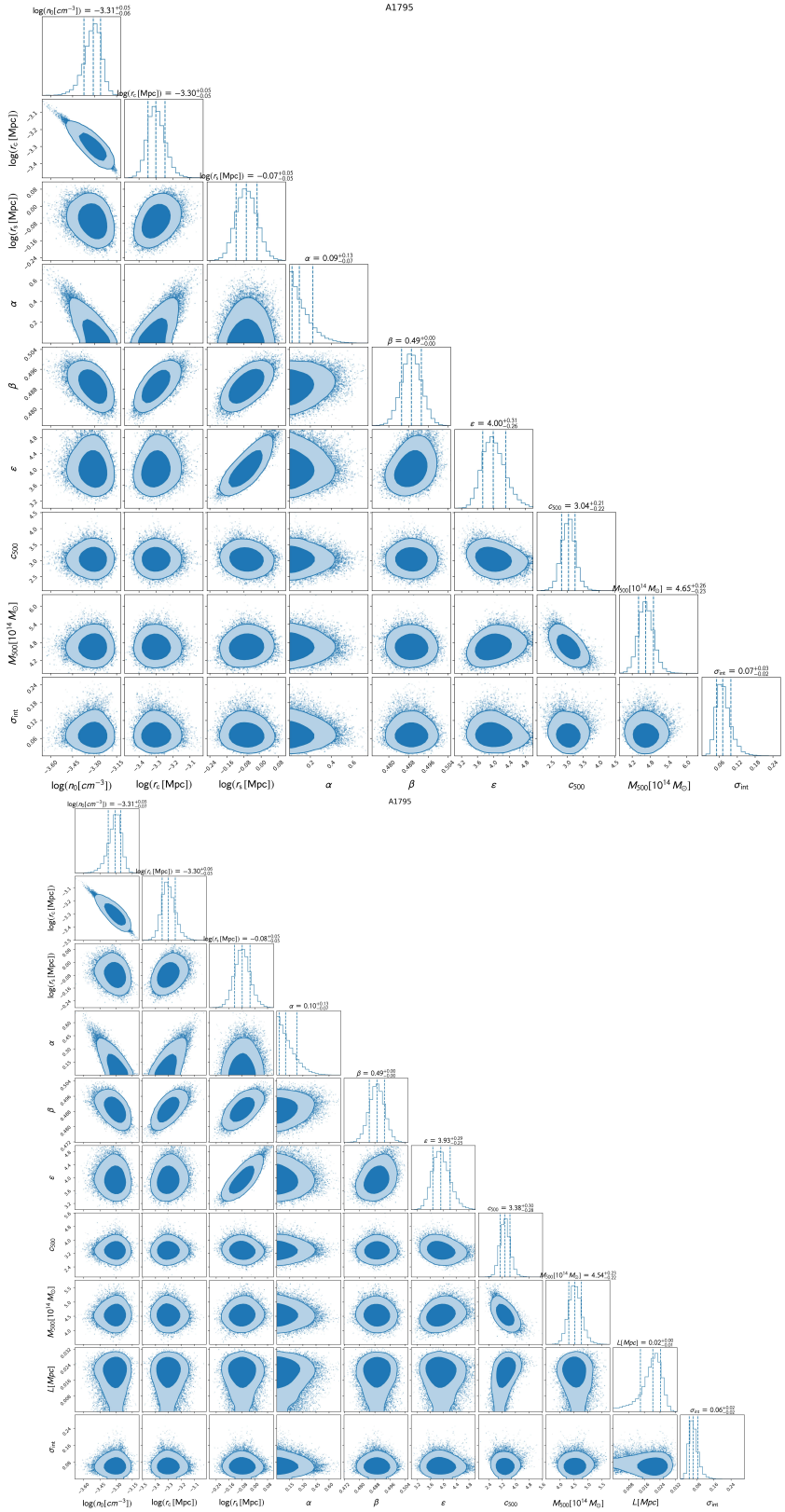

Figure E.6: A1795 contour plots for the NFW pressure profile (top) and NMC DM pressure profile (bottom).

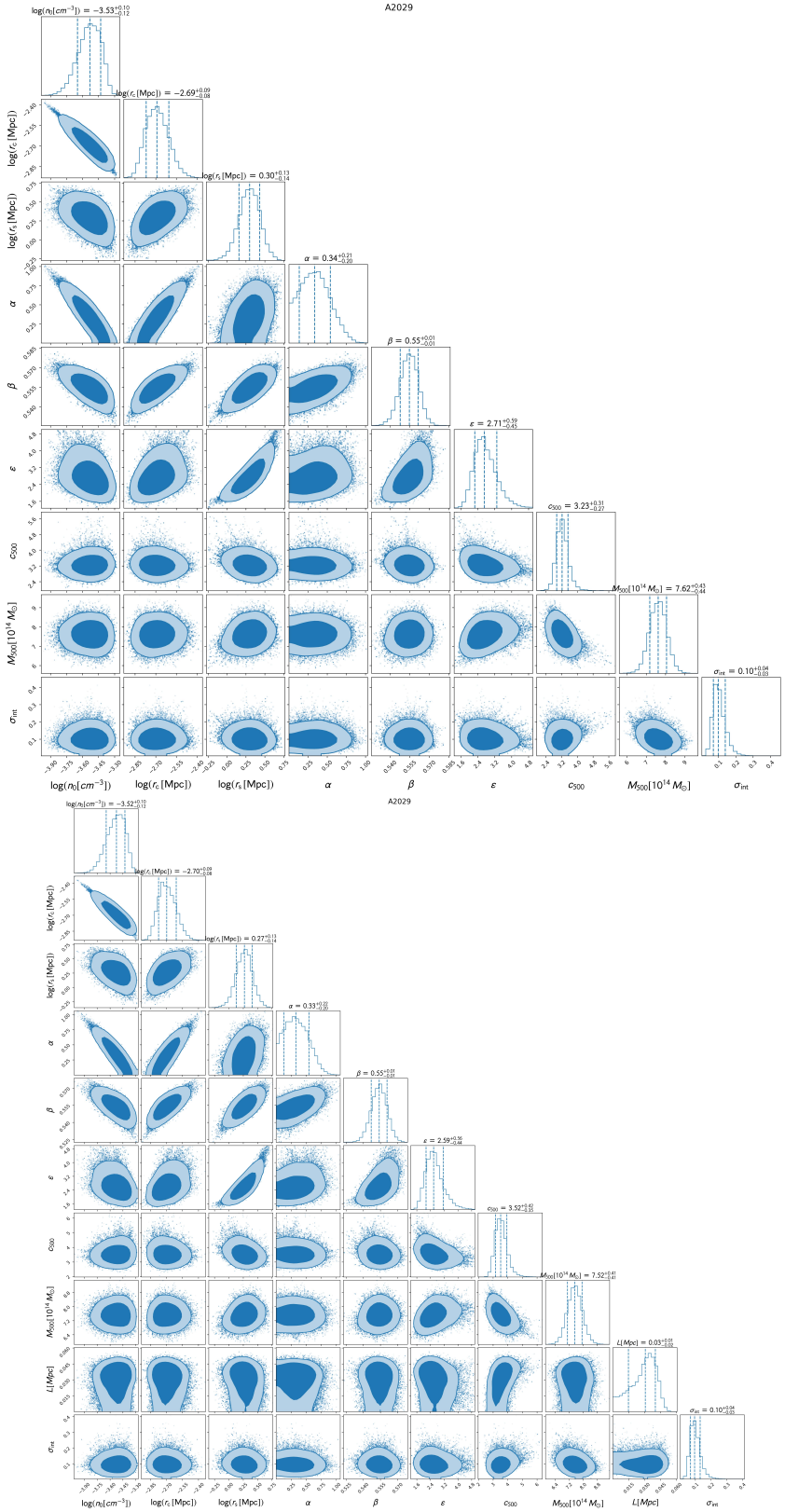

Figure E.7: A2029 contour plots for the NFW pressure profile (top) and NMC DM pressure profile (bottom).

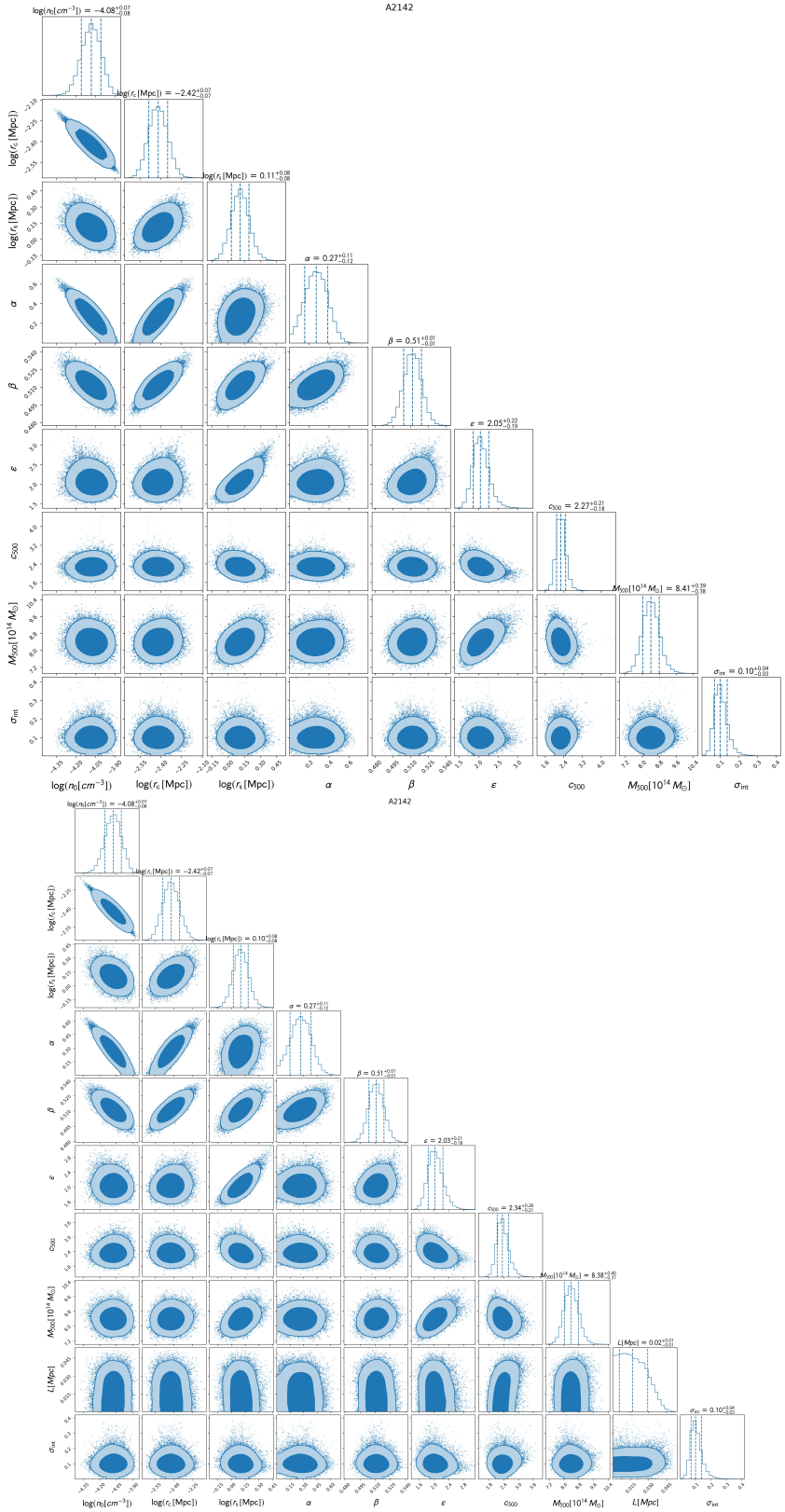

Figure E.8: A2142 contour plots for the NFW pressure profile (top) and NMC DM pressure profile (bottom).

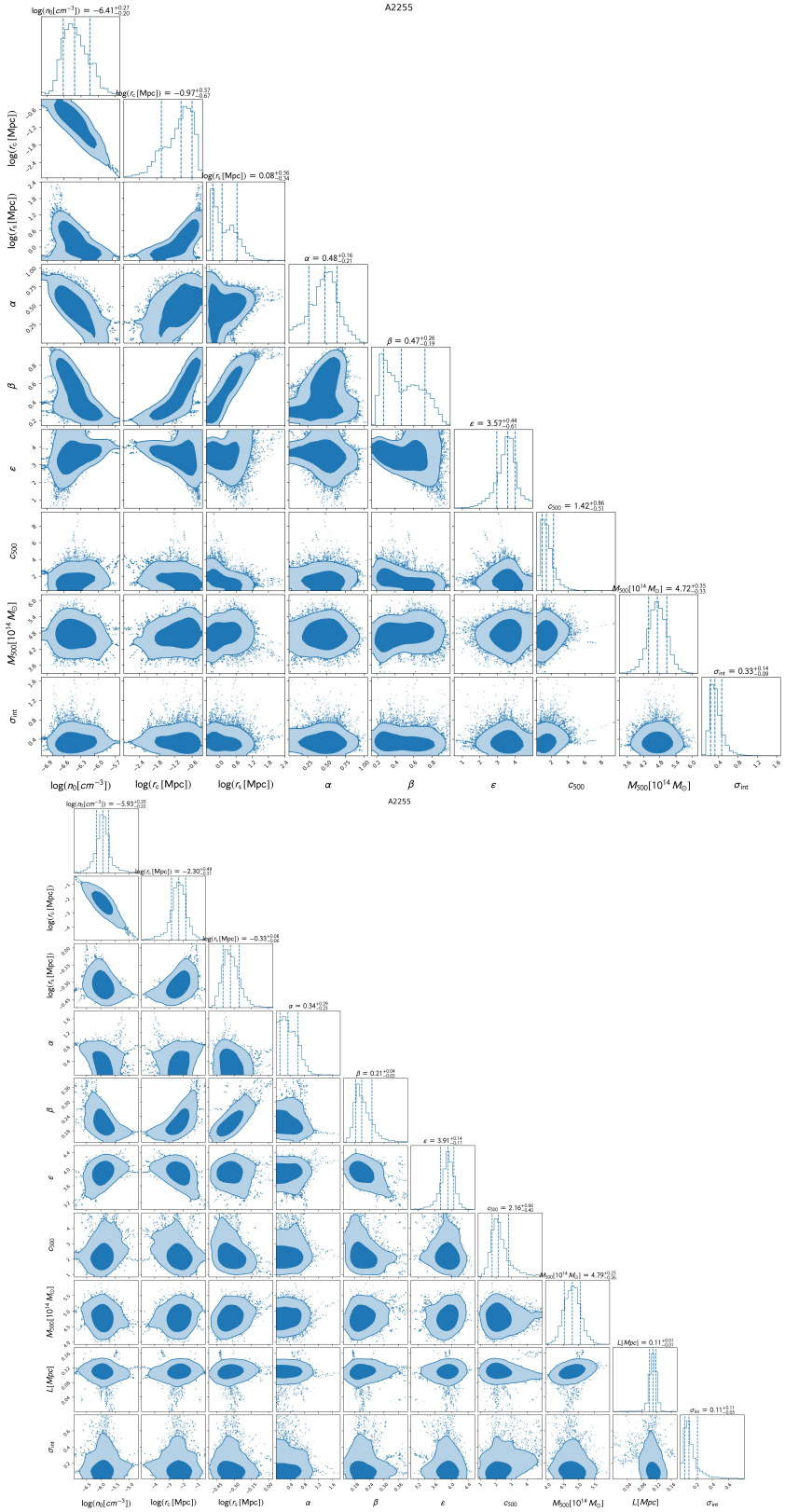

Figure E.9: A2255 contour plots for the NFW pressure profile (top) and NMC DM pressure profile (bottom).

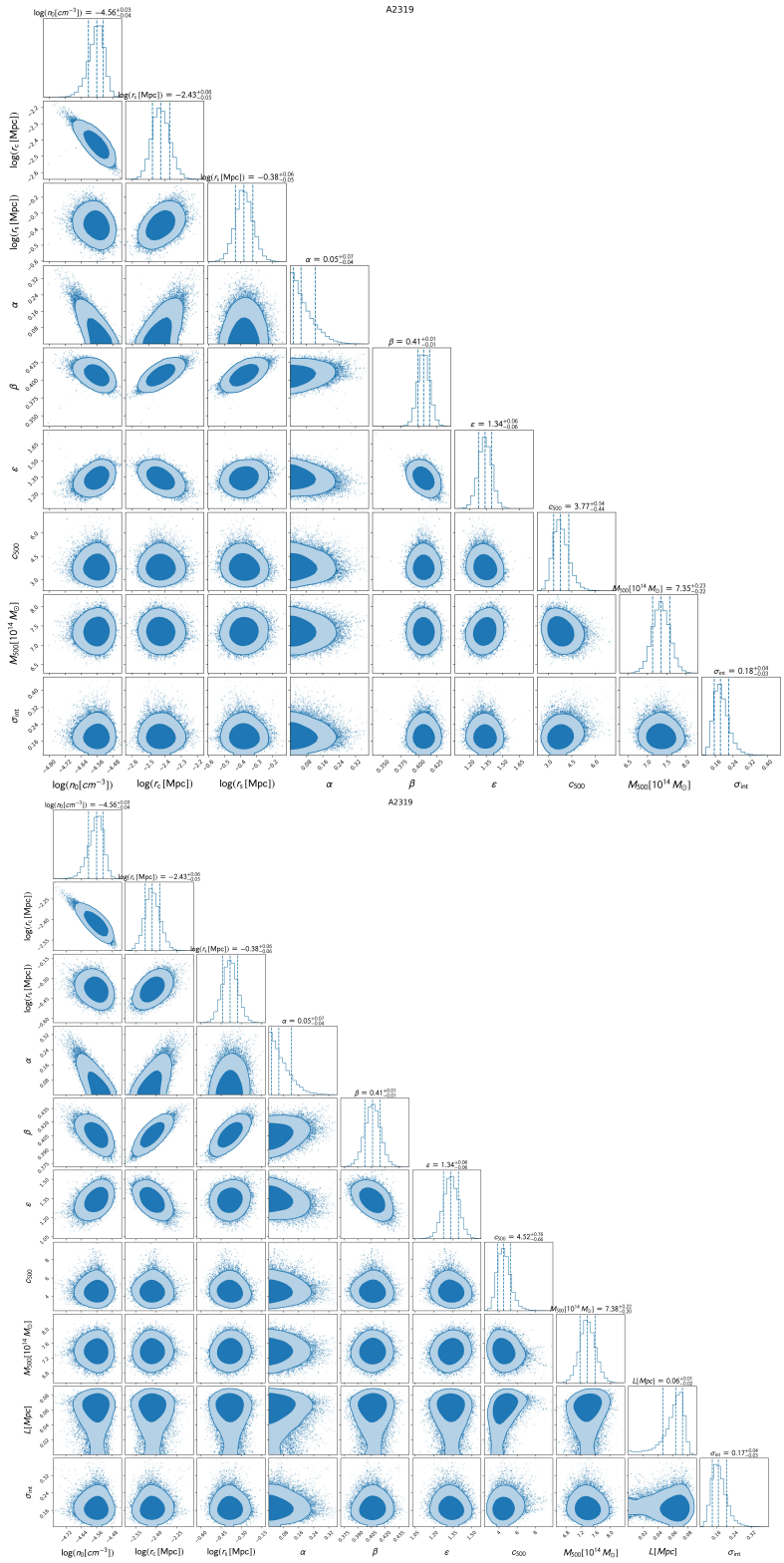

Figure E.10: A2319 contour plots for the NFW pressure profile (top) and NMC DM pressure profile (bottom).

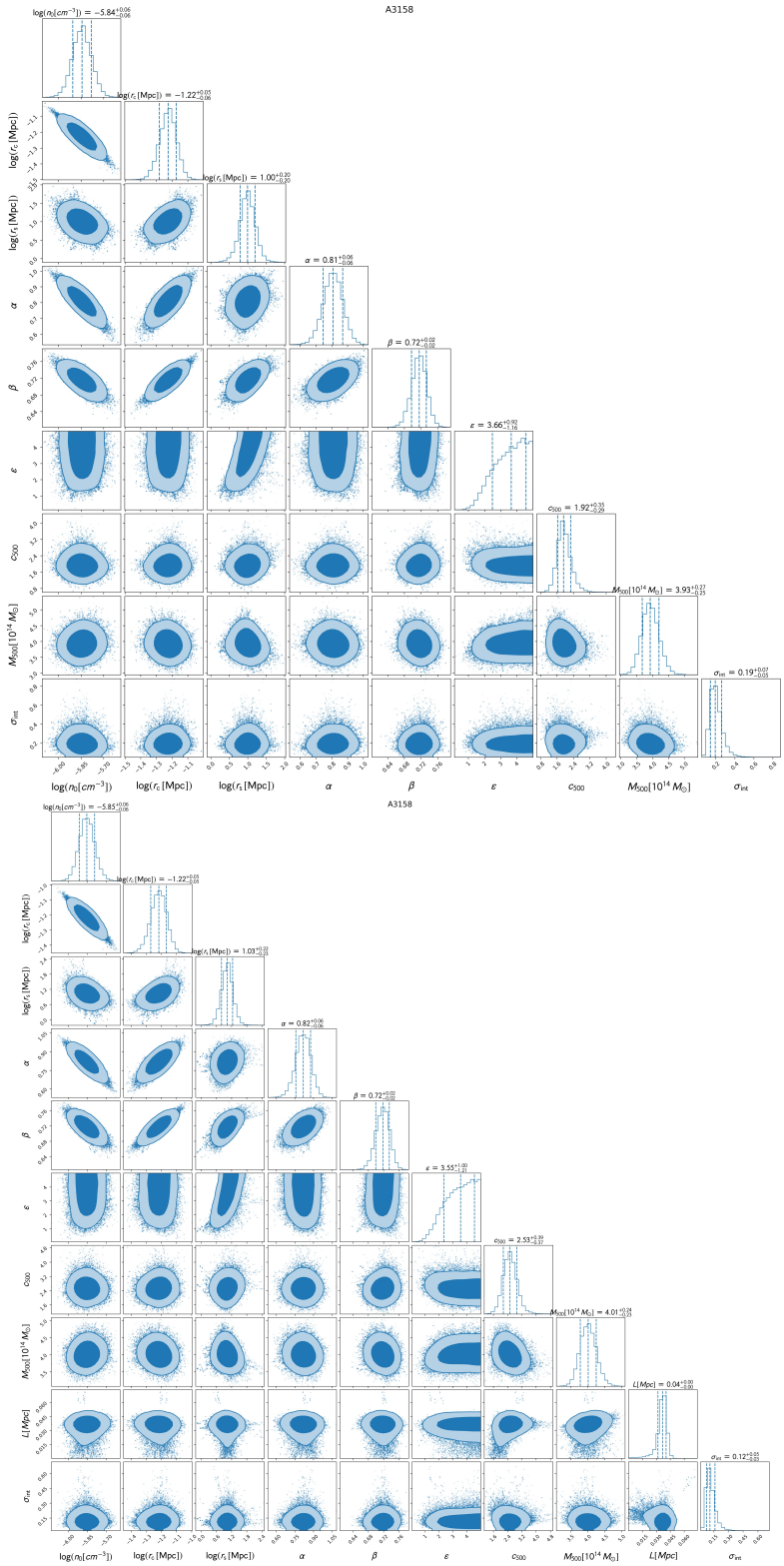

Figure E.11: A3158 contour plots for the NFW pressure profile (top) and NMC DM pressure profile (bottom).

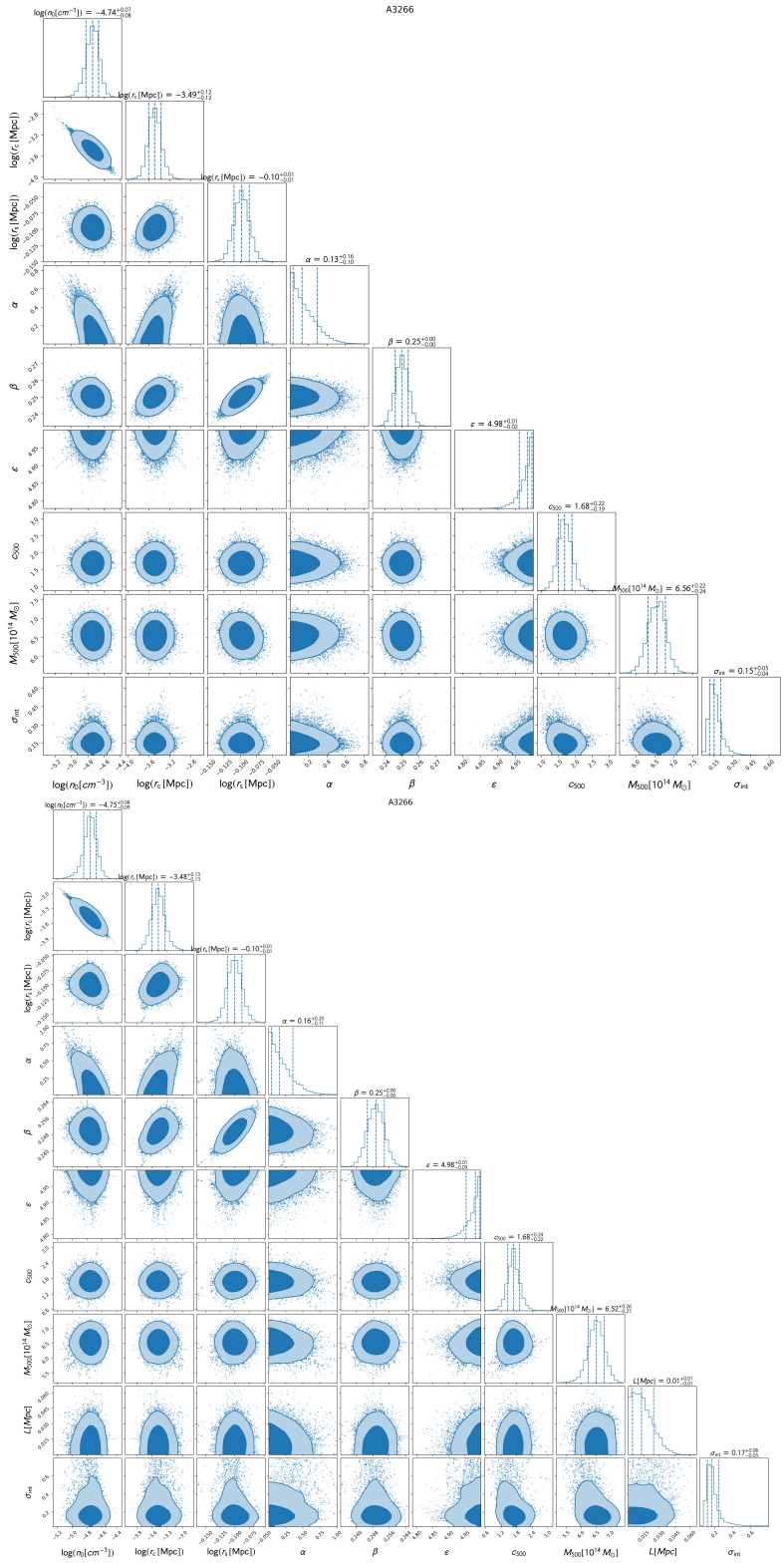

Figure E.12: A3268 contour plots for the NFW pressure profile (top) and NMC DM pressure profile (bottom).

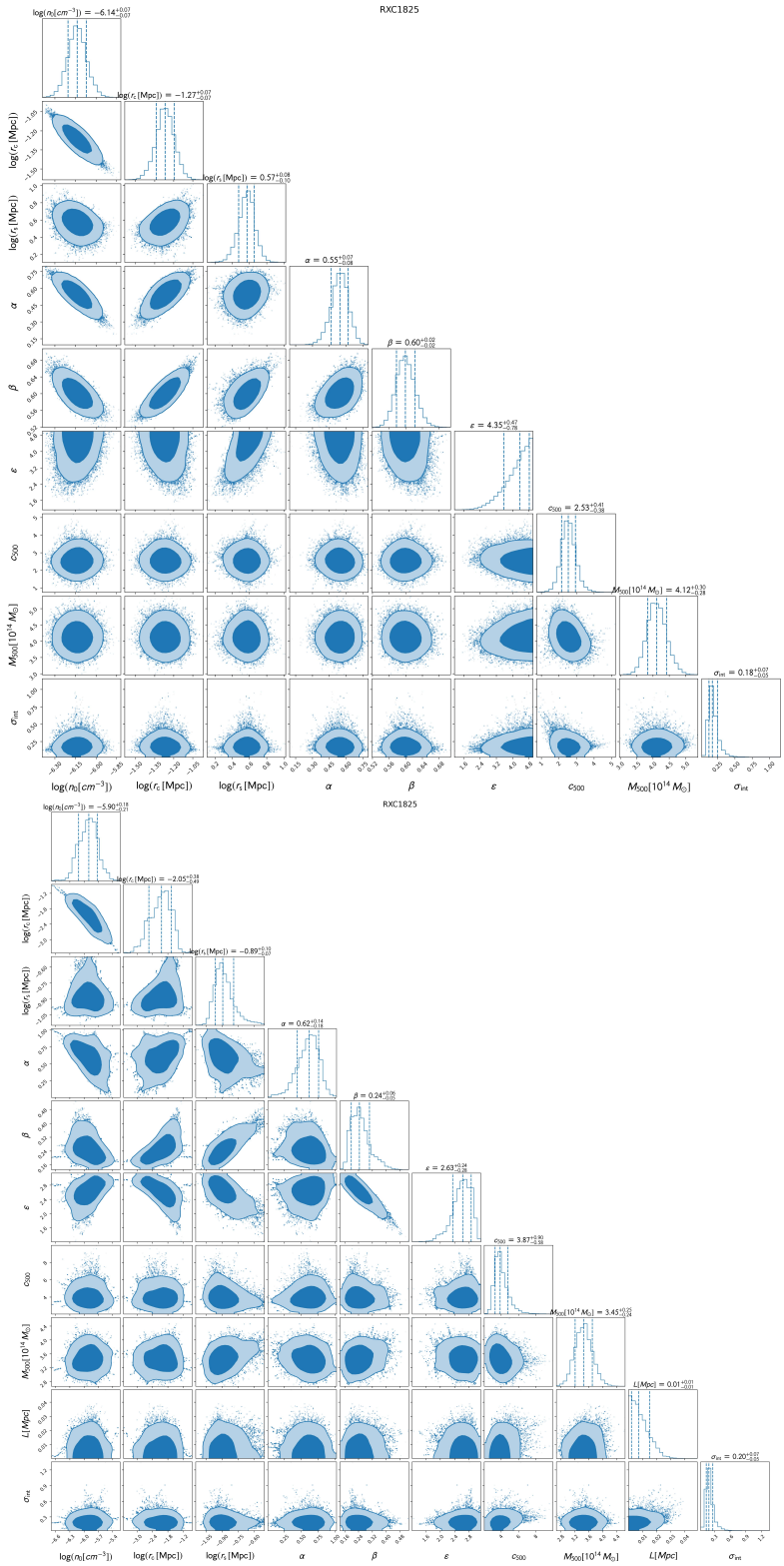

Figure E.13: RXC1825 contour plots for the NFW pressure profile (top) and NMC DM pressure profile (bottom).

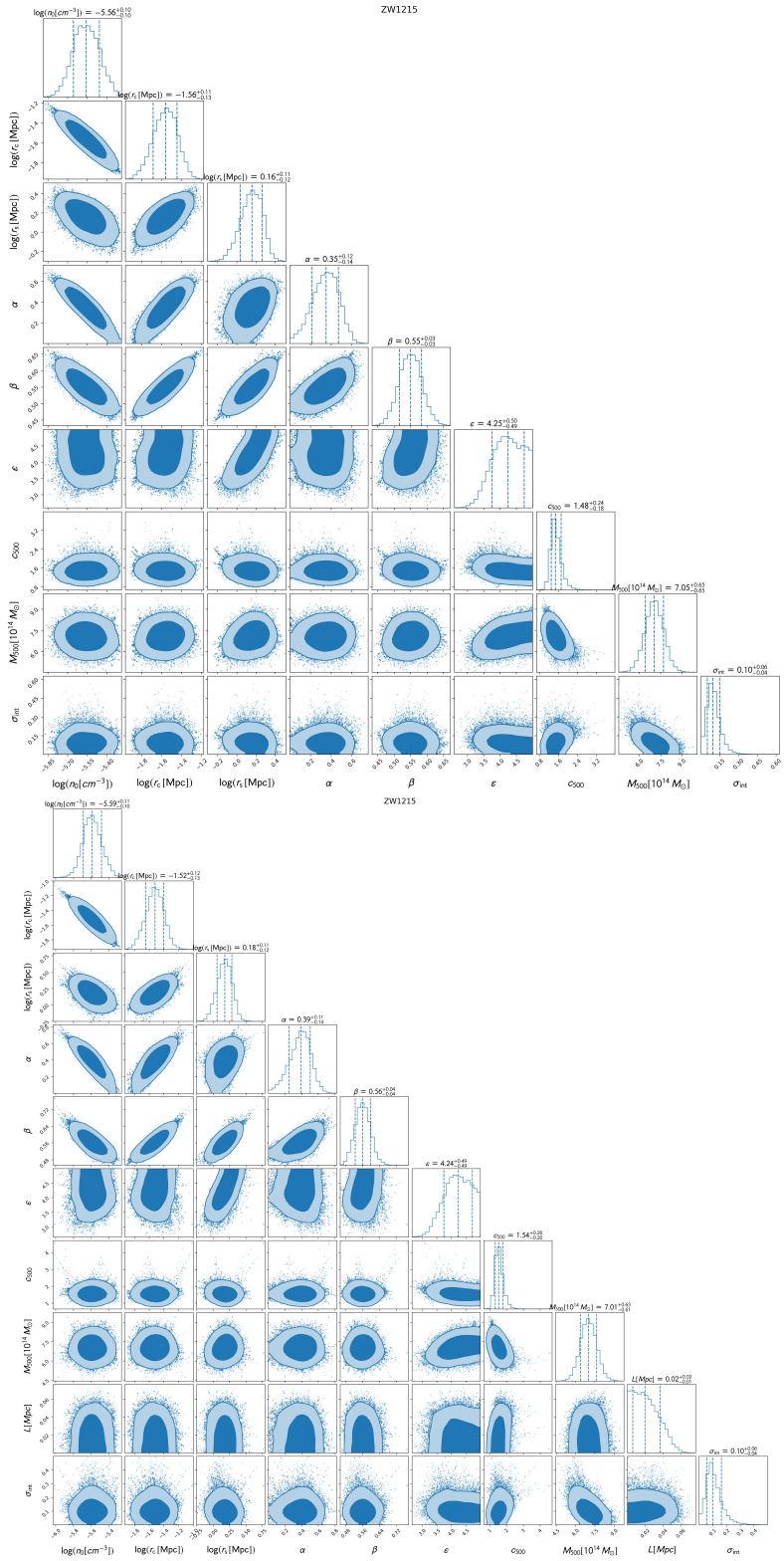

Figure E.14: ZW1215 contour plots for the NFW pressure profile (top) and NMC DM pressure profile (bottom).

Bibliography

[1] Abazajian, K., Fuller, G. M., & Tucker, W. H. 2001, ApJ, 562, 593, doi: 10.1086/323867 19

[2] Abazajian, K., Adelman-McCarthy, J. K., Agüeros, M. A., et al. 2003, AJ, 126, 2081, doi: 10.1086/378165 4

[3] Abbott, B. P., et al. 2017a, ApJL, 848, L12, doi: 10.3847/2041-8213/aa91c9 32

[4] Abbott, B. P., Abbott, R., Abbott, T. D., et al. 2017b, Phys. Rev. Lett., 119, 161101, doi: 10.1103/PhysRevLett.119.161101 32

[5] Acuna, A., Barakat, A., & Wheeler, C. 2023, in American Astronomical Society Meeting Abstracts, Vol. 55, American Astronomical Society Meeting Abstracts, 336.06 12

[6] Adams, J. J., Simon, J. D., Fabricius, M. H., et al. 2014, ApJ, 789, 63, doi: 10.1088/0004-637X/789/1/63 23

[7] Adams, N. J., Conselice, C. J., Ferreira, L., et al. 2023, MNRAS, 518, 4755, doi: 10.1093/mnras/stac3347 87

[8] Ade, P. A. R., et al. 2016, A&A, 594, A24, doi: 10.1051/0004-6361/201525833 74

[9] Adhikari, S., Banerjee, A., Boddy, K. K., et al. 2022, arXiv e-prints, arXiv:2207.10638, doi: 10.48550/arXiv.2207.10638 23

[10] Adil, S. A., Mukhopadhyay, U., Sen, A. A., & Vagnozzi, S. 2023, arXiv e-prints, arXiv:2307.12763, doi: 10.48550/arXiv.2307.12763 88

[11] Agertz, O., Kravtsov, A. V., Leitner, S. N., & Gnedin, N. Y. 2013, ApJ, 770, 25, doi: 10.1088/0004-637X/770/1/25 17

[12] Aghanim, N., et al. 2020, A&A, 641, A6, doi: 10.1051/0004-6361/201833910 1, 2, 3, 4, 5, 10

[13] Allahverdi, R., Brandenberger, R., Cyr-Racine, F.-Y., & Mazumdar, A. 2010, Ann. Rev. of Nuc. and Part. Sci., 60, 27, doi: 10.1146/annurev.nucl.012809.104511 3

[14] An, J., & Zhao, H. 2013, MNRAS, 428, 2805, doi: 10.1093/mnras/sts175 41

[15] Anderhalden, D., Schneider, A., Macciò, A. V., Diemand, J., & Bertone, G. 2013, JCAP, 2013, 014, doi: 10.1088/1475-7516/2013/03/014 19

[16] Anderson, M. H., Ensher, J. R., & Matthews, M. R. 1995, AAAS, 269, doi: 10.1126/science.269.5221.198 21

[17] Angulo, R. E., Springel, V., White, S. D. M., et al. 2012, MNRAS, 426, 2046, doi: 10.1111/j.1365-2966.2012.21830.x 9

[18] Archidiacono, M., Hannestad, S., Mirizzi, A., Raffelt, G., & Wong, Y. Y. Y. 2013, JCAP, 2013, 020, doi: 10.1088/1475-7516/2013/10/020 18

[19] Arora, A., & Williams, L. L. R. 2020, ApJ, 893, 53, doi: 10.3847/1538-4357/

ab7f2e 34
[20] Arrabal Haro, P., Dickinson, M., Finkelstein, S. L., et al. 2023, arXiv e-prints, arXiv:2303.15431, doi: 10.48550/arXiv.2303.15431 89
[21] Asaka, T., Nakamura, S., & Yamaguchi, M. 2006, Phys. Rev. D, 74, 023520, doi: 10.1103/PhysRevD.74.023520 19
[22] Atek, H., Shuntov, M., Furtak, L. J., et al. 2023a, MNRAS, 519, 1201, doi: 10.1093/mnras/stac3144 87
[23] Atek, H., Chemerynska, I., Wang, B., et al. 2023b, MNRAS, 524, 5486, doi: 10.1093/mnras/stad1998 87
[24] Austin, C. G., Williams, L. L. R., Barnes, E. I., Babul, A., & Dalcanton, J. J. 2005, ApJ, 634, 756, doi: 10.1086/497133 36
[25] Aversa, R., Lapi, A., de Zotti, G., Shankar, F., & Danese, L. 2015, ApJ, 810, 74, doi: 10.1088/0004-637X/810/1/74 93
[26] Babcock, H. W. 1939, Lick Obs. Bull., 498, 41, doi: 10.5479/ADS/bib/1939LicOB.19.41B 2
[27] Bae, K. J., Kamada, A., Pei Liew, S., & Yanagi, K. 2018, JCAP, 2018, 054, doi: 10.1088/1475-7516/2018/01/054 19
[28] Bakx, T. J. L. C., Zavala, J. A., Mitsuhashi, I., et al. 2023, MNRAS, 519, 5076, doi: 10.1093/mnras/stac3723 89
[29] Baltz, E. A., & Murayama, H. 2003, JHEP, 2003, 067, doi: 10.1088/1126-6708/2003/05/067 19
[30] Banik, N., Bovy, J., Bertone, G., Erkal, D., & de Boer, T. J. L. 2021, JCAP, 10, 043, doi: 10.1088/1475-7516/2021/10/043 19, 20
[31] Barkana, R., Haiman, Z., & Ostriker, J. P. 2001, ApJ, 558, 482, doi: 10.1086/322393 103
[32] Bechtol, K., Drlica-Wagner, A., Balbinot, E., et al. 2015, ApJ, 807, 50, doi: 10.1088/0004-637X/807/1/50 12
[33] Behroozi, P., Wechsler, R. H., Hearin, A. P., & Conroy, C. 2019, MNRAS, 488, 3143, doi: 10.1093/mnras/stz1182 93
[34] Behroozi, P. S., Wechsler, R. H., & Conroy, C. 2013, ApJ, 770, 57, doi: 10.1088/0004-637X/770/1/57 63
[35] Bekenstein, J., & Milgrom, M. 1984, ApJ, 286, 7, doi: 10.1086/162570 25
[36] Bekenstein, J. D. 1993, Phys. Rev. D, 48, 3641, doi: 10.1103/PhysRevD.48.3641 28
[37] Bekenstein, J. D. 2009, Nuclear Physics A, 827, 555, doi: 10.1016/j.nuclphysa.2009.05.122 24
[38] Beltran Jimenez, J., Heisenberg, L., Olmo, G. J., & Rubiera-Garcia, D. 2018, Phys. Rept., 727, 1, doi: 10.1016/j.physrep.2017.11.001 32
[39] Benetti, F., Lapi, A., Gandolfi, G., et al. 2023c, Universe, 9, 478, doi: 10.3390/universe9110478 105, 106
[40] Benetti, F., Lapi, A., Gandolfi, G., Haridasu, B. S., & Danese, L. 2023b, MDPI Univ., 9, 329, doi: 10.3390/universe9070329 23, 105, 106, 107, 111
[41] Benetti, F., Lapi, A., Gandolfi, G., Salucci, P., & Danese, L. 2023a, ApJ, 949, 65, doi: 10.3847/1538-4357/acc8ca 23, 105, 106, 109, 110, 111
[42] Benítez-Llambay, A., Navarro, J. F., Frenk, C. S., & Ludlow, A. D. 2017, MNRAS, 473, 1019, doi: 10.1093/mnras/stx2420 17

[43] Bertone, G., & Hooper, D. 2018, Rev. of Modern Phys., 90, 045002, doi: 10.1103/RevModPhys.90.045002 5
[44] Bertschinger, E. 1985, ApJS, 58, 39, doi: 10.1086/191028 34
[45] Bessel, F. W. 1844, MNRAS, 6, 136, doi: 10.1093/mnras/6.11.136 2
[46] Bettoni, D., Colombo, M., & Liberati, S. 2014, JCAP, 2014, 004, doi: 10.1088/1475-7516/2014/02/004 iii, 27, 28, 30, 31, 32, 34, 84, 105, 123
[47] Bettoni, D., & Liberati, S. 2013, Phys. Rev. D, 88, 084020, doi: 10.1103/PhysRevD.88.084020 30
[48] Bettoni, D., & Liberati, S. 2015, JCAP, 2015, 023, doi: 10.1088/1475-7516/2015/08/023 27, 28, 30, 31, 32, 84
[49] Bettoni, D., Liberati, S., & Sindoni, L. 2011, JCAP, 11, 007, doi: 10.1088/1475-7516/2011/11/007 27, 28, 31
[50] Bettoni, D., Pettorino, V., Liberati, S., & Baccigalupi, C. 2012, JCAP, 2012, 027, doi: 10.1088/1475-7516/2012/07/027 27, 28, 30, 85, 86
[51] Bevington, P. R., & Robinson, D. K. 2003, Data reduction and error analysis for the physical sciences; 3rd ed. (McGraw-Hill). https://cds.cern.ch/record/1305448 58
[52] Binney, J. 1978, MNRAS, 183, 779, doi: 10.1093/mnras/183.4.779 48
[53] Binney, J., & Tremaine, S. 1987, Galactic dynamics (Princeton Series in Astrophysics) 52
[54] Bisigello, L., Gandolfi, G., Grazian, A., et al. 2023, A&A, 676, A76, doi: 10.1051/0004-6361/202346219 xiv, 105, 111, 112, 114
[55] Bland-Hawthorn, J., Sutherland, R., & Webster, D. 2015, ApJ, 807, 154, doi: 10.1088/0004-637X/807/2/154 17
[56] Blumenthal, G. R., Faber, S. M., Flores, R., & Primack, J. R. 1986, ApJ, 301, 27, doi: 10.1086/163867 17
[57] Blumenthal, G. R., Faber, S. M., Primack, J. R., & Rees, M. J. 1984, Nat, 311, 517, doi: 10.1038/311517a0 3
[58] Blumenthal, G. R., Pagels, H., & Primack, J. R. 1982, Nat, 299, 37, doi: 10.1038/299037a0 19
[59] Bocquet, S., Saro, A., Dolag, K., & Mohr, J. J. 2016, MNRAS, 456, 2361, doi: 10.1093/mnras/stv2657 9
[60] Boehmer, C. G., & Harko, T. 2007, JCAP, 06, 025, doi: 10.1088/1475-7516/2007/06/025 21
[61] Bond, J. R., Szalay, A. S., & Turner, M. S. 1982, Phys. Rev. Lett., 48, 1636, doi: 10.1103/PhysRevLett.48.1636 19
[62] Borjon-Espejel, S., Escalante-Martinez, J. E., & Padilla-Longoria, P. 2022, Indian J. of Phys., 96, 3405, doi: 10.1007/s12648-022-02296-1 106
[63] Bose, S., Frenk, C. S., Jenkins, A., et al. 2019, MNRAS, 486, 4790, doi: 10.1093/mnras/stz1168 17
[64] Bosma, A. 1978, PhD thesis, - 3
[65] Bourliot, F., Ferreira, P. G., Mota, D. F., & Skordis, C. 2007, Phys. Rev. D, 75, 063508, doi: 10.1103/PhysRevD.75.063508 25
[66] Bouwens, R. J., Illingworth, G., Ellis, R. S., Oesch, P., & Stefanon, M. 2022, ApJ, 940, 55, doi: 10.3847/1538-4357/ac86d1 89, 90, 91, 92, 95, 96, 102
[67] Bouwens, R. J., Illingworth, G. D., Oesch, P. A., et al. 2014, ApJ, 793, 115,

doi: 10.1088/0004-637X/793/2/115 90, 91
[68] Bouwens, R. J., Oesch, P. A., Stefanon, M., et al. 2021, AJ, 162, 47, doi: 10.3847/1538-3881/abf83e 89, 90, 91, 92, 94, 96, 101
[69] Boyarsky, A., Drewes, M., Lasserre, T., Mertens, S., & Ruchayskiy, O. 2019, Prog. in Part. and Nucl. Phys., 104, 1, doi: 10.1016/j.ppnp.2018.07.004 19
[70] Boylan-Kolchin, M. 2023, Nat, 7, 731, doi: 10.1038/s41550-023-01937-7 87, 88
[71] Boylan-Kolchin, M., Bullock, J. S., & Kaplinghat, M. 2011, MNRAS, 415, L40, doi: 10.1111/j.1745-3933.2011.01074.x 12
[72] Boylan-Kolchin, M., Bullock, J. S., & Kaplinghat, M. 2012, Monthly Notices of the Royal Astronomical Society, 422, 1203, doi: 10.1111/j.1365-2966.2012.20695.x 12
[73] Boylan-Kolchin, M., & Ma, C.-P. 2004, MNRAS, 349, 1117, doi: 10.1111/j.1365-2966.2004.07585.x 12
[74] Bradley, C. C., Sackett, C. A., Tollett, J. J., & Hulet, R. G. 1995, Phys. Rev. Lett., 75, 1687, doi: 10.1103/PhysRevLett.75.1687 21
[75] Brammer, G. B., van Dokkum, P. G., & Coppi, P. 2008, ApJ, 686, 1503, doi: 10.1086/591786 88
[76] Brandt, F. C. 1965, MNRAS, 129, 309, doi: 10.1093/mnras/129.4.309 3
[77] Bringmann, T., Kahlhoefer, F., Schmidt-Hoberg, K., & Walia, P. 2017, Phys. Rev. Lett., 118, 141802, doi: 10.1103/PhysRevLett.118.141802 104
[78] Bromm, V., Yoshida, N., Hernquist, L., & McKee, C. F. 2009, Nat, 459, 49, doi: 10.1038/nature07990 4
[79] Brouwer, M. M., Oman, K. A., Valentijn, E. A., et al. 2021, A&A, 650, A113, doi: 10.1051/0004-6361/202040108 14
[80] Bruneton, J.-P., & Esposito-Farese, G. 2007, Phys. Rev. D, 76, 124012, doi: 10.1103/PhysRevD.76.129902 28
[81] Bruneton, J.-P., Liberati, S., Sindoni, L., & Famaey, B. 2009, JCAP, 03, 021, doi: 10.1088/1475-7516/2009/03/021 27, 28, 30, 44, 84
[82] Buchbinder, I. L., Odintsov, S. D., & Shapiro, I. L. 1992, Effective action in quantum gravity (CRC Press) 27
[83] Bullock, J. S., Kolatt, T. S., Sigad, Y., et al. 2001, MNRAS, 321, 559, doi: 10.1046/j.1365-8711.2001.04068.x 48
[84] Burkert, A. 1995, ApJL, 447, L25, doi: 10.1086/309560 11
[85] Burkert, A. 2015, ApJ, 808, 158, doi: 10.1088/0004-637X/808/2/158 20, 46, 65, 84
[86] Burkert, A. 2020, ApJ, 904, 161, doi: 10.3847/1538-4357/abb242 20, 46, 47, 65, 104
[87] Butsky, I., Macciò, A. V., Dutton, A. A., et al. 2016, MNRAS, 462, 663, doi: 10.1093/mnras/stw1688 34
[88] Cai, Z.-Y., Lapi, A., Bressan, A., et al. 2014, ApJ, 785, 65, doi: 10.1088/0004-637X/785/1/65 90
[89] Calabrese, E., & Spergel, D. N. 2016, MNRAS, 460, 4397, doi: 10.1093/mnras/stw1256 104
[90] Calcagni, G. 2013, JCAP, 2013, 041, doi: 10.1088/1475-7516/2013/12/041 106

[91] Calcagni, G., & Varieschi, G. U. 2022, JHEP, 2022, 24, doi: 10.1007/JHEP08(2022)024 106
[92] Carnall, A. C., McLure, R. J., Dunlop, J. S., & Davé, R. 2018, MNRAS, 480, 4379, doi: 10.1093/mnras/sty2169 111
[93] Carucci, I. P., & Corasaniti, P.-S. 2019, Phys. Rev. D, 99, 023518, doi: 10.1103/PhysRevD.99.023518 103
[94] Carucci, I. P., Villaescusa-Navarro, F., Viel, M., & Lapi, A. 2015, JCAP, 07, 047, doi: 10.1088/1475-7516/2015/07/047 104
[95] Castellano, M., Fontana, A., Treu, T., et al. 2022, ApJL, 938, L15, doi: 10.3847/2041-8213/ac94d0 87
[96] Chabrier, G. 2003, PASP, 115, 763, doi: 10.1086/376392 2
[97] Chae, K.-H. 2014, ApJL, 788, L15, doi: 10.1088/2041-8205/788/1/L15 35
[98] Chae, K.-H. 2022, Astrophys. J., 941, 55, doi: 10.3847/1538-4357/ac93fc 25
[99] Chae, K.-H., Bernardi, M., Sheth, R. K., & Gong, I.-T. 2019, ApJ, 877, 18, doi: 10.3847/1538-4357/ab18f8 14
[100] Chae, K.-H., Desmond, H., Lelli, F., McGaugh, S. S., & Schombert, J. M. 2021, ApJ, 921, 104, doi: 10.3847/1538-4357/ac1bba 25, 70
[101] Chae, K.-H., Lelli, F., Desmond, H., et al. 2020, ApJ, 904, 51, doi: 10.3847/1538-4357/abbb96 25, 70, 71
[102] Chan, M. H., & Del Popolo, A. 2020, MNRAS, 492, 5865, doi: 10.1093/mnras/staa225 14
[103] Chatterjee, A., Dayal, P., Choudhury, T. R., & Hutter, A. 2019, MNRAS, 487, 3560, doi: 10.1093/mnras/stz1444 104
[104] Chen, S.-R., Schive, H.-Y., & Chiueh, T. 2017, MNRAS, 468, 1338, doi: 10.1093/mnras/stx449 20
[105] Cheng, H.-C., Feng, J. L., & Matchev, K. T. 2002, Phys. Rev. Lett., 89, 211301, doi: 10.1103/PhysRevLett.89.211301 6
[106] Cherry, J. F., & Horiuchi, S. 2017, Phys. Rev. D, 95, 083015, doi: 10.1103/PhysRevD.95.083015 19
[107] Choi, E., Ostriker, J. P., Naab, T., et al. 2017, ApJ, 844, 31, doi: 10.3847/1538-4357/aa7849 12
[108] Chrobáková, Ž., López-Corredoira, M., Sylos Labini, F., Wang, H. F., & Nagy, R. 2020, A&A, 642, A95, doi: 10.1051/0004-6361/202038736 85
[109] Clifton, T., & Zlosnik, T. G. 2010, Phys. Rev. D, 81, 103525, doi: 10.1103/PhysRevD.81.103525 25
[110] Clowe, D., Bradač, M., Gonzalez, A. H., et al. 2006, ApJL, 648, L109, doi: 10.1086/508162 26
[111] Cole, S., Lacey, C. G., Baugh, C. M., & Frenk, C. S. 2000, MNRAS, 319, 168, doi: 10.1046/j.1365-8711.2000.03879.x 13
[112] Corasaniti, P. S., Agarwal, S., Marsh, D. J. E., & Das, S. 2017, Phys. Rev. D, 95, 083512, doi: 10.1103/PhysRevD.95.083512 104
[113] Cornell, E. A., & Wieman, C. E. 2002, Rev. Mod. Phys., 74, 875, doi: 10.1103/RevModPhys.74.875 21
[114] Couchman, H. M. P., & Thacker, R. J. 2003, in Astrophysical Supercomputing using Particle Simulations, ed. J. Makino & P. Hut, Vol. 208, 227 17
[115] Creasey, P., Sameie, O., Sales, L. V., et al. 2017, MNRAS, 468, 2283, doi: 10.

1093/mnras/stx522 23
[116] Cristofari, P., & Ostriker, J. P. 2019, MNRAS, 482, 4364, doi: 10.1093/mnras/sty2966 93
[117] Crăciun, M., & Harko, T. 2020, Eur. Phys. J. C, 80, 735, doi: 10.1140/epjc/s10052-020-8272-4 22
[118] Curti, M., D'Eugenio, F., Carniani, S., et al. 2023, MNRAS, 518, 425, doi: 10.1093/mnras/stac2737 88
[119] Cyr-Racine, F.-Y., & Sigurdson, K. 2013, Phys. Rev. D, 87, 103515, doi: 10.1103/PhysRevD.87.103515 23
[120] Cyr-Racine, F.-Y., Sigurdson, K., Zavala, J., et al. 2016, Phys. Rev. D, 93, 123527, doi: 10.1103/PhysRevD.93.123527 23
[121] Dalal, N., & Kravtsov, A. 2022, arXiv e-prints, arXiv:2203.05750, doi: 10.48550/arXiv.2203.05750 20
[122] Dalfovo, F., Giorgini, S., Pitaevskii, L. P., & Stringari, S. 1999, Rev. of Modern Phys., 71, 463, doi: 10.1103/RevModPhys.71.463 21
[123] Das, S., Maharana, A., Poulin, V., & Sharma, R. K. 2022, Phys. Rev. D, 105, 103503, doi: 10.1103/PhysRevD.105.103503 18
[124] Davis, K. B., Mewes, M. O., Andrews, M. R., et al. 1995, Phys. Rev. Lett., 75, 3969, doi: 10.1103/PhysRevLett.75.3969 21
[125] Davis, M., Efstathiou, G., Frenk, C. S., & White, S. D. M. 1985, ApJ, 292, 371, doi: 10.1086/163168 3
[126] Dayal, P., Choudhury, T. R., Bromm, V., & Pacucci, F. 2017, ApJ, 836, 16, doi: 10.3847/1538-4357/836/1/16 103
[127] Dayal, P., & Giri, S. K. 2023, arXiv e-prints, arXiv:2303.14239, doi: 10.48550/arXiv.2303.14239 19, 103
[128] de Blok, W. J. G. 2010, Adv. in Astro., 2010, 789293, doi: 10.1155/2010/789293 12, 69
[129] de Blok, W. J. G., McGaugh, S. S., Bosma, A., & Rubin, V. C. 2001, ApJL, 552, L23, doi: 10.1086/320262 23
[130] de Souza, R. S., Mesinger, A., Ferrara, A., et al. 2013, MNRAS, 432, 3218, doi: 10.1093/mnras/stt674 103
[131] de Vega, H., Salucci, P., & Sanchez, N. 2012, New Astron., 17, 653, doi: https://doi.org/10.1016/j.newast.2012.04.001 19
[132] de Vega, H. J., Salucci, P., & Sanchez, N. G. 2014, MNRAS, 442, 2717, doi: 10.1093/mnras/stu972 19
[133] de Vega, H. J., & Sanchez, N. G. 2010, MNRAS, 404, 885, doi: 10.1111/j.1365-2966.2010.16319.x 19, 112
[134] de Vega, H. J., & Sanchez, N. G. 2012, Phys. Rev. D, 85, 043516, doi: 10.1103/PhysRevD.85.043516 19
[135] de Vega, H. J., & Sanchez, N. G. 2012, Phys. Rev. D, 85, 043517, doi: 10.1103/PhysRevD.85.043517 19
[136] Dehghani, R., Salucci, P., & Ghaffarnejad, H. 2020, A&A, 643, A161, doi: 10.1051/0004-6361/201937079 xiii, xiv, 51, 53, 55, 60, 135, 136, 137, 138
[137] Dehnen, W., & McLaughlin, D. 2005, MNRAS, 363, 1057, doi: 10.1111/j.1365-2966.2005.09510.x 36
[138] Dekker, A., Ando, S., Correa, C. A., & Ng, K. C. Y. 2022, Phys. Rev. D, 106,

123026, doi: 10.1103/PhysRevD.106.123026 19
[139] Deliduman, C., Kasikci, O., & Keles Tugyanoglu, V. 2023, arXiv e-prints, arXiv:2310.02914, doi: 10.48550/arXiv.2310.02914 88
[140] Deng, H., Hertzberg, M. P., Namjoo, M. H., & Masoumi, A. 2018, Phys. Rev. D, 98, 023513, doi: 10.1103/PhysRevD.98.023513 46, 47
[141] Deruelle, N. 2011, Gen. Rel. Grav., 43, 3337, doi: 10.1007/s10714-011-1247-x 25
[142] Desmond, H. 2017, MNRAS: Letters, 472, L35, doi: 10.1093/mnrasl/slx134 13
[143] Desmond, H. 2017, MNRAS, 464, 4160, doi: 10.1093/mnras/stw2571 16
[144] Desmond, H. 2023, Mon. Not. Roy. Astron. Soc., 526, 3342, doi: 10.1093/mnras/stad2762 25
[145] Desmond, H., Bartlett, D. J., & Ferreira, P. G. 2023, MNRAS, 521, 1817, doi: 10.1093/mnras/stad597 25
[146] Desmond, H., Ferreira, P. G., Lavaux, G., & Jasche, J. 2018, MNRAS, 474, 3152, doi: 10.1093/mnras/stx3062 70
[147] Despali, G., Giocoli, C., Angulo, R. E., et al. 2016, MNRAS, 456, 2486, doi: 10.1093/mnras/stv2842 9
[148] Destri, C., de Vega, H., & Sanchez, N. 2013a, New Astron., 22, 39, doi: https://doi.org/10.1016/j.newast.2012.12.003 19
[149] Destri, C., de Vega, H. J., & Sanchez, N. G. 2013b, Astropart. Phys., 46, 14, doi: 10.1016/j.astropartphys.2013.04.004 19
[150] Destri, C., de Vega, H. J., & Sanchez, N. G. 2013, Phys. Rev. D, 88, 083512, doi: 10.1103/PhysRevD.88.083512 19
[151] Di Casola, E., Liberati, S., & Sonego, S. 2015, American J. of Phys., 83, 39, doi: 10.1119/1.4895342 27
[152] Di Cintio, A., Brook, C. B., Dutton, A. A., et al. 2014, MNRAS, 441, 2986, doi: 10.1093/mnras/stu729 16, 65
[153] Di Cintio, A., & Lelli, F. 2016, MNRAS, 456, L127, doi: 10.1093/mnrasl/slv185 13, 16
[154] Di Paolo, C., Salucci, P., & Fontaine, J. P. 2019, ApJ, 873, 106, doi: 10.3847/1538-4357/aaffd6 14, 110
[155] Diemer, B. 2018, ApJS, 239, 35, doi: 10.3847/1538-4365/aaee8c 10, 92
[156] Diemer, B. 2020, Astrophys. J., 903, 87, doi: 10.3847/1538-4357/abbf52 9
[157] Dodelson, S. 2011, Int. J. Mod. Phys. D, 20, 2749, doi: 10.1142/S0218271811020561 26
[158] Dolgov, A. D. 2023, arXiv e-prints, arXiv:2310.00671, doi: 10.48550/arXiv.2310.00671 88
[159] Donato, F., & Salucci, P. 2004, MNRAS, 353, L17, doi: 10.1111/j.1365-2966.2004.08220.x 14, 44, 46
[160] Donato, F., Gentile, G., Salucci, P., et al. 2009, MNRAS, 397, 1169, doi: 10.1111/j.1365-2966.2009.15004.x 65
[161] Donnan, C. T., McLeod, D. J., McLure, R. J., et al. 2023, MNRAS, 520, 4554, doi: 10.1093/mnras/stad471 87
[162] Dooley, G. A., Peter, A. H. G., Vogelsberger, M., Zavala, J., & Frebel, A. 2016, MNRAS, 461, 710, doi: 10.1093/mnras/stw1309 23

[163] Drlica-Wagner, A., et al. 2015, ApJ, 813, 109, doi: 10.1088/0004-637X/813/2/109 12
[164] Dutton, A. A., & Macciò, A. V. 2014, MNRAS, 441, 3359, doi: 10.1093/mnras/stu742 53, 59, 65, 81, 83
[165] Dutton, A. A., Macciò, A. V., Obreja, A., & Buck, T. 2019, MNRAS, 485, 1886, doi: 10.1093/mnras/stz531 14, 24
[166] Dutton, A. A., & van den Bosch, F. C. 2009, MNRAS, 396, 141, doi: 10.1111/j.1365-2966.2009.14742.x 17
[167] Dwornik, M., Keresztes, Z., & Gergely, L. Á. 2013, arXiv e-prints, arXiv:1312.3715, doi: 10.48550/arXiv.1312.3715 22
[168] Eckert, D., Ettori, S., Pointecouteau, E., et al. 2017, Astron. Nachr., 338, 293, doi: 10.1002/asna.201713345 73
[169] Eckert, D., Ettori, S., Pointecouteau, E., van der Burg, R. F. J., & Loubser, S. I. 2022, A&A, 662, A123, doi: 10.1051/0004-6361/202142507 14
[170] Eckert, D., et al. 2019, A&A, 621, A40, doi: 10.1051/0004-6361/201833324 73, 75
[171] Eddine Ennadifi, S. 2022, arXiv e-prints, arXiv:2211.11663, doi: 10.48550/arXiv.2211.11663 18
[172] Efstathiou, G. 1992, MNRAS, 256, 43P, doi: 10.1093/mnras/256.1.43P 92
[173] Efstathiou, G. 2000, Mon. Not. Roy. Astron. Soc., 317, 697, doi: 10.1046/j.1365-8711.2000.03665.x 16
[174] El-Zant, A., Freundlich, J., & Combes, F. 2016, MNRAS, 461, 1745, doi: 10.1093/mnras/stw1398 18
[175] El-Zant, A., Shlosman, I., & Hoffman, Y. 2001, ApJ, 560, 636, doi: 10.1086/322516 17
[176] El-Zant, A. A., Hoffman, Y., Primack, J., Combes, F., & Shlosman, I. 2004, ApJL, 607, L75, doi: 10.1086/421938 17
[177] Enzi, W., Murgia, R., Newton, O., et al. 2021, MNRAS, 506, 5848, doi: 10.1093/mnras/stab1960 104
[178] Ettori, S., Ghirardini, V., Eckert, D., et al. 2019, A&A, 621, A39, doi: 10.1051/0004-6361/201833323 73, 74
[179] Fall, S. M., & Efstathiou, G. 1980, MNRAS, 193, 189, doi: 10.1093/mnras/193.2.189 13
[180] Famaey, B., & Binney, J. 2005, MNRAS, 363, 603, doi: 10.1111/j.1365-2966.2005.09474.x 70
[181] Famaey, B., & McGaugh, S. 2012, Living Rev. Rel., 15, 10, doi: 10.12942/lrr-2012-10 24
[182] Feng, J. L. 2010, ARA&A, 48, 495, doi: 10.1146/annurev-astro-082708-101659 5
[183] Feng, J. L., Kaplinghat, M., Tu, H., & Yu, H.-B. 2009, JCAP, 2009, 004, doi: 10.1088/1475-7516/2009/07/004 23
[184] Ferrero, I., Abadi, M. G., Navarro, J. F., Sales, L. V., & Gurovich, S. 2012, MNRAS, 425, 2817, doi: 10.1111/j.1365-2966.2012.21623.x 17
[185] Finkelstein, S. L., D'Aloisio, A., Paardekooper, J.-P., et al. 2019, ApJ, 879, 36, doi: 10.3847/1538-4357/ab1ea8 90, 92, 96
[186] Finkelstein, S. L., Bagley, M. B., Ferguson, H. C., et al. 2023, ApJL, 946, L13,

doi: 10.3847/2041-8213/acade4 87, 111, 112, 114
[187] Folkes, S., Ronen, S., Price, I., et al. 1999, MNRAS, 308, 459, doi: 10.1046/j.1365-8711.1999.02721.x 4
[188] Foreman-Mackey, D., Hogg, D. W., Lang, D., & Goodman, J. 2013, PASP, 125, 306, doi: 10.1086/670067 53
[189] Frandsen, M. T., & Petersen, J. 2018, arXiv e-prints, arXiv:1805.10706, doi: 10.48550/arXiv.1805.10706 24
[190] Freeman, K. C. 1970, ApJ, 160, 811, doi: 10.1086/150474 3, 51
[191] Freundlich, J., Dekel, A., Jiang, F., et al. 2020, MNRAS, 491, 4523, doi: 10.1093/mnras/stz3306 41
[192] Freundlich, J., El-Zant, A., & Combes, F. 2016, in SF2A-2016: Proceedings of the Annual meeting of the French Society of Astronomy and Astrophysics, ed. C. Reylé, J. Richard, L. Cambrésy, M. Deleuil, E. Pécontal, L. Tresse, & I. Vauglin, 153–156 17
[193] Freundlich, J., Famaey, B., Oria, P.-A., et al. 2022, A&A, 658, A26, doi: 10.1051/0004-6361/202142060 110
[194] Freundlich, J., Jiang, F., Dekel, A., et al. 2020, MNRAS, 499, 2912, doi: 10.1093/mnras/staa2790 48
[195] Fujimoto, S., Finkelstein, S. L., Burgarella, D., et al. 2023, ApJ, 955, 130, doi: 10.3847/1538-4357/aceb67 89
[196] Fukugita, M., Hogan, C. J., & Peebles, P. J. E. 1998, ApJ, 503, 518, doi: 10.1086/306025 6
[197] Gadotti, D. A. 2009, MNRAS, 393, 1531, doi: 10.1111/j.1365-2966.2008.14257.x 64
[198] Galianni, P., Feix, M., Zhao, H., & Horne, K. 2012, Phys. Rev. D, 86, 044002, doi: 10.1103/PhysRevD.86.044002 25
[199] Gandolfi, G., Haridasu, B. S., Liberati, S., & Lapi, A. 2023, Astrophys. J., 952, 105, doi: 10.3847/1538-4357/acd755 27
[200] Gandolfi, G., Lapi, A., & Liberati, S. 2021, ApJ, 910, 76, doi: 10.3847/1538-4357/abe460 27
[201] Gandolfi, G., Lapi, A., & Liberati, S. 2022a, ApJ, 929, 48, doi: 10.3847/1538-4357/ac5970 27, 75
[202] Gandolfi, G., Lapi, A., Ronconi, T., & Danese, L. 2022b, Universe, 8, 589, doi: 10.3390/universe8110589 89
[203] Gao, L., Frenk, C. S., Jenkins, A., Springel, V., & White, S. D. M. 2012, MNRAS, 419, 1721, doi: 10.1111/j.1365-2966.2011.19836.x 34
[204] Gao, L., White, S. D. M., Jenkins, A., Stoehr, F., & Springel, V. 2004, MNRAS, 355, 819, doi: 10.1111/j.1365-2966.2004.08360.x 17
[205] Garaldi, E., Romano-Díaz, E., Porciani, C., & Pawlowski, M. S. 2018, Phys. Rev. Lett., 120, 261301, doi: 10.1103/PhysRevLett.120.261301 14
[206] García-Aspeitia, M. A., Fernandez-Anaya, G., Hernández-Almada, A., Leon, G., & Magaña, J. 2022, MNRAS, 517, 4813, doi: 10.1093/mnras/stac3006 106
[207] Garrison-Kimmel, S., Boylan-Kolchin, M., Bullock, J. S., & Kirby, E. N. 2014, MNRAS, 444, 222, doi: 10.1093/mnras/stu1477 12
[208] Garrison-Kimmel, S., Rocha, M., Boylan-Kolchin, M., Bullock, J., & Lally, J. 2013, MNRAS, 433, 3539, doi: 10.1093/mnras/stt984 17

[209] Genel, S., Vogelsberger, M., Springel, V., et al. 2014, MNRAS, 445, 175, doi: 10.1093/mnras/stu1654 13
[210] Ghari, A., Famaey, B., Laporte, C., & Haghi, H. 2019a, A&A, 623, A123, doi: 10.1051/0004-6361/201834661 14
[211] Ghari, A., Haghi, H., & Zonoozi, A. H. 2019b, MNRAS, 487, 2148, doi: 10.1093/mnras/stz1272 14
[212] Ghirardini, V., Ettori, S., Eckert, D., et al. 2018, A&A, 614, A7, doi: 10.1051/0004-6361/201731748 73, 74
[213] Ghirardini, V., et al. 2019, A&A, 621, A41, doi: 10.1051/0004-6361/201833325 73
[214] Gilman, D., Birrer, S., Nierenberg, A., et al. 2020, MNRAS, 491, 6077, doi: 10.1093/mnras/stz3480 19
[215] Gilman, D., Bovy, J., Treu, T., et al. 2021, MNRAS, 507, 2432, doi: 10.1093/mnras/stab2335 19
[216] Giusti, A. 2020, Phys. Rev. D, 101, 124029, doi: 10.1103/PhysRevD.101.124029 106
[217] Giusti, A., Garrappa, R., & Vachon, G. 2020, Eur. Phys. J. Plus, 135, 798, doi: 10.1140/epjp/s13360-020-00831-9 106
[218] Gnedin, O. Y., Kravtsov, A. V., Klypin, A. A., & Nagai, D. 2004, ApJ, 616, 16, doi: 10.1086/424914 17
[219] Gnedin, O. Y., & Primack, J. R. 2004, Phys. Rev. Lett., 93, 061302, doi: 10.1103/PhysRevLett.93.061302 18
[220] Gnedin, O. Y., & Zhao, H. 2002, MNRAS, 333, 299, doi: 10.1046/j.1365-8711.2002.05361.x 17
[221] Goerdt, T., Read, J. I., Moore, B., & Stadel, J. 2010, ApJ, 725, 1707, doi: 10.1088/0004-637X/725/2/1707 18
[222] Gonzalez, A. H., Sivanandam, S., Zabludoff, A. I., & Zaritsky, D. 2013, ApJ, 778, 14, doi: 10.1088/0004-637X/778/1/14 2
[223] Gorbunov, D., Khmelnitsky, A., & Rubakov, V. 2008, JHEP, 2008, 055, doi: 10.1088/1126-6708/2008/12/055 19
[224] Governato, F., Brook, C., Mayer, L., et al. 2010, Nat, 463, 203, doi: 10.1038/nature08640 17
[225] Governato, F., Zolotov, A., Pontzen, A., et al. 2012, MNRAS, 422, 1231, doi: 10.1111/j.1365-2966.2012.20696.x 17
[226] Graham, A. W., Merritt, D., Moore, B., Diemand, J., & Terzic, B. 2006, AJ, 132, 2701, doi: 10.1086/508990 41
[227] Grand, R. J. J., & White, S. D. M. 2022, MNRAS, 511, L55, doi: 10.1093/mnrasl/slac011 104
[228] Green, M. A., & Moffat, J. W. 2019, Phys. Dark Univ., 25, 100323, doi: 10.1016/j.dark.2019.100323 14
[229] Griest, K. 1993, in Texas/PASCOS 1992: Relativistic Astrophysics and Particle Cosmology, ed. C. W. Akerlof & M. A. Srednicki, Vol. 688, 390, doi: 10.1111/j.1749-6632.1993.tb43912.x 5
[230] Griffin, A., Nikuni, T., & Zaremba, E. 2009, Bose-Condensed Gases at Finite Temperatures (Cambridge University Press) 21
[231] Gruppioni, C., Béthermin, M., Loiacono, F., et al. 2020, A&A, 643, A8,

doi: 10.1051/0004-6361/202038487 95, 96, 101
[232] Gupta, R. P. 2023, MNRAS, 524, 3385, doi: 10.1093/mnras/stad2032 88
[233] Gustafsson, M., Fairbairn, M., & Sommer-Larsen, J. 2006, Phys. Rev. D, 74, 123522, doi: 10.1103/PhysRevD.74.123522 17
[234] Hainline, K. N., Hviding, R. E., Rieke, M., et al. 2020, ApJ, 892, 125, doi: 10.3847/1538-4357/ab7dc3 111
[235] Hannestad, S., Mirizzi, A., & Raffelt, G. 2005, JCAP, 2005, 002, doi: 10.1088/1475-7516/2005/07/002 18
[236] Hannestad, S., Mirizzi, A., Raffelt, G. G., & Wong, Y. Y. Y. 2007, JCAP, 2007, 015, doi: 10.1088/1475-7516/2007/08/015 18
[237] Hannestad, S., Mirizzi, A., Raffelt, G. G., & Wong, Y. Y. Y. 2008, JCAP, 04, 019, doi: 10.1088/1475-7516/2008/04/019 18
[238] Hannestad, S., Mirizzi, A., Raffelt, G. G., & Wong, Y. Y. Y. 2010, JCAP, 2010, 001, doi: 10.1088/1475-7516/2010/08/001 18
[239] Hansen, S. H. 2004, MNRAS, 352, L41, doi: 10.1111/j.1365-2966.2004.08204.x 36
[240] Hansen, S. H., Juncher, D., & Sparre, M. 2010, ApJL, 718, L68, doi: 10.1088/2041-8205/718/2/L68 35
[241] Hansen, S. H., & Moore, B. 2006, New Astron., 11, 333, doi: 10.1016/j.newast.2005.09.001 49
[242] Hargis, J. R., Willman, B., & Peter, A. H. G. 2014, ApJL, 795, L13, doi: 10.1088/2041-8205/795/1/L13 12
[243] Haridasu, B. S., Karmakar, P., De Petris, M., Cardone, V. F., & Maoli, R. 2022, in EPJ Web of Conf., Vol. 257, mm Universe @ NIKA2 - Observing the mm Universe with the NIKA2 Camera, 00021, doi: 10.1051/epjconf/202225700021 74
[244] Harikane, Y., Ouchi, M., Oguri, M., et al. 2023, ApJS, 265, 5, doi: 10.3847/1538-4365/acaaa9 89, 90, 91, 95, 96, 101, 102
[245] Harko, T. 2011, JCAP, 05, 022, doi: 10.1088/1475-7516/2011/05/022 22
[246] Harko, T. 2011, Phys. Rev. D, 83, 123515, doi: 10.1103/PhysRevD.83.123515 22
[247] Harko, T. 2011, MNRAS, 413, 3095, doi: 10.1111/j.1365-2966.2011.18386.x 22
[248] Harko, T. 2014, Phys. Rev. D, 89, 084040, doi: 10.1103/PhysRevD.89.084040 22
[249] Harko, T. 2019, Eur. Phys. J. C, 79, 787, doi: 10.1140/epjc/s10052-019-7285-3 22
[250] Harko, T., Hertoiu, D., Stefanescu, S., & Visa, D. 2022, in Theory, Observations and Data Processing in Astronomy, Astrophysics, Space and Planetary Sciences, 30 22
[251] Harko, T., Liang, P., Liang, S.-D., & Mocanu, G. 2015, JCAP, 11, 027, doi: 10.1088/1475-7516/2015/11/027 22
[252] Harko, T., & Lobo, F. S. N. 2015, Phys. Rev. D, 92, 043011, doi: 10.1103/PhysRevD.92.043011 22
[253] Harko, T., & Madarassy, E. J. 2022, Eur. Phys. J. C, 82, 401, doi: 10.1140/epjc/s10052-022-10344-7 22

[254] Harko, T., & Madarassy, E. J. M. 2012, JCAP, 2012, 020, doi: 10.1088/1475-7516/2012/01/020 22
[255] Harko, T., & Mocanu, G. 2012, Phys. Rev. D, 85, 084012, doi: 10.1103/PhysRevD.85.084012 22
[256] Haslbauer, M., Banik, I., Kroupa, P., Wittenburg, N., & Javanmardi, B. 2022, ApJ, 925, 183, doi: 10.3847/1538-4357/ac46ac 13, 25
[257] Hayashi, K., Ferreira, E. G. M., & Chan, H. Y. J. 2021, ApJL, 912, L3, doi: 10.3847/2041-8213/abf501 20
[258] Heavens, A., Fantaye, Y., Mootoovaloo, A., et al. 2017a, "". https://arxiv.org/abs/1704.03472 74
[259] Heavens, A., Fantaye, Y., Sellentin, E., et al. 2017b, Phys. Rev. Lett., 119, 101301, doi: 10.1103/PhysRevLett.119.101301 74
[260] Hernquist, L. 1990, ApJ, 356, 359, doi: 10.1086/168845 41, 64
[261] Hervas Peters, F., Schneider, A., Bucko, J., Giri, S. K., & Parimbelli, G. 2023, arXiv e-prints, arXiv:2309.03865, doi: 10.48550/arXiv.2309.03865 18
[262] Hinshaw, G., et al. 2007, ApJS, 170, 288, doi: 10.1086/513698 4
[263] Horiuchi, S., Humphrey, P. J., Onorbe, J., et al. 2014, Phys. Rev. D, 89, 025017, doi: 10.1103/PhysRevD.89.025017 104
[264] Horner, E. L., Mungia Wulftange, F., Ianora, I. A., & Kishimoto, C. T. 2023, Phys. Rev. D, 108, 083503, doi: 10.1103/PhysRevD.108.083503 19
[265] Hossenfelder, S., & Mistele, T. 2018, Int. J. Mod. Phys. D, 27, 1847010, doi: 10.1142/S0218271818470107 14
[266] Hu, W., Barkana, R., & Gruzinov, A. 2000, Phys. Rev. Lett., 85, 1158, doi: 10.1103/PhysRevLett.85.1158 19
[267] Hubble, E., & Humason, M. L. 1931, ApJ, 74, 43, doi: 10.1086/143323 2
[268] Hui, L., Joyce, A., Landry, M. J., & Li, X. 2021, JCAP, 2021, 011, doi: 10.1088/1475-7516/2021/01/011 19
[269] Hui, L., Ostriker, J. P., Tremaine, S., & Witten, E. 2017, Phys. Rev. D, 95, 043541, doi: 10.1103/PhysRevD.95.043541 20
[270] Huo, R., Kaplinghat, M., Pan, Z., & Yu, H.-B. 2018, Phys. Lett. B, 783, 76, doi: 10.1016/j.physletb.2018.06.024 23, 92, 93
[271] Ilie, C., Levy, C., Pilawa, J., Freese, K., & Zhang, S. 2023, in AAS/High Energy Astrophysics Division, Vol. 55, AAS/High Energy Astrophysics Division, 116.08 103
[272] Iršič, V., Viel, M., Haehnelt, M. G., Bolton, J. S., & Becker, G. D. 2017a, Phys. Rev. Lett., 119, 031302, doi: 10.1103/PhysRevLett.119.031302 20, 103
[273] Iršič, V., Viel, M., Haehnelt, M. G., et al. 2017b, Phys. Rev. D, 96, 023522, doi: 10.1103/PhysRevD.96.023522 19, 103
[274] Islam, T., & Dutta, K. 2020, Phys. Rev. D, 101, 084015, doi: 10.1103/PhysRevD.101.084015 14
[275] Ivanov, D., & Liberati, S. 2020, JCAP, 07, 065, doi: 10.1088/1475-7516/2020/07/065 30, 32
[276] Jaffe, W. 1983, MNRAS, 202, 995, doi: 10.1093/mnras/202.4.995 41
[277] Jedamzik, K., & Pospelov, M. 2009, New J. Phys., 11, 105028, doi: 10.1088/1367-2630/11/10/105028 4
[278] Jeffreys, H. 1961, The Theory of Probability, 3rd edn. (Oxford University

Press) 74
[279] Jethwa, P., Erkal, D., & Belokurov, V. 2018, MNRAS, 473, 2060, doi: 10.1093/mnras/stx2330 12
[280] Ji, S. U., & Sin, S. J. 1994, Phys. Rev. D, 50, 3655, doi: 10.1103/PhysRevD.50.3655 21
[281] Jungman, G., Kamionkowski, M., & Griest, K. 1995, PR, 267, 195. https://api.semanticscholar.org/CorpusID:119067698 5, 6
[282] Kahlhoefer, F., Schmidt-Hoberg, K., Frandsen, M. T., & Sarkar, S. 2014, MNRAS, 437, 2865, doi: 10.1093/mnras/stt2097 85
[283] Kahn, F. D., & Woltjer, L. 1959, ApJ, 130, 705, doi: 10.1086/146762 2
[284] Kamada, A., Kaplinghat, M., Pace, A. B., & Yu, H.-B. 2017, Phys. Rev. Lett., 119, 111102, doi: 10.1103/PhysRevLett.119.111102 23
[285] Kamionkowski, M. 1998, in High Energy Physics and Cosmology, 1997 Summer School, Vol. 14, 394, doi: 10.48550/arXiv.hep-ph/9710467 5
[286] Karukes, E. V., & Salucci, P. 2017, MNRAS, 465, 4703, doi: 10.1093/mnras/stw3055 xiii, 51, 55, 61
[287] Kashfi, T., & Roshan, M. 2022, JCAP, 2022, 029, doi: 10.1088/1475-7516/2022/10/029 25
[288] Katz, H., Desmond, H., Lelli, F., et al. 2018, MNRAS, 480, 4287, doi: 10.1093/mnras/sty2129 17
[289] Keller, B. W., & Wadsley, J. W. 2017, ApJL, 835, L17, doi: 10.3847/2041-8213/835/1/L17 16
[290] Kelvin, W. 1904, Baltimore Lectures on Molecular Dynamics and the Wave Theory of Light (Clay & Sons). https://books.google.it/books?id=QrTDvwEACAAJ 2
[291] Kennedy, R., Frenk, C., Cole, S., & Benson, A. 2014, MNRAS, 442, 2487, doi: 10.1093/mnras/stu719 18, 104
[292] Kennicutt, R. C., & Evans, N. J. 2012, ARA&A, 50, 531, doi: 10.1146/annurev-astro-081811-125610 90
[293] Kereš, D., Katz, N., Davé, R., Fardal, M., & Weinberg, D. H. 2009, MNRAS, 396, 2332, doi: 10.1111/j.1365-2966.2009.14924.x 17
[294] Kim, J. E. 2002, in Dark Matter in Astro- and Particle Physics, DARK 2002, 246–254, doi: 10.48550/arXiv.astro-ph/0205146 19
[295] Kim, S. Y., Peter, A. H. G., & Hargis, J. R. 2018, Phys. Rev. Lett., 121, 211302, doi: 10.1103/PhysRevLett.121.211302 12
[296] Kistler, M. D., Yüksel, H., Beacom, J. F., Hopkins, A. M., & Wyithe, J. S. B. 2009, ApJL, 705, L104, doi: 10.1088/0004-637X/705/2/L104 95, 96, 101
[297] Klypin, A. A., Kravtsov, A. V., Valenzuela, O., & Prada, F. 1999, ApJ, 522, 82, doi: 10.1086/307643 12
[298] Kocevski, D. D., Onoue, M., Inayoshi, K., et al. 2023, ApJL, 954, L4, doi: 10.3847/2041-8213/ace5a0 89
[299] Koposov, S. E., Belokurov, V., Torrealba, G., & Evans, N. W. 2015, ApJ, 805, 130, doi: 10.1088/0004-637X/805/2/130 12
[300] Kroupa, P., Banik, I., Haghi, H., et al. 2018, Nat, 2, 925, doi: 10.1038/s41550-018-0622-x 25
[301] Kuzio de Naray, R., Martinez, G. D., Bullock, J. S., & Kaplinghat, M. 2010,

ApJL, 710, L161, doi: 10.1088/2041-8205/710/2/L161 23
[302] Kuzio de Naray, R., & Spekkens, K. 2011, ApJL, 741, L29, doi: 10.1088/2041-8205/741/2/L29 17
[303] Labbé, I., van Dokkum, P., Nelson, E., et al. 2023, Nat, 616, 266, doi: 10.1038/s41586-023-05786-2 87
[304] Lange, R., Driver, S. P., Robotham, A. S. G., et al. 2015, MNRAS, 447, 2603, doi: 10.1093/mnras/stu2467 64
[305] Lapi, A., & Cavaliere, A. 2009, ApJ, 692, 174, doi: 10.1088/0004-637X/692/1/174 34
[306] Lapi, A., & Cavaliere, A. 2009, Nucl. Phys. B Proc. Suppl., 194, 91, doi: 10.1016/j.nuclphysbps.2009.07.007 34, 36
[307] Lapi, A., & Cavaliere, A. 2011, ApJ, 743, 127, doi: 10.1088/0004-637X/743/2/127 34, 48
[308] Lapi, A., & Danese, L. 2015, JCAP, 09, 003, doi: 10.1088/1475-7516/2015/09/003 93, 103
[309] Lapi, A., Mancuso, C., Celotti, A., & Danese, L. 2017, ApJ, 835, 37, doi: 10.3847/1538-4357/835/1/37 103
[310] Lapi, A., Ronconi, T., Boco, L., et al. 2022, MDPI Univ., 8, 476, doi: 10.3390/universe8090476 95, 103
[311] Lapi, A., Salucci, P., & Danese, L. 2018, ApJ, 859, 2, doi: 10.3847/1538-4357/aabf35 xiii, 13, 44, 45, 51
[312] Laroche, A., Gilman, D., Li, X., Bovy, J., & Du, X. 2022, MNRAS, 517, 1867, doi: 10.1093/mnras/stac2677 20
[313] Larson, R. L., Hutchison, T. A., Bagley, M., et al. 2022, arXiv e-prints, arXiv:2211.10035, doi: 10.48550/arXiv.2211.10035 88
[314] Lasserre, T., Afonso, C., Albert, J. N., et al. 2000, A&A, 355, L39, doi: 10.48550/arXiv.astro-ph/0002253 6
[315] Lazar, A., et al. 2020, MNRAS, 497, 2393, doi: 10.1093/mnras/staa2101 41
[316] Lee, J.-W., & Lim, S. 2010, JCAP, 01, 007, doi: 10.1088/1475-7516/2010/01/007 22
[317] Lelli, F., McGaugh, S. S., & Schombert, J. M. 2016, ApJL, 816, L14, doi: 10.3847/2041-8205/816/1/L14 13
[318] Lelli, F., McGaugh, S. S., & Schombert, J. M. 2016, Astron. J., 152, 157, doi: 10.3847/0004-6256/152/6/157 14, 24, 25
[319] Lelli, F., McGaugh, S. S., Schombert, J. M., Desmond, H., & Katz, H. 2019, MNRAS, 484, 3267, doi: 10.1093/mnras/stz205 13
[320] Lelli, F., McGaugh, S. S., Schombert, J. M., & Pawlowski, M. S. 2017, ApJ, 836, 152, doi: 10.3847/1538-4357/836/2/152 14, 63, 69, 71, 110
[321] Lelli, F., Zhang, Z.-Y., Bisbas, T. G., et al. 2023, A&A, 672, A106, doi: 10.1051/0004-6361/202245105 24, 25
[322] Leung, G. C. K., Bagley, M. B., Finkelstein, S. L., et al. 2023, ApJL, 954, L46, doi: 10.3847/2041-8213/acf365 103
[323] Lewis, A. 2019, arXiv e-prints. https://arxiv.org/abs/1910.13970 74
[324] Li, P., Lelli, F., McGaugh, S., & Schombert, J. 2018, A&A, 615, A3, doi: 10.1051/0004-6361/201732547 14, 24
[325] Li, S., Li, R., Zhu, K., et al. 2023, arXiv e-prints, arXiv:2310.13278, doi: 10.

48550/arXiv.2310.13278 17
[326] Li, X., Li, M.-H., Lin, H.-N., & Chang, Z. 2013, Mon. Not. Roy. Astron. Soc., 428, 2939, doi: 10.1093/mnras/sts237 26
[327] Li, X., Zhao, S.-P., Lin, H.-N., & Zhou, Y. 2021, Chinese Physics C, 45, 025107, doi: 10.1088/1674-1137/abce53 24
[328] Li, X. Y., Harko, T., & Cheng, K. S. 2012, JCAP, 2012, 001, doi: 10.1088/1475-7516/2012/06/001 22
[329] Liddle, A. R. 2004, MNRAS, 351, L49, doi: 10.1111/j.1365-2966.2004.08033.x 98
[330] Łokas, E. L., & Mamon, G. A. 2001, MNRAS, 321, 155, doi: 10.1046/j.1365-8711.2001.04007.x 10
[331] López-Corredoira, M., & Betancort-Rijo, J. E. 2021, ApJ, 909, 137, doi: 10.3847/1538-4357/abe381 24, 25
[332] López-Corredoira, M., Betancort-Rijo, J. E., Scarpa, R., & Chrobáková, Ž. 2022, MNRAS, 517, 5734, doi: 10.1093/mnras/stac3117 26
[333] Lovell, M. R., Frenk, C. S., Eke, V. R., et al. 2014, MNRAS, 439, 300, doi: 10.1093/mnras/stt2431 18
[334] Lovell, M. R., Gonzalez-Perez, V., Bose, S., et al. 2017, MNRAS, 468, 2836, doi: 10.1093/mnras/stx621 12, 18
[335] Lovell, M. R., Eke, V., Frenk, C. S., et al. 2012, MNRAS, 420, 2318, doi: 10.1111/j.1365-2966.2011.20200.x 19
[336] Lovell, M. R., Bose, S., Boyarsky, A., et al. 2016, MNRAS, 461, 60, doi: 10.1093/mnras/stw1317 104
[337] Ludlow, A. D., Navarro, J. F., White, S. D. M., et al. 2011, MNRAS, 415, 3895, doi: 10.1111/j.1365-2966.2011.19008.x 34
[338] Ludlow, A. D., Benítez-Llambay, A., Schaller, M., et al. 2017, Phys. Rev. Lett., 118, 161103, doi: 10.1103/PhysRevLett.118.161103 14, 16
[339] Mac Low, M.-M., & Ferrara, A. 1999, ApJ, 513, 142, doi: 10.1086/306832 17
[340] Macciò, A. V., Dutton, A. A., van den Bosch, F. C., et al. 2007, MNRAS, 378, 55, doi: 10.1111/j.1365-2966.2007.11720.x 48
[341] Madau, P., & Dickinson, M. 2014, ARA&A, 52, 415, doi: 10.1146/annurev-astro-081811-125615 90, 101
[342] Madelung, E. 1926, Naturwissenschaften, 14, 1004, doi: 10.1007/BF01504657 22, 123
[343] Maio, U., & Viel, M. 2023, A&A, 672, A71, doi: 10.1051/0004-6361/202345851 103
[344] Mamon, G. A., Cava, A., Biviano, A., et al. 2019, A&A, 631, A131, doi: 10.1051/0004-6361/201935081 41
[345] Marra, V., Rodrigues, D. C., & de Almeida, A. O. F. 2020, MNRAS, 494, 2875, doi: 10.1093/mnras/staa890 14
[346] Mashchenko, S., Wadsley, J., & Couchman, H. M. P. 2008, AAAS, 319, 174, doi: 10.1126/science.1148666 17
[347] Massey, R., Kitching, T., & Richard, J. 2010, Rept. Prog. Phys., 73, 086901, doi: 10.1088/0034-4885/73/8/086901 4
[348] May, S., & Springel, V. 2023, MNRAS, 524, 4256, doi: 10.1093/mnras/stad2031 93

[349] McGaugh, S., Lelli, F., & Schombert, J. 2016, Phys. Rev. Lett., 117, 201101, doi: 10.1103/PhysRevLett.117.201101 14, 110
[350] McGaugh, S., & Milgrom, M. 2013, ApJ, 775, 139, doi: 10.1088/0004-637X/775/2/139 25
[351] McGaugh, S. S. 2015, Can. J. Phys., 93, 250, doi: 10.1139/cjp-2014-0203 26
[352] McGaugh, S. S. 2021, Studies in Hist. and Phil. of Science, 88, 220, doi: 10.1016/j.shpsa.2021.05.008 17
[353] McGaugh, S. S., Katz, H., Teuben, P., & Angus, G. 2012, in American Astronomical Society Meeting Abstracts, Vol. 220, American Astronomical Society Meeting Abstracts, 435.03 25
[354] McGaugh, S. S., Schombert, J. M., Bothun, G. D., & de Blok, W. J. G. 2000, ApJL, 533, L99, doi: 10.1086/312628 13
[355] Menci, N., Grazian, A., Castellano, M., & Sanchez, N. G. 2016, ApJL, 825, L1, doi: 10.3847/2041-8205/825/1/L1 104, 112, 113
[356] Meneghetti, M., Davoli, G., Bergamini, P., et al. 2020, AAAS, 369, 1347, doi: 10.1126/science.aax5164 81
[357] Merritt, D., Milosavljevic, M., Verde, L., & Jimenez, R. 2002, Phys. Rev. Lett., 88, 191301, doi: 10.1103/PhysRevLett.88.191301 18
[358] Meurer, G. R., Heckman, T. M., & Calzetti, D. 1999, ApJ, 521, 64, doi: 10.1086/307523 90
[359] Milgrom, M. 1983, ApJ, 270, 365, doi: 10.1086/161130 23, 24, 25
[360] Milgrom, M. 2002, New Astron. Rev., 46, 741, doi: 10.1016/S1387-6473(02)00243-9 24
[361] Milgrom, M. 2014, MNRAS, 437, 2531, doi: 10.1093/mnras/stt2066 25
[362] Milgrom, M. 2022, Phys. Rev. D, 106, 084010, doi: 10.1103/PhysRevD.106.084010 25
[363] Milgrom, M. 2023, arXiv e-prints, arXiv:2310.14334. https://arxiv.org/abs/2310.14334 25
[364] Milgrom, M. 2023, Phys. Rev. D, 108, 063009, doi: 10.1103/PhysRevD.108.063009 25
[365] Milgrom, M., & Sanders, R. H. 2005, MNRAS, 357, 45, doi: 10.1111/j.1365-2966.2004.08578.x 24
[366] Mo, H. J., & Mao, S. 2004, MNRAS, 353, 829, doi: 10.1111/j.1365-2966.2004.08114.x 17
[367] Mo, H. J., Mao, S., & White, S. D. M. 1998, MNRAS, 295, 319, doi: 10.1046/j.1365-8711.1998.01227.x 13
[368] Mocz, P., Vogelsberger, M., Robles, V. H., et al. 2017, MNRAS, 471, 4559, doi: 10.1093/mnras/stx1887 20
[369] Mocz, P., Fialkov, A., Vogelsberger, M., et al. 2019, Phys. Rev. Lett., 123, 141301, doi: 10.1103/PhysRevLett.123.141301 20
[370] Mocz, P., et al. 2020, Mon. Not. Roy. Astron. Soc., 494, 2027, doi: 10.1093/mnras/staa738 20
[371] Moffat, J. W. 2005, JCAP, 05, 003, doi: 10.1088/1475-7516/2005/05/003 23
[372] Mohanty, S., & Harish, R. 2023, Indian J. of Phys., doi: 10.1007/s12648-023-02961-z 24
[373] Moore, B., Ghigna, S., Governato, F., et al. 1999, ApJL, 524, L19, doi: 10.

1086/312287 12
[374] Moran, S. M., Heckman, T. M., Kauffmann, G., et al. 2012, ApJ, 745, 66, doi: 10.1088/0004-637X/745/1/66 64
[375] Morishita, T., & Stiavelli, M. 2023, ApJL, 946, L35, doi: 10.3847/2041-8213/acbf50 87
[376] Moster, B. P., Naab, T., & White, S. D. M. 2013, MNRAS, 428, 3121, doi: 10.1093/mnras/sts261 46
[377] Moster, B. P., Naab, T., & White, S. D. M. 2018, MNRAS, 477, 1822, doi: 10.1093/mnras/sty655 93
[378] Müller, O., Lelli, F., Famaey, B., et al. 2022, A&A, 662, A57, doi: 10.1051/0004-6361/202142351 110
[379] Munari, E., Biviano, A., & Mamon, G. A. 2014, A&A, 566, A68, doi: 10.1051/0004-6361/201322450 35
[380] Nadler, E. O., Birrer, S., Gilman, D., et al. 2021, ApJ, 917, 7, doi: 10.3847/1538-4357/abf9a3 19, 104
[381] Nadler, E. O., Gluscevic, V., Boddy, K. K., & Wechsler, R. H. 2019, ApJL, 878, L32, doi: 10.3847/2041-8213/ab1eb2 19
[382] Nadler, E. O., Mao, Y.-Y., Wechsler, R. H., Garrison-Kimmel, S., & Wetzel, A. 2018, ApJ, 859, 129, doi: 10.3847/1538-4357/aac266 34
[383] Nadler, E. O., Drlica-Wagner, A., Bechtol, K., et al. 2021, Phys. Rev. Lett., 126, 091101, doi: 10.1103/PhysRevLett.126.091101 20
[384] Naidu, R. P., Oesch, P. A., Setton, D. J., et al. 2022a, arXiv e-prints, arXiv:2208.02794, doi: 10.48550/arXiv.2208.02794 87
[385] Naidu, R. P., Oesch, P. A., van Dokkum, P., et al. 2022b, ApJL, 940, L14, doi: 10.3847/2041-8213/ac9b22 87
[386] Natarajan, P. 1999, ApJL, 512, L105, doi: 10.1086/311877 16
[387] Navarro, J. 2006, in KITP Conference: Applications of Gravitational Lensing: Unique Insights into Galaxy Formation and Evolution, ed. L. V. E. Koopmans, C.-P. Ma, B. Moore, P. Schneider, & T. Treu, 30 12
[388] Navarro, J. F., Benítez-Llambay, A., Fattahi, A., et al. 2017, MNRAS, 471, 1841, doi: 10.1093/mnras/stx1705 12, 16
[389] Navarro, J. F., & Benz, W. 1991, ApJ, 380, 320, doi: 10.1086/170590 13
[390] Navarro, J. F., Eke, V. R., & Frenk, C. S. 1996, MNRAS, 283, L72, doi: 10.1093/mnras/283.3.L72 10, 17
[391] Navarro, J. F., Ludlow, A., Springel, V., et al. 2010, MNRAS, 402, 21, doi: 10.1111/j.1365-2966.2009.15878.x 34
[392] Nemiroff, R. J. 1987, PhD thesis, University of Pennsylvania 6
[393] Newton, O., Cautun, M., Jenkins, A., Frenk, C. S., & Helly, J. C. 2018, MNRAS, 479, 2853, doi: 10.1093/mnras/sty1085 12
[394] Newton, O., Leo, M., Cautun, M., et al. 2021, JCAP, 2021, 062, doi: 10.1088/1475-7516/2021/08/062 104
[395] Niemeyer, J. C. 2020, Prog. in Part. and Nucl. Phys., 113, 103787, doi: 10.1016/j.ppnp.2020.103787 20
[396] Nieuwenhuizen, T. M., Morandi, A., & Limousin, M. 2018, MNRAS, 476, 3393, doi: 10.1093/mnras/sty380 23
[397] Nolting, C., Williams, L. L. R., Boylan-Kolchin, M., & Hjorth, J. 2016, JCAP,

2016, 042, doi: 10.1088/1475-7516/2016/09/042 34
[398] O'Brien, J. G., Chiarelli, T. L., Falcone, M. A., & AlQurashi, M. H. 2019, Astro. Nach., 340, 95, doi: 10.1002/asna.201913568 14
[399] Oesch, P. A., Bouwens, R. J., Illingworth, G. D., Labbé, I., & Stefanon, M. 2018, ApJ, 855, 105, doi: 10.3847/1538-4357/aab03f 89, 91, 96, 101
[400] Ogle, P. M., Jarrett, T., Lanz, L., et al. 2019, ApJL, 884, L11, doi: 10.3847/2041-8213/ab459e 14
[401] Oman, K. A., Brouwer, M. M., Ludlow, A. D., & Navarro, J. F. 2020, arXiv e-prints, arXiv:2006.06700, doi: 10.48550/arXiv.2006.06700 14
[402] Oman, K. A., Navarro, J. F., Fattahi, A., et al. 2015, MNRAS, 452, 3650, doi: 10.1093/mnras/stv1504 23
[403] Oria, P. A., Famaey, B., Thomas, G. F., et al. 2021, ApJ, 923, 68, doi: 10.3847/1538-4357/ac273d 25
[404] O'Shea, B. W., & Norman, M. L. 2006, ApJ, 648, 31, doi: 10.1086/505684 19
[405] Ostriker, J. P., Choi, E., Chow, A., & Guha, K. 2019, ApJ, 885, 97, doi: 10.3847/1538-4357/ab3288 13
[406] Ostriker, J. P., & Hausman, M. A. 1977, ApJL, 217, L125, doi: 10.1086/182554 12
[407] Oñorbe, J., Boylan-Kolchin, M., Bullock, J. S., et al. 2015, MNRAS, 454, 2092, doi: 10.1093/mnras/stv2072 17
[408] Pacucci, F., Mesinger, A., & Haiman, Z. 2013, MNRAS: Letters, 435, L53, doi: 10.1093/mnrasl/slt093 103
[409] Paczynski, B. 1986, ApJ, 304, 1, doi: 10.1086/164140 6
[410] Pagels, H., & Primack, J. R. 1982, Phys. Rev. Lett., 48, 223, doi: 10.1103/PhysRevLett.48.223 19
[411] Papastergis, E., Adams, E. A. K., & van der Hulst, J. M. 2016, A&A, 593, A39, doi: 10.1051/0004-6361/201628410 13
[412] Papastergis, E., Cattaneo, A., Huang, S., Giovanelli, R., & Haynes, M. P. 2012, ApJ, 759, 138, doi: 10.1088/0004-637X/759/2/138 63, 64
[413] Papastergis, E., & Shankar, F. 2016, A&A, 591, A58, doi: 10.1051/0004-6361/201527854 12
[414] Paranjape, A., & Sheth, R. K. 2021, MNRAS, 507, 632, doi: 10.1093/mnras/stab2141 14
[415] Peñarrubia, J., Pontzen, A., Walker, M. G., & Koposov, S. E. 2012, ApJL, 759, L42, doi: 10.1088/2041-8205/759/2/L42 17
[416] Peebles, P. J. E. 1982, ApJL, 263, L1, doi: 10.1086/183911 3
[417] Peeples, M. S., Werk, J. K., Tumlinson, J., et al. 2014, ApJ, 786, 54, doi: 10.1088/0004-637X/786/1/54 63
[418] Peirani, S., Durier, F., & de Freitas Pacheco, J. A. 2006, MNRAS, 367, 1011, doi: 10.1111/j.1365-2966.2006.10149.x 17, 34
[419] Pérez-González, P. G., Costantin, L., Langeroodi, D., et al. 2023, ApJL, 951, L1, doi: 10.3847/2041-8213/acd9d0 103
[420] Persic, M., & Salucci, P. 1995, ApJS, 99, 501, doi: 10.1086/192195 xiv, 125, 126, 127, 128, 129, 130, 131, 132, 133, 134
[421] Persic, M., Salucci, P., & Stel, F. 1996, MNRAS, 281, 27, doi: 10.1093/mnras/278.1.27 xiii, 44, 45, 51, 53, 55, 59

[422] Peter, A. H. G., Rocha, M., Bullock, J. S., & Kaplinghat, M. 2013, MNRAS, 430, 105, doi: 10.1093/mnras/sts535 22
[423] Petersen, J. 2019, arXiv e-prints, arXiv:1906.09798, doi: 10.48550/arXiv.1906.09798 24
[424] Petersen, J., & Frandsen, M. T. 2017, arXiv e-prints, arXiv:1710.03096, doi: 10.48550/arXiv.1710.03096 24
[425] Petersen, J., & Lelli, F. 2020, A&A, 636, A56, doi: 10.1051/0004-6361/201936964 14, 24
[426] Pethick, C., & Smith, H. 2002, Bose-Einstein condensation in dilute gases (Cambridge University Press) 21
[427] Pires, M. O. C., & de Souza, J. C. C. 2012, JCAP, 2012, 024, doi: 10.1088/1475-7516/2012/11/024 22
[428] Plummer, H. C. 1911, MNRAS, 71, 460, doi: 10.1093/mnras/71.5.460 41
[429] Poincare, H. 1906, Pop. Astro., 14, 475 2
[430] Polisensky, E., & Ricotti, M. 2011, Phys. Rev. D, 83, 043506, doi: 10.1103/PhysRevD.83.043506 19
[431] Pontzen, A., & Governato, F. 2012, MNRAS, 421, 3464, doi: 10.1111/j.1365-2966.2012.20571.x 17
[432] Pontzen, A., & Governato, F. 2014, Nat, 506, 171, doi: 10.1038/nature12953 17
[433] Posti, L., Marasco, A., Fraternali, F., & Famaey, B. 2019, A&A, 629, A59, doi: 10.1051/0004-6361/201935982 13
[434] Pozo, A., Emami, R., Mocz, P., et al. 2023, arXiv e-prints, arXiv:2310.12217, doi: 10.48550/arXiv.2310.12217 20
[435] Pradyumna, S., & Desai, S. 2021, Phys. Dark Univ., 33, 100854, doi: 10.1016/j.dark.2021.100854 14
[436] Pradyumna, S., & Desai, S. 2021, Phys. Dark Univ., 33, 100854, doi: https://doi.org/10.1016/j.dark.2021.100854 25
[437] Pradyumna, S., Gupta, S., Seeram, S., & Desai, S. 2021, Phys. Dark Univ., 31, 100765, doi: 10.1016/j.dark.2020.100765 14
[438] Press, W. H., & Schechter, P. 1974, ApJ, 187, 425, doi: 10.1086/152650 9
[439] Prugniel, P., & Simien, F. 1997, A&A, 321, 111 41
[440] Ray, T. S., Sarkar, S., & Shaw, A. K. 2022, JCAP, 09, 011, doi: 10.1088/1475-7516/2022/09/011 22
[441] Read, J. I., Agertz, O., & Collins, M. L. M. 2016, MNRAS, 459, 2573, doi: 10.1093/mnras/stw713 17
[442] Read, J. I., & Gilmore, G. 2005, MNRAS, 356, 107, doi: 10.1111/j.1365-2966.2004.08424.x 17
[443] Read, J. I., Iorio, G., Agertz, O., & Fraternali, F. 2016, MNRAS, 462, 3628, doi: 10.1093/mnras/stw1876 41
[444] Ren, T., Kwa, A., Kaplinghat, M., & Yu, H.-B. 2019, Physical Review X, 9, 031020, doi: 10.1103/PhysRevX.9.031020 23
[445] Ritondale, E., Vegetti, S., Despali, G., et al. 2019, MNRAS, 485, 2179, doi: 10.1093/mnras/stz464 104
[446] Roberts, M. S. 1966, ApJ, 144, 639, doi: 10.1086/148645 3
[447] Roberts, M. S., & Rots, A. H. 1973, A&A, 26, 483 3

[448] Robertson, A., Massey, R., Eke, V., et al. 2018, MNRAS, 476, L20, doi: 10.1093/mnrasl/sly024 23
[449] Robertson, B. E., Ellis, R. S., Dunlop, J. S., McLure, R. J., & Stark, D. P. 2010, Nat, 468, 49, doi: 10.1038/nature09527 4
[450] Robertson, B. E., Ellis, R. S., Furlanetto, S. R., & Dunlop, J. S. 2015, ApJL, 802, L19, doi: 10.1088/2041-8205/802/2/L19 90
[451] Robertson, B. E., et al. 2023, Nat, 7, 611, doi: 10.1038/s41550-023-01921-1 87
[452] Rodighiero, G., Bisigello, L., Iani, E., et al. 2023, MNRAS, 518, L19, doi: 10.1093/mnrasl/slac115 87, 114
[453] Rodrigues, D. C., & Marra, V. 2020, in IAU Symposium 359: Galaxy Evolution and Feedback Across Different Environments, doi: 10.1017/S1743921320001684 14, 25
[454] Rogers, K. K., & Peiris, H. V. 2021, Phys. Rev. Lett., 126, 071302, doi: 10.1103/PhysRevLett.126.071302 20
[455] Rogstad, D. H., & Shostak, G. S. 1972, ApJ, 176, 315, doi: 10.1086/151636 3
[456] Romano-Diaz, E., Shlosman, I., Hoffman, Y., & Heller, C. 2008, ApJL, 685, L105, doi: 10.1086/592687 18
[457] Rong, Y., Li, H., Wang, J., et al. 2018, MNRAS, 477, 230, doi: 10.1093/mnras/sty697 14
[458] Rubin, V. C., Ford, W. K., J., & Thonnard, N. 1978, ApJL, 225, L107, doi: 10.1086/182804 3
[459] Rubin, V. C., & Ford, W. Kent, J. 1970, ApJ, 159, 379, doi: 10.1086/150317 3
[460] Rudakovskyi, A., Savchenko, D., & Tsizh, M. 2020, MNRAS, 497, 3393, doi: 10.1093/mnras/staa2194 104
[461] Safarzadeh, M., & Spergel, D. N. 2020, ApJ, 893, 21, doi: 10.3847/1538-4357/ab7db2 20
[462] Saintonge, A., Kauffmann, G., Kramer, C., et al. 2011, MNRAS, 415, 32, doi: 10.1111/j.1365-2966.2011.18677.x 64
[463] Salucci, P., & Burkert, A. 2000, ApJL, 537, L9, doi: 10.1086/312747 20, 46, 53, 65, 84
[464] Salucci, P., Lapi, A., Tonini, C., et al. 2007, MNRAS, 378, 41, doi: 10.1111/j.1365-2966.2007.11696.x 46
[465] Sanchez, N. G., Paduroiu, S., & Biermann, P. L. 2016, Warm Dark Matter Astrophysics in Agreement with Observations and keV Sterile Neutrinos: Synthesis of Highlights and Conclusions of the Chalonge -de Vega Meudon Workshop 2016 . In Memoriam Héctor J. de Vega. https://hal.science/hal-01773092 19
[466] Sanders, R. H. 2018, Int. J. Mod. Phys. D, 27, 14, doi: 10.1142/S0218271818470272 25
[467] Sanders, R. H. 2019, MNRAS, 485, 513, doi: 10.1093/mnras/stz353 25
[468] Santos-Santos, I. M., Brook, C. B., Stinson, G., et al. 2016, MNRAS, 455, 476, doi: 10.1093/mnras/stv2335 16
[469] Sawala, T., Scannapieco, C., Maio, U., & White, S. 2010, MNRAS, 402, 1599, doi: 10.1111/j.1365-2966.2009.16035.x 17
[470] Scannapieco, C., Wadepuhl, M., Parry, O. H., et al. 2012, MNRAS, 423, 1726,

doi: 10.1111/j.1365-2966.2012.20993.x 17
[471] Schaye, J., Crain, R. A., Bower, R. G., et al. 2015, MNRAS, 446, 521, doi: 10.1093/mnras/stu2058 13
[472] Schive, H.-Y., Chiueh, T., & Broadhurst, T. 2014a, Nat, 10, 496, doi: 10.1038/nphys2996 19, 20, 42
[473] Schive, H.-Y., Chiueh, T., Broadhurst, T., & Huang, K.-W. 2016, ApJ, 818, 89, doi: 10.3847/0004-637X/818/1/89 20, 92, 93
[474] Schive, H.-Y., Liao, M.-H., Woo, T.-P., et al. 2014b, Phys. Rev. Lett., 113, 261302, doi: 10.1103/PhysRevLett.113.261302 20, 42
[475] Schmidt, K. B., Hansen, S. H., & Macciò, A. V. 2008, ApJL, 689, L33, doi: 10.1086/595783 35
[476] Schmidt, M. 1957, Bull. Astro. Inst. of the Netherlands, 13, 247 2
[477] Schneider, A., Smith, R. E., Macciò, A. V., & Moore, B. 2012, MNRAS, 424, 684, doi: 10.1111/j.1365-2966.2012.21252.x 92, 93
[478] Schneider, A., Smith, R. E., & Reed, D. 2013, MNRAS, 433, 1573, doi: 10.1093/mnras/stt829 93
[479] Schultz, C., Oñorbe, J., Abazajian, K. N., & Bullock, J. S. 2014, MNRAS, 442, 1597, doi: 10.1093/mnras/stu976 104
[480] Schwarz, G. 1978, The Ann. of Stat., 6, 461 98
[481] Schwarzschild, M. 1954, AJ, 59, 273, doi: 10.1086/107013 2
[482] Sen, M. 2021, in Journal of Physics Conference Series, Vol. 2156, J. of Phys. Conf. Series, 012018, doi: 10.1088/1742-6596/2156/1/012018 19
[483] Sérsic, J. L. 1963, Boletin de la Asociacion Argentina de Astronomia La Plata Argentina, 6, 41 41
[484] Seto, O., & Yamaguchi, M. 2009, in American Institute of Physics Conference Series, Vol. 1166, Sources and Detection of Dark Matter and Dark Energy in the Universe, ed. D. B. Cline, 126–131, doi: 10.1063/1.3232169 19
[485] Shabani, H., & Moraes, P. H. R. S. 2023, Physica Scripta, 98, 065302, doi: 10.1088/1402-4896/acd36d 23
[486] Shafieloo, A., & Hazra, D. K. 2017, JCAP, 04, 012, doi: 10.1088/1475-7516/2017/04/012 4
[487] Shen, S., Madau, P., Conroy, C., Governato, F., & Mayer, L. 2014, ApJ, 792, 99, doi: 10.1088/0004-637X/792/2/99 12, 16
[488] Shen, S., Mo, H. J., White, S. D. M., et al. 2003, MNRAS, 343, 978, doi: 10.1046/j.1365-8711.2003.06740.x 64
[489] Sheth, R. K., & Tormen, G. 1999, MNRAS, 308, 119, doi: 10.1046/j.1365-8711.1999.02692.x 9
[490] Shevchuk, T., Kovetz, E. D., & Zitrin, A. 2023, "". https://arxiv.org/abs/2308.14640 85
[491] Shirasaki, M., Ishiyama, T., & Ando, S. 2021, ApJ, 922, 89, doi: 10.3847/1538-4357/ac214b 112
[492] Shobbrook, R. R., & Robinson, B. J. 1967, Austr. J. of Phys., 20, 131, doi: 10.1071/PH670131 3
[493] Simon, J. D., Bolatto, A. D., Leroy, A., Blitz, L., & Gates, E. L. 2005, ApJ, 621, 757, doi: 10.1086/427684 23
[494] Sin, S.-J. 1994, Phys. Rev. D, 50, 3650, doi: 10.1103/PhysRevD.50.3650 21

[495] Skordis, C., & Zlosnik, T. 2012, Phys. Rev. D, 85, 044044, doi: 10.1103/PhysRevD.85.044044 24
[496] Skordis, C., & Złośnik, T. 2021, Phys. Rev. Lett., 127, 161302, doi: 10.1103/PhysRevLett.127.161302 25
[497] Smercina, A., Bell, E. F., Price, P. A., et al. 2018, ApJ, 863, 152, doi: 10.3847/1538-4357/aad2d6 12
[498] Sobacchi, E., & Mesinger, A. 2013, MNRAS, 432, 3340, doi: 10.1093/mnras/stt693 92
[499] Sonego, S., & Faraoni, V. 1993, Class. Quant. Grav., 10, 1185, doi: 10.1088/0264-9381/10/6/015 27
[500] Sotiriou, T. P., & Faraoni, V. 2010, Rev. of Modern Phys., 82, 451, doi: 10.1103/RevModPhys.82.451 23
[501] Spergel, D. N., & Steinhardt, P. J. 2000, Phys. Rev. Lett., 84, 3760, doi: 10.1103/PhysRevLett.84.3760 23
[502] Spiegelhalter, D. J., Best, N. G., Carlin, B. P., & Van Der Linde, A. 2002, J. of the Royal Stat. So., 64, 583 98
[503] Steinhardt, C. L., Kokorev, V., Rusakov, V., Garcia, E., & Sneppen, A. 2023, ApJL, 951, L40, doi: 10.3847/2041-8213/acdef6 88
[504] Stinson, G. S., Bovy, J., Rix, H.-W., et al. 2013, MNRAS, 436, 625–634, doi: 10.1093/mnras/stt1600 65
[505] Subramanian, K., Cen, R., & Ostriker, J. P. 2000, ApJ, 538, 528, doi: 10.1086/309152 34
[506] Swaters, R. A., Sancisi, R., van Albada, T. S., & van der Hulst, J. M. 2009, A&A, 493, 871, doi: 10.1051/0004-6361:200810516 14
[507] Tam, S.-I., Umetsu, K., Robertson, A., & McCarthy, I. G. 2023, ApJ, 953, 169, doi: 10.3847/1538-4357/ace33f 14
[508] Teyssier, R., Chieze, J.-P., & Alimi, J.-M. 1997, ApJ, 480, 36, doi: 10.1086/303965 34
[509] Teyssier, R., Pontzen, A., Dubois, Y., & Read, J. I. 2013, MNRAS, 429, 3068, doi: 10.1093/mnras/sts563 17
[510] Thomas, D. B., Mozaffari, A., & Zlosnik, T. 2023, JCAP, 2023, 006, doi: 10.1088/1475-7516/2023/06/006 25
[511] Tian, Y., Umetsu, K., Ko, C.-M., Donahue, M., & Chiu, I.-N. 2020, ApJ, 896, 70, doi: 10.3847/1538-4357/ab8e3d 14
[512] Timberlake, C., Vinante, A., Shankar, F., Lapi, A., & Ulbricht, H. 2021, arXiv e-prints, arXiv:2110.02263. https://arxiv.org/abs/2110.02263 70
[513] Tinker, J., Kravtsov, A. V., Klypin, A., et al. 2008, ApJ, 688, 709, doi: 10.1086/591439 9, 92
[514] Tiret, O., & Combes, F. 2007, A&A, 464, 517, doi: 10.1051/0004-6361:20066446 24
[515] Tisserand, P., et al. 2007, A&A, 469, 387, doi: 10.1051/0004-6361:20066017 6
[516] Tollerud, E. J., Bullock, J. S., Strigari, L. E., & Willman, B. 2008, ApJ, 688, 277, doi: 10.1086/592102 12
[517] Tollet, E., Macciò, A. V., Dutton, A. A., et al. 2016, MNRAS, 456, 3542, doi: 10.1093/mnras/stv2856 48

[518] Tomozeiu, M., Mayer, L., & Quinn, T. 2016, ApJL, 827, L15, doi: 10.3847/2041-8205/827/1/L15 12
[519] Tonini, C., Lapi, A., & Salucci, P. 2006, ApJ, 649, 591, doi: 10.1086/506431 18
[520] Tremaine, S. D., & Richstone, D. O. 1977, ApJ, 212, 311, doi: 10.1086/155049 12
[521] Trenkel, C., & Wealthy, D. 2014, Phys. Rev. D, 90, 084037, doi: 10.1103/PhysRevD.90.084037 25
[522] Trotta, R. 2008, Contemp. Phys., 49, 71, doi: 10.1080/00107510802066753 74
[523] Trotta, R. 2017, in Bayesian Methods in Cosmology 74
[524] Turner, M. S. 1983, Phys. Rev. D, 28, 1243, doi: 10.1103/PhysRevD.28.1243 32
[525] Umetsu, K., Zitrin, A., Gruen, D., et al. 2016, ApJ, 821, 116, doi: 10.3847/0004-637X/821/2/116 85
[526] Valli, M., & Yu, H.-B. 2018, Nat, 2, 907, doi: 10.1038/s41550-018-0560-7 23
[527] van de Hulst, H. C., Raimond, E., & van Woerden, H. 1957, Bull. Astro. Inst. of the Netherlands, 14, 1 2
[528] Varieschi, G. U. 2020, Found. Phys., 50, 1608, doi: 10.1007/s10701-020-00389-7 106
[529] Varieschi, G. U. 2021, MNRAS, 503, 1915, doi: 10.1093/mnras/stab433 106
[530] Vegetti, S., Despali, G., Lovell, M. R., & Enzi, W. 2018, MNRAS, 481, 3661, doi: 10.1093/mnras/sty2393 104
[531] Veltmaat, J., Niemeyer, J. C., & Schwabe, B. 2018, Phys. Rev. D, 98, 043509, doi: 10.1103/PhysRevD.98.043509 20
[532] Viel, M., Becker, G. D., Bolton, J. S., & Haehnelt, M. G. 2013, Phys. Rev. D, 88, 043502, doi: 10.1103/PhysRevD.88.043502 103
[533] Vikhlinin, A., Kravtsov, A., Forman, W., et al. 2006, ApJ, 640, 691, doi: 10.1086/500288 73
[534] Villanueva-Domingo, P., Gnedin, N. Y., & Mena, O. 2018, ApJ, 852, 139, doi: 10.3847/1538-4357/aa9ff5 19
[535] Villasenor, B., Robertson, B., Madau, P., & Schneider, E. 2023, Phys. Rev. D, 108, 023502, doi: 10.1103/PhysRevD.108.023502 103
[536] Vogel, C. M., & Abazajian, K. N. 2023, Phys. Rev. D, 108, 043520, doi: 10.1103/PhysRevD.108.043520 19
[537] Vogelsberger, M., Zavala, J., & Loeb, A. 2012, MNRAS, 423, 3740, doi: 10.1111/j.1365-2966.2012.21182.x10.1002/asna.19141991009 23
[538] Voit, G. M. 2005, Rev. Mod. Phys., 77, 207, doi: 10.1103/RevModPhys.77.207 2, 4
[539] Wang, H.-F., Chrobáková, Ž., López-Corredoira, M., & Sylos Labini, F. 2023, ApJ, 942, 12, doi: 10.3847/1538-4357/aca27c 85
[540] Warren, M. S., Abazajian, K., Holz, D. E., & Teodoro, L. 2006, ApJ, 646, 881, doi: 10.1086/504962 9
[541] Weinberg, D. H., Dave, R., Katz, N., & Kollmeier, J. A. 2003, AIP Conf. Proc., 666, 157, doi: 10.1063/1.1581786 4

[542] Weinberg, S. 1979, The First Three Minutes: A Modern View of the Origin of the Universe, Bantam books (Bantam Books). https://books.google.it/books?id=nvgoAAAAYAAJ 4
[543] Weisz, D. R., & Boylan-Kolchin, M. 2017, MNRAS, 469, L83, doi: 10.1093/mnrasl/slx043 104
[544] Weisz, D. R., Johnson, B. D., & Conroy, C. 2014, ApJL, 794, L3, doi: 10.1088/2041-8205/794/1/L3 104
[545] Wheeler, C., Hopkins, P. F., & Doré, O. 2019, ApJ, 882, 46, doi: 10.3847/1538-4357/ab311b 16
[546] Wheeler, C., Phillips, J. I., Cooper, M. C., Boylan-Kolchin, M., & Bullock, J. S. 2014, MNRAS, 442, 1396, doi: 10.1093/mnras/stu965 12, 16
[547] Williams, L. L. R., Austin, C., Barnes, E., Babul, A., & Dalcanton, J. 2004, PoS, BDMH2004, 020, doi: 10.22323/1.014.0020 36
[548] Yan, H., Ma, Z., Ling, C., Cheng, C., & Huang, J. 2023, in American Astronomical Society Meeting Abstracts, Vol. 55, American Astronomical Society Meeting Abstracts, 177.41 87
[549] Yunis, R., Argüelles, C. R., López Nacir, D., et al. 2023, in The Sixteenth Marcel Grossmann Meeting: On Recent Developments in Theoretical and Experimental General Relativity, 2127–2138, doi: 10.1142/9789811269776_0166 19
[550] Zackrisson, E., Calissendorff, P., Asadi, S., & Nyholm, A. 2015, ApJ, 810, 23, doi: 10.1088/0004-637X/810/1/23 13
[551] Zavala, J., Lovell, M. R., Vogelsberger, M., & Burger, J. D. 2019, Phys. Rev. D, 100, 063007, doi: 10.1103/PhysRevD.100.063007 23
[552] Zelko, I. A., Treu, T., Abazajian, K. N., et al. 2022, Phys. Rev. Lett., 129, 191301, doi: 10.1103/PhysRevLett.129.191301 19
[553] Zentner, A., Dandavate, S., Slone, O., & Lisanti, M. 2022, JCAP, 2022, 031, doi: 10.1088/1475-7516/2022/07/031 16
[554] Zhang, X., Chan, M. H., Harko, T., Liang, S.-D., & Leung, C. S. 2018, Eur. Phys. J. C, 78, 346, doi: 10.1140/epjc/s10052-018-5835-8 22
[555] Zhang, Y. Y., & Dai, C. P. 2021, Acta Astronomica Sinica, 62, 65 17
[556] Zhao, H. 1996, MNRAS, 278, 488, doi: 10.1093/mnras/278.2.488 41
[557] Zhao, H. S., & Famaey, B. 2006, ApJL, 638, L9, doi: 10.1086/500805 70
[558] Zlosnik, T. G., Ferreira, P. G., & Starkman, G. D. 2008, Phys. Rev. D, 77, 084010, doi: 10.1103/PhysRevD.77.084010 25
[559] Zonoozi, A. H., Lieberz, P., Banik, I., Haghi, H., & Kroupa, P. 2021, MNRAS, 506, 5468, doi: 10.1093/mnras/stab2068 25
[560] Zwicky, F. 1933, Helv. Phys. Acta, 6, 110 2
[561] Zwicky, F. 1937, Astrophys. J., 86, 217, doi: 10.1086/143864 2